APPROVAL SHEET

Title of Dissertation: Impact of cell substratum adhesion pattern and cluster spatial distribution on the development of *Staphylococcus aureus* biofilm under physiologically-relevant shear rates.

Name of Candidate: Opeyemi O. Ajayi

Doctor of Philosophy, 2018

Dissertation and Abstract Approved: _____

Dr. Julia M. Ross

Paul and Dorothea Torgersen Dean of Engineering

Virginia Tech College of Engineering

_____

Dr. Jennie B. Leach

Graduate Program Director

Chemical, Biochemical and Environmental Engineering

University of Maryland, Baltimore County

Date Approved: _____

ABSTRACT

Title of Dissertation: Impact of cell substratum adhesion pattern and cluster spatial distribution on the development of *Staphylococcus aureus* biofilm under physiologically-relevant shear rates.

Opeyemi O. Ajayi, Doctor of Philosophy, 2018

Dissertation directed by: Dr. Julia M. Ross

Paul and Dorothea Torgersen Dean of Engineering

Virginia Tech College of Engineering

Dr. Jennie B. Leach

Graduate Program Director

Chemical, Biochemical and Environmental Engineering

University of Maryland, Baltimore County

Bacterial cells, in nature, prefer to exist as a surface-attached coalescent community of slime-encased cells known as biofilms. This biofilm-forming existence offers several advantages to the cells, including evasion of host immune response, resistance to antimicrobials and antibiotics, communal expression of metabolites, and overall increased survivability in unfavorable environmental conditions. Biofilm formation has been observed for several species of bacteria across multiple scientific disciplines and affecting a wide variety of industries including the food industry, waste treatment, and healthcare. In healthcare settings, *S. aureus* is a major etiological agent of biofilm-based infections in humans. Furthermore, the hydrodynamic environment of the cardiovascular system complicates the eradication of biofilm-based infection due to metastasis of eroded cells to

multiple infection sites. Therefore, remediation efforts of staphylococcal infections are aimed at the prevention and disruption of biofilm development.

Regardless of infection site, pathogenesis is initiated by adhesion of planktonic cells to host tissue or implanted biomaterials, culminating in the formation of mature biofilm that can subsequently seed planktonic cells. In *S. aureus* the transition of adhered bacterial cells into biofilm depends on cellular production and detection of a signal peptide molecule called auto-inducer peptide (AIP). Biofilm development and virulence are regulated by the sensing mechanism of the cells to their local AIP concentration. With this in mind, I hypothesized that biofilm development may be inhibited by specifying initial parameters within the biofilm environment that influence local AIP concentrations; these parameters include fluid shear stress as well as the geometric features of initial cell-substrate adhesion, including distance between adhesion sites and the area of the adhesion sites on the substrate.

The broad objectives of this study were to characterize and quantify the morphology of *S. aureus* biofilms under fluid flow that were initiated on substrates with micropatterned cell-adhesion sites of controlled spacing, size, and total area. First, the underlying mechanism of biofilm-dependent growth was predicted via *in silico* simulation of AIP concentration. Then laboratory experiments demonstrated that: 1) increased spacing between microcolonies correlated with diminished *S. aureus* biofilm development; and 2) inhibition of biofilm development was greater when exposed to increased fluid shear stress. These findings unveil new strategies to potentially slow down or prevent biofilm-based infections in the human cardiovascular system.

Impact of cell substratum adhesion pattern and cluster spatial distribution on the development of *Staphylococcus aureus* biofilm under physiologically-relevant shear rates.

By

Opeyemi O. Ajayi

Dissertation submitted to the Faculty of the Graduate School

of the University of Maryland, Baltimore County, in partial fulfillment

of the requirements for the degree of

Doctor of Philosophy

2018

Dedicated to:

Aramide, Angelina and Alessandra

ACKNOWLEDGEMENT

As I reflect on the years it has taken to achieve this milestone, I have to begin by expressing my profound gratitude to Dr. Julia Ross, my advisor and mentor. Not only did my doctoral studies involve a switch in my professional discipline, but it also involved applying techniques of which I had no prior knowledge. Nevertheless, Dr. Ross gave me the tools I needed to begin, the guidance I needed to get through, and the motivation that I needed to complete this work. All while allowing me the autonomy to develop as a researcher, scientist and professional. I would also like to expresses a deep gratitude to Dr. Jennie Leach, my co-advisor and coach, for picking up the mantle in my final year-and-a-half and offering me an additional support system. I thank my dissertation committee comprised of Dr. Douglas Frey, Dr. Theresa Good and Dr. Patrick Ymele-Leki for offering me the expert advice that helped guide and advance this dissertation. Additionally, I would like to thank all my colleagues including my fellow graduate students and the undergraduates that help bring all our work to completion. I thank you all for the friendships that I've acquired and for making the time in graduate school a lot of fun. I would like to thank the rest of the faculty and staff of the Chemical, Biochemical and Environmental Engineering department. I would like to thank my family and friends for all the love and support over the years. I thank my mom and dad, my siblings – Bisi, Dapsy, Gbenga, Titi, Biodun and Lola for all of your love. Additionally, I thank my mother- and father-in-law, especially for all the support in the final year of my studies. Finally, I thank my wonderful wife, Ara, for all of the wonderful years she has been in my life and for bringing our two amazing girls – Angelina and Alessandra into my world.

TABLE OF CONTENTS

LIST OF TABLES

LIST OF FIGURES

Chapter 1: Introduction

1.1 Motivation for study

Staphylococcus aureus, a gram-positive opportunistic pathogen, is a leading etiological agent of bacterial infectious diseases in humans and animals. In both livestock animals and humans, *S. aureus* is found, asymptomatically, in healthy carriers such as in the nasal cavity of ~20% of humans [1-4], and on the skin of 90% of poultry, ~42% of pigs and ~20% of cows [5, 6]. However, *Staphylococcal* skin infection such as dermatitis is common in animals and more serious infections are possible such as infective mastitis in farmed dairy cows [4]. For these reasons, antibiotic use has long been common practice among livestock farmers [7]. In humans, *S. aureus* causes benign external diseases such as skin infections but more importantly, they cause invasive acute infections such as arthritis, osteomyelitis and sepsis [8-10]. *S. aureus* is also a major etiological agent of cardiovascular infections and diseases affecting implanted medical devices such as infective endocarditis [11-15]. Despite technological improvements in the medical field and on diagnosis, infective endocarditis still carries a high mortality rate in humans with 15-20% mortality reported in 2009 [12, 15, 16] and up to 30% as recently as 2015 [17]. Blood-borne *S. aureus* infections can be nosocomial or community-acquired [1, 18] and a recent report shows that 30% of all infective endocarditis cases are nosocomial in origin [17]. In general, cases of *S. aureus* infections are usually associated with the high healthcare costs of prevention, diagnosis, and treatment [19].

There are many reasons for the prevalence of *S. aureus* infections. One such reason is that *S. aureus* expresses a wide variety of virulent factors [20]. These virulent factors confer the ability to cause infection in a wide variety of systems from external systems like the skin to the blood [2, 9]. Additionally, the prevalence of infections is exacerbated by the evolution

of multiple antibiotic resistant isolates that further complicates the therapeutic challenges faced when combating infections [2, 18, 21-24]. Methicillin resistant *S. aureus* (MRSA) is the most common antibiotic resistant strain that has been associated with a wide variety of community-acquired (CA) infections in countries around the world [18]. In addition to antibiotics resistance, CA-MRSA, due to unknown factors, is reported to possess increased virulence, causing new diseases to emerge, compared to nosocomial strains [18].

The invasiveness of *S. aureus* has been attributed to its capacity for adherence onto several host matrix proteins including collagen and fibronectin [25-28]. Further invasion and colonization of non-motile cells at the infection site leads to the formation of an aggregation of cells known as a biofilm. Biofilm-based *S. aureus* infections are a major etiological agent of recurring infections and of diseases involving indwelling medical implant devices in humans [9, 29, 30]. These biofilm-based *S. aureus* cells differ from their planktonic counterparts, notably by exhibiting a greater resistance to host immune responses and antimicrobial therapies [9, 17, 23, 29, 31]. It is largely accepted that the formation of biofilm by bacteria is in part a survival strategy of the cells resulting in antibiotic resistance [2]. This antibiotic resistance strategy of bacteria has led to an increase in the study of biofilms by the scientific community.

In all cases of biofilm infection, including those caused by *S. aureus,* adherent cells communicate with each other via the release and detection of small signal molecules. In the case of *S. aureus*, auto-inducer peptide (AIP) molecules are released and detected by individual cells and their neighbors, resulting in the phenomenon widely known as quorum sensing (QS) [31-34]. The formation and secretion of the AIP signaling molecules is

metabolically “inexpensive” and the sensing of these molecules directly affects other cellular expression patterns [34, 35]. Thus, it has been proposed that cells utilize the sensing of these signal molecules to detect the mass transfer conditions of their immediate environment by “efficiency sensing”. Additionally, efficiency sensing is for the purpose of detecting a suitable state for the production of expensive metabolites such as those involved in virulence or biofilm formation [35, 36]. Independent studies have corroborated that single bacteria cells confined within an enclosed matrix exhibit quorum response to a signal molecule that they produce [37, 38]. In those works, it was shown that the local AIP concentration around an individual cell, not the presence of other cells in the vicinity forming a quorum, determines its response to the signal molecule.

Parameters of the cellular environment that increase local AIP concentration therefore have the potential to promote biofilm development and virulence, and vice versa. Such parameters include the physical spacing of individual bacterial cells and cell clusters and the total density of adherent cells. In this work, I hypothesized that the geometrical arrangement of adherent *S. aureus* cells affects a biofilm’s physical and morphological development under physiologically-relevant shear conditions. The focus on physiological shear rates, such as those found in the human cardiovascular system, allows for direct implication of the findings of this work towards achieving improved therapies for bloodborne *S. aureus* infections.

Previous studies have described the use of substratum manipulation of adherent cells to study biofilm development [39-41]. However, these studies were performed under static experimental conditions and they relied on large time scale experiments (24 hours to several weeks) for biofilm development in relation to the focus of each study. These studies have

made significant contributions to investigating the effects of surface modification to biofilm development. However, the influence of physiological shear on the manipulated adhesion is unknown. One of the main purposes of research is to mimic, as closely as possible, the conditions of the target of the findings. Hence, the relevance of investigating the impact of physiological shear on the manipulated adhesion is necessary for elucidation of infection mechanisms during, for example, the infection of indwelling implant devices.

Additionally, the focus of this work is on the microscale control of *S. aureus* adhesion. Therefore, the focus is largely on biofilm development for shorter time scales. The primary reason for this is that at large time scales, differences in biofilm development by micropattern configurations are obscured by the complex heterogeneities that develop as time passes. The goal of this study is to determine how specific physiological shear promotes or diminish *S. aureus* biofilm development during the early stages of biofilm development following controlled adhesion of cells in micropatterned colonies. Achievement of this study goal could lead to the development of better preventive therapies for biofilm development on implant medical devices.

1.2 Pathogenesis of biofilm infections

Biofilms are sessile communities of cells that grow in a communal manner, on both biotic and abiotic surfaces, within a matrix of polysaccharide molecules that the cells themselves produce. Bacterial biofilms in nature can be formed from a single species or comprised of multiple species, and the phenotype of biofilm cells differ from that of their planktonic counterpart [42-45]. Studies into the development of biofilms is challenging due to their complex and heterogeneous nature. One of the main challenges arise from the lack of standardized biofilm study protocols largely due to the study of biofilms being relatively new compared to the study of suspension cultures [46, 47]. Additionally, there are currently no set standards for the numerical analyses of biofilms. In fact, software capable of quantifying biofilm structures were only made possible by advances in confocal laser scanning microscopy [48].

As a mature microbial biofilm develops, its three-dimensional architecture becomes more complex [42]. As this happens, porous channels are formed as part of the three-dimensional structure that enable the transport of nutrients and waste to and from cells within the biofilm community [42, 49]. This three-dimensional structure is primarily maintained by the secretion of an exo-polymeric slime (EPS) slime by the cells [42, 50]. The EPS confers encased cells with added protection against antimicrobial agents, while the presence of the porous channels promotes their survival. From a public health perspective, host defense responses have a diminished effectiveness against biofilm-based infections [42]. Furthermore, as a result of the physiological shear imposed by the bloodstream, biofilm infections possess the cancer-like possibility to metastasize to other infection sites [51]. This

metastasis is due to non-rigid, fluid properties of the EPS and its ability to slough off chunks of itself or seed individual cells.

1.2.1 Development of *S. aureus* biofilm under hydrodynamic shear

S. aureus is one of the most important etiological bacterial agents of bloodborne diseases and implant device-based infections. Regardless of the infection site, the pathogenesis of *S. aureus* infection is initiated by the invasion and adhesion of the individual cells to host extracellular matrix (ECM) protein or an implanted biomaterial [23, 42, 43, 49-52]. This critical adhesion step ultimately leads to the formation of mature biofilm by a complex process that includes other important milestone steps including colony formation, accumulation and dispersion (Figure 1.1). Following adhesion to a surface, cells quickly begin to accumulate by adhesion of other cells in the vicinity to already attached cells or by clonal multiplication [9, 10, 43]. The accumulation of these planktonic cells onto the infection site initiates a pathway to the formation of a biofilm [2, 9, 27, 43, 49, 50, 52-54].

The adhesion step, which initiates pathogenesis for *S. aureus* infection can occur through a variety of pathways. Adhesion can proceed in static non-flow environments via sedimentation, Brownian motion of cells or in the case of motile bacterial, active movement to infection site [55, 56]. Within a dynamic environment, convection currents within a bulk liquid containing bacteria can transport cells to a suitable surface. Consequently, electrostatic and physical interactions between the cells and surface facilitate cell adhesion [55, 56]. The adhesion of *S. aureus* cells to components of host plasma and ECM proteins is mediated by

its cell surface adhesins collective referred to as “microbial surface components recognizing adhesive matrix molecules” (MSCRAMMs) [20, 29].

The adhesion and growth of *S. aureus* cells on various host ECM proteins under physiologically relevant hydrodynamic shear conditions has been extensively studied [25, 51, 57-63]. Additionally, varying the hydrodynamic shear conditions experienced by adherent cells influences the development of *S. aureus* biofilm (Figure 1.2) [64]. Furthermore, at lower shear rates, nutrient mass transfer impact biofilm development significantly more than at higher shear rates (Figure 1.3) [64]. The implications of these observations are that higher shear rates result in biofilm developmental changes that cannot be attributed to nutrient limitations affecting the normal cellular growth. The question thus remains of the mechanistic influence that variation of shear rates has on biofilm development in the absence of nutrient limitation.

1.2.2 *S. aureus* cell-to-cell communication

Adherent *S. aureus* cells that form microcolonies recognize and respond to one another by quorum sensing (QS) [31-34, 36, 65]. In *S. aureus* the accessory gene regulator (*agr*) locus is responsible for regulating the quorum sensing system. The *agr* locus comprises two divergent transcription units, P2 and P3, that code for the *agrBDCA* and RNAIII transcripts respectively. The *agrBDCA* transcript exhibits a feedback loop in the production and detection of the signal molecule, AIP, with the RNAIII transcript acting as an effector of the feedback response [34, 66-70]. RNAIII expression increases the transcription of several

secreted virulence factors including toxic shock syndrome toxin and δ-hemolysins as well as regulating biofilm development [34, 71].

1.2.2.1 Role of the *agr* system in *S. aureus* biofilm development

The *S. aureus agr* locus is responsible for the production and detection of AIP (Figure 1.4 A). A product of *agrD* transcript expression, AIP is processed and transferred extracellularly by the transmembrane transcript of *agrB* gene. The extracellular AIP molecules are subsequently detected by the transmembrane product of *agrC* that, through a cascade of phosphorylation reactions, activates the *agrA* transcript byproduct [34, 68, 69, 72, 73]. The a*grC* transcript is a histidine protein kinase sensor while agrA is the response regulator – this *agrC-agrA* couple acts as a two-component regulator system to detect the extracellular AIP molecules [73].

There are four distinct classes of *agr* systems (*agr* I – IV) that have been identified in different *S. aureus* strains and each encode and detect a unique autoinducer structure (AIP I – IV) shown in Figure 1.4 B [68, 73, 74]. The four AIP structures differ in their peptide chain, ranging from seven to nine residues. However, a thiolactone ring is conserved among all four types [74, 75]. Although the exact function of the thiolactone ring is yet unknown, it is formed during the processing and subsequent extracellular transport of AIP by the *agrB* transcript [76, 77].

The *agr* locus contributes to *S. aureus* virulence expression in biofilm-associated infections such as endocarditis and osteomyelitis. However, the precise mechanism of

executing this role varies depending on the infection type [34]. Although the function of the *agr* locus of *S. aureus* is primarily to promote the cell-to-cell communication by AIP biosynthesis, secretion and detection, this function shifts alongside the phenotype change that occurs following the detection of a quorum [34, 67, 70, 78-80]. For example, the *agr* locus is also involved in *agr*-mediated dispersal of biofilm [67, 81]. The delineation of the *agr* locus function and its involvement in QS has contributed to its potential as a target for therapeutic treatment of bacterial infections [65, 75, 82, 83].

1.2.2.2 Quorum, diffusion and efficiency sensing

Quorum sensing (QS) is commonly described as the phenomenon of bacterial cell-to-cell communication relying on the interaction of a diffusible signal molecule and a sensor, for the purpose of detecting a quorum. This QS enables cells to couple gene expression with perceived local cell population density detected by each individual cell [32, 34, 36, 73, 84]. This mechanism allows each cell that makes up the quorum to detect the population density based on the local concentration of the signal molecule. Thus, facilitating the detection of optimal conditions for a phenotypic shift where-in the quorum behave collectively as one organism; disregarding individual phenotypic gene expression. Several bacterial strains utilize the QS signaling system. For example, *Pseudomonas aeruginosa* cells utilize the intercellular signaling system to regulate a phenotypic shift to biofilm formation [85].

Traditionally, QS has been applied as an encompassing term describing all signal-based cell-to-cell communication and response. Following this theory, an underlying

criterion of QS is that multiple cells are present to benefit and cooperate as a group. However, the group requirement of cell-to-cell signaling has been debunked as a requirement for cells to exhibit a phenotypic response. For example, in one study, a single *S. aureus* cell was isolated within a nanostructured matrix and it self-induced the QS pathway, as well as developed a group-like virulence response [37]. Similar behavior has also been observed in *P. aeruginosa* [38]. This concept of cell-signaling, refined to account for the local cell environment as a factor in the communication mechanism, was referred to as diffusion sensing (DS) [36, 84].

Hense *et al* proposed a unifying terminology encompassing all cell-signaling communication pathways known as efficiency sensing (ES) [35]. The ES hypothesis states that cells measure a combination of environmental qualities – cell density, spatial distribution, and limitations to autoinducer mass transfer – for the purpose of detecting optimal conditions of all three qualities for production of more metabolically taxing transcription products [35, 36]. Regardless of terminology used to describe the phenomenon of cell-to-cell sensing, it is scientifically accepted that once the signal molecules leave the cell, factors such as fluid dynamics and spatial geometry influence its mass transfer within that environment. This phenomenon, in part, contributes to the research field focused on discovery of QS analogs that may be applied in therapeutic treatments [65, 86-88]. A summary of the three cell-to-cell sensing mechanisms is provided in Table 1.1.

1.3 Applications of microfabrication in biological studies

Microtechnological tools are becoming increasingly popular additions to the repertoire of tools utilized in studying biological systems. Microtechnology involves the fabrication and application of micron and sub-micron scale structures as diagnostic tools in studying and manipulating microorganisms in their immediate cellular microenvironment [89-91]. Specific microtechnology tools that have frequently been employed in biological research include lithography and microfabrication. Photo-lithography, a process that was originally developed for the manufacture of microelectronic circuits, was first employed for the development of DNA microarrays in landmark studies that introduced the possibilities of microtechnology in biological research [92-95]. Photo-lithography is an expensive process for microfabrication and it has limitations over the properties of the substrate as well as the material that is patterned [90].

Soft-lithography is a more accessible process for the microfabrication and printing of surfaces with biologically relevant materials. This lithography process is more flexible with respect to the surfaces that can be printed on as well as the material of the ink used in printing. For biological studies, it is often necessary to fabricate surface prints with properties that allow linkage with biological organisms of interest. For example, self-assembled monolayers of thiolates on gold or glass surfaces have been utilized in studying biologically relevant surface modification [90]. Additional research opportunities that have been facilitated by the application of soft-lithography include the isolation of single cells in microfabricated structures for studying quorum sensing [37, 38], fabrication of rigid poly

(dimethyl siloxane) (PDMS) structures for studying the effect of physical barriers to biofilm formation [39-41, 96-99], and investigating multispecies biofilm formation [100, 101].

1.3.1 Influence of microtopography on biofilm development

Toward the end of the last decade, researchers from the laboratory of Dr. Anthony Brennan at the University of Florida discovered that unlike large marine vessels such as submarines and freightliners and large marine wildlife such as whales and manatees, sharks do not get fouled by marine bio-organisms like algae and barnacles [102]. Further investigation revealed that shark skin, unlike the other large marine animals', possessed what have been referred to as dermal denticles – micro-scale-sized diamond-shaped scales that have micropatterned ridges, on the surface of their skin [103, 104]. Furthermore, topographical diamond-shaped pattern of 2 – 10 μm spaced ridges varying in length from 4 – 16 μm diminished biofilm development compared to a non-patterned surface by a variety of bacterial species including *Escherichia coli*, *P. aeruginosa* and *S. aureus* [39-41, 104-107]. However, the underlying mechanism for this inhibitive effect is unknown.

Conventional methods for treatment of biofilm-based infections involve the use of antimicrobials to kill the pathogen. However, this antimicrobial use has led to the existence and proliferation of increased resistance in bacterial pathogens to antibiotics like methicillin and vancomycin. Therefore, new therapeutic strategies are needed to manage bacterial growth while avoiding antimicrobials that contribute to the observed trend in bacterial resistance. Such a strategy may be found in the use of these topographical features to control

the adhesion of the bacterial pathogen, thus influencing biofilm development. This body of work focuses on *S. aureus* as the target bacterium, thus, the micropattern dimensions designed here are influenced first by its cell size (~ 1 µm). The micropatterns in this work were designed in the form of microcolony arrays of equally spaced dots. The size of each microcolony was 10 µm so that following adhesion of *S. aureus* cells by sedimentation, the number of cells in each microcolony is ~ 100 cells-per-dot.

1.3.2 Micro-contact printing

Micro-contact printing (µCP) is a soft-lithography process that employs mechanically soft materials such as PDMS to develop micron scale patterns of biological material [108]. µCP is the most common soft-lithography technique utilized in biological studies due to being a relatively inexpensive process that does not need very specialized equipment to achieve complex micropatterns. The process involves the development of a PDMS stamp with surface relief features matching the desired printing pattern. The patterned surface is then inked and printed onto a desired substrate in a process that is analogous to a traditional document stamping [90, 100, 108, 109]. In this study, µCP was utilized for controlling the adhesion pattern of *S. aureus* cells by printing the protein, fibronectin, on glass.

1.4 Quantification of biofilm morphology by image analysis

The common analytical method in biofilm studies utilizes two-dimensional image analysis. However, these two-dimensional images do not adequately capture some of the structural characteristics of developed biofilm such as the surface heterogeneity and roughness, biofilm thickness, and porosity. The introduction of confocal laser scanning microscopy (CLSM) expanded biofilm analyses to include three-dimensional image capture. These three-dimensional images enabled qualitative analyses for the structural characteristics not possible via two-dimensional image analysis such as the roughness and biofilm thickness. The evaluation of biofilm internal structure was yet not possible via qualitative evaluation of the three-dimensional images.

In traditional scientific dogma, the ability to recreate experimental data among peers is a crucial tool in verifying findings as well as improving studies for further advances. In biological studies, verification of findings is typically difficult to achieve due to the variations that are inherent to experiments involving living organisms. With biofilms in particular, this a specific challenge because of the wide heterogeneities that make up an intrinsic part of biofilm development. Comparing data from separate experiments is challenging due to the personal bias introduced by individual investigators having different perspectives of the visual observations of developed biofilm from qualitative analyses of two- or three-dimensional images. Finally, these challenges are exacerbated by the lack of standardizations for visual or numerical characterization of biofilms.

To this end, numerical methods are increasingly utilized as a tool in standardizing the quantitation of developed biofilms' structural features. Parameterizing these features can

provide an additional tool for the study of biofilms since they can provide experimental values for statistical analyses of biofilm characteristics [48, 110]. Numerical software currently utilized in quantifying three-dimensional biofilm structures include COMSTAT and image structure analyzer – both of which utilize exported image output of CSLM. Image structure analyzer in three dimensions (ISA3D) was utilized in this study to quantify the features of developed biofilm structure such as biovolume, biofilm thickness, and porosity among others. The MATLAB-based software utilizes the image output of CSLM to reconstruct a three-dimensional representation of the biofilm for analysis by ISA3D [48, 110-112].

To maintain consistency in the analysis of these parameters, an automated image threshold was applied by ISA3D. This threshold is done by converting the exported CSLM images to black-and-white images representing biofilm material and interstitial space [113]. Due to the variations in CSLM image acquisition originating from different laser settings and fluorophore intensity, the image threshold offers a route to consistency. The automated image threshold eliminates bias among multiple users, thus ensuring a more robust analysis. A summary of the parameters calculated by ISA3D are provided in Table 1.2, while a brief description of the biovolume, porosity, thickness and roughness utilized in characterizing biofilms in this body of work are described below. It is important to note that each of these parameters by themselves do not completely describe a biofilm but taken together, provide a description of biofilm physiological characteristics.

1.4.1 Biovolume

Three-dimensional biofilm structures are inherently volumetric. Thus, one of the first parameters that was used to quantify biofilm structure was biovolume [114]. The biovolume represents an estimate of the biomass within biofilms as well as their bulk volume [115]. It is determined by the numerical integration of the voxels – the pixels in all three dimensions (x, y (along the plane of each CSLM image), and z (the distance between each image)) – across the stack of images [114-117].

1.4.2 Biofilm thickness

The thickness of biofilms is another measure of the physical properties that determines biomass accumulation during biofilm development. Due to the variability of the surface of biofilms, two thickness parameters are calculated; the mean and maximum thicknesses. The maximum thickness is determined as an average over the maximum 5% of the thickness measurements across the surface of the measured biofilm [111].

1.4.3 Porosity

As the three-dimensional matrix of biofilms develop, porous channels are formed. These porous channels enable the transport of solutes both within biofilms and between biofilm and bulk fluid [42, 112]. This feature is therefore important to determine the progression of biofilm development. The parameterization of this feature is achieved by

calculating the ratio of the total volume of interstitial space (or void space within biofilm) to the total volume of biofilm [110-112].

1.4.4 Diffusion distance

The diffusion distance for a cluster is a measure of the distance from the cells in the cluster to interstitial space [110, 111]. The maximum diffusion distance is the largest calculated value within any cluster [111]. Unlike the traditional diffusion distance that involves diffusion coefficient and molecular weight of a diffusible solute, the diffusion distance calculated by ISA3D is the physical distance through the biofilm that any solute has to travel from interstitial space.

1.4.5 Roughness

The roughness coefficient is determined based on the variability in the calculated thickness across the surface of biofilms [115]. This parameter is used to determine the overall increase in heterogeneity of the developed biofilm structure that is often represented by an increase in the surface roughness. The roughness is due to the formation of structures of varying height across the surface of the biofilm [110, 111, 115].

Table 1.1: A summary of descriptions for quorum sensing, diffusion sensing and efficiency sensing [35]. In each row, the descriptions of what cells are sensing, why cells are sensing and the benefits of the sensing mechanism to either individual cells or groups/clusters of cells.

	Quorum Sensing (QS)	**Diffusion Sensing (DS)**	**Efficiency Sensing (ES)**
How Cells Sense	Individual cells emit small diffusible autoinducer molecules that are sensed by themselves and others, leading to regulation of gene expression. This mechanism is referred to as autoinducer sensing to avoid implying what and why cells sense and who benefits from the sensing		
What Cells Sense	Cell density (or, less accurately, the cell number). An ensemble property on the population scale, not only defined at the positions of individual cells.	Mass-transfer properties of the environment surrounding a focal cell. Independent of cell density and spatial distribution.	A combination of cell density, mass-transfer properties and spatial cell distribution as the cell cannot determine density, mass transfer or clustering alone.
Why Cells Sense	To detect situations where cell density is sufficient to make a coordinated response of a group of cooperating cells worthwhile.	To detect situations where mass transfer is sufficiently limited for single cells to respond by producing extracellular diffusible effectors.	To estimate the efficiency of producing extracellular diffusible effectors and to respond only when this is efficient.
Benefits	Hypothesis suggests QS evolved because of group fitness benefits.	Hypothesis suggests DS evolved because of individual fitness benefits, making DS a simpler hypothesis than QS.	Hypothesis suggests ES evolved because of both individual and group fitness benefits. Both work in the same direction, yielding broader conditions where ES would be selected for.

Table 1.2: Summarized description of parameters calculated by Image structure analyzer (ISA3D). These parameters are used to quantify the physiological properties of developed biofilms from CLSM images [48, 110, 111, 113-118].

Parameter	Description
Biovolume (BV)	Average three-dimensional coverage of biofilms, calculated as an integral over all pixels with the biomass present.
Volume to Surface-area Ratio (V2SA)	Ratio of the biovolume to the total surface area of a cell cluster. This is another parameter for determining the three-dimensional biofilm coverage.
Porosity (P)	The porosity is defined as the ratio of void volume to total volume.
Mean Diffusion distance (ADD) & Maximum diffusion distance (MDD)	The diffusion distance for a cluster is a measure of the distance from the cells in the cluster to interstitial space. The maximum diffusion distance is the largest calculated value within any cluster.
Aspect ratio (AR)	The aspect ratio is defined as the ratio of the average length of biofilm in the x-direction to the average in the y-direction. It is used to indicate symmetry (or asymmetry) of cluster growth in either the x- or y-direction.
Mean thickness (MT) & Maximum thickness (MaxT)	The thickness describes the vertical direction height of biofilms calculated from the substratum to its surface. The maximum thickness is calculated from the highest 5% values of biofilm thickness.
Fractal dimension (FD)	Fractal dimension is used for quantifying the roughness of the boundaries of cell clusters. A higher fractal dimension indicates a more irregular cell cluster surface.
Roughness	The roughness coefficient indicates the variability in biofilm thickness. This differs from the FD that describes the variability in the surface of the cell clusters in three-dimensions. The roughness coefficient specifically describes the variability in the z-direction only.

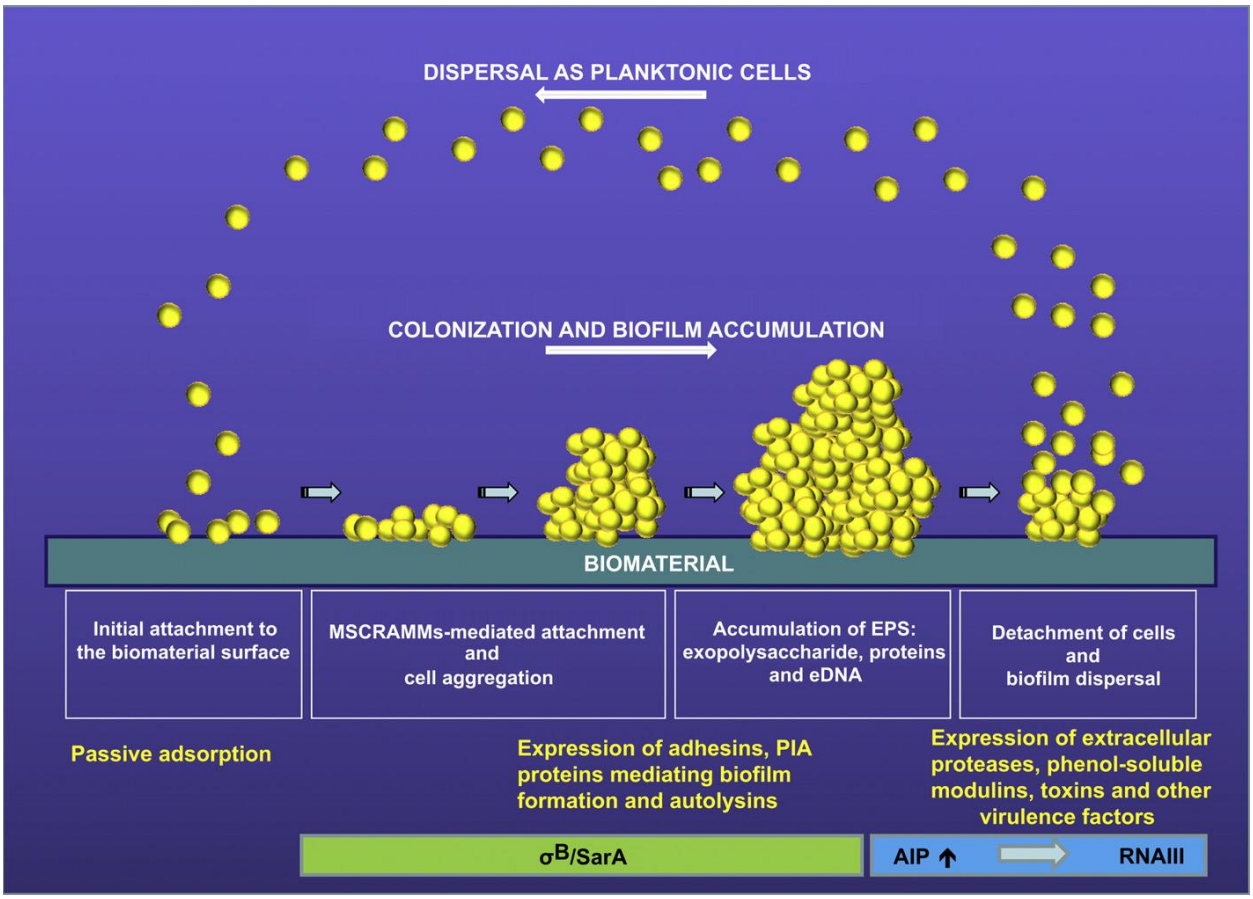

Figure 1.1: Pathogenesis of *S. aureus* biofilm development. [29]

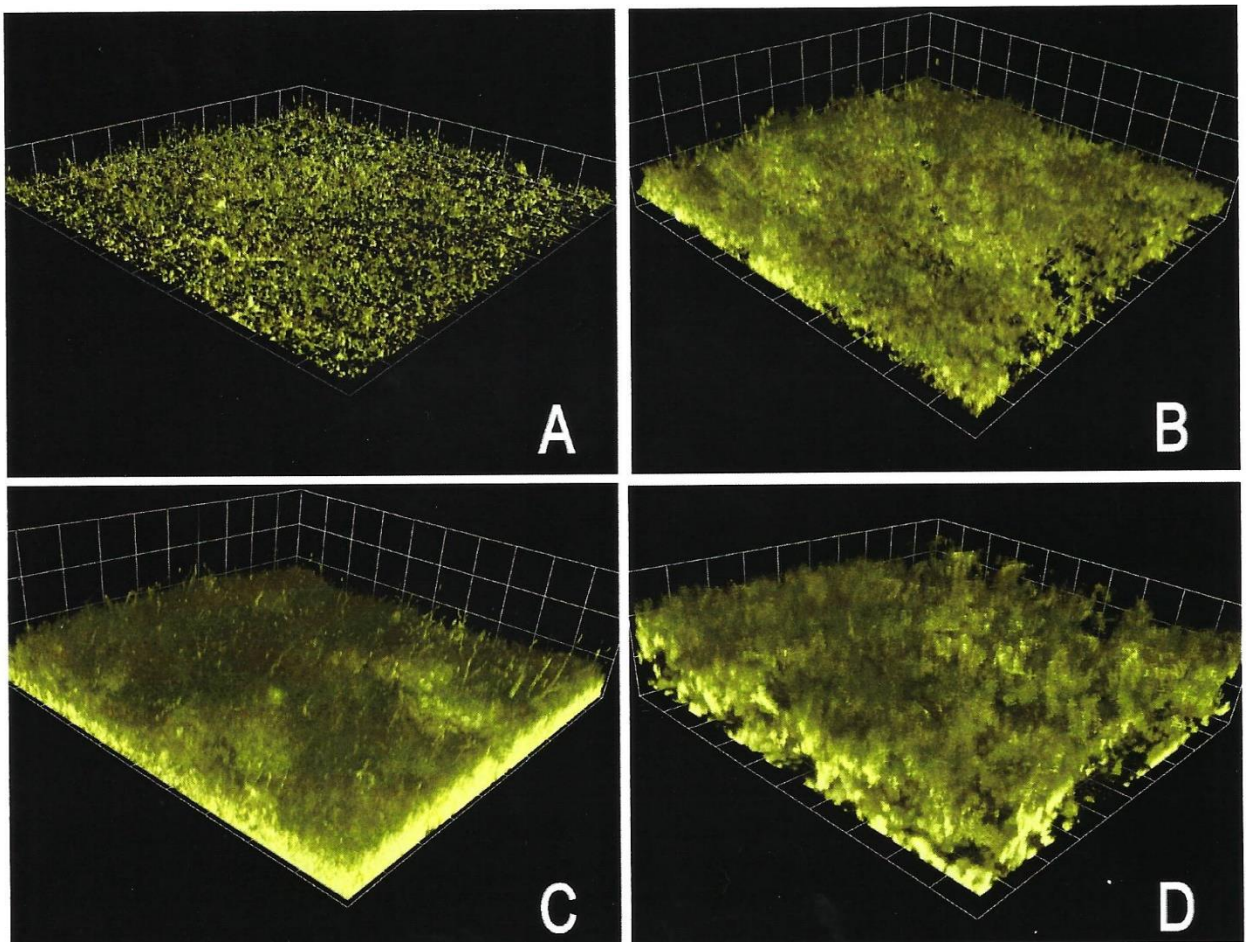

Figure 1.2: Influence of fluid shear on *S. aureus* biofilm development. Adherent cells at a density of ~20000 cells mm^{-2} on collagen was subjected to physiologically relevant shear of (**A**) 50 s^{-1}; (**B**) 100s^{-1}; (**C**) 300s^{-1}; (**D**) 500s^{-1} by continuous flow of TSB media for 8 hours. [64]

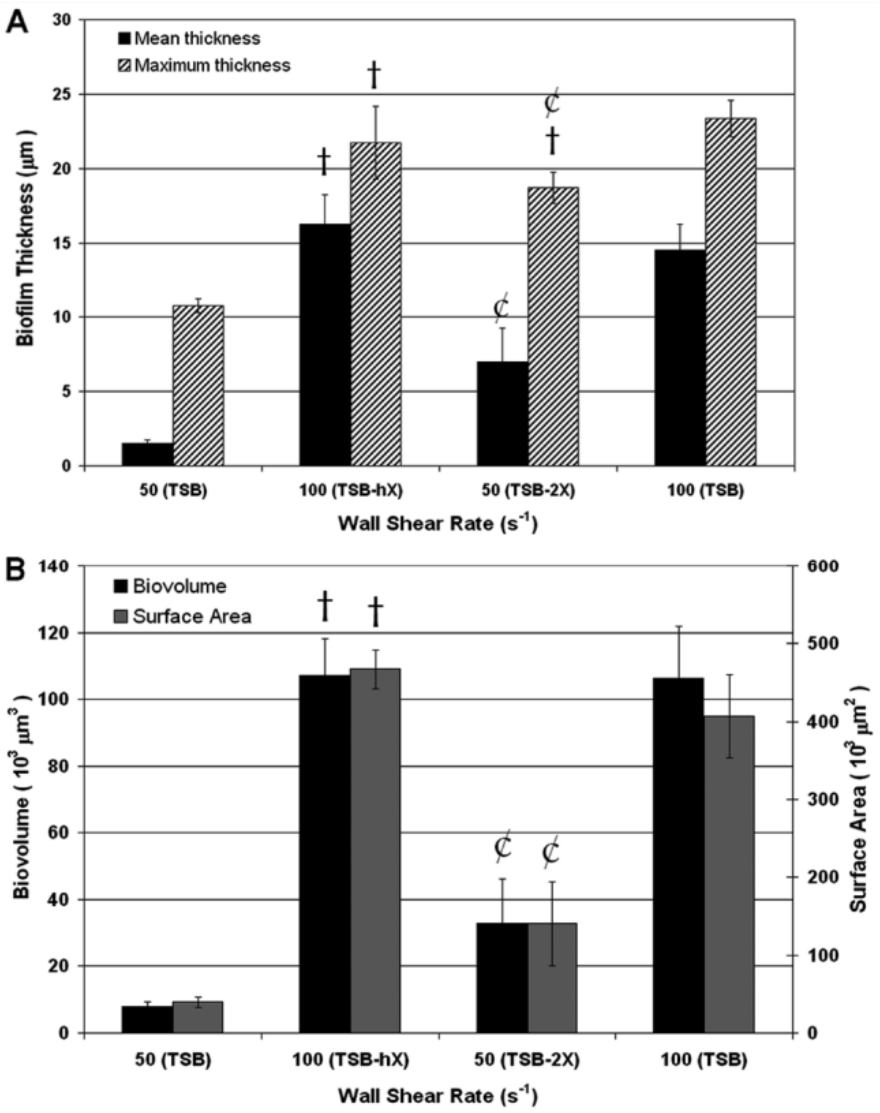

Figure 1.3: Influence of media concentration on *S. aureus* biofilm development under fluid shear [64]. Adherent cells at a density of ~20000 cells mm^{-2} on collagen was subjected to flow and (**A**) mean and maximum thickness, and (**B**) biovolume and surface area are shown. An increase in media concentration at 50 s^{-1} increased biovolume and thickness, while at the higher 100 s^{-1} an increase in media concentration did not significantly change the biofilm characteristics. † indicates statistically significant difference ($p < 0.05$) versus biofilms at 50 s^{-1} in TSB. ¢ indicates statistically significant difference against biofilms at 100 s^{-1} in TSB.

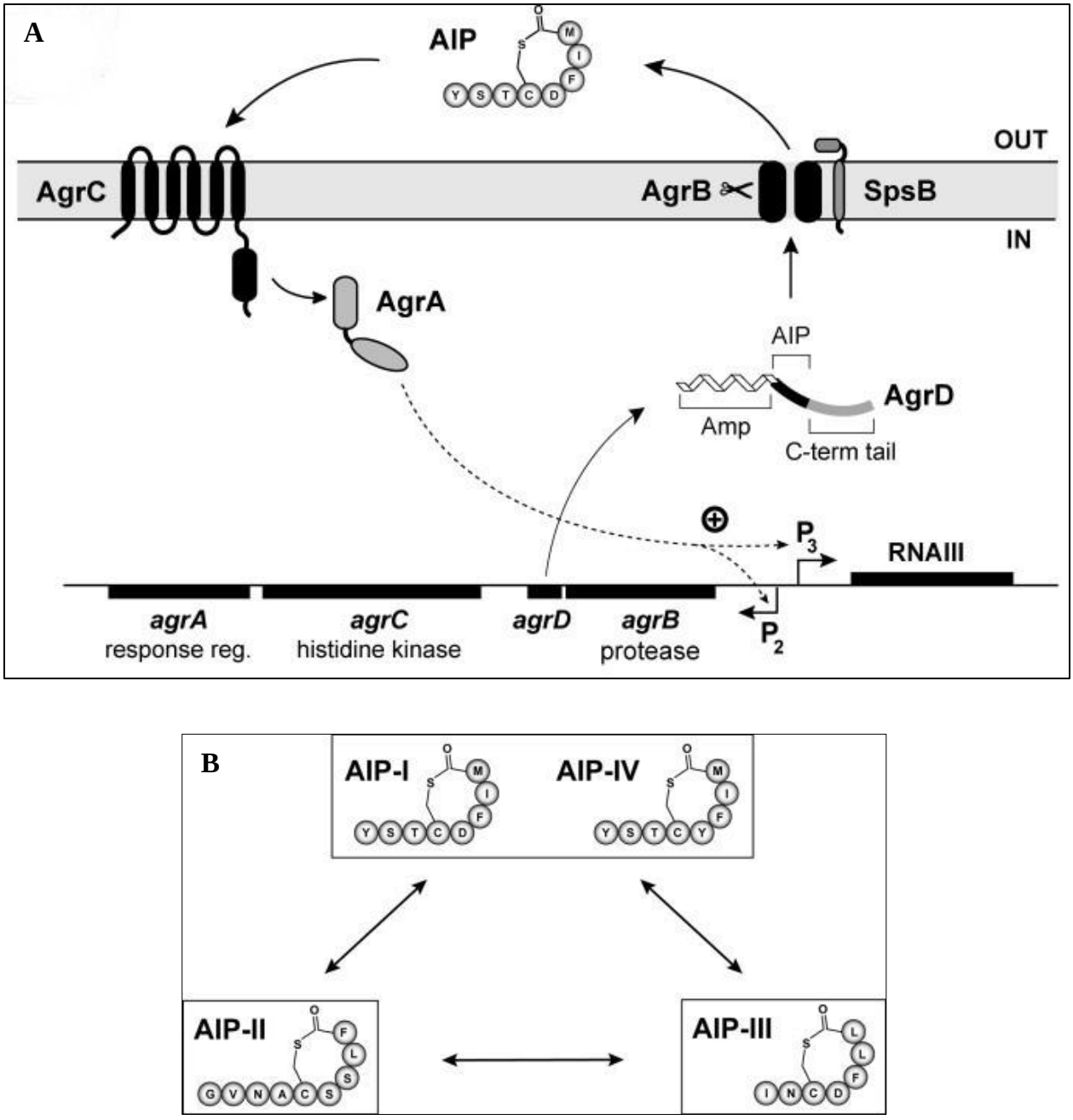

Figure 1.4 (A): The *S. aureus agrBDCA* locus showing the divergent P2 and P3 transcripts; as well as a breakdown of the production and detection of the AIP [68]. **(B):** The four different autoinducer peptides produced by different *S. aureus* species. The groupings and arrows indicate cross inhibitory groups [74].

Chapter 2: Materials, methods & preliminary Data

2.1 *S. aureus* strains

The following selection of S. aureus strains were kindly provided by the laboratory of Dr. Alexander Horswill (Department of Immunology & Microbiology, University of Colorado Anschutz Medical Campus). A summary of the selection is listed in Table 2.1. All strains are self-reporting (as described below), which eliminated the need for biofilm staining during the entire procedure.

S. aureus strain AH1979 is a fluorescent self-reporting strain transformed with plasmid for staphylococcal accessory regulator A P1 promoter (*sarA* P1)-dependent superfolder green fluorescent protein (sGFP) expression. Due to this transformation, each cell expresses sGFP at all times during growth. The plasmid was maintained by the presence of chloramphenicol (CAM) resistance. This strain was selected for all principal experiments in this study due to the sGFP having better stability and greater fluorescence intensity than yellow fluorescent protein (YFP) and mCherry [119].

S. aureus strain AH1218 is a fluorescent self-reporter strain with plasmids for *agr* P3-dependent mCherry expression and *sarA* P1-dependent YFP10B expression. Due to the *sarA* P1 transformation, the cells express YFP at all times during growth. Due to the agr P3 transformation, the cells express mCherry in response to *agr* activation. *S. aureus* strain AH1219 is a knockout *agr* mutant strain of *S. aureus* AH1218 [119, 120]. Both of these strains were selected and utilized for initial preliminary experiments involving fluorescent reporters for biofilm development. In both strains, plasmids for *agr* P3 and *sarA* P1 were maintained by CAM and erythromycin (ERM), respectively.

2.2 *S. aureus* strains characterization and growth conditions

2.2.1 Preparation of stock reagents

Stock antibiotic solutions were prepared as 50 mg mL^{-1} aliquots each of chloramphenicol (CAM; Sigma-Aldrich Cat. No. C0378) or erythromycin (ERM; Sigma-Aldrich E5389). Stock media solution was prepared as 27.5 g L^{-1} of tryptic soy broth (TSB; Fisher Scientific Cat. No. DF0370-17-3). *S. aureus* AH1979 required 10 µg mL^{-1} of CAM only to maintain the plasmid. *S. aureus* AH1218 and 1219 each required both antibiotics at 10 µg mL^{-1} of CAM and 10 µg mL^{-1} of ERM to maintain the plasmid [119]. To achieve this, 10 µL of the respective stock antibiotic was added to 50 mL of TSB in the flask prior to inoculation.

2.2.2 Tryptic soy agar plates for plasmid purification

Agar stab cultures for each of *S. aureus* strains AH1979, AH1218 and AH1219 were received from the laboratory of Dr. Horswill; the transformed strains were purified and cultured in preparation for cryogenic storage. Tryptic soy agar (TSA) was prepared by adding 27.5 g of TSB and 15 g of agar (Fisher Scientific Cat. No. BP1423) to 1 L of deionized water. Following sterilization by autoclave, the relevant antibiotic was added to a final concentration of 10 µg ml^{-1}. The resulting TSA was poured into a petri-dish, allowed to cool and samples from the stab cultures were streaked onto the plates. The plates were incubated overnight at 37°C under aerobic conditions. A single colony was selected from

each plate and used to inoculate a suspension culture and each flask was incubated for 14 hours. Frozen cell cultures were prepared by mixing 20% glycerol (Sigma-Aldrich Cat. No. G7893) solution and the suspension culture at a 1:1 ratio and aliquot into 1-mL freeze vials. Vials were stored at -80°C until ready to use.

2.2.3 *S. aureus* suspension cultures

Primary suspension culture was prepared by transferring 10 µL of thawed glycerol stock culture into 50 mL of appropriate media + antibiotic solution in a 250 mL Erlenmeyer flask and incubated with shaking at 140 rpm and at 37°C in a M1247-0004 incubator-shaker (New Brunswick Scientific), for the desired duration. To generate the characteristic growth curve for each strain (Figure 2.1 & 2.2), samples were collected every hour or two from the primary suspension cultures and the optical density at 600nm wavelength (OD_{600nm}) was recorded with an Evolution 600 Spectrophotometer (Thermo Scientific). Cell counts were performed with a Multisizer 3 Coulter Counter (Beckman Coulter, Inc.).

2.2.4 Confirming the ability of the *S. aureus* strains to form biofilm by the Congo red agar assay

A bacterial strain's ability to form a biofilm is tested by staining for polysaccharide slime production by the Congo red agar (CRA) assay [64, 121, 122]. In this assay, biofilm producers typically turn black in color, indicating the presence of exo-polymeric slime [64, 121, 122]. CRA plates were prepared as previously described [64]; 0.08% (w/v) of Congo

red (Sigma-Aldrich Cat. No. C6277) and 36 g of sucrose (Sigma-Aldrich Cat. No. S7903) were added to 1 L of brain heart infusion (BHI) agar (Fisher Scientific Cat. No. DF0418-15-9) [121]. To maintain the plasmids, appropriate antibiotic was also added to each plate to a final antibiotic concentration of 10 µg ml^{-1}.

Suspension culture flasks with each strain were cultured for ~14 hours before being harvested and diluted 1:20 in phosphate buffered saline (PBS; Sigma-Aldrich Cat. No. P3813). The diluted suspension was then streaked onto the CRA plates and incubated at 37°C for a minimum of 24 hours. The *S. aureus* Phillips strain was used as a positive control for the CRA assay. *S. aureus* Phillips is a clinical isolate strain that has been extensively studied and has been shown to be an excellent biofilm-forming strain [51, 57, 58]. Dark colored bacterial colonies confirmed the biofilm forming capabilities of the strains (Figure 2.3)

2.3 Development of microfabricated protein patterns on glass coverslips

2.3.1 Design of photomask and fabrication of silicone master

The desired protein pattern was initially designed using the computer-aided design (CAD) software AutoCAD (Autodesk) as an array of 10-μm dots with varying spacing. The total area of each array was designed to cover either a 2 mm × 2 mm square or a 4 mm × 4 mm square representing low and high total area of coverage, respectively. The detailed pattern dimensions are listed in Table 2.2. Each pattern design was printed on a 5-inch × 5-inch glass photomask (Front Range Photomask, LLC) with the CAD data printed as chrome ink on the glass substrate. The photomask was subsequently used as the mask template for development of the silicone master.

The silicone master was fabricated as previously described [108] with modifications. A thin layer of SU-8 2010 (MicroChem Corp.), a negative photoresist material, was applied onto a clean 4-inch silicon wafer (University Wafers, Cat. No. 1196). The wafer was cleaned by immersion in a solution of three-parts sulfuric acid and one-part sodium hydroxide, supplied by the UMD NanoCenter FabLab (FabLab), for 30 minutes at 90°C and subsequent rinsing in deionized water. This was followed by secondary cleaning in buffered oxide etch solution (supplied by the FabLab) and a second deionized water rinse. To ensure that the wafer was completely dried, it was set on a hot plate preheated to 120°C for 10 minutes to evaporate any residual water on the wafer surface.

Prior to developing the master, the desired relief thickness was determined using the suggested optimization guidelines outlined in Figure 2.4. In order to prevent the collapse or sagging of pattern features on the PDMS stamp, the ratio of the relief thickness (H) to the patterned rod sizes (L) must be between 0.5 and 5 [108]. In addition to this, the ratio of H to the distance between adjacent patterned rod (D) must be greater than 0.05 [108]. To achieve these ratios, the optimal relief thickness was determined to be in the range of 20 µm to 40 µm.

SU8-2010 was applied to the wafer by spin coating using the manufacturer recipe on a WS-650MZ-23 (Laurell Technologies) programmable spin coater. The spin coating recipe was a low revolution spin at 500 rpm for 10 seconds immediately followed by a high revolution spin at 1250 rpm for 30 seconds to achieve a 20 µm thickness. The photoresist coated wafer was prebaked using a two-step heating process – comprising placement on a hotplate preheated to 65°C for 3 minutes followed by transfer to a second hotplate preheated to 95°C for 6 minutes – prior to ultraviolet (UV) light exposure.

Following a cooling period of 10 minutes, the coated wafer was exposed to UV light for 8 seconds using an EVG 620 Mask Aligner (EV Group) with light intensity of approximately 26 mW cm^{-2}. The UV light was filtered through the previously printed photomask as well as a PL-300-LP filter (Omega Optical, Cat. No. 2007308) to prevent light scatter. The exposed areas of the negative photoresists undergo a photochemical cross-linking reaction of the epoxy groups catalyzed by the generation of a photoacid [123, 124]. The wafer was immediately transferred to a 65°C hotplate for 1 minute then to a 95°C hotplate for 6 minutes.

Finally, the wafer was developed by immersing in SU-8 developer (MicroChem Corp.) for 5 minutes followed by rinsing in isopropyl alcohol (IPA; supplied by UMD NanoCenter FabLab). All non-cross-linked photoresist was removed during the development phase. The wafer was subsequently placed on a 120°C hotplate for 10 minutes for hard-baking the cured photoresist. This developed wafer containing the micro-patterns is henceforth referred to as the "master".

Acknowledgement is given for the support of the University of Maryland, College Park NanoCenter and its FabLab. Additional acknowledgement is given to the Micro-Fabrication, Machining and Electronics Center at UMBC and Innopsys Inc. for their support in microfabrication as well as consultation. An illustrative summary of the steps involved in developing the protein patterns on glass coverslips is provided in Figure 2.5.

2.3.2 Developing the PDMS master stamp

The master was used as a mold to cast a PDMS stamp. Prior to fabricating the PDMS elastomer, a layer of tridecafluoro-1, 1, 2, 2-tetrahydrooctyl-1-trichlorosilane (TFOCS; United Chemical Technologies, Cat. No. T2492) was deposited on the surface of the master by placing a drop of TFOCS in a petri dish, which was placed along with the master (in its own petri dish) inside a vacuum chamber. This process was performed in a chemical hood. The vacuum chamber was evacuated, allowing TFOCS to vaporize and fill the chamber. The deposition was allowed to continue for 1 hour and then the vacuum chamber was vented.

This modification was necessary in order to facilitate the separation of the elastomer from the master after curing.

The PDMS was formed using the Sylgard-184 elastomer kit (Dow Corning), which contains an elastomer and a curing agent; the components were mixed at a 10:1 ratio by weight of elastomer and curing agent, respectively. The mixed compound was degassed by spinning in a Sorvall Legend X1R centrifuge (Thermo-Fisher Scientific) at 3000 rpm for 2 minutes. The elastomer mixture was poured on the master and placed in an oven preheated to 120ºC and allowed to cure for 3 hours. The cured PDMS was peeled off of the master and the individual patterns were cut to size with a razor. The patterned PDMS will henceforth be referred to as the stamp.

2.3.3 Developing protein patterns on glass coverslips

After fabrication, PDMS stamp was cleaned by sonication in ethanol for 5 minutes then rinsed in deionized water and dried by a nitrogen stream. The protein solution to be inked was prepared by, (a) serially diluting FITC-conjugated collagen-IIA from bovine articular cartilage (Sigma-Aldrich, Cat. No. C4486) to a final concentration of 100 µg ml-1 in 0.01 M acetic acid, or (b) serially diluting fibronectin from bovine plasma (Sigma Aldrich, Cat. No. F1141) to a final concentration of 200 µg ml-1 in PBS.

The PDMS stamp was inked by pipetting 100 µL of protein solution to the surface ensuring that the entire surface was covered. The protein-covered stamp was incubated at room temperature for 2 minutes then gently dried in a stream of nitrogen. The stamp was

subsequently placed in conformal contact with a glass coverslip for 2 minutes to transfer the protein pattern onto the coverslip. To prevent non-specific binding of cells on the non-patterned surfaces of the coverslip, the uncoated areas of the coverslip were treated by incubating in a solution of PBS supplemented with 1 % bovine serum albumin (BSA, Sigma Aldrich, Cat. No A9418). Fabricated patterns of FITC conjugated collagen-IIA on glass is shown in Figure 2.6.

2.4 Development of biofilm cultures under physiologically-relevant shear

This study focuses on the development of biofilm by *S. aureus* under the influence of physiological shear after controlled adhesion of the cells into micropatterned clusters. In humans, the physiological shear imposed by the flow of blood through the vasculature applies a dynamic environment on *S. aureus* cells during its infection pathogenesis. A list of physiological shear rates in the human vasculature is provided in Table 2.3. The observed shear rate in the cardiovascular system range from 20 s^{-1} – 2000 s^{-1}, however, the shear rates selected for this body of work were based on previous findings [51, 64]. For this study, I focused on the effect of the shear rates of 100 s^{-1} and 300 s^{-1}. Nutrient mass transfer limitations impact biofilm development at the shear rate of 50 s^{-1} [64]. Additionally, above 300 s^{-1} shear rate, differences in developed biofilm were statistically insignificant as the shear rate was increased from 300 s^{-1} to 500 s^{-1} [64].

2.4.1 Parallel plate flow chamber system

Although the human vasculature can be considered cylindrical in geometry [125], the *in vivo* shear conditions are mimicked experimentally by using parallel plate geometry. The parallel plate flow chamber system consisted of two glass coverslips attached to the top and bottom plates of a PFC-1 ProFlow chamber (Warner Instruments, Cat. No. 641860) separated by a silicone gasket (Figure 2.7 A). The distance between the parallel plates and the width of the flow channel were determined by the thickness and cutout geometry of the gasket, respectively. The ProFlow 250 µm thick silicone gaskets (Warner Instruments, Cat.

No. 641861) that has a 10-mm-wide channel cutout was utilized. A 15-mm round glass coverslip was used as the top of the parallel plate and a 25-mm round glass coverslip were each coated with the appropriate protein and then used as the top and bottom of the parallel plate, respectively.

This parallel plate flow chamber system is governed by the Hagen-Poiseuille flow for a Newtonian fluid. The mathematical model of the Hagen-Poiseuille equation is derived from resolving the Navier-Stokes equation for a fully developed, laminar, steady state flow of a Newtonian fluid through a parallel plate geometry. The relationship between the volumetric flow rate (Q) and the theoretical wall shear rate ($\dot{\gamma} = 100\ s^{-1}\ or\ 300\ s^{-1}$), of a parallel plate geometry with height ($h = 250\ \mu m$) and width ($w = 10\ mm$) is given by the following equation [64]:

$$\dot{\gamma} = \frac{6Q}{h^2 w}$$

Thus, the volumetric flow rate that was controlled by a syringe pump was derived for the respective wall shear rates.

2.4.2 Flow apparatus assembly and pump system setup

The perfusion of media through the flow apparatus was achieved by a syringe pump (Harvard Apparatus) connected to the parallel plate flow chamber setup (Figure 2.7 B). Upstream of the flow chamber, the perfusion is initiated from a 140-ml Piston Syringe (Covidien Monoject) mounted on the syringe pump. This syringe contained, (a) the TSB

media for perfusion during biofilm growth or, (b) phosphate buffered saline supplemented with 0.2 % w/v sodium azide (PBS-Az) for washing after cell adhesion and after biofilm development. Sodium azide was used as a bacteriostatic agent – stopping bacterial growth without deteriorating cell viability at the concentration applied [126]. To maintain laminar flow, a 0.063-inch ID silastic tube (Dow Corning) was applied as the in-line tube that connects system components to each other. The syringe was connected to a bubble trap (Cole Parmer, Cat. No. EW-75955-90), which was subsequently connected to flow chamber. The in-line bubble trap prevented air bubbles from entering the flow chamber. Downstream of the flow chamber the outlet tubing is connected to waste collector. The entire flow setup was assembled and filled with PBS-Az prior to the start of the experiment to check for leaks and the presence of any air bubbles. The entire flow chamber was maintained at 37°C by placing in an air curtain incubator.

2.4.3 Biofilm development

Biofilm experiments were initiated by inoculation of a primary shake flask from glycerol stock as previously described [64]. Briefly, 10 µL of thawed glycerol stock for the desired *S. aureus* strain was suspended in 50 mL of tryptic soy broth media + appropriate antibiotic and incubated at 37°C with agitation at 140 rpm for 10 hours. A sample of the suspension was extracted at this time when the cells were at mid-exponential phase of growth (Figure 2.1) and suspended at a ratio of 1:20 in PBS-Az. This diluted suspension was used as the inoculum for the biofilm experiment.

Prior to inoculation, a 25-mm round glass coverslip was coated with fibronectin (FN) using the desired pattern as previously described and mounted onto the bottom plate of the flow chamber device. Subsequently, 200 µL of the diluted cell suspension was transferred onto the coverslip and incubated at 37°C for 15 minutes to allow attachment of the *S. aureus* cells onto the protein substratum by sedimentation. Afterwards, the flow chamber was assembled and PBS-Az was perfused through at $100s^{-1}$ for 10 minutes to remove unattached cells. The TSB media was then perfused through for 8 hours at the desired shear rate to allow for biofilm development. Following biofilm development, PBS-Az was perfused for an additional 10 minutes at the same flow rate for biofilm development. The images of the biofilm were captured on via CLSM.

2.5 Qualitative and quantitative analyses of developed biofilm

2.5.1 Confocal microscopy

Biofilm images were captured on a TCS SP5 (Leica Microsystems) CLSM system. The procedure for capturing biofilm images was adapted from previously described protocols [64]. Images for qualitative analysis were captured at 63× magnification, 1024 × 1024-pixel format at a speed of 400 Hz. The capture field of view at this magnification was 246 µm × 246 µm. The z-direction distance between each captured frame of the CLSM scan was 0.13 µm and the entire biofilm was captured from the substratum to the surface. The excitation wavelength of sGFP fluorophore was 488 nm with an emission bandwidth in the range of 500 nm – 550 nm. The three-dimensional CLSM images were compiled using Imaris (Bitplane Software). For the quantitative analysis of biofilm, the images were acquired at a magnification of 63× with an additional zoom factor of 10. All other scan settings were unchanged. The increased magnification resulted in a capture field that was further refined to 24.6 µm × 24.6 µm while the z-direction distance between each captured frame was unchanged. These images were individually exported as a z-direction stack of files that would go on to be evaluated by image structure analyzer.

2.5.2 Three-dimensional quantitative analysis of developed biofilm

Quantitative analysis of the exported image stacks collected via CLSM was performed using image structure analyzer in three dimensions (ISA3D). The ISA3D software

was kindly provided by Dr. Haluk Beyenal (School of Chemical Engineering and Bioengineering, Washington State University).

The settings for performing the ISA3D analysis are important to ensure consistent calculation of biofilm parameters (Figure 2.8). The threshold method selected was the iterative method. This method assigns a per-pixel numerical value to the image and performs linear iterations for the values between adjacent CLSM image layers [48, 110, 111, 113, 118]. The *dxy* value is defined by the per-pixel size of each image in the x- and y-direction. For the square CLSM image the x- and y-direction pixel sizes were equal to the field size of 24.6 µm divided by the image size 1024 pixels; giving a value of 0.024 µm per pixel. The value of *dz* was equivalent to the distance between adjacent images in the stack, or the step height of the CLSM scan that was 0.13 µm. Finally, the distance mapping method used in calculations was quasi-Euclidean.

2.6 Developing flow chamber and cell micro-pattern simulations in COMSOL

COMSOL Multiphysics (COMSOL) is a finite element method simulation software package with the capability to simulate a plethora of physical phenomena such as structural engineering, electromagnetic potential, and fluid dynamics. It is becoming an increasingly useful tool in many scientific fields from analytical chemistry to mechanical engineering [127-129]. COMSOL was applied in this study to simulate the concentration profile of AIP within the parallel plate flow chamber accompanied by fully developed fluid flow. In conducting these simulations, several assumptions were made, including 1) the properties of the bulk fluid system in the flow chamber are equivalent to that of water; 2) the stamping of protein in the experimental system is complete without missing spots; 3) all flow is one dimensional with no cross-flow; and 4) each patterned spot is completely saturated with cells that are attached adjacent to one another. Additional assumptions for specific conditions are described later.

Prior to building the flow chamber geometry and setting up the simulations in COMSOL, global parameters and variables were compiled in the solver in order to mimic the conditions within the experimental flow chamber (Table 2.4). The parameter definitions also allowed for changing the conditions of the simulations with respect to the changing parameters of the experiments while eliminating the need to rebuild the simulation from the ground. While the experimental system was three-dimensional, all simulations were performed in two-dimensional geometry mode. This was due to the assumption that there was no cross-flow within the system.

2.6.1 Developing the “laminar flow” simulation design

The laminar flow within the flow chamber was modeled using computational fluid dynamics that were calculated by COMSOL. The laminar flow physics was added to the geometry and the material property of the domain was set to water. Boundary conditions were added to the geometry to simulate no slip at the top and bottom walls of the flow chamber. The inlet of fluid flow was set equivalent to the velocity of fluid set by the syringe pump, while the exit was set to zero pressure with no backflow. The simulation was then executed by the stationary solver to determine the steady state solution. The velocity profiles for the fully developed flow simulations for shear rate values at 100 s^{-1} and 300 s^{-1} are shown in Figure 2.9.

2.6.2 Developing the “transfer of diluted species” simulation design

The transport of AIP within the flow chamber during biofilm development was modeled using computational fluid dynamics within COMSOL. The transport of diluted species physics was added to the geometry and the material property of the domain was as previously described. Boundary conditions were added to the geometry to simulate no flux of the species at the walls and entrance of the flow chamber geometry. The inlet flux of diluted species (AIP) was set to a second geometry that was built as a series of rectangular dots in series to the simulate patterned surfaces. This second geometry was unified with the geometry of the flow chamber by union difference in order to have a continuous boundary for the mathematical solution. The exit of the species was set to the exit of the chamber as

previously described. The simulation was then executed by the time-dependent solver to determine the unsteady state solution over a period of 8 hours corresponding to the duration of the experimental runs. The results of the steady state solver were set as the initial values for the execution of the time-dependent solver. The inlet flux of AIP into the flow system was extrapolated from reported data of the suspension culture concentrations observed by ultra-high-performance liquid chromatography [130]. This value was then varied along the direction of flow by multiplying by a factor equivalent to the growth rate based on the doubling time of *S. aureus* ($t_d = 22\ minutes$). The doubling time was determined from the growth curve of the AH1979 strain based on the linear portion of the growth curve (Figure 2.2). Finally, the diffusion coefficient for AIP was equivalent to reported values at approximately 1×10^{-9} m^2 s^{-1} [131]. Figure 2.10 shows preliminary simulation models performed for the concentration profiles at steady state. The preliminary simulation was executed for steady state to assess the simulation. The concentrations rose steadily along the length of the cell coverage suggesting accumulation of the diluted species along the direction of flow.

2.7 Statistical analysis

Unless otherwise specified, reported data represent the mean of a minimum of four experimental runs, and the error bars represent the 95% confidence interval about the mean. Where applicable, the statistical significance was determined either using students *t*-test or a single factor analysis of variance (ANOVA) each with 95 % confidence (corresponding to significance value $p < 0.05$).

The design of experiments for the impact of pattern dimensions on biofilm development was a multilevel generalized full factorial created and analyzed in Minitab 18 (Minitab Inc., State College, PA) (Table 2.2). The factors and levels of the factorial design include: (1) shear of 100 s^{-1} or 300 s^{-1}; (2) square pattern size of 2 mm × 2 mm or 4 mm × 4 mm; and (3) pattern spacing of 20 µm, 50 µm, or 110 µm.

Table 2.1: List of *S. aureus* strains utilized in this study. The *S. aureus* SH1000 strain is derived from the parent strain NCTC 8325-4 that has been corrected for *rbsU+* [120]. *S. aureus* SH1001 is a mutant derivative of SH1000 with a knockout in *agr* locus [67, 76, 119]. The indicated plasmid was transformed into either SH1000 or SH1001 to derive the strains outlined [119].

Strain Alias	**Description**
AH1218	Parent Strain: SH1000 Plasmids: *agr P3*-dependent mCherry + chloramphenicol and *sarA* P1-dependent YFP10Bs + erythromycin
AH1219	Parent strain: SH1001 Plasmids: *agr P3*-dependent mCherry + chloramphenicol and *sarA* P1-dependent YFP10B + erythromycin
AH1979	Parent strain: SH1000 Plasmids: *sarA* P1-dependent sGFP + chloramphenicol

Table 2.2: Table of pattern dimensions showing the generalized full factorial design of experiment. The levels for each factor are indicated in the columns. For the pattern dimensions, the "Full Coverage" dimension refers to a total non-patterned coverage of protein on the glass surface. Otherwise, the patterns comprise an array of 10 μm dots adjacently spaced by the distance shown. The "Full Coverage" pattern dimension was used as a control for comparison of pattern-developed biofilms to their respective non-patterned counterparts.

	Shear (s^{-1})	**Patterns designed for CAD printing**	
		Pattern Size (mm × mm)	**Pattern Dimensions (μm)**
1	100	2 × 2	Full Coverage
2			20
3			50
4			110
5		4 × 4	Full Coverage
6			20
7			50
8			110
9	300	2 × 2	Full Coverage
10			20
11			50
12			110
13		4 × 4	Full Coverage
14			20
15			50
16			110

Table 2.3: Physiological shear rates reported in human vasculature [125, 132].

Blood Vessel	**Mean Wall Shear Rate (s^{-1})**
Venules	400 – 450
Veins	20 – 100
Small Arteries	1000 – 2000
Large Arteries	300 – 800
Capillaries	250 – 2000
Vena Cava	20 – 60

Table 2.4: List of COMSOL global parameters and variables with descriptions relating to the experimental flow chamber system.

Parameters List		
Parameter	**Value**	**Description**
D_cell	1 µm	*S. aureus* cell diameter used to build the geometrical height of patterned structures
D_dot	10 µm	Diameter of individual patterned structures
S_dot	20, 50, 110 (µm)	Spacing between adjacent patterned structures
T_double	22 minutes	Doubling time to S. aureus based on the average of reported values
Q	0.625, 1.875 (ml min^{-1})	Volumetric inflow rate used to control wall shear rate (100 s^{-1}, 300 s^{-1})
PPFC_h	250 µm	Parallel plate flow chamber dimensions used to build the overall boundary of the entire simulation domain
PPFC_w	10 mm	
PPFC_l	10 mm	
Variables List		
Variable	**Value**	**Description**
Area_c	PPFC_h × PPFC_w	Used to define the axial cross-sectional area of the flow chamber
V	Q/Area_c	Used to define the inlet velocity as a function of the volumetric flow rate and cross-sectional area

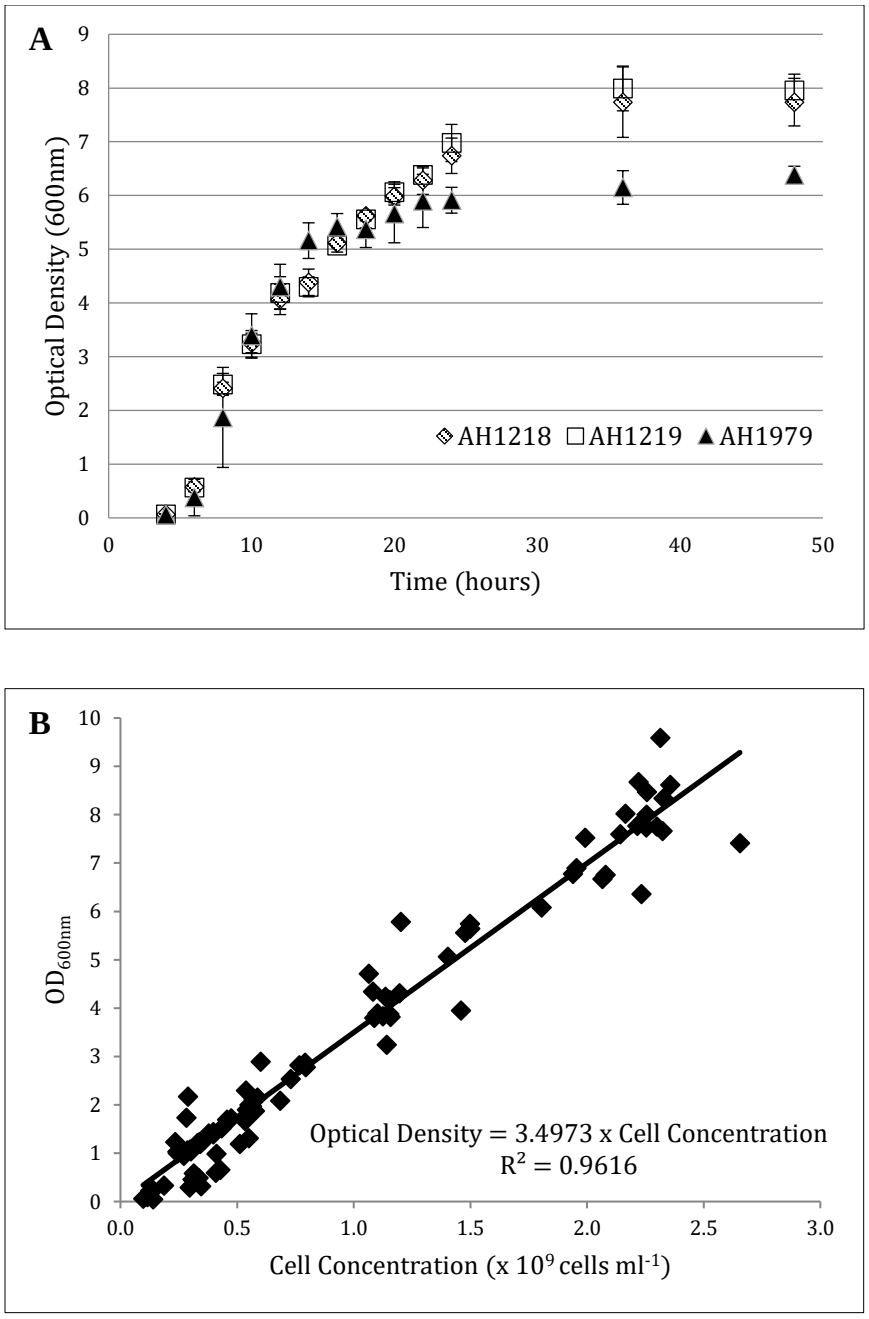

Figure 2.1 (A): Cumulative growth curve for *S. aureus* strains AH1218, AH1219 and AH1979. **(B):** Scatterplot of OD_{600nm} versus Cell count curve for *S. aureus*.

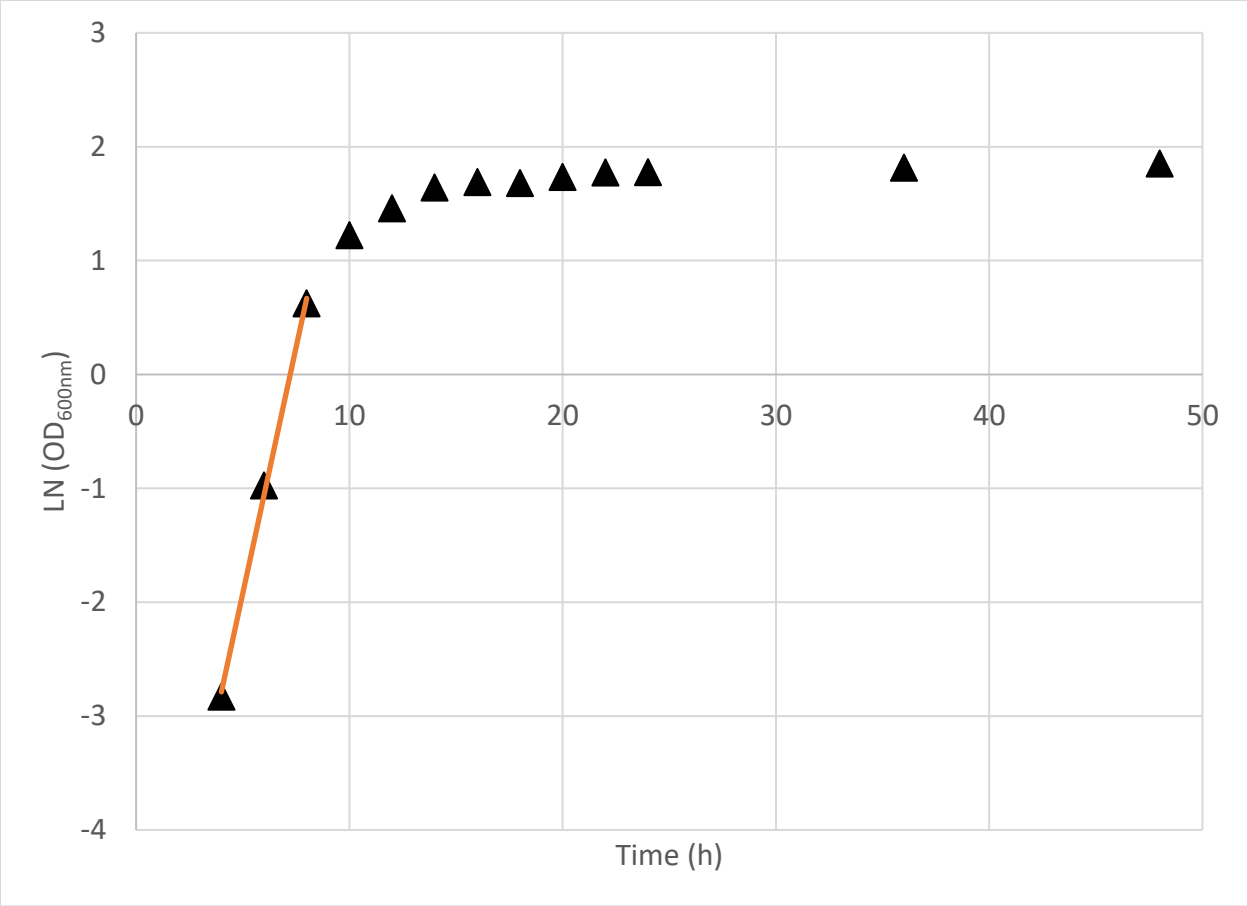

Figure 2.2: Growth curve for *S. aureus* strains AH1979 in terms of natural logarithm of the optical density values. The linear portion of the chart was used to determine the doubling time for this strain.

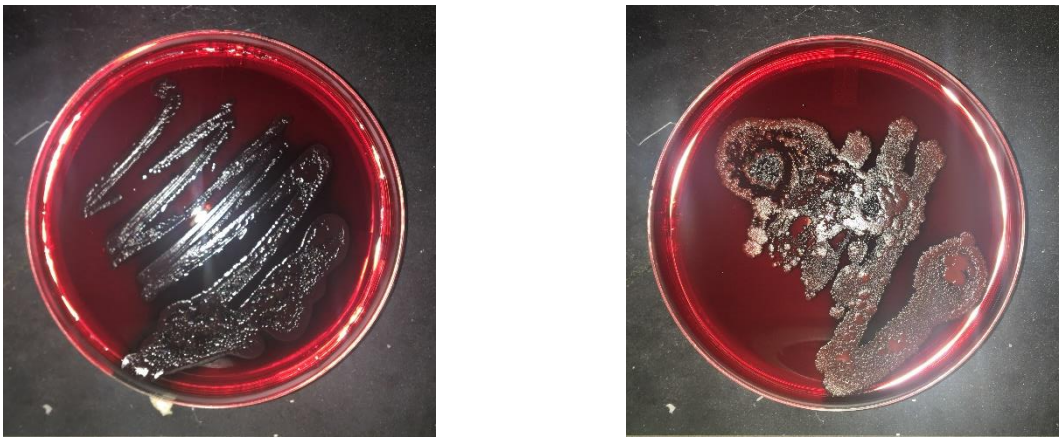

Phillips **AH1979**

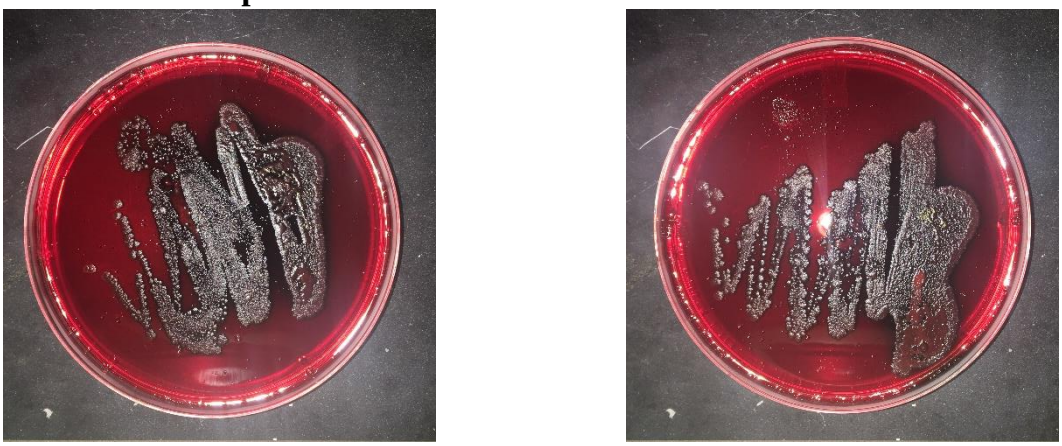

AH1218 **AH1219**

Figure 2.3: Biofilm forming capabilities confirmed for *S. aureus* strains by CRA assay. *S. aureus* Phillips was used due to its known biofilm forming capabilities as a positive screen for CRA.

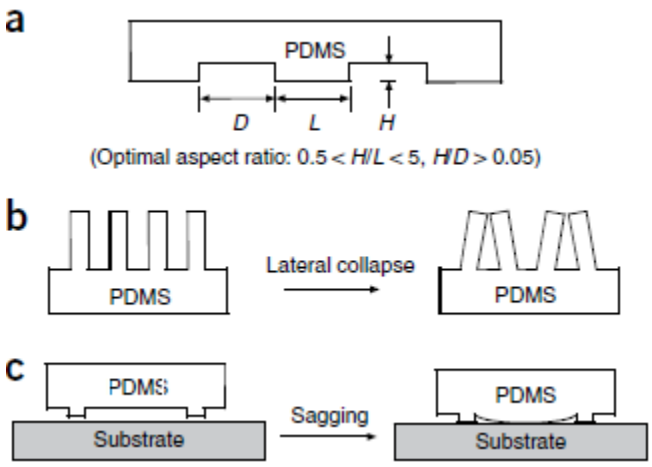

Figure 2.4: Guidelines for the prevention of sagging or collapse of PDMS features showing, (**a**) optimal ratios where sagging or collapse can be prevented; (**b**) Lateral collapse due to large ratio of H/L and (**c**) sagging that occurs when H/D was too low [108].

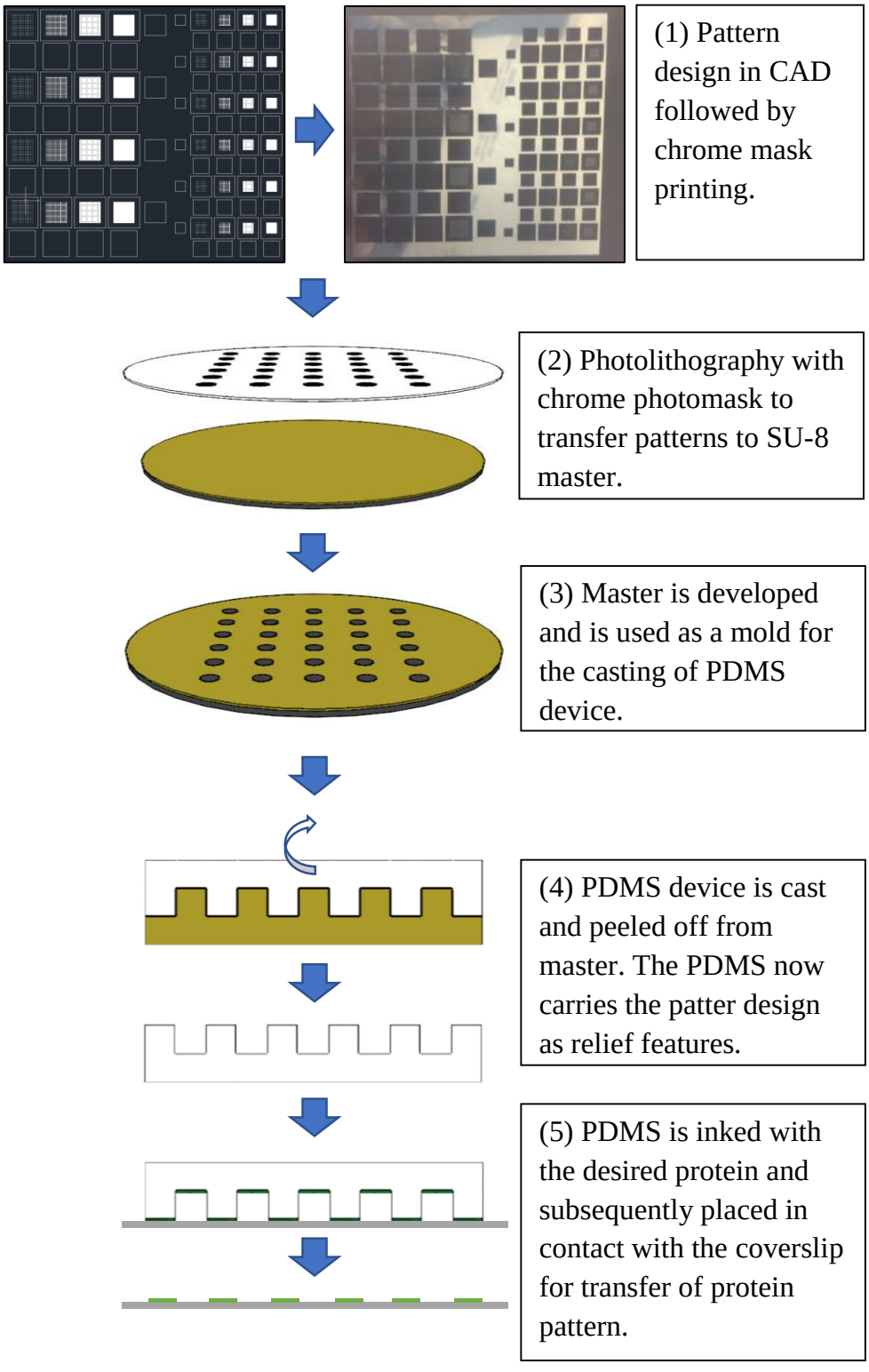

Figure 2.5: Illustrative summary of the steps involved in the microfabrication of protein patterns onto a glass coverslip.

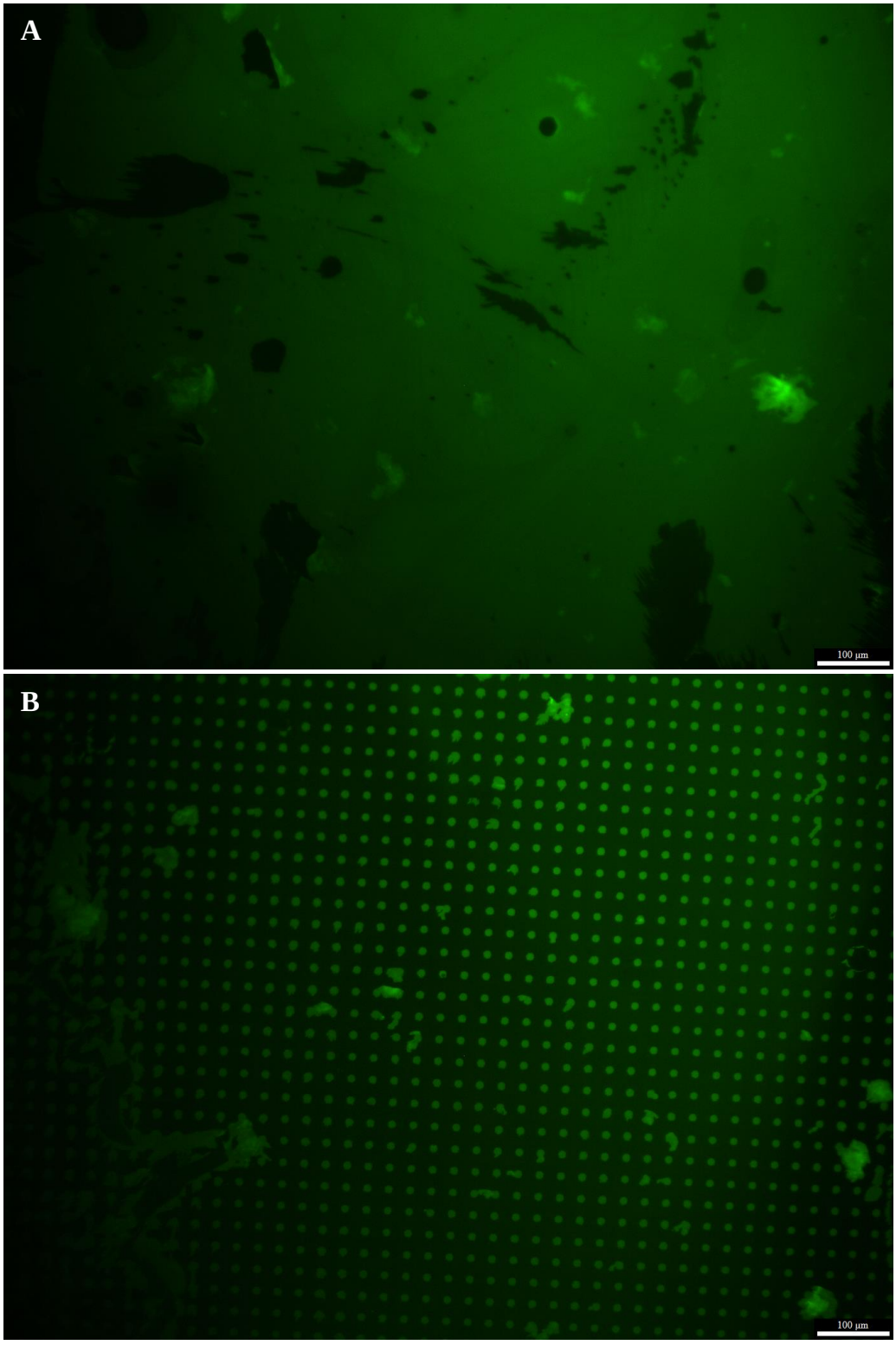
A
100 µm
B
100 µm

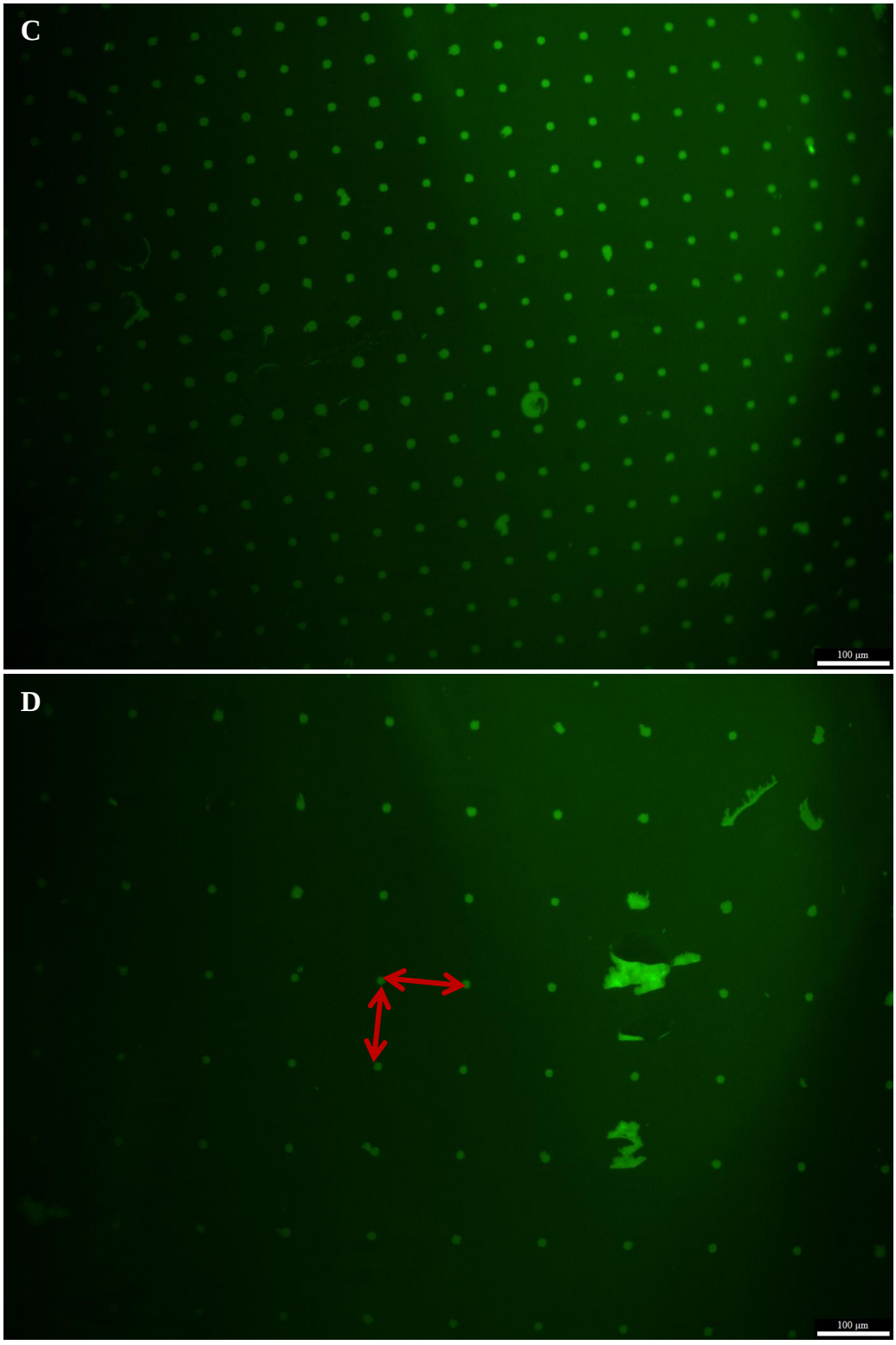

Figure 2.6: Images showing print patterns of FITC conjugated collagen-II A. Pattern descriptions for each image include **(A)** Full coverage, an array of 10 µm dots that are

equally spaced **(B)** 20 µm, **(C)** 50 µm, and **(D)** 110 µm apart. The dimensionality of the spacing is indicated in **(D)** where the red arrows represent a distance of 110 µm between adjacent dots. The full coverage coat **(A)** represents non-patterned surface where cells can adhere randomly at any position. The patterned coats allow for controlled adhesion of cells only on the patterned dots. All non-patterned surfaces are coated with PBS + BSA to ensure non-specific binding did not occur. White scale bars represent 100 µm.

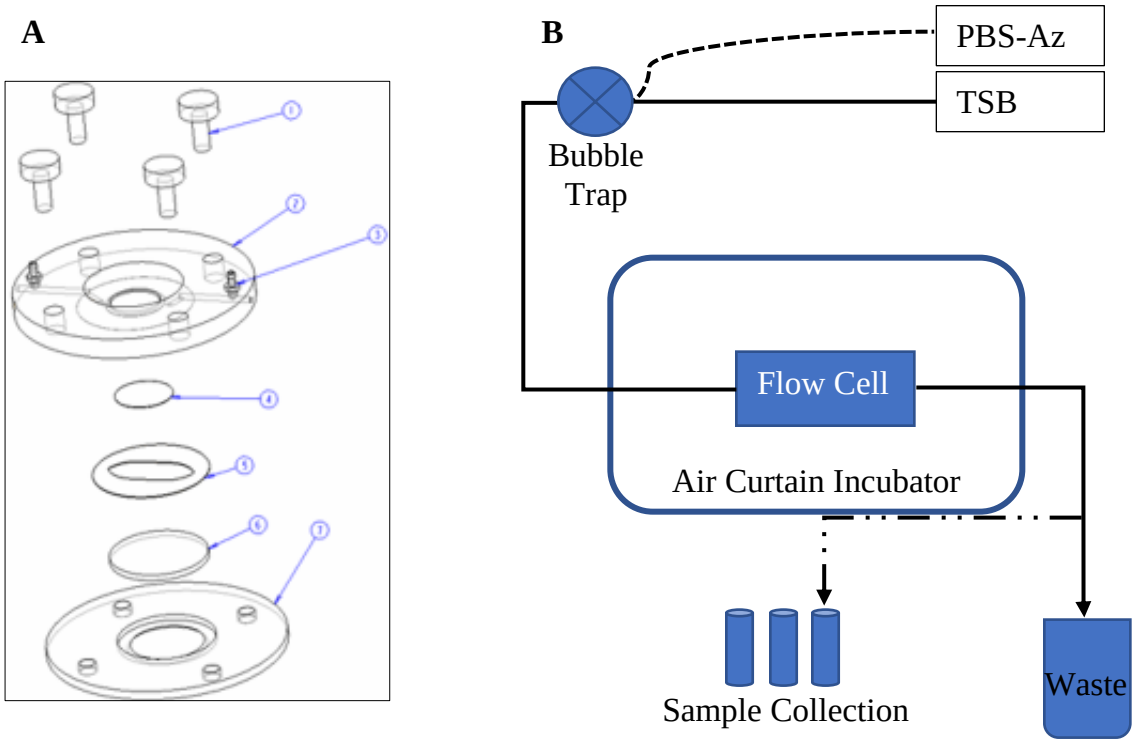

Figure 2.7 (A): Outline of ProFlow chamber setup showing (1) fastening thumb screws, (2) top chamber plate, (3) inlet/outlet flow ports, (4) 15 mm round glass coverslip, (5) silicone gasket, (6) 25 mm round glass coverslip, (7) bottom chamber plate [133]. **(B):** Setup of flow system from the start of the line at the syringe pump through to the effluent stream. Dashed connecting lines indicates streams that were added or removed as described in the methods section. PBS-Az stream was added and removed for washes before and after biofilm development, while sample collection was collected for UHPLC-MS analysis.

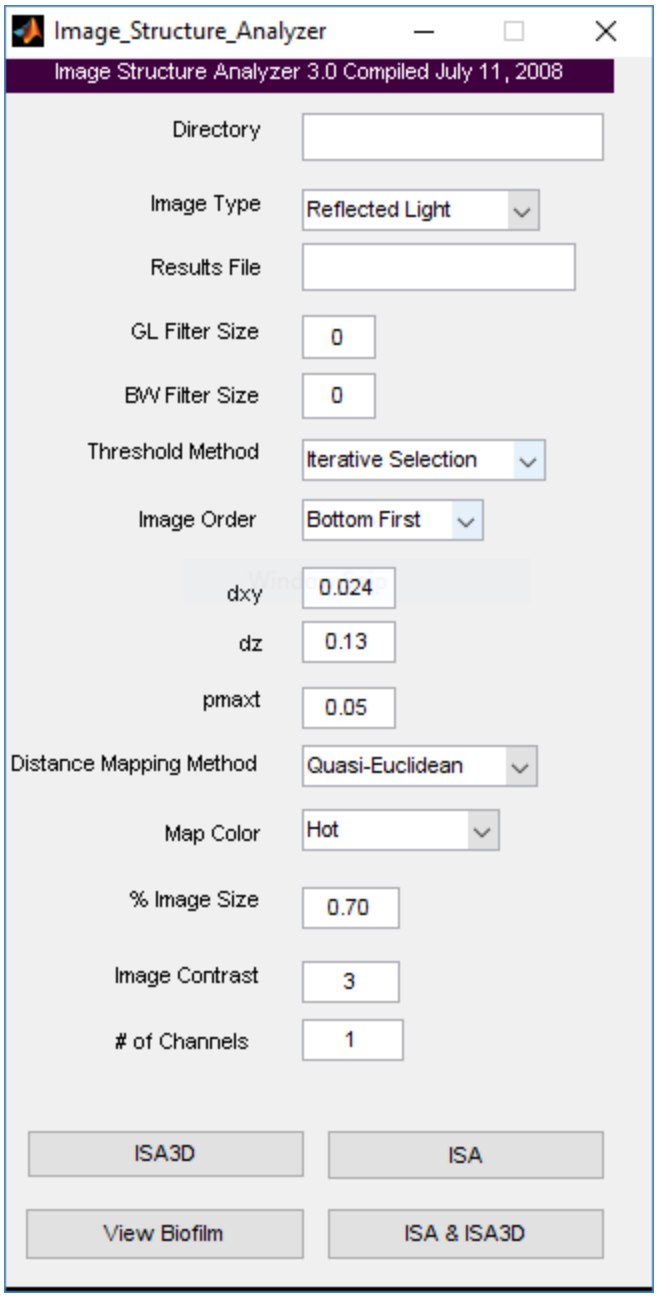

Figure 2.8: ISA3D settings used to perform quantitative analysis. The directory and results file indicate the location of confocal images and the destination for the results respectively. The CLSM utilizes reflected light microscopy and images are left for automatic threshold using the iterative method.

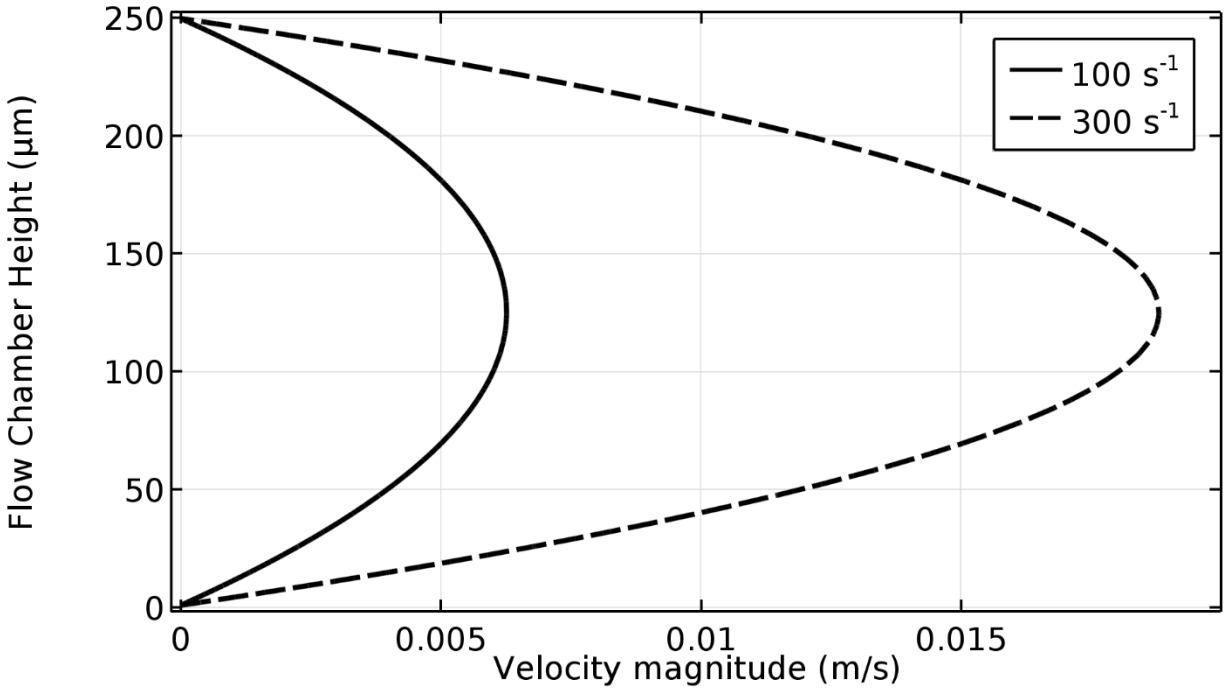

Figure 2.9: Velocity profiles for parallel plate flow chamber simulations performed in COMSOL showing 100 s^{-1} and 300 s^{-1} laminar flow profiles of a fully developed incompressible, Newtonian fluid. The no slip boundary condition results in zero velocity at the top and bottom walls, resulting in maximum wall shear rates.

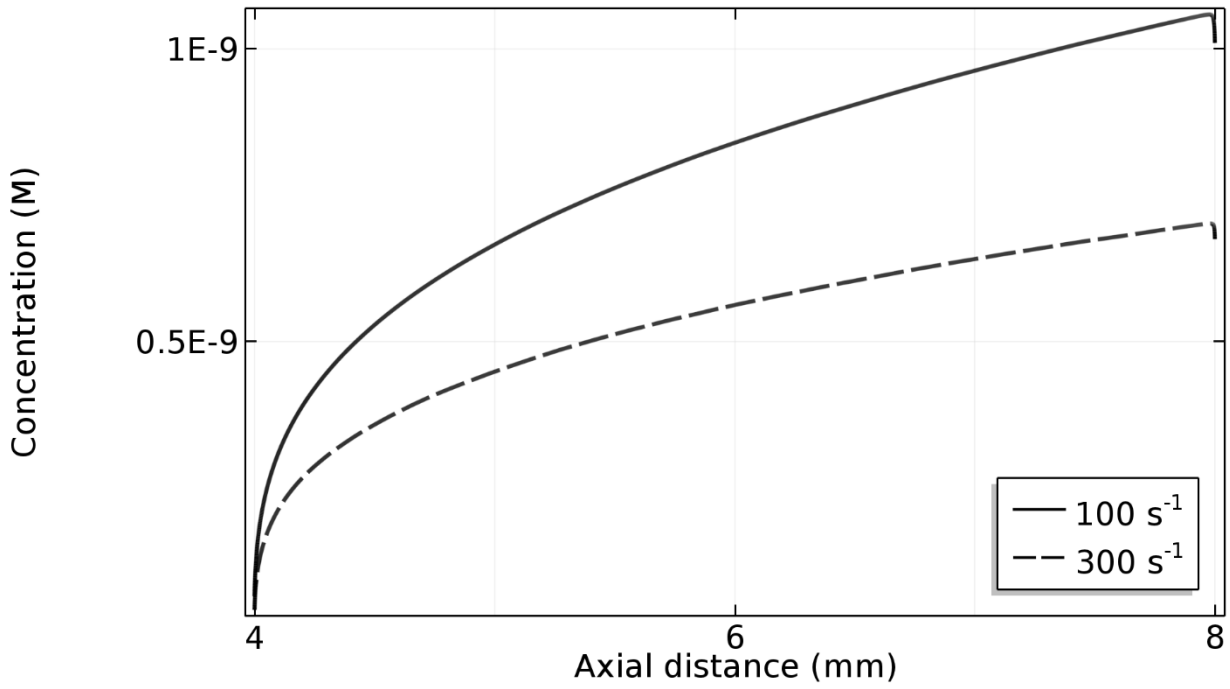

Figure 2.10: Concentration profiles for transport of diluted species simulations performed in COMSOL showing steady state profiles at the surface of the cell layer at both 100 s^{-1} and 300 s^{-1} shear rates. The axial distance represents the distance along the length of a 4 mm × 4 mm full coverage of cells along the bottom plate of the flow chamber.

Chapter 3: Simulation model of autoinducer peptide mass transfer during *Staphylococcus aureus* biofilm development under fluid flow

3.1 Rationale for study

During the functional evaluation of biological organisms and their systems, in addition to discovery of involved metabolites, it is important to develop a thorough understanding of interactions between metabolites and the pathways associated with the biological system of interest. As part of the tools of functional evaluation, researchers assess biological processes via mathematical models for measurable parameters such as metabolite concentration and gene expression. Therefore, complex processes can be represented by simple sets of mathematical equations. These mathematical equations enable the characterization of how complex cellular processes connect to one another; and they aid in postulating the effect of interruptions in these processes [134-136]. For example, metabolism comprises a large number of pathways that include the citric acid cycle, glycolytic cycle, and oxidative phosphorylation, among others [137]. Each of these complex pathways connect to one-another either by sharing or transferring metabolites. Mathematical models enable evaluation of this complex system by assignment of mathematical equations to individual processes involved in each cycle. These equations can subsequently be manipulated for their effects on the overall metabolic pathway prior to conducting laboratory experiments. Ultimately, the development of mathematical models aids in the analysis of system changes, and may help guide development of new hypotheses and experimental designs.

Modeling of biofilm systems are generally driven by the goal of predicting the structure of developed biofilm, or the mechanisms associated with biofilm development in a mathematical way [138]. These biofilm development models include reaction and mass transfer models of metabolites [138-141], the effects of shear on growth and detachment of

cells during biofilm development [142-146], and models describing the release and detection of signal peptides during cell-to-cell communication [147-149]. These models have been useful in predicting outcomes of experimental biofilm development. For example, simulation models predicted a relationship between shear rates and mass transfer of nutrients from bulk fluid to biofilm components [145, 146]. In those studies, it was predicted that increased fluid flow velocity (resulting in higher shear) results in reduced influence of mass transfer-limited biofilm growth. These predictions were verified independently by another study showing that at lower shear rate of 50 s^{-1}, biofilm developed higher biovolume in response to doubling of growth media concentration; however, at 100 s^{-1}, doubling the growth media concentration did not change the biovolume of developed biofilm [64].

Following the adhesion of cells on host matrix proteins or implanted medical device, *S. aureus* biofilm-based infections progress by the release and detection of AIP molecules. Following the detection of a threshold local concentration of AIP, the cells initiate biofilm-dependent growth [31, 32, 34-36, 84]. In this study, AIP concentration profiles were predicted for geometric clusters (representing adhered cell clusters that are releasing and detecting AIP) that were patterned within a parallel plate flow geometry and were exposed to fluid shear. The concentration profiles of AIP were predicted using COMSOL. These concentration profiles offer predictive information for the underlying AIP convective mass transfer within the flow chamber. This was subsequently useful in interpreting experimental data following biofilm development in the laboratory setting. Additionally, time course studies were evaluated for the threshold local AIP concentration within the dynamic environment of the flow chamber. Experimentally, the threshold local AIP concentration

refers to the concentration at which cell clusters initiate biofilm-dependent growth. These models were useful in further development of the hypothesis by providing a means to refining parameters that were tested experimentally. Furthermore, they provide an additional basis for understanding the experimental results that follows in this body of work.

3.2 Results

3.2.1 Simulation model equations, boundary conditions and assumptions

The governing equations and boundary conditions evaluated with the simulation model are summarized in Table 3.1. The laminar flow simulation solved the momentum and continuity equations for two-dimensional Cartesian coordinate for steady state, unidirectional fluid flow. The boundary conditions include: a single inlet of flow with a constant velocity, no-slip at the top and bottom walls of the parallel plate, and no back-flow at the outlet. The transport of diluted species simulation solved the continuity equation for a species that includes the combined effect of diffusion and convection. The boundary conditions include: the inlet of concentration species located at the cluster geometry boundary, and no flux through the boundary of the flow chamber or the inlet of flow.

To perform the model simulations, several assumptions of the overall experimental system were adopted. The geometry was constructed with the parallel plate chamber having the array of cell clusters begin precisely at the middle of the bottom plate of the chamber. The fluid property utilized in the simulation was water. The dynamic viscosity (μ) and density (ρ) values of water were assumed to be approximately 0.001 Kg m^{-1} s^{-1} and 1000 Kg m^{-3}, respectively. These property values are equivalent to approximate property of water. The laminar flow simulations were developed as incompressible fully developed flow of a Newtonian fluid – thus the viscosity and density were constant. To confirm fully developed flow throughout the region containing cell clusters at both 100 s^{-1} and 300 s^{-1} shear rates, the

flow profile for a full coverage pattern configuration is shown in Figure 3.1. At shear rates of 100 s^{-1} and 300 s^{-1}, the resulting average velocity (v_{avg}) of fluid flow (calculated as two-thirds of the maximum velocity, Table 3.1) were approximately 0.0042 m s^{-1} and 0.013 m s^{-1}, respectively. To confirm fluid flow was laminar, the Reynolds number ($Re = \rho v_{avg} L/\mu$) values were evaluated at the exit of the parallel plate flow region ($L = 10\ mm$). The Re was equivalent to 42 and 130 corresponding to fluid flow at 100 s^{-1} and 300 s^{-1} shear rate, respectively. Flow between parallel plates is laminar if Re is less than 1400 [150].

Additionally, it was assumed that the release and uptake of AIP by the cells resulted in a net flux in the direction from cell to fluid. The value of the net flux was adapted from reported values in literature of the concentration of AIP in bulk suspension cultures during the exponential growth phase [130]. To do this, the AIP concentration (μM) and the corresponding cellular concentration (cells mL^{-1}) was evaluated at two points during the exponential growth phase of the reported data [130]. The slope of these two points was subsequently evaluated as an estimate of the average flux-per-cell of AIP during exponential growth phase and was equivalent to approximately 1.9×10^{-8} μM $Cell^{-1}$ mL^{-1}. To validate this estimated flux, a simulation model was developed for the AIP concentration profile of a single 1-μm diameter sphere isolated within a larger 20-μm diameter hemisphere. This was done to mimic reported experimental geometry of a single *S. aureus* cell isolated within a nanostructured matrix [37]. In that experiment, it was reported that individually-isolated *S. aureus* cells initiated AIP-response (indicated by the expression of GFP) after 1 hour. The validation simulation agrees with the experimental results. The predicted time to achieve

threshold AIP concentration, based on the flux value, was approximately 55 minutes (Figure 3.2).

The complete simulation was performed in two-dimensions with the x- and y-direction representing the chamber length and height, respectively. The z-direction, representing the width of the flow chamber, was ignored for the simulations – so spatial dependencies were ignored. The was due to fluid flow being only in the x-direction. This meant that the 2 mm × 2 mm and 4 mm × 4 mm arrays of cell clusters, discussed in subsequent chapters were simulated as a single row of 2 mm and 4 mm clusters, respectively. During execution of the simulation, the geometry representing the cell cluster was held constant. To simulate cell growth, the release rate of AIP was assumed to increase with time based on the growth doubling time (22 minutes) for *S. aureus* during exponential growth phase (therefore the lag phase of normal microbial growth was omitted). Finally, it was assumed that at time = 0, there was no AIP present within the system. These assumptions were reflective of approximate conditions within the flow chamber.

3.2.2 Simulated convective mass transfer decreases local AIP concentration at higher wall shear rates

To determine the effects of wall shear rate on the concentration profile of AIP within the flow chamber, simulations were performed with wall shear rates of 100 s^{-1} and 300 s^{-1} on similar cluster configurations. Simulation results are shown in Figures 3.3 and 3.4, wherein the AIP concentration profiles are shown as colored heat maps where numerical values are

indicated from red to blue representing highest to lowest values. Additionally, for values represented by similar color hues, the higher values are indicated by a higher intensity of the hue. A closer look at the last cluster geometry is shown in Figure 3.5. For each colored map, the magnitudes of the color hues are represented by their accompanying legend. All simulations showed a similar effect of convection on the concentration of AIP along the direction of flow (Figures 3.3 & 3.4). This meant that for a 4 mm × 4 mm pattern coverage where the 0 mm and 4 mm end are located upstream and downstream of flow, respectively, the highest concentration of AIP was located at the 4 mm end of the pattern coverage. The simulations also showed that the maximum AIP concentration achieved at 8 hours was higher at 100 s^{-1} than at 300 s^{-1} (Figure 3.6). For example, for the 4 mm × 4 mm total pattern size with 20-µm spacing between clusters, the maximum AIP concentration achieved at 100 s^{-1} was 0.23 M while 0.16 M was the maximum at 300 s^{-1} (Figure 3.6). Similar results were observed for all pattern configurations.

Finally, the effect of shear on the time taken to achieve the threshold AIP concentration was evaluated for each cluster configurations (Figure 3.7). To do this, the simulation results were probed for the concentration magnitude at the location equivalent to the position of the last cluster geometry within the simulation. For example, the 4 mm × 4 mm 20-µm spacing configuration was probed at the cluster geometry located at the 4-mm distance and at 1-µm height as indicated in Figure 3.4 A. Due to the influence of convection ensuring that this location possessed the highest concentration of AIP at any time-point during the simulation, this location was selected as the probe point. The theoretical threshold value utilized in the simulation was equivalent to 100 nM (1×10^{-7} M) and was based on

reported data [37]. The simulation results predicted that for all the cluster configurations, an increase in shear from 100 s^{-1} to 300 s^{-1} resulted in an increase in time to achieve the AIP threshold concentration. The magnitude of the time difference in all cases was on the order of a few minutes. For example, the 4 mm × 4 mm full coverage cluster configuration achieved the threshold AIP concentration after approximately 1 hour 50 minutes at 100 s^{-1} shear rate, whereas at 300 s^{-1}, the threshold AIP concentration was achieved after approximately 1 hour 55 minutes (Figure 3.7). This represents an increase of 5 minutes for the full coverage configuration response to increase in shear rate. The response of the 20 µm and 110 µm spacing configurations to the same change in shear rate was approximately 10 minutes in each case (Figure 3.7). Overall, these simulations suggested that an increase in wall shear rate from 100 s^{-1} to 300 s^{-1} resulted in higher convective mass transfer of the AIP that is released into the bulk fluid by the clusters.

3.2.3 Greater cluster spacing decreases local AIP concentration under flow

Next, the effect of patterned cluster configuration on the concentration profile of AIP under fluid flow was explored. For a constant fluid shear rate, an increase in the distance between clusters from full coverage to 20 µm to 110 µm correlates with decreased AIP concentration local to the clusters (Figure 3.4). For example, for a 4 mm × 4 mm area exposed to 100 s^{-1} wall shear rate, it was predicted that the maximum local AIP concentration achieved at full coverage was 0.51 M, while the maximum concentrations achieved for patterns with cluster spacing of 20 µm and 110 µm were 0.23 M and 0.09 M, respectively. This concentration change represented an approximate two-fold and five-fold reduction in

AIP concentration, respectively. Similar trends were predicted for simulations performed at 300 s^{-1} shear rate.

Additionally, the effect of cluster patterned configuration on the time to achieve the threshold AIP concentration local to the cell clusters was evaluated at different positions along the 4 mm coverage (Figure 3.8). It took longer for threshold local AIP concentration achievement with increased distance between adjacent clusters. For example, for a 4 mm × 4 mm area exposed to 100 s^{-1} wall shear rate, it was predicted that the time taken for the full coverage configuration to achieve threshold AIP concentration at the 4 mm coverage location was 1 hour 50 minutes. The time taken for the 20 µm and 110 µm spacing was predicted to be 2 hours and 2.5 hours, respectively. However, along the entire length of the 4 mm coverage, the simulations predicted that three-quarters of the full coverage configuration achieved the threshold concentration in approximately 2 hours at both 100 s^{-1} and 300 s^{-1} shear rates. The time taken for three-quarters of the 20 µm and 110 µm spacing configurations was predicted to be approximately 2 hours 10 minutes and 2 hours 40 minutes at 100 s^{-1}, respectively. At 300 s^{-1} the time taken was approximately 2 hours 20 minutes and 2 hours 35 minutes, respectively. In summary, these simulations predict that increased spacing between adjacent clusters results in decreased local concentration of AIP at the surfaces of the clusters, which results in an overall longer time to achieve local threshold AIP concentration at the surfaces of the clusters.

3.2.4 Simulated effect of total cluster number on AIP concentration profile under flow

Finally, the simulations were assessed for the effect of a smaller total cluster number on the achievement time for threshold local AIP concentration. This was done by decreasing the total coverage length in the simulations from 4 mm to 2 mm, reducing the total cluster number by half. The simulations predicted that a larger total cluster number resulted in an increased maximum concentration at the end the cluster region after 8 hours at equivalent shear rates (Figure 3.9). For example, at 100 s^{-1}, the maximum concentration at end of the 2 mm cluster region was 0.19 M while 0.23 M was the maximum at the end of the 4 mm region. Additionally, the concentrations at locations equidistant from the start of the cluster configuration was compared between the 2 mm and 4 mm configurations. This comparison was done to check for similarities between the concentration at the end of the 2 mm coverage and at the midpoint of 4 mm coverage (equal to a distance of 2 mm from the cluster starting-point) may be equivalent. Similarities in the concentration may further agree with the suggestion in subsequent chapters that for corresponding cluster spacing configurations, local AIP concentration may depend on their position along the axis of flow. The comparative analysis showed that except for the full coverage cluster at both 100 s^{-1} and 300 s^{-1} wall shear rates, the concentrations at these equidistant locations were approximately of equal magnitude (Figure 3.10). Finally, the 2 mm × 2 mm coverage simulations were also assessed for the time taken to achieve the threshold local AIP concentration (Figure 3.11). Similar to simulation results for the 4 mm × 4 mm coverage, an increase in shear at the same pattern configurations only slightly increased the threshold concentration achievement time. Likewise, at the same shear rate, increasing the distance between adjacent clusters resulted in longer threshold concentration achievement times. However, the time to achieve threshold local AIP concentration for similar pattern configurations and shear rate increased with

smaller total number of clusters (Figure 3.11). For example, for a 4 mm × 4 mm area exposed to 300 s^{-1} wall shear rate, it was predicted that the time taken for the 20 μm coverage to achieve threshold AIP concentration was approximately 2 hours 10 minutes (Figure 3.7B). The time taken for a 2 mm × 2 mm coverage was approximately 2 hours 15 minutes (Figure 3.11B). Taken together, these results suggested that increasing the total cluster number resulted in increased local AIP concentration and therefore a quicker time to local threshold concentration achievement.

3.3 Discussion

In a previous study, it was observed that nutrient mass transport played a lesser role in biofilm development at a shear rate of 100 s^{-1} and above versus at 50 s^{-1} shear rate [64]. In that study, a limited change in biomass (indicated by biovolume and thickness data) was observed when nutrient concentration doubled at 100 s^{-1} shear rate; however, at 50 s^{-1}, doubling the nutrient concentration was accompanied by an approximate doubling of the biomass. In this body of work, wall shear rates of 100 s^{-1} and 300 s^{-1} were selected in order that nutrient mass transfer limitation was negligible. Therefore, theoretical considerations for the mechanism of biofilm development on micropatterned clusters under flow include the hydrodynamic forces and local concentration profile of the solutes and metabolites involved in biofilm development. These simulations provide a means of correlating the convective mass transfer of AIP within the flow chamber with biofilm development within the experimental system described in subsequent chapters.

The events involved in *S. aureus* biofilm development include adhesion of cells followed by accumulation and colony formation and ultimately biofilm development that is mediated by the *agr* locus produced AIP [34, 71, 84]. Evaluations of these biofilm development steps have revealed that environmental conditions, in addition to cell population density, play a role in the cell signaling phenomenon involving AIP [34-38, 80]. In this study, evaluation, via *in silico* modeling of micropatterned topography and hydrodynamic shear on the mass transfer of AIP was performed. The simulation results demonstrate that the theoretical mass transfer of AIP in a dynamic environment is influenced by the magnitude of the hydrodynamic shear within the experimental flow chamber. This influence of shear rate

was observed in the difference in concentration magnitude at both shear rates of 100 s^{-1} and 300 s^{-1} for similar pattern configurations. The shear rate influence was also evident by the concentration profiles along the axis of flow. These profiles predict an increase concentration on the surface of the clusters and in the direction of flow from entrance to exit; thus, predicting location dependent variation in AIP concentration within the experimental system.

Conversely, the increase in spacing of cell clusters leads to an increase in the length of time taken to achieve the theoretical threshold local concentration of AIP within the flow chamber. The concentration magnitude at a specific location equivalent to the last cluster geometry in each simulation was probed as a function of time. In simulations executed at equivalent shear rates, the time taken to achieve the local AIP concentration at this location increased with spacing from full coverage to 20 µm to 110 µm. Experimentally, this means that configurations in which cells achieve the threshold concentration of AIP earlier, develop biofilm faster. This should consequently lead to more developed biofilm (exhibiting greater biovolume and thickness) than configurations that achieved AIP threshold concentration at later times. Additionally, over an 8-hour time course, the magnitude of concentration at this probe location increases at a faster pace at 20 µm versus at 110 µm – particularly past the 5-hour time point. Therefore, in an experimental system, these simulation results predict that the influence of pattern spacing alone should lead to improved biofilm growth at 20 µm spacing versus at 110 µm. Therefore, in the experimental system, cell clusters that are spaced a distance of 20 µm apart are predicted to exhibit higher biovolume and thickness (indicative of biofilm progression) versus the 110 µm spacing. Additionally, the analysis suggests that for clusters of similar size and coverage under an equal influence of shear, there may exist a

critical spacing between adjacent clusters at which the threshold local AIP concentration is not achieved.

It is noted that the predicted time to achieve local threshold AIP concentration in these simulations predominantly differ in magnitudes of minutes. These time variations were demonstrated by the progressively increasing time to threshold concentration in the following two scenarios: as the cluster spacing was increased from full coverage to 20 μm and eventually to 110 μm at equivalent shear rates; and as the shear rate increased from 100 s^{-1} to 300 s^{-1} at equivalent pattern configurations. For an 8-hour experimental period, this time difference alone may not adequately explain differences in biofilm structures that may be observed experimentally. During biofilm development, cells do not cease production, secretion and detection of AIP upon achievement of threshold local AIP [68, 74, 77, 130]. The production of AIP occurs on a feedback loop where the detection of extracellular AIP further promotes the pathway towards production of more AIP [68, 76]. This was considered in the simulations by the continuous production of AIP through the entire 8-hour period. Therefore, the magnitude of time difference at which achievement of local threshold AIP concentration was low for the overall time scale, however, coupled with the pace of local AIP concentration increase, the simulations predict that the actual local concentration of AIP may additionally influence biofilm structures developed under the influence of flow.

Table 3.1: Summary of governing equations and boundary conditions for the simulations

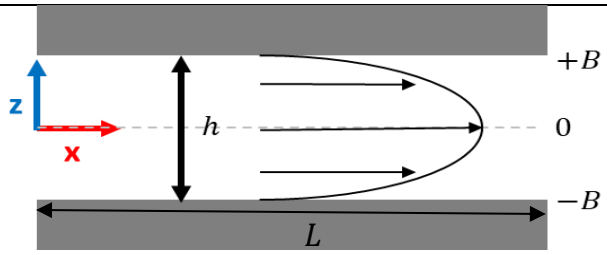	
Laminar flow equations solved	$\rho\nabla.v = 0$ $-\nabla p + \mu\nabla^2 v + \rho g = 0$
Laminar flow boundary conditions	No-slip: at $z = -B \; and \; z = +B, v = 0$ Single inflow: $x = \; 0$ No back flow: at $x = \; L, P = 0$
Maximum velocity (v_{max})	From the velocity profile equation: $v_x = \frac{1}{2\mu}\frac{\partial P}{\partial x}(z^2 - B^2)$, at $z = 0, v_{max} = -\frac{1}{2\mu}\frac{\partial P}{\partial x}B^2$
Average velocity (v_{avg})	From the volume flow rate: $Q = \int_{-B}^{B} v_x \, (w.dz) = -\frac{w}{2\mu}\frac{\partial P}{\partial x}\left(\frac{4B^3}{3}\right)$, and from the cross-sectional area: $A = 2Bw$ $v_{avg} = \frac{Volumetric\ flow\ rate}{Cross\ sectional\ area} = \frac{Q}{A}$ $v_{avg} = -\frac{1}{3\mu}\frac{\partial P}{\partial x}B^2 = \frac{2}{3}v_{max}$
Transport of diluted species equations solved	$N_i = -D_i\nabla c_i + c_i v$ $\frac{\partial c_i}{\partial t} + \nabla.N_i = R_i$
Transport of diluted species boundary conditions	In-flux: at cluster geometry surface $N_i = N_0$ No flux: at $x = 0, z = +B \; and \; z = -B, N_i = 0$

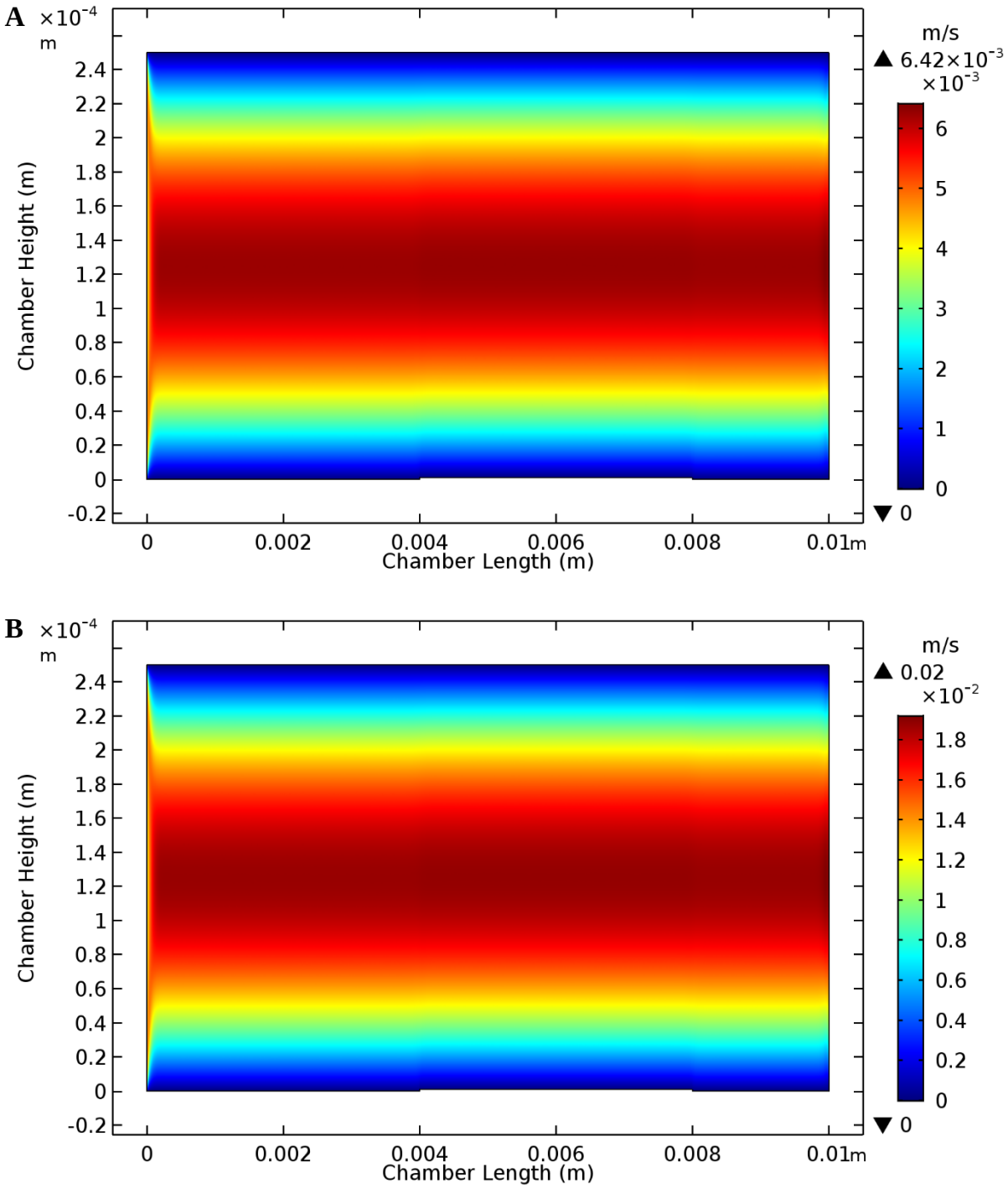

Figure 3.1: Simulated velocity profile for the parallel plate geometry using the experimental flow chamber dimensions. The figure shows velocity (m/s) heat map versus chamber length and height (m) for simulations of **(A)** 100 s^{-1} and **(B)** 300 s^{-1} shear.

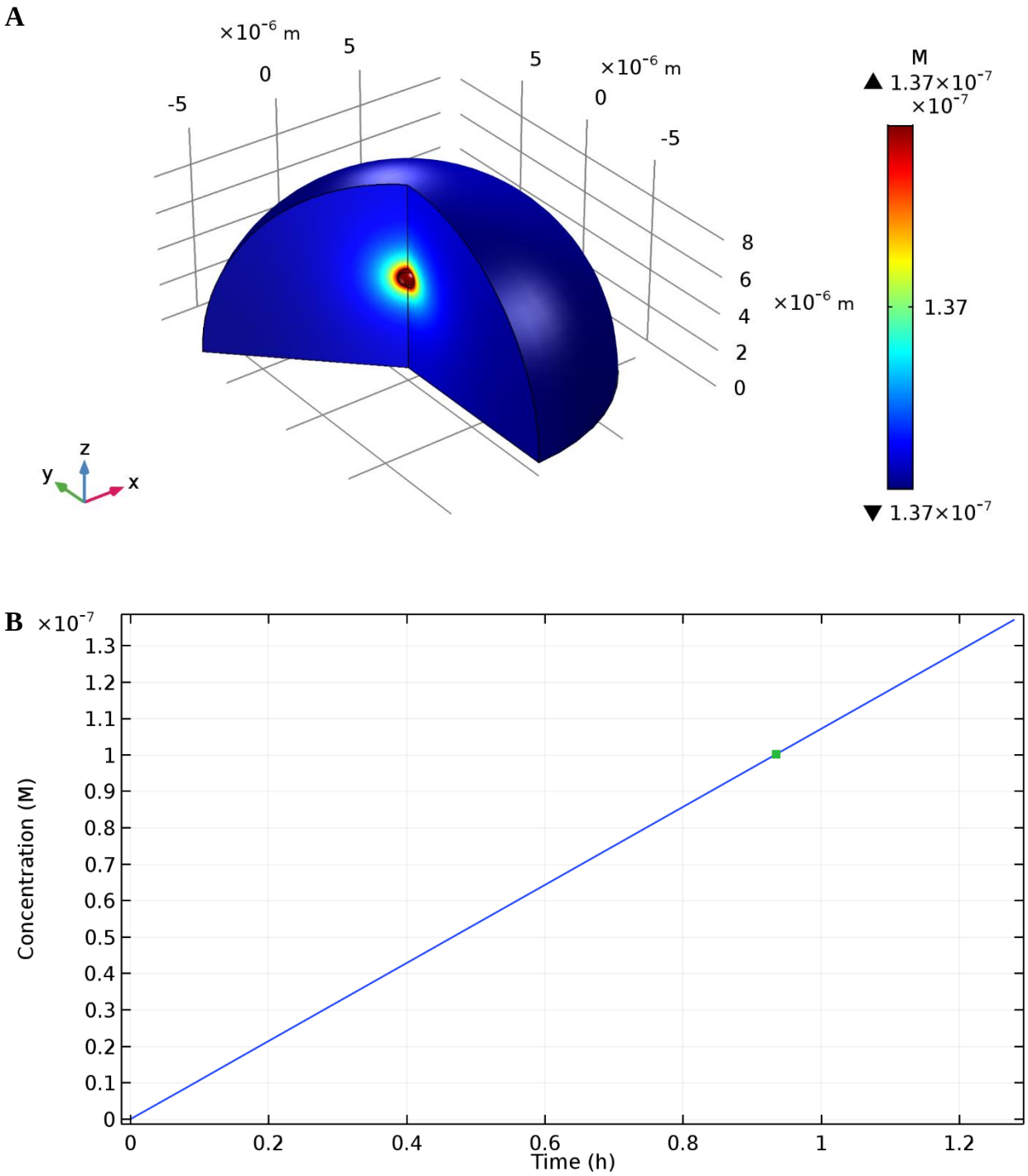

Figure 3.2: Simulated concentration profile for a single sphere isolated within a larger fluid filled hemisphere. **(A)** Concentration (M) color map and **(B)** Plot of AIP concentration at the surface of the inner sphere as a function of time showing threshold concentration point.

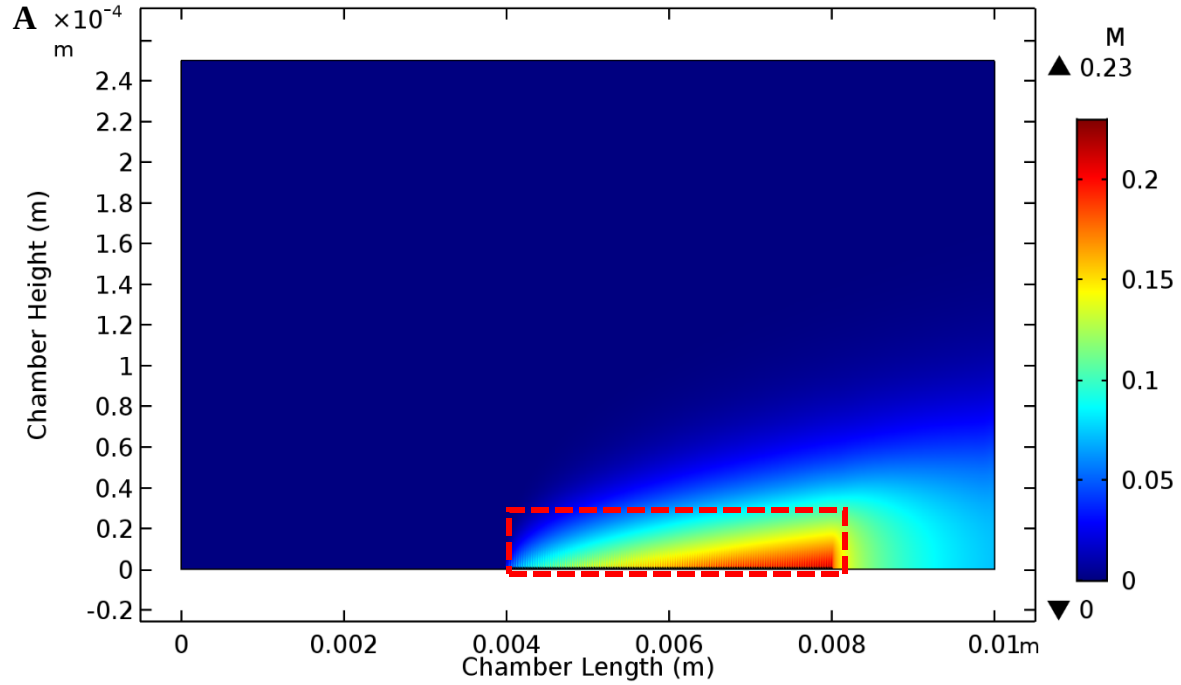
A
×10^-4
m
Chamber Height (m)
2.4
2.2
2
1.8
1.6
1.4
1.2
1
0.8
0.6
0.4
0.2
0
-0.2
0
0.002
0.004
0.006
0.008
0.01m
Chamber Length (m)
M
▲ 0.23
0.2
0.15
0.1
0.05
0
▼ 0

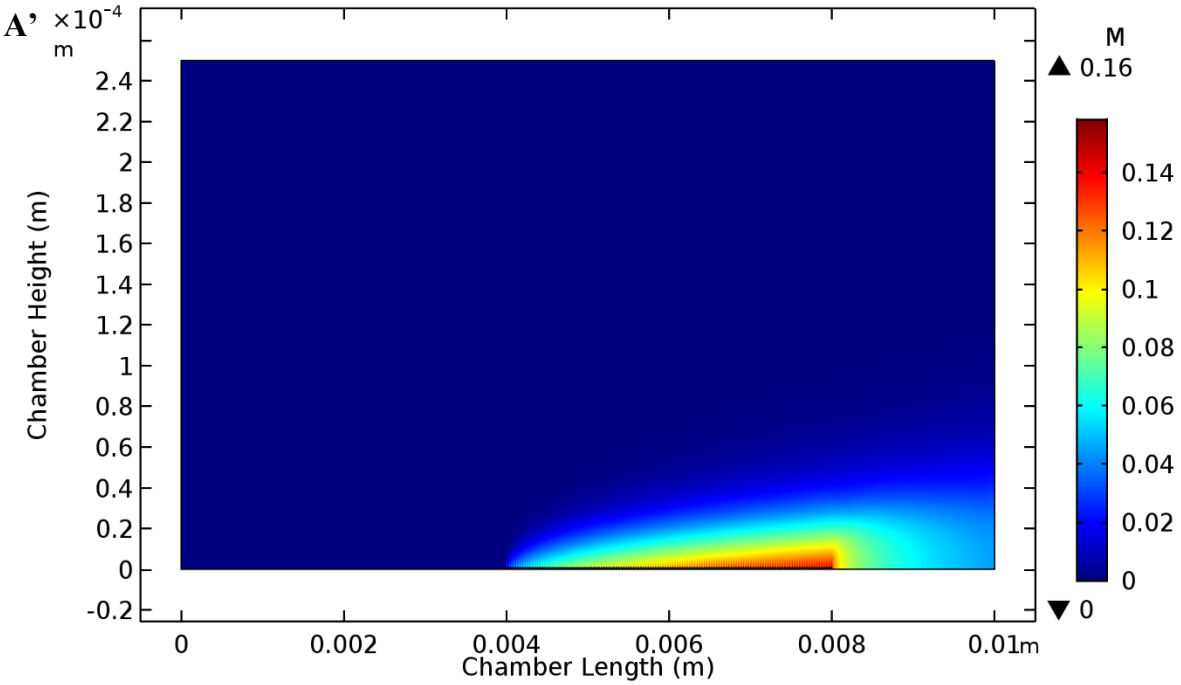
A'
×10^-4
m
Chamber Height (m)
2.4
2.2
2
1.8
1.6
1.4
1.2
1
0.8
0.6
0.4
0.2
0
-0.2
0
0.002
0.004
0.006
0.008
0.01m
Chamber Length (m)
M
▲ 0.16
0.14
0.12
0.1
0.08
0.06
0.04
0.02
0
▼ 0

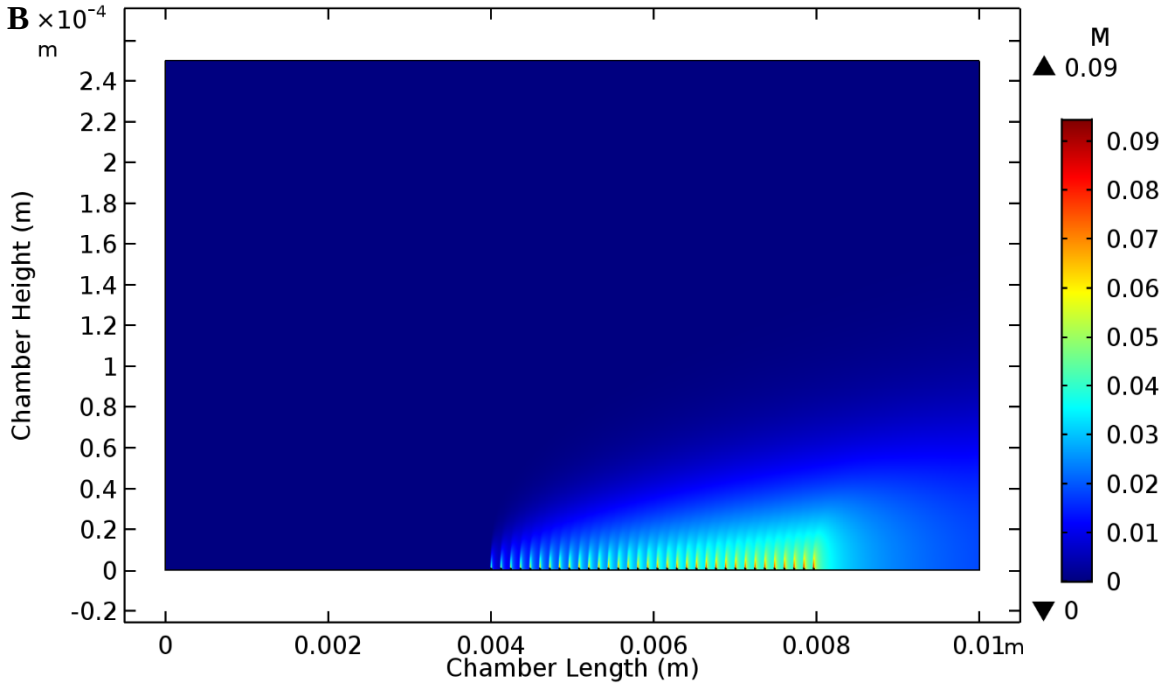
B
×10⁻⁴
m
Chamber Height (m)
2.4
2.2
2
1.8
1.6
1.4
1.2
1
0.8
0.6
0.4
0.2
0
-0.2
0
0.002
0.004
0.006
0.008
0.01m
Chamber Length (m)
M
▲ 0.09
0.09
0.08
0.07
0.06
0.05
0.04
0.03
0.02
0.01
0
▼ 0

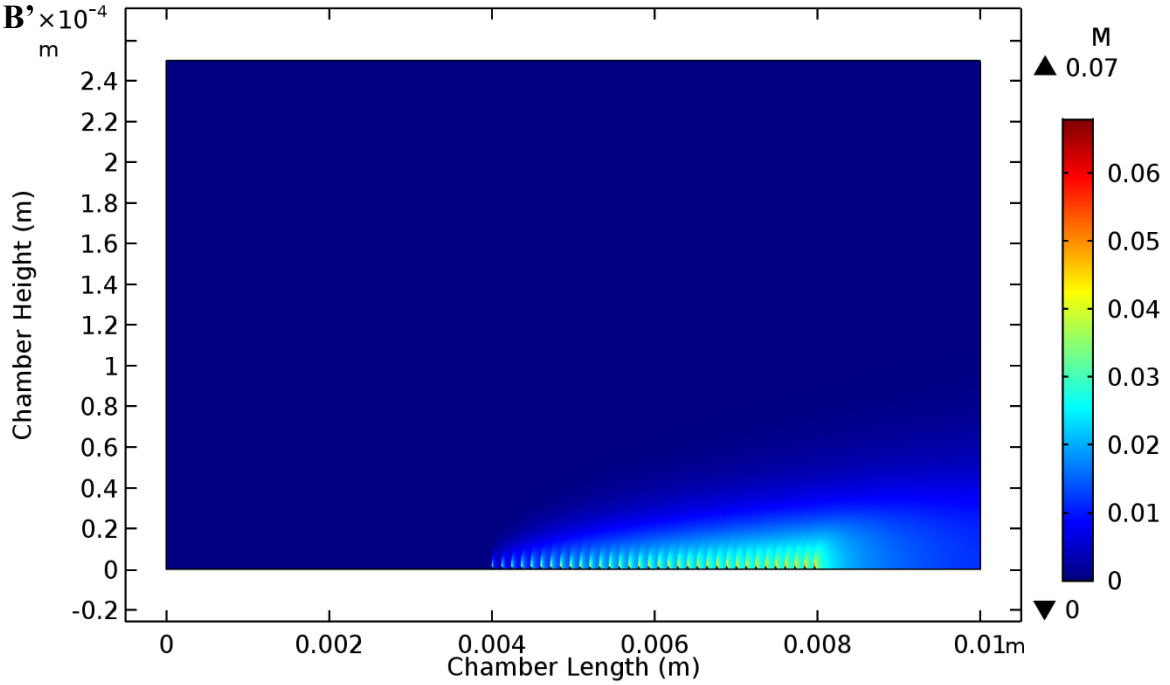
B'
×10⁻⁴
m
Chamber Height (m)
2.4
2.2
2
1.8
1.6
1.4
1.2
1
0.8
0.6
0.4
0.2
0
-0.2
0
0.002
0.004
0.006
0.008
0.01m
Chamber Length (m)
M
▲ 0.07
0.06
0.05
0.04
0.03
0.02
0.01
0
▼ 0

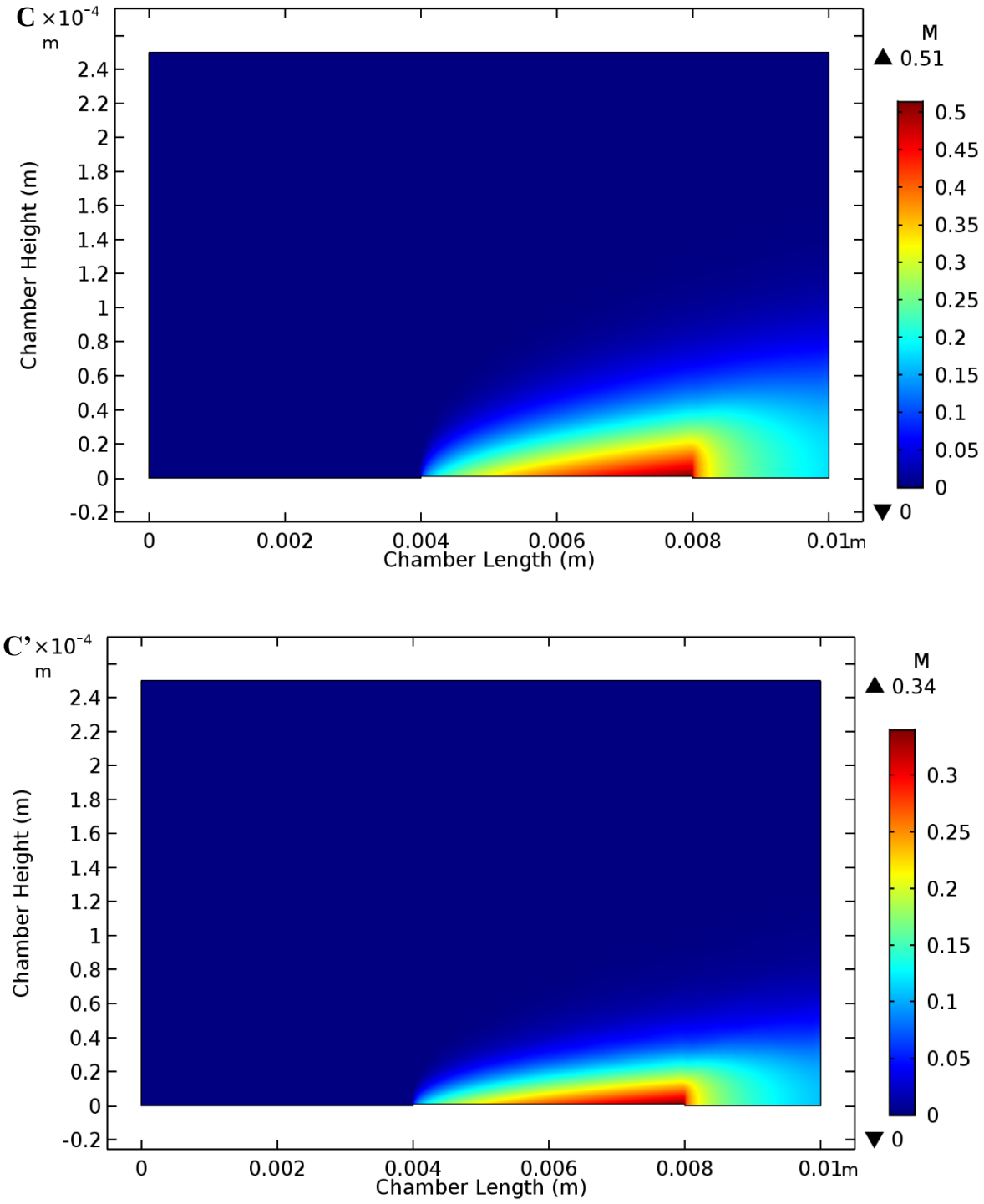

Figure 3.3: Simulated concentration profile at the end of 8 hours. The figures show concentration (M) heat map versus chamber length and height (m) for simulations of 4 mm × 4 mm coverage, **(#)** 100 s^{-1} or **(#')** 300 s^{-1}, **(A)** 20 µm, **(B)** 110 µm, and **(C)** full coverage

spacing. The direction of flow is along the chamber length with the entrance and exit located at 0 m and 0.01 m, respectively. The reference bars show corresponding concentration magnitudes with the maximum and minimum values indicated. Figure 3.3 shows the detailed view of the patterned region in each image indicated by the red dashed triangle in **(A)**.

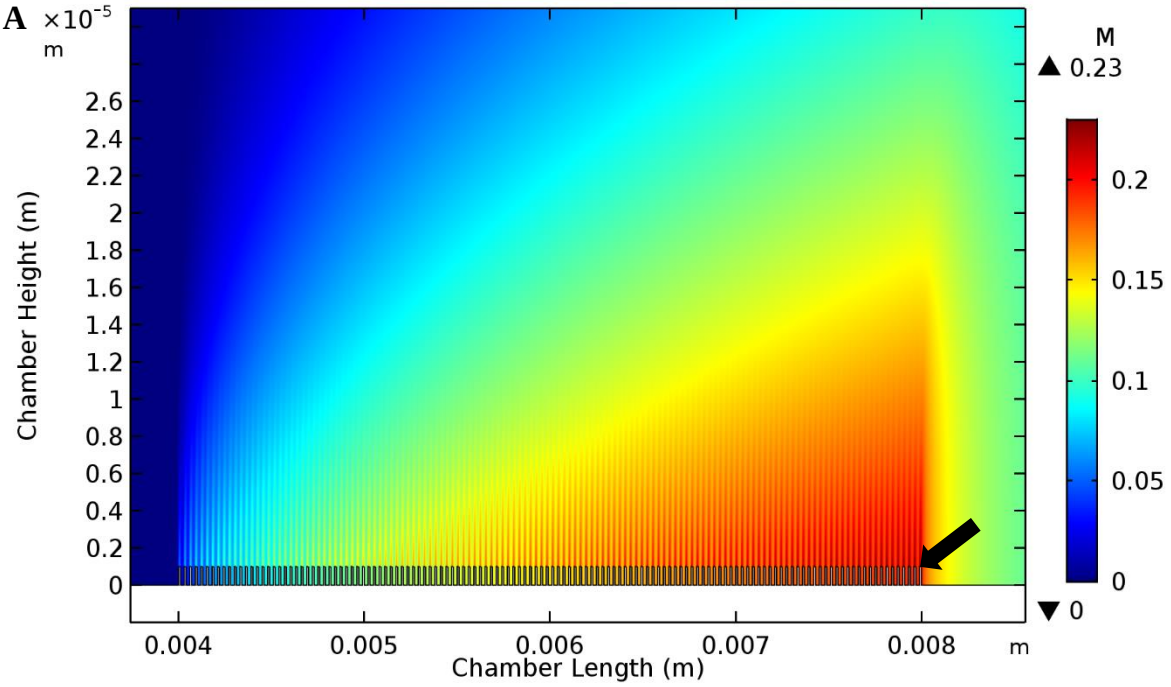
A
×10^-5
m
Chamber Height (m)
2.6
2.4
2.2
2
1.8
1.6
1.4
1.2
1
0.8
0.6
0.4
0.2
0
0.004
0.005
0.006
0.007
0.008
m
Chamber Length (m)
M
▲ 0.23
0.2
0.15
0.1
0.05
0
▼ 0

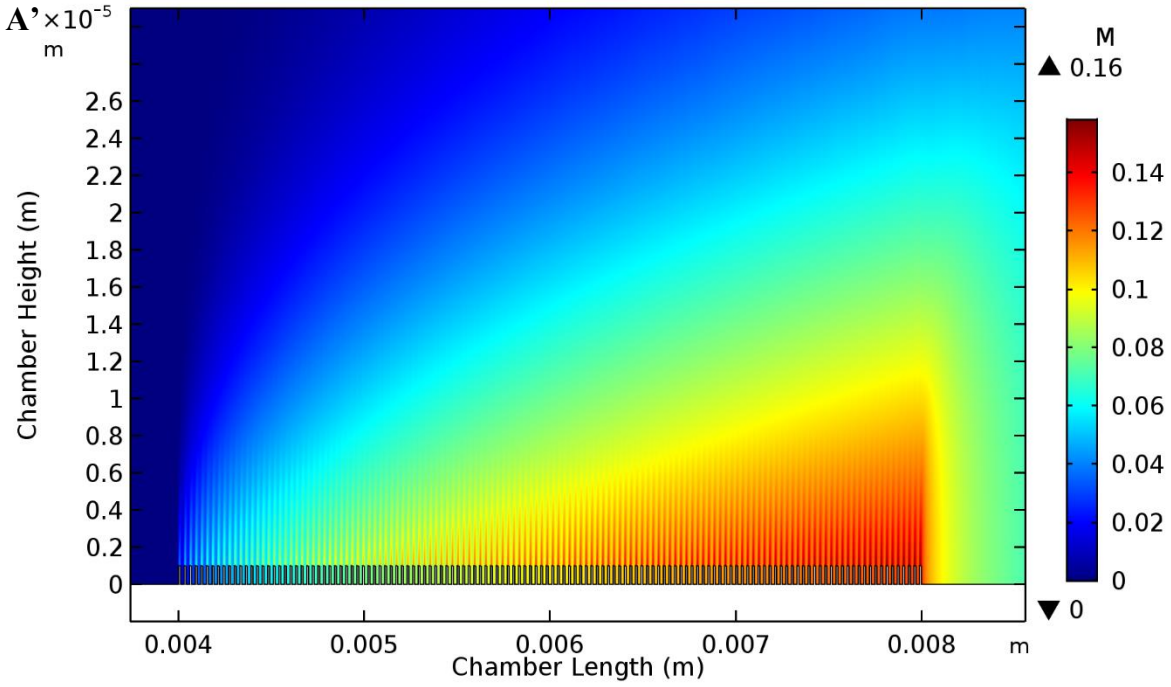
A'
×10^-5
m
Chamber Height (m)
2.6
2.4
2.2
2
1.8
1.6
1.4
1.2
1
0.8
0.6
0.4
0.2
0
0.004
0.005
0.006
0.007
0.008
m
Chamber Length (m)
M
▲ 0.16
0.14
0.12
0.1
0.08
0.06
0.04
0.02
0
▼ 0

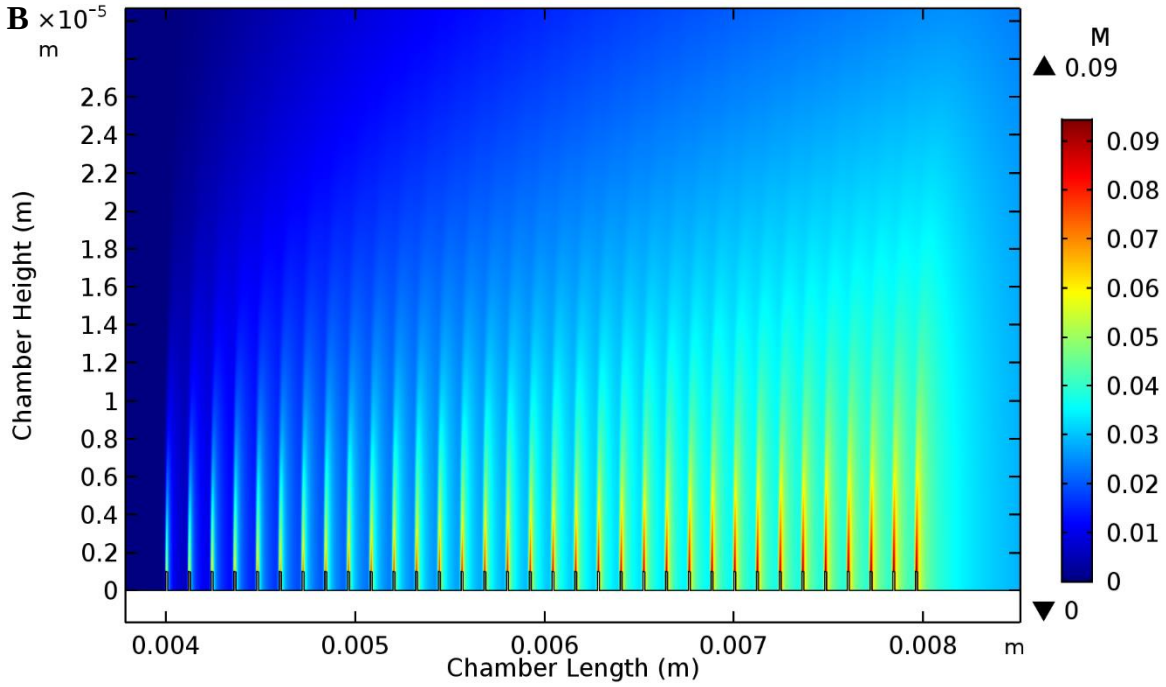
B ×10^-5
m
Chamber Height (m)
2.6
2.4
2.2
2
1.8
1.6
1.4
1.2
1
0.8
0.6
0.4
0.2
0
0.004
0.005
0.006
0.007
0.008
m
Chamber Length (m)
M
▲ 0.09
0.09
0.08
0.07
0.06
0.05
0.04
0.03
0.02
0.01
0
▼ 0

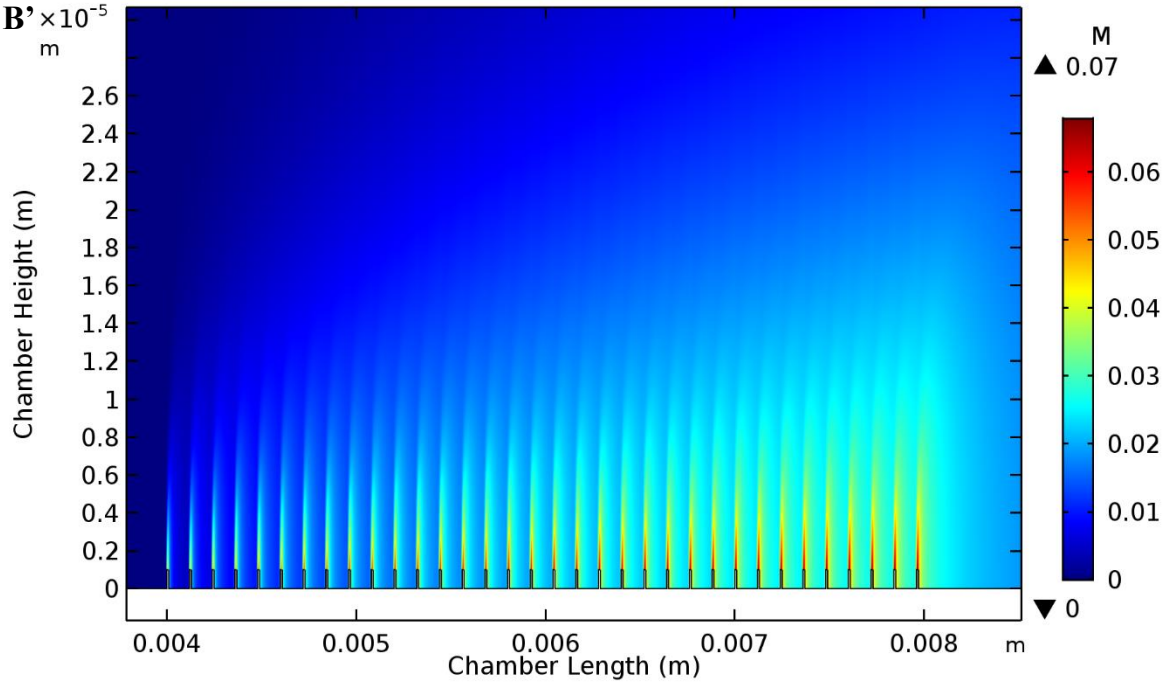
B' ×10^-5
m
Chamber Height (m)
2.6
2.4
2.2
2
1.8
1.6
1.4
1.2
1
0.8
0.6
0.4
0.2
0
0.004
0.005
0.006
0.007
0.008
m
Chamber Length (m)
M
▲ 0.07
0.06
0.05
0.04
0.03
0.02
0.01
0
▼ 0

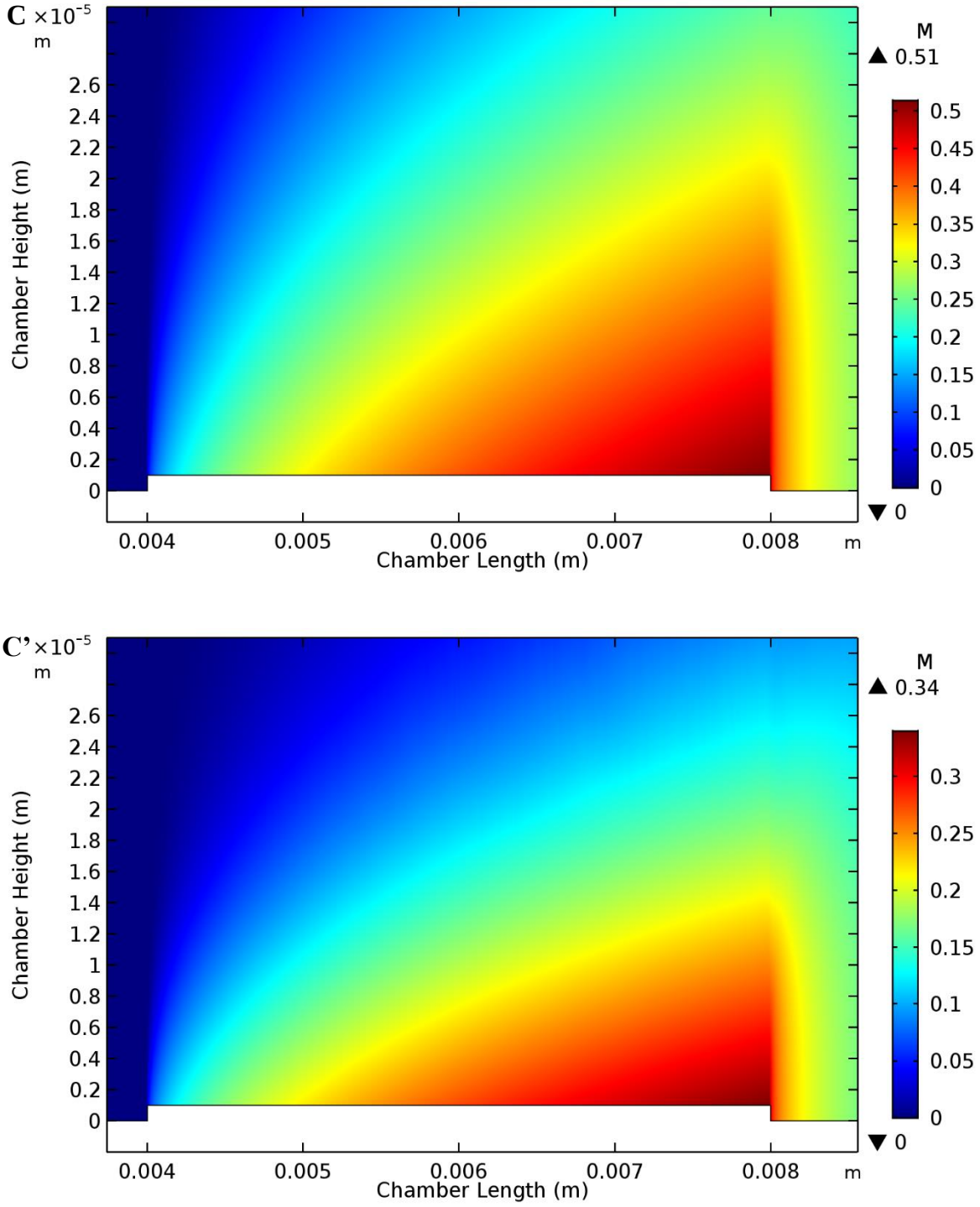

Figure 3.4: Detailed view of patterned surface simulated concentration profile at the end of 8 hours. The figures show concentration (M) heat map versus chamber length and height (m) for simulations of 4 mm × 4 mm coverage, **(#)** 100 s^{-1} or **(#')** 300 s^{-1}, **(A)** 20 µm, **(B)** 110 µm,

and **(C)** full coverage spacing. The direction of flow is along the chamber length axis from left to right. These images indicate concentration increases on the individual pattern protrusions and a decrease between adjacent patterns. The full coverage simulation shows a steady accumulation of AIP along the flow direction. Figure 3.4 shows the time-dependent concentration profile at the end point of patterned coverage indicated by the black arrow shown in **(A)**.

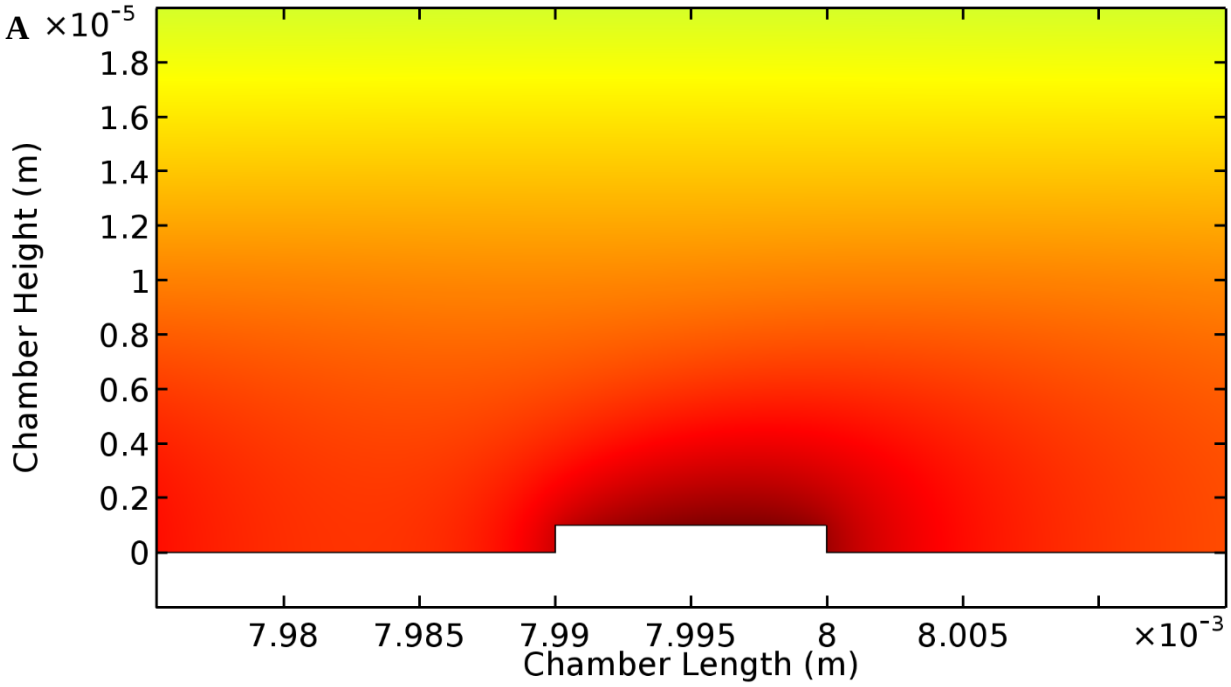
A
×10^-5
1.8
1.6
1.4
1.2
1
0.8
0.6
0.4
0.2
0
Chamber Height (m)
7.98
7.985
7.99
7.995
8
8.005
×10^-3
Chamber Length (m)

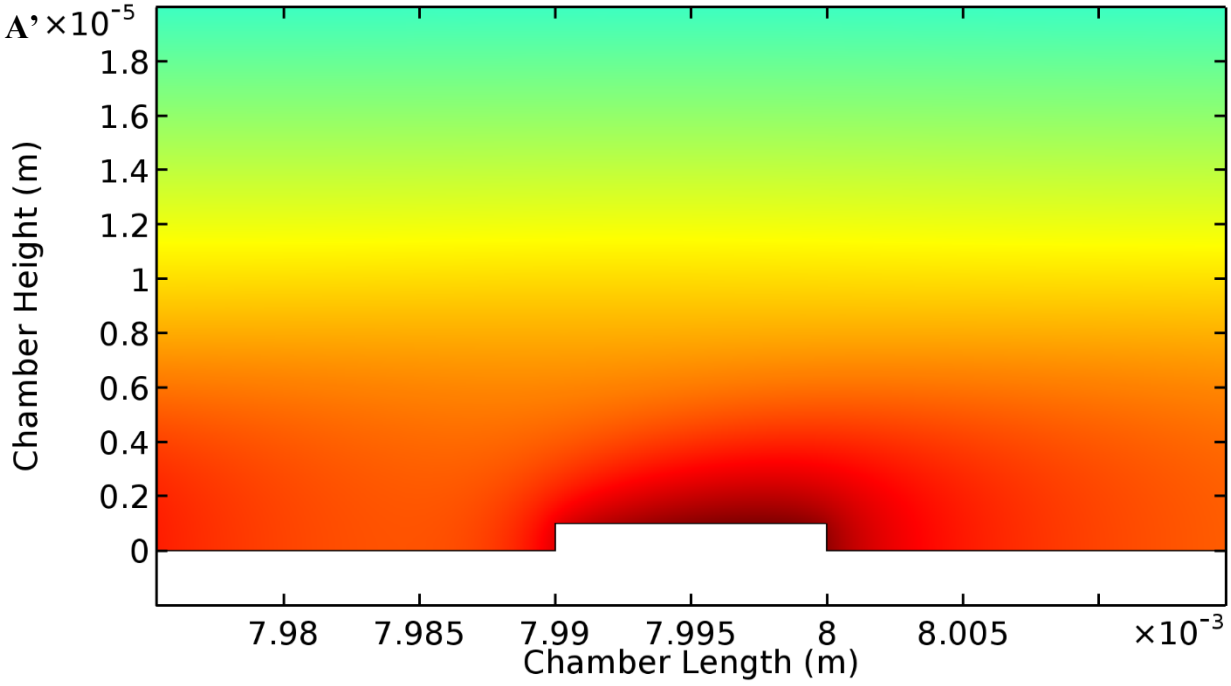
A'
×10^-5
1.8
1.6
1.4
1.2
1
0.8
0.6
0.4
0.2
0
Chamber Height (m)
7.98
7.985
7.99
7.995
8
8.005
×10^-3
Chamber Length (m)

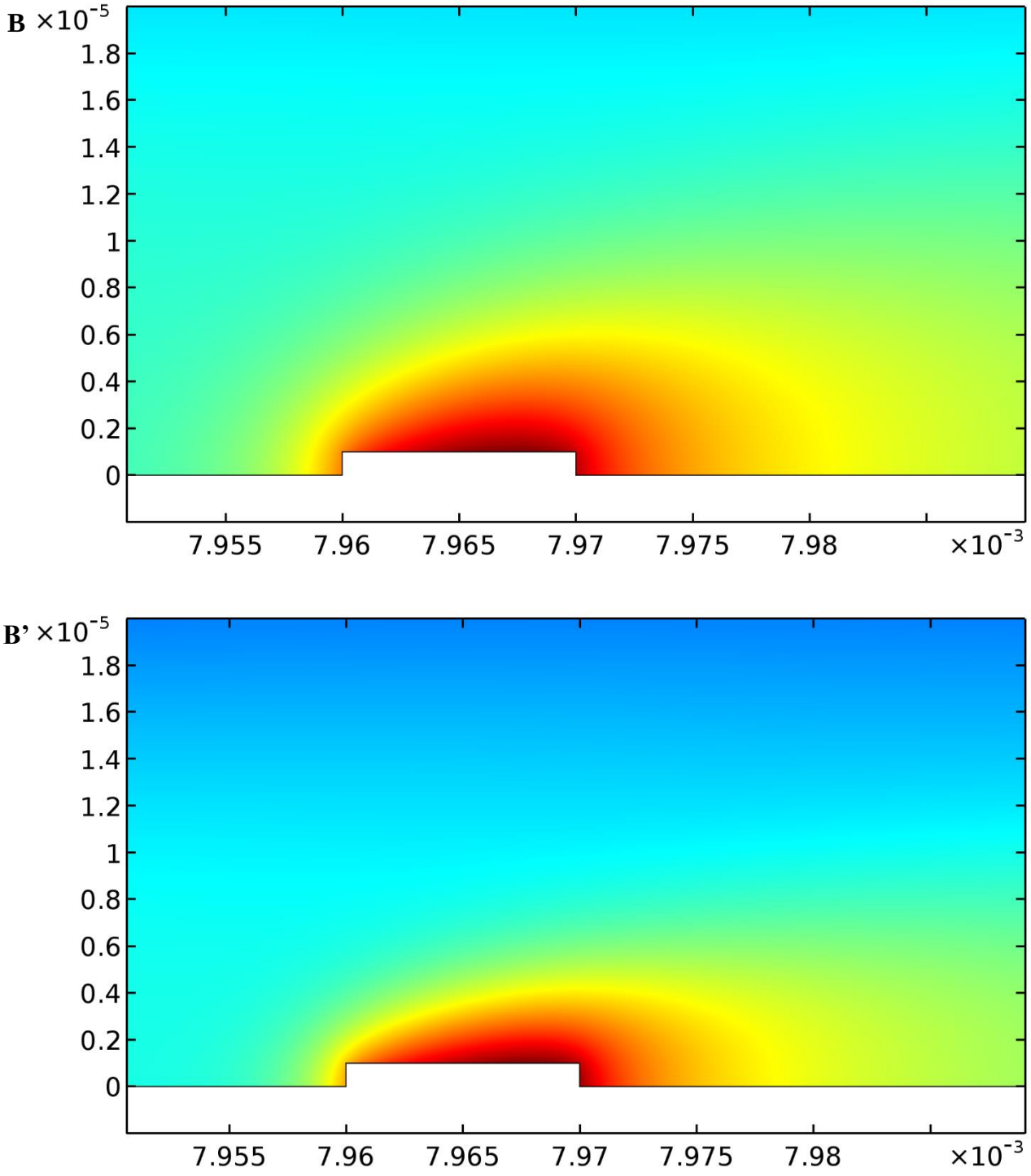

Figure 3.5: View of concentration profile at the location of final geometry cluster at the end of 8 hours for 4 mm × 4 mm cluster geometry for simulations of 4 mm × 4 mm coverage, **(#)** 100 s^{-1} or **(#')** 300 s^{-1}, **(A)** 20 µm, **(B)** 110 µm.

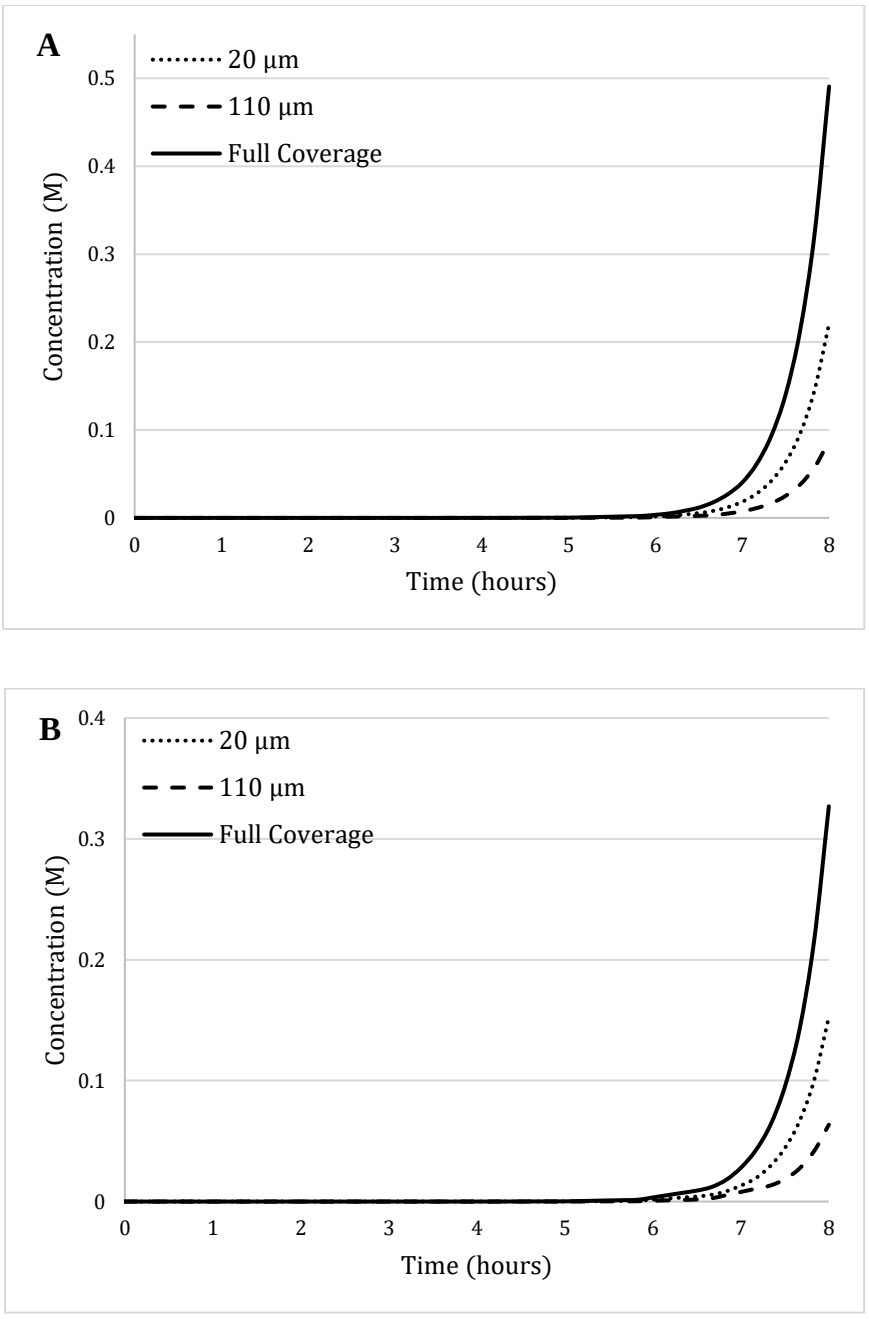

Figure 3.6: Concentration profile as a function of time at the end point of 4 mm × 4 mm pattern coverage at shear rates, **(A)** 100 s^{-1}, and **(B)** 300 s^{-1}. Each chart shows the increasing concentration during the 8-hour simulation and the reduction in concentration magnitude due to the cluster pattern configurations.

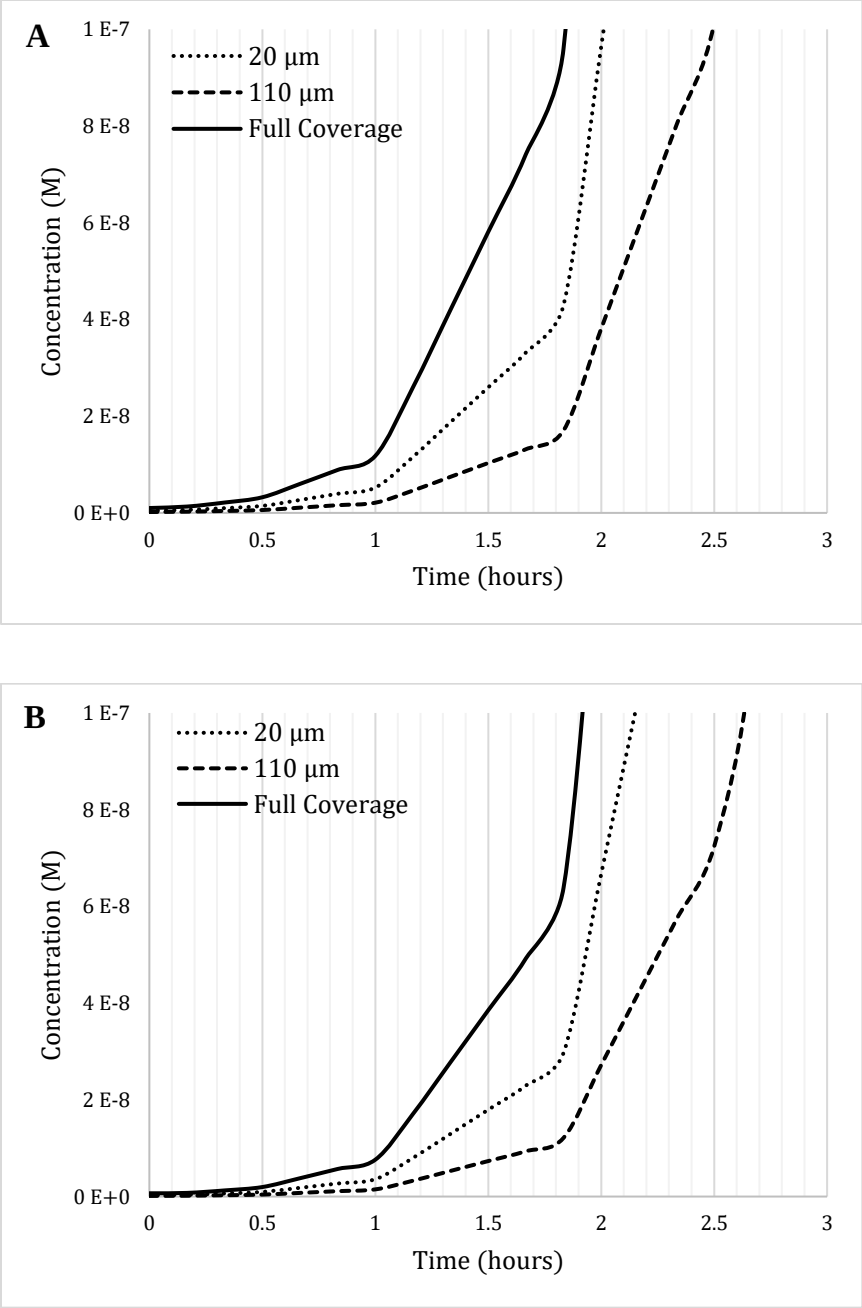

Figure 3.7: Concentration profile showing the time taken to achieve threshold AIP concentration value of 1×10^{-7} M at the end point of 4 mm × 4 mm pattern coverage and shear rates **(A)** 100 s^{-1}, and **(B)** 300 s^{-1}. These charts were generated from the data shown in Figure 3.4 by setting the maximum concentration to the threshold value.

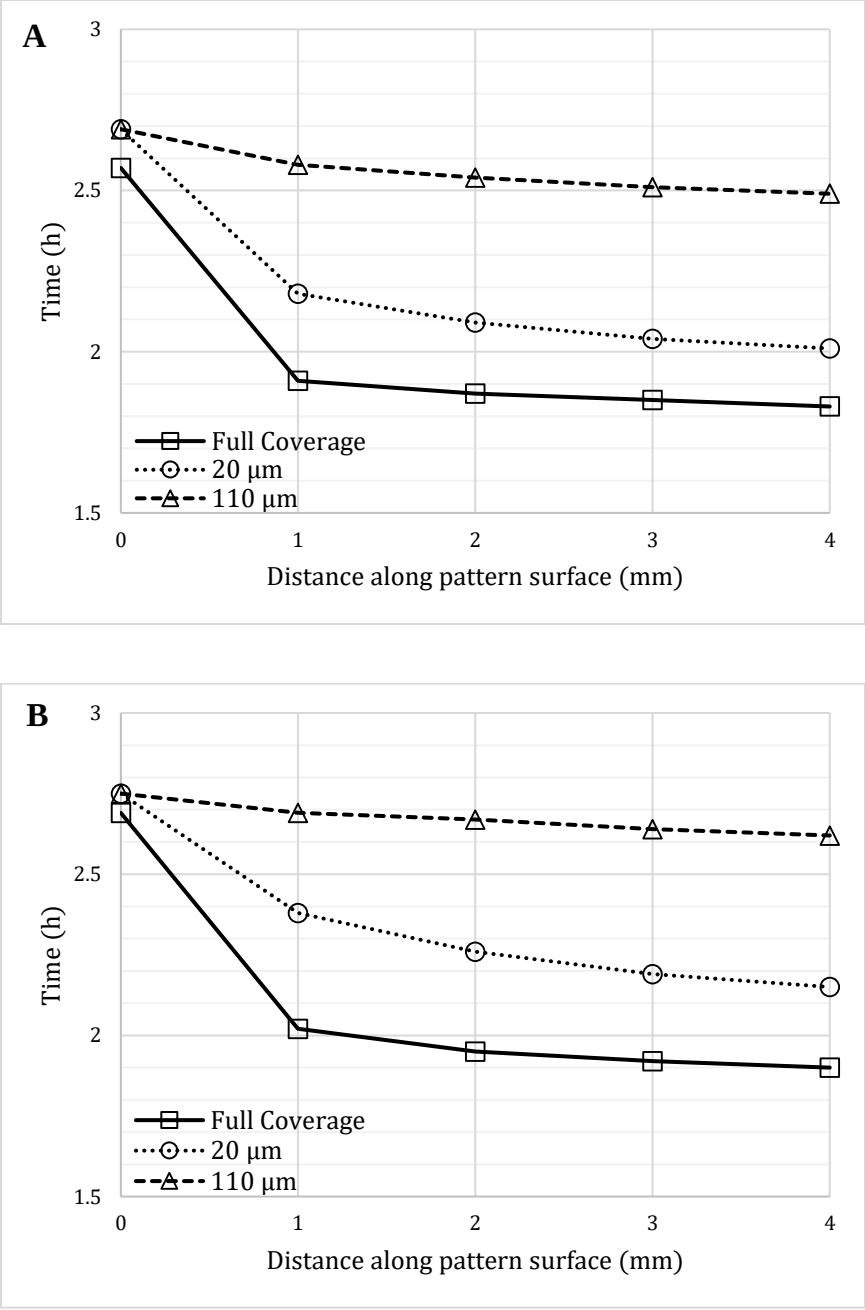

Figure 3.8: Plot showing the time taken to achieve threshold AIP concentration value of 1×10^{-7} M at various points along the 4 mm × 4 mm pattern coverage at shear rates **(A)** 100 s^{-1}, and **(B)** 300 s^{-1}.

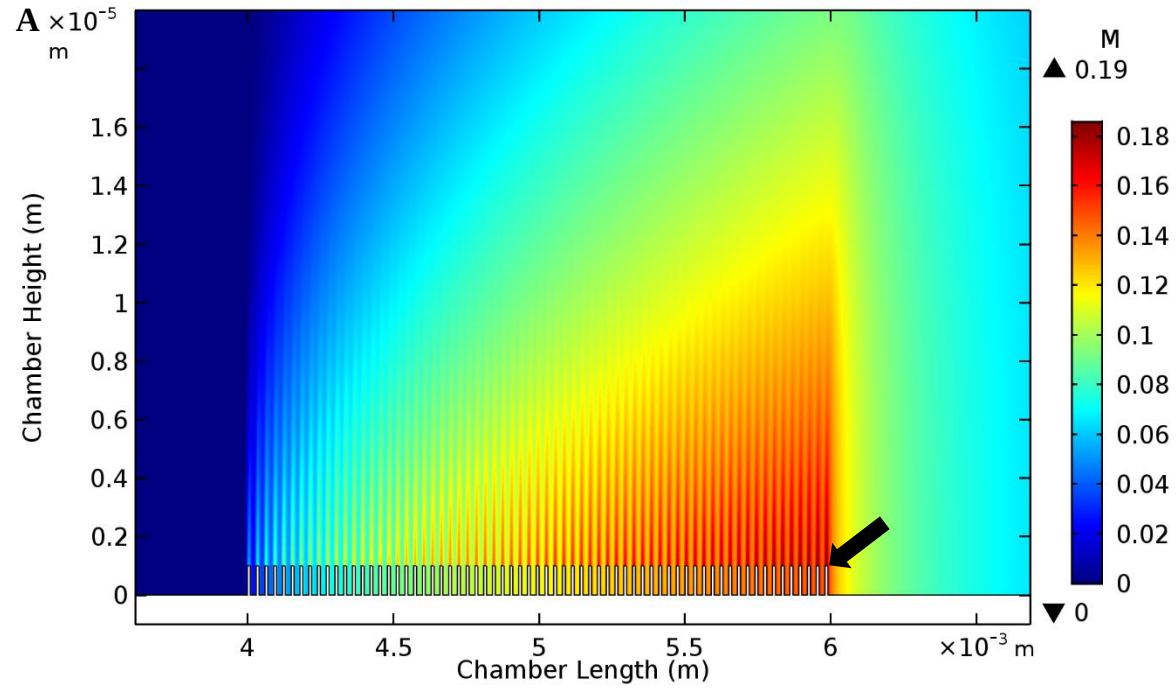
A
×10^-5
m
Chamber Height (m)
1.6
1.4
1.2
1
0.8
0.6
0.4
0.2
0
4
4.5
5
5.5
6
×10^-3 m
Chamber Length (m)
M
▲ 0.19
0.18
0.16
0.14
0.12
0.1
0.08
0.06
0.04
0.02
0
▼ 0

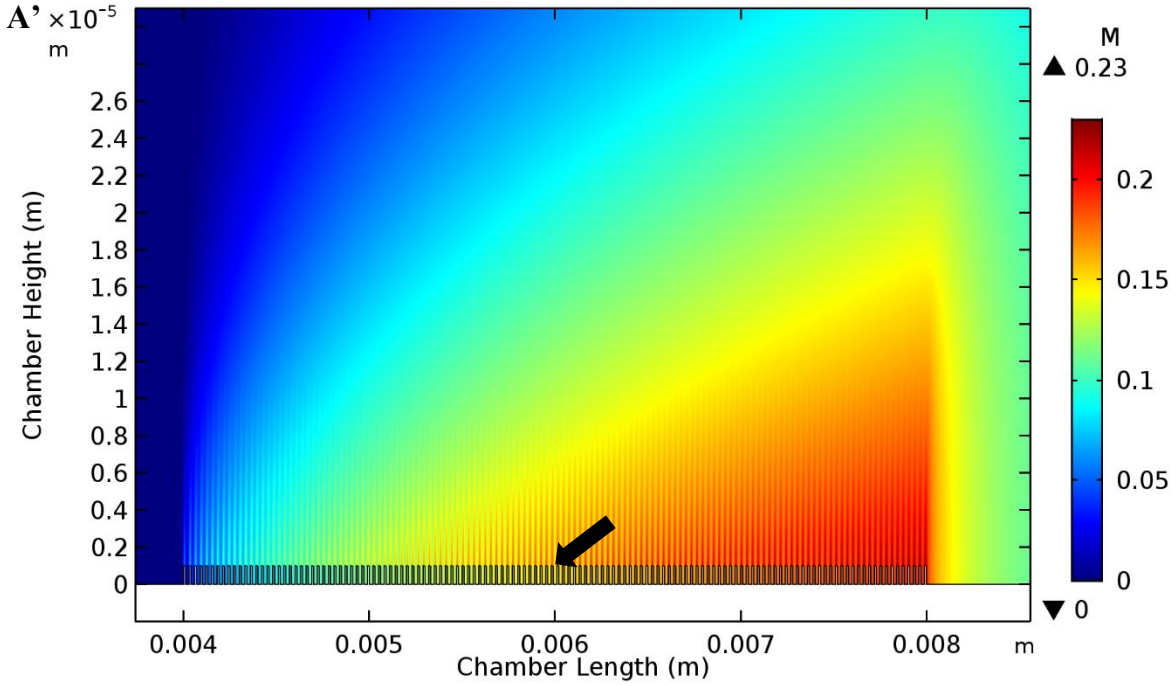
A'
×10^-5
m
Chamber Height (m)
2.6
2.4
2.2
2
1.8
1.6
1.4
1.2
1
0.8
0.6
0.4
0.2
0
0.004
0.005
0.006
0.007
0.008
m
Chamber Length (m)
M
▲ 0.23
0.2
0.15
0.1
0.05
0
▼ 0

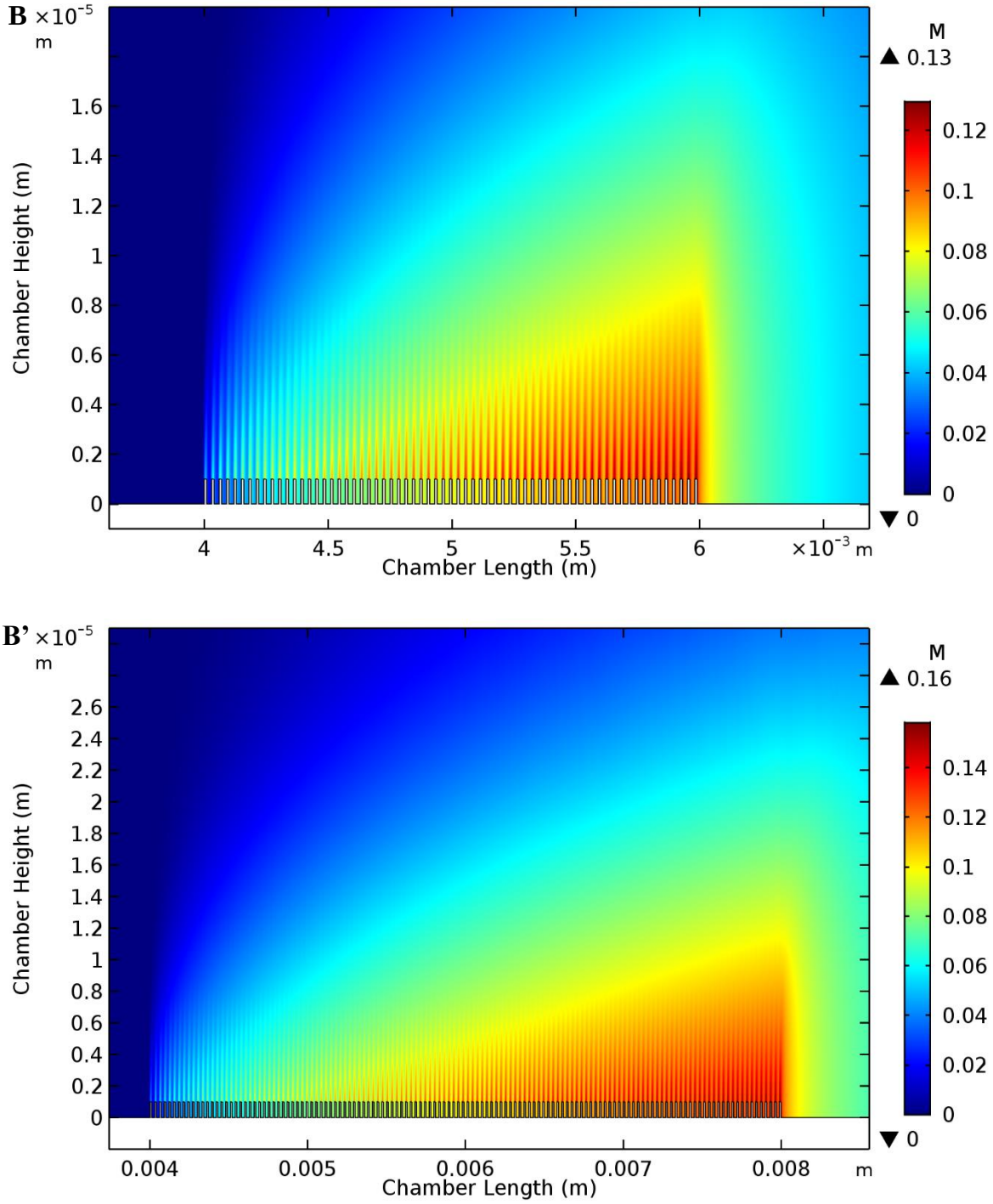

Figure 3.9: Effect of total cluster number on AIP concentration profile after 8 hours under flow. The images show the concentration (M) heat map of 20 µm cluster spacing at **(#)** 2 mm

× 2 mm and **(#')** 4 mm × 4 mm coverage, and **(A)** 100 s^{-1} and **(B)** 300 s^{-1} wall shear rate. Arrows indicate reference points for data shown in Figure 3.8.

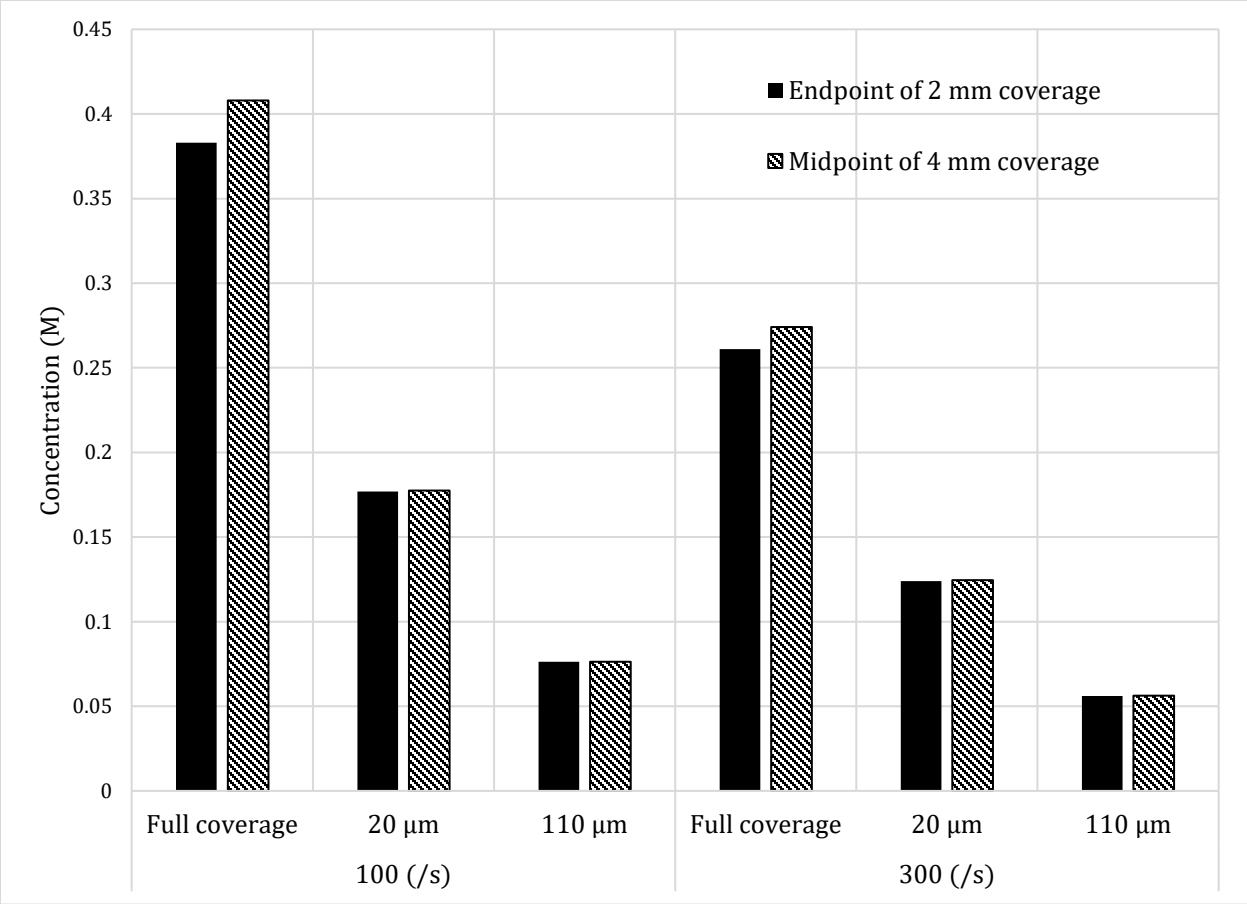

Figure 3.10: Comparison of the concentration (M) at the end of 2 mm × 2 mm cluster coverage versus at the midpoint of 4 mm × 4 mm cluster coverage. The concentration at the endpoint of 2 mm × 2 mm coverage was captured at the location indicated in Figure 3.6A for all 2 mm × 2 mm simulations and the concentration at the midpoint of 4 mm × 4 mm coverage was captured at the location indicated in Figure 3.6A' for all 4 mm × 4 mm simulations.

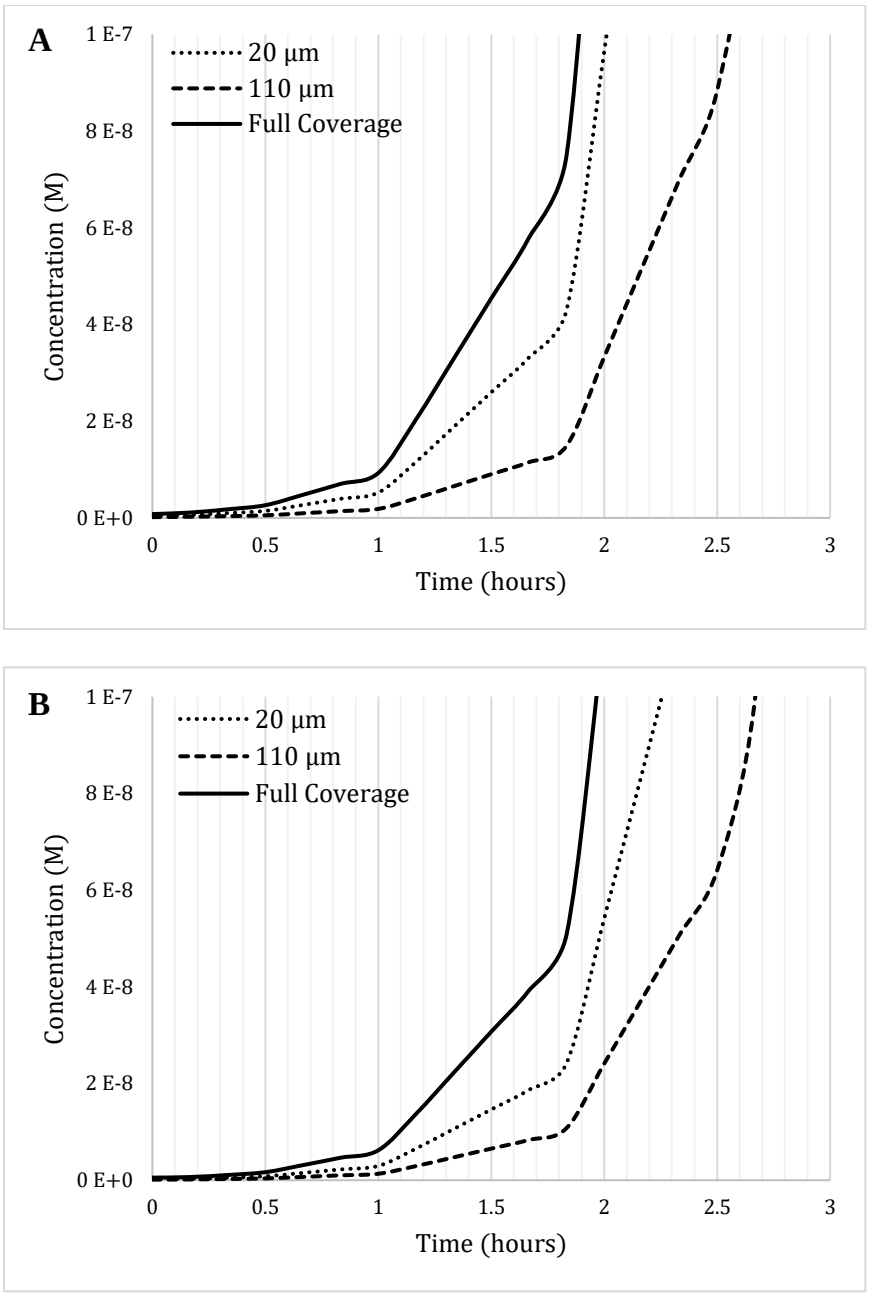

Figure 3.11: Concentration profile showing the time taken to reach the threshold AIP concentration value of 1×10^{-7} M at the end point of 2 mm × 2 mm pattern coverage at shear rates **(A)** 100 s^{-1}, and **(B)** 300 s^{-1}.

Chapter 4: Influence of the substratum adhesion pattern of cells on the early development of *Staphylococcus aureus* biofilms

4.1 Rationale for study

On their path to biofilm development, adherent *S. aureus* cells on host implant-device surface or matrix protein accumulate forming small adherent cluster colonies that are a precursor to biofilm development [35, 43, 151-153]. This cluster formation is accomplished either by clonal multiplication, or by the adherence of multiple cells within a local vicinity [35, 43]. To become virulent biofilm, adhered clusters of cells communicate with each other as well as with adjacent clusters by releasing and detecting small AIP molecules – a phenomenon commonly referred to as QS [31-36, 43, 72-76, 84, 85]. The difficulty of eradicating *S. aureus* infections has been attributed to its ability to evade host defenses via selective release of virulent material until the establishment of a suitable quorum of cells [2, 9, 34, 75, 154].

For this reason, the QS pathway has become a viable target for therapeutic strategies aimed towards *S. aureus* biofilm-based infections [75]. One such strategy involves the direct targeting of the *agr*-locus, where ongoing research proceeds with either of the following goals: 1) inhibiting the autoinducer characteristics of AIP by targeting or mutating genes of primary metabolites of the locus [80, 82, 155-157] or 2) introducing secondary metabolic molecules to compete with the *agr*-locus' AIP synthesis and/or detection pathways [86, 88, 158-164].

While the *agr*-targeting therapeutic strategies have resulted in some success in animal models [54, 80, 83, 87], this method still faces some challenges toward the successful application to potential human drug remedies. One of the main challenges to *agr*-targeting therapeutics is the existence of four *agr* groups, corresponding to four different AIP types

synthesized, among *S. aureus* strains [74]. An inhibitory molecule or *agr*-targeting metabolite that targets all four groups simultaneously has not been discovered. Similarly, other biofilm therapies have an increased failure rate due to the increased resistance of biofilm structures to antimicrobials. For this reason, other biofilm prevention strategies that rely on bioengineering of physical or chemical barriers on indwelling devices are on the horizon [41, 103, 104, 106].

There is increasing scientific evidence that bacterial attachment and subsequent biofilm formation are significantly impacted by surface topography [39, 40, 97, 101, 107, 165-168]. Physical micropatterned PDMS barriers were shown to decrease biofilm development by *E. coli* as well as revealing evidence of interaction among adjacent cell clusters [39, 40]. In addition, other studies revealed that defined spatial localizations of clusters influence the formation of biofilm by various other bacterial strains [101, 107, 168]. However, these studies have mostly focused on limiting the adhesion of cells [104, 106, 169], rather than studying the events that follow adhesion. Also, little is known of the three-dimensional development of *S. aureus* biofilm developed under flow on a micropatterned substratum that is free from physical barriers that may limit the mass transfer of metabolites

The study discussed in this chapter focuses on the understanding how adhesion pattern and spacing of adhered *S. aureus* cell clusters influences three-dimensional biofilm structure. In the previous chapter, the effect of different spacing between adjacent clusters was theorized via *in silico* simulation, suggesting that a larger distance between clusters results in a longer time to achieve threshold local AIP concentration. Thus, in the absence of nutrient mass transfer limitation (due to experimentation at the shear rates of 100 s^{-1} and 300

s^{-1}), this section aims to experimentally investigate the effect of the adhered cell-cluster spatial arrangement on developed biofilm. These studies, in addition to the information from the previous chapter, can further elucidate the underlying processes governing biofilm development under hydrodynamic fluid conditions.

4.2 Results

4.2.1 Evaluation of *S. aureus* biomass accumulation during biofilm development on patterned substratum under fluid flow

To evaluate the effect of the substratum configuration on the development of *S. aureus* biofilm, experiments were performed under flow with different substratum pattern configuration of cells at the start of experiments. Substratum configurations consisted of single layers of cells seeded to saturation within a clustered circular geometry of 10 µm diameter with 20 µm, 50 µm, or 110 µm distance between adjacent clusters. The overall configuration was repeated within a total 4 mm × 4 mm square array. A full coverage single layer of cells covering a total 4 mm × 4 mm square area was used as a control. Following 8 hours of media exposure under flow, images were captured using CLSM that revealed differences in the overall growth of biofilm among the different configurations (Figures 4.1 & 4.2). Biofilms developed on the patterned configurations showed a diminished volume and thickness when compared with those grown at full coverage. Biofilms developed on the 20 µm spacing configurations exhibited a significant increase in the overall biomass observed when compared with the biofilm developed at both 50 µm and 110 µm spacing (Figure 4.2). The 20 µm spacing configurations also displayed a higher tendency for linkage across adjacent clusters (Figure 4.1 B) while no such linkages were observed in either the 50 µm or 110 µm spacing configurations (Figures 4.1 C & D). Overall, the images reveal an increase in volume and thickness of the bacterial biomass as the distance between adjacent cell clusters was reduced.

Quantitative characterization was performed with ISA3D, a MATLAB-based image analysis software, on exported image output of the individual fields represented in Figure 4.3. To characterize the overall structure of developed biofilm, both biovolume and biofilm thickness (mean and maximum) were utilized. The biovolume of biofilm clusters diminished as the spacing between adjacent clusters increased during development under flow (Figure 4.4). Statistical analysis revealed a significant difference in the biovolume of the full coverage biofilms compared to any of the patterned configurations. Furthermore, the difference in biovolume decreases significantly as the spacing configurations increased from 20 μm to 50 μm, however, further increase in spacing to 110 μm did not decrease the biovolume further. Analysis of the mean and maximum biofilm thickness revealed a significant decrease in both when comparing full coverage control to all pattern configurations. Additionally, the mean and maximum thickness of biofilm decreased when the cluster spacing was increased from 20 μm to 50 μm, but the 110 μm spacing showed no further significant decrease compared to the 50 μm spacing (Figure 4.5 A). The surface roughness coefficient was also evaluated to determine the extent of structural disturbance on the biofilm surface (Figure 4.5 B). The heterogeneity captured by the roughness coefficient indicated no statistically significant difference among the patterned biofilm surfaces compared to the full coverage biofilm (Figure 4.5 B). Interestingly, the roughness coefficient of biofilms developed from all the patterned spacing configurations showed no statistically significant difference among each other. However, the roughness of the full coverage control was significantly lower indicating overall that the surface of the full coverage biofilm was smoother than the surface of biofilms developed from the patterned substratum. Overall,

these data suggest that the introduction of micropatterned substratum diminishes the accumulation of biomass during the development of biofilm under flow.

4.2.2 Influence of cluster spacing on the porosity and diffusion distance of *S. aureus* biofilm

To further characterize the structural parameters that are useful in describing the internal development of biofilms, additional analysis was performed to evaluate porosity and diffusion distance of developed biofilms (Figure 4.6). The analysis was performed on the basis of individual clusters as represented in Figure 4.3. The porosity describes the fraction of the entire three-dimensional biovolume that is made up of interstitial or void space. It is calculated mathematically as the ratio of the volume of interstitial space and the volume of the whole biofilm. The diffusion distance parameter describes the physical distance from any point within the three-dimensional biofilm to the nearest void space. This parameter is numerically calculated by ISA3D using a quasi-Euclidean distance mapping method, which measures the straight-line distance between a set of three-dimensional segments [48, 110, 111].

A completely dense biofilm with little to no porous channels will have a porosity value closer to zero and the value increases as porosity does to one representing complete interstitial space free of biomass. Conversely, higher diffusion distance values indicate the presence of large chunks of continuous biomass compared to the location of voids. The lower porosity of the full coverage biofilm compared to the patterned biofilm thus indicates a more

densely packed internal structure when compared with biofilms cultured on micropatterned substrata (Figure 4.6). Furthermore, the 20 µm pattern spacing exhibits significantly less porous biofilm compared to the 50 µm and 110 µm configurations. In addition, there was no significant difference in the porosity between the 50 µm and 110 µm spacing. In contrast, the diffusion distance increased as the patterned configurations was introduced compared with the full coverage control (Figure 4.6). However, the diffusion distance increased significantly as the distance between adjacent clusters increased from 20 µm to 50 µm, and also from 50 µm to 110 µm.

Additional analysis was performed to determine the distribution of porosity and diffusion distance as a function of the distance from the base of the developed biofilm (Figure 4.7). To do this, the areal porosity and diffusion distance were numerically calculated using image structure analyzer in two dimensions (ISA2D). Single two-dimensional images that comprise the CLSM image stack was analyzed to determine the local or textural porosity and diffusion distance of each image layer. The total biofilm height was then normalized by percentage and the porosity was evaluated in increments of 10 % of total biofilm height beginning at the substratum. For the sake of perspective, the volumetric porosity can be considered as the integration of the areal porosity across all CLSM image layers [111]. The data shows that the full coverage control biofilms generally had a consistent porosity and diffusion distance along the height of the developed biofilm (Figure 4.7). However, the 20 µm spacing developed biofilms that were less porous at the bases and exhibited increased porosity after approximately 30 % of the total biofilm height (Figure 4.7 A). Also, the diffusion distance for the 20 µm, 50 µm and 110 µm spacing showed that biofilms developed

at these configurations generally possessed more biomass at the base (Figure 4.7 B). The shape of these curves indicate that the biomass generally tended to tapering at the top of the developed film. Overall, these data provide evidence of the multifaceted and complex nature of the internal structure of biofilms and indicate that the events that lead to mature biofilm development can further be influenced by the configuration of the initial adhesion substratum.

4.2.3 Cluster spacing influence individual cluster expansion during *S. aureus* biofilm development

Finally, the data were analyzed for expansion of individual patterned clusters that occurs during biofilm development. Each biofilm experiment began as a cluster of cells adhered in an arrayed pattern of 10 μm-diameter dots. During biofilm growth, it was possible for the cell clusters to grow radially so that when viewed in the top-down direction, they would appear to expand. As previously indicated, this expansion was apparent during the visual inspection by CLSM, where the 20 μm spacing configuration patterns exhibited linkages with adjacent clusters. These linkages are accompanied by an overall expansion of the cluster when compared to the initial inoculum that was confined within the 10 μm dot. To measure this expansion, further analysis was performed for the two-dimensional projected area of biofilm cell cluster (Figure 4.8 A). To do this analysis, the complete stack of images that make up a CLSM scan was collapsed into a single two-dimensional image and converted to a gray scale image. Binary analysis was subsequently performed using the public domain, National Institute of Health supplied, image analysis software, ImageJ.

The 20 µm spacing configurations had an overall significantly higher area compared to the 50 µm and 110 µm configurations. In fact, the 20 µm spacing had a more than two-fold expansion when compared to the 50 µm spacing configuration. Conversely, the difference in expansion between the 50 µm and 110 µm spacing was not statistically significant. In addition, the shape factor distribution of the clusters was also analyzed in ImageJ, where a numerical value is used to describe the overall cluster shape (Figure 4.8 B). The shape factor is numerically described by the circularity parameter – defined as the ratio of the area and perimeter-squared. A value of unity represents a perfect circle and the shape factor approaches zero as the shape stretches along an axis. The distribution data shows that the 20 µm spacing configuration had more clusters with shapes approaching a circle while also possessing a wider range of shape factors as evident by the range of circularity from 0.4 – 0.7. However, the 50 µm and 110 µm configurations generally exhibited more irregularly shaped clusters and are mostly distributed around the 0.4 circularity value. These data suggest that during biofilm development, the closer 20 µm spacing configurations expands to adjacent clusters evenly in all directions. Since all clusters are equidistant from each other this expansion mostly maintains the initial circular shape of the original surface pattern.

4.3 Discussion

Biofilm development is an important step in the pathogenesis of *S. aureus* related infections in humans [9, 54, 72]. Surface attachment of individual cells forming one or more cell clusters within a local vicinity is a critical initiation step in biofilm development [10, 35, 42, 51, 52]. In the case of *S. aureus*, these adherent cells communicate via the release and detection of AIP [34, 42, 72, 76, 158]. The detection of AIP by *S. aureus* occurs with positive feedback where AIP detection leads to upregulation of genes for further AIP production [9, 31, 32, 72, 80]. Depending on the environmental mass transfer properties, this subsequently leads to an increase in the local concentration of AIP that individual cells experience. It was therefore theorized that controlling the adhesion of cells, thereby limiting the cell-to-cell signaling phenomena affects the development of *S. aureus* biofilm.

Topographical variations of the adhesion surface available for bacterial attachment affects the formation and development of biofilms by various microbial species [104-106, 170]. This phenomenon was initially described following the observation that sharks, unlike other large marine animals, are not fouled by microbial invasion of its skin [171]. Further investigation into this phenomenon revealed the reason for the non-fouling property of shark skin was based in its intricate diamond shaped micropatterned topography [41, 104, 171]. Shark skin patterns comprise microscale diamond shaped protrusions that act as physical barriers to both microbial attachment and biofilm development [41, 104, 106]. Few studies have investigated the effects of these topographical variations on *S. aureus* biofilm development, and most topographical studies focus on long term biofilm development lasting several days [41, 104, 106, 171].

This body of work focuses on micropatterned surfaces, rather than surface relief modifications, to evaluate the effects of spatial segregation on *S. aureus* biofilm development. This implies that rather than separating adherent cell colonies by physical barriers such as pillars or rods, separation by increased spatial distance between adjacent colonies was utilized. This was intended to closely match conditions of bacterial invasion of host matrix or indwelling medical devices where surface topographies may be absent. Furthermore, this study was targeted towards the early development of *S. aureus* biofilm with growth duration no longer than 8 hours to investigate the effects of these micropattern configurations on the early phase of biofilm development. Thus, revealing the relationship between the spacing of adjacent clusters and the cell-signaling mechanism in this early developmental phase.

Observation of the developed biofilms immediately revealed differences in the biomass volume of micropatterned substratum coverage compared to a control of non-patterned substratum. These visual differences were observed when the CLSM images of these biofilms were compared. Quantitative analyses confirmed these biomass differences with all patterned configurations having significantly lower biovolume compared to the control. Furthermore, the effect of the pattern spacing on the biomass and thickness was revealed in the differences observed when the 20 μm spacing configurations was compared with both the 50 μm and 100 μm spacing configurations. There was however, no significant difference observed in the biomass of the 50 μm and 100 μm configurations. This suggests the existence of a critical combination of cluster size and adjacent cluster spacing that significantly diminishes the development of biofilm under fluid flow.

The concept of a critical dimension that inhibit biofilm development was suggested in a study of how topographical changes affect development of *E. coli* biofilm in static environments [39, 40]. In those experiments, pillar-like topographical patterns act as physical barriers between colonies of adhered cells. The pillars were cuboid-shaped with 10 μm height and equal length and depth that were systematically varied from 5 μm to 100 μm. This meant that the larger pillar sizes resulted in larger microcolonies that were closer to each other. Their findings indicated that the cells exhibited reduced biomass as the size of the barrier was decreased, thus increasing the spacing. Additionally, they found that at the feature sizes in those studies, the critical pillar size at which biofilm development was significant inhibited was at 20 μm pillar size. Although those experiments were conducted in static environments with a different microbial species, there was indication that cell-to-cell interaction was essential for the formation of the multicellular structure of biofilms. Developing biofilm is impacted by physical or spatial separation of adherent bacteria colonies possibly due to an interference of the communication pathway that slows down biofilm progression.

In the previous chapter, the mass transfer characteristics of the cell-signal peptide, AIP, was simulated under flow within geometry equivalent to the experimental flow chamber. These simulations suggested that the time taken for the local AIP concentration to achieve the theoretical threshold for induction was lower for the full coverage control compared to the patterned cluster configurations. Experimentally, this suggested that adhered cells in the full coverage configuration would initiate biofilm-dependent-growth faster than the patterned configurations. The results appear to agree with the simulation data. The full

coverage biofilms developed under the influence of 300 s^{-1} wall shear rate developed thick, dense biomass compared to all pattern-developed biofilms. Additionally, the simulations suggested that the 20 µm spacing configuration achieved local AIP concentration threshold earlier than the 110 µm spacing; further implying that the wider spacing may result in further delay in biofilm development. In the experimental system described in this chapter, the 20 µm spacing developed thicker biofilms with less porosity and diffusion distance than the 50 µm and 110 µm spacing. However, there were no significant differences between the biofilm structures developed at 50 µm and 110 µm spacing. This suggests that for cluster size and wall shear rate of 10 µm and 300 s^{-1}, respectively, the critical spacing at which biofilm development is significantly inhibited exists in the 20 µm – 50 µm range; and once that critical spacing is achieved, further increase in spacing yields no significant inhibition of biofilm development.

The individual cell clusters of the micropatterned colonies in this study are able to communicate with adjacent clusters as they multiply. Cluster multiplication leads to the release of higher concentrations of AIP by the clusters that is transferred along the flow direction by convection. Due to the fact that the array of clusters for all patterned configurations cover the same total area (4 mm × 4 mm), this implies that the 20 µm spacing has more clusters covering the entire region than the 50 µm and the 110 µm. Based on the results of this study, the convective mass transfer of AIP due to the fluid flow influences the differences observed in biofilm development on the micropatterned cell clusters. Overall, these data agree with reports that the function of the cell-signaling pathway was not only influenced by the achievement of a suitable quorum, but also influenced by environmental

dynamics [35, 36, 44, 84]. The data presented in this chapter suggest that the cell-signaling phenomenon exhibited by the cell clusters agrees with the concept of efficiency sensing. However, this study represents the first reports of the influence of barrier-free spatial segregation of adhered cell clusters on biofilm development under hydrodynamic flow. The experiments in this study present a better representation of real-world dynamic environments where *S. aureus* biofilm grows. Specifically, relating to the subject matter of discovering antibiotic-free therapies for biofilm-based infections, this study, in addition to the data from the previous chapter, provide insight on the underlying mass transfer mechanism for biofilm development under physiological wall shear rates.

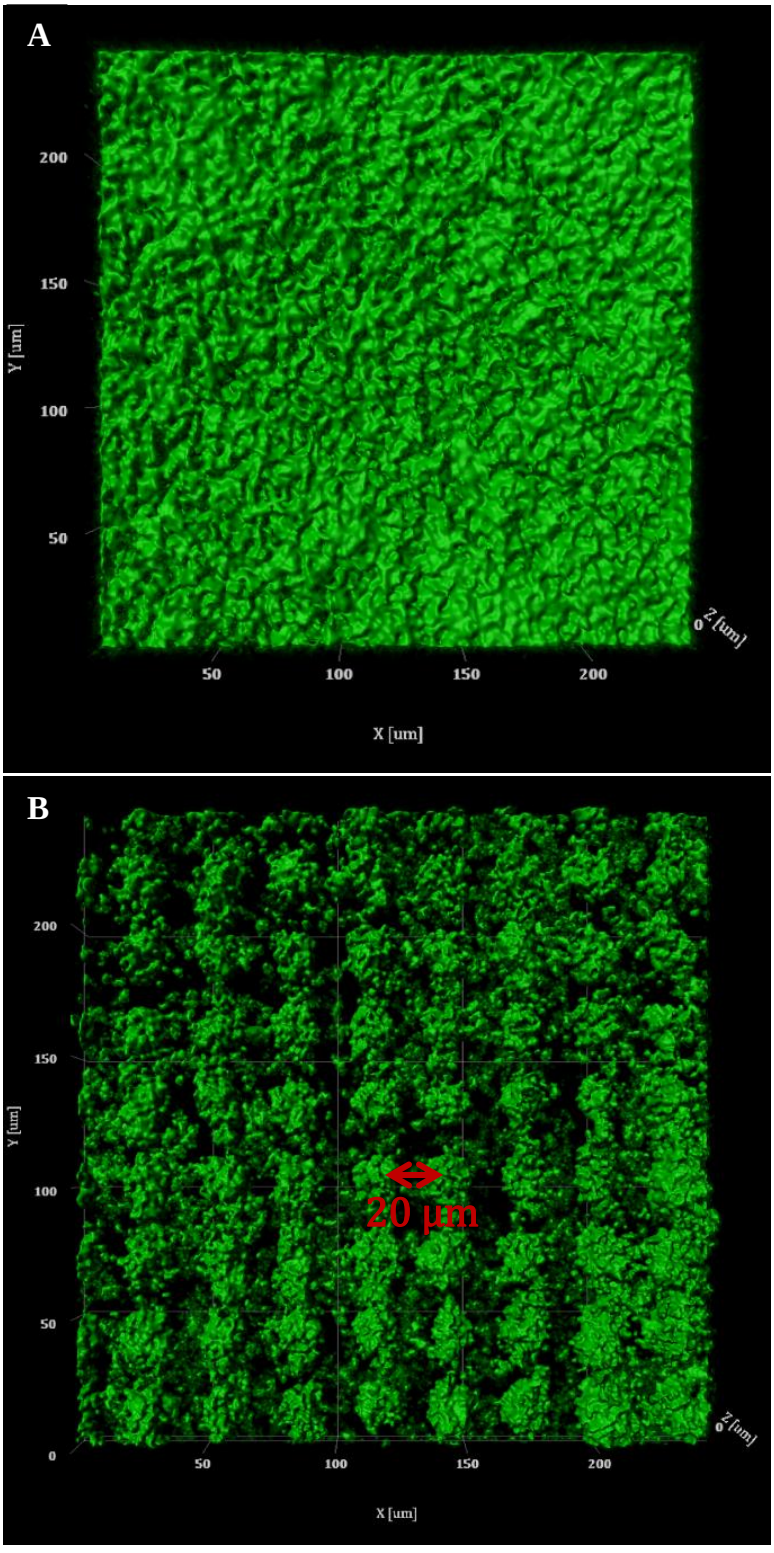
A
200
150
Y [um]
100
50
0
Z [um]
50
100
150
200
X [um]
B
200
150
Y [um]
20 µm
100
50
0
Z [um]
50
100
150
200
X [um]

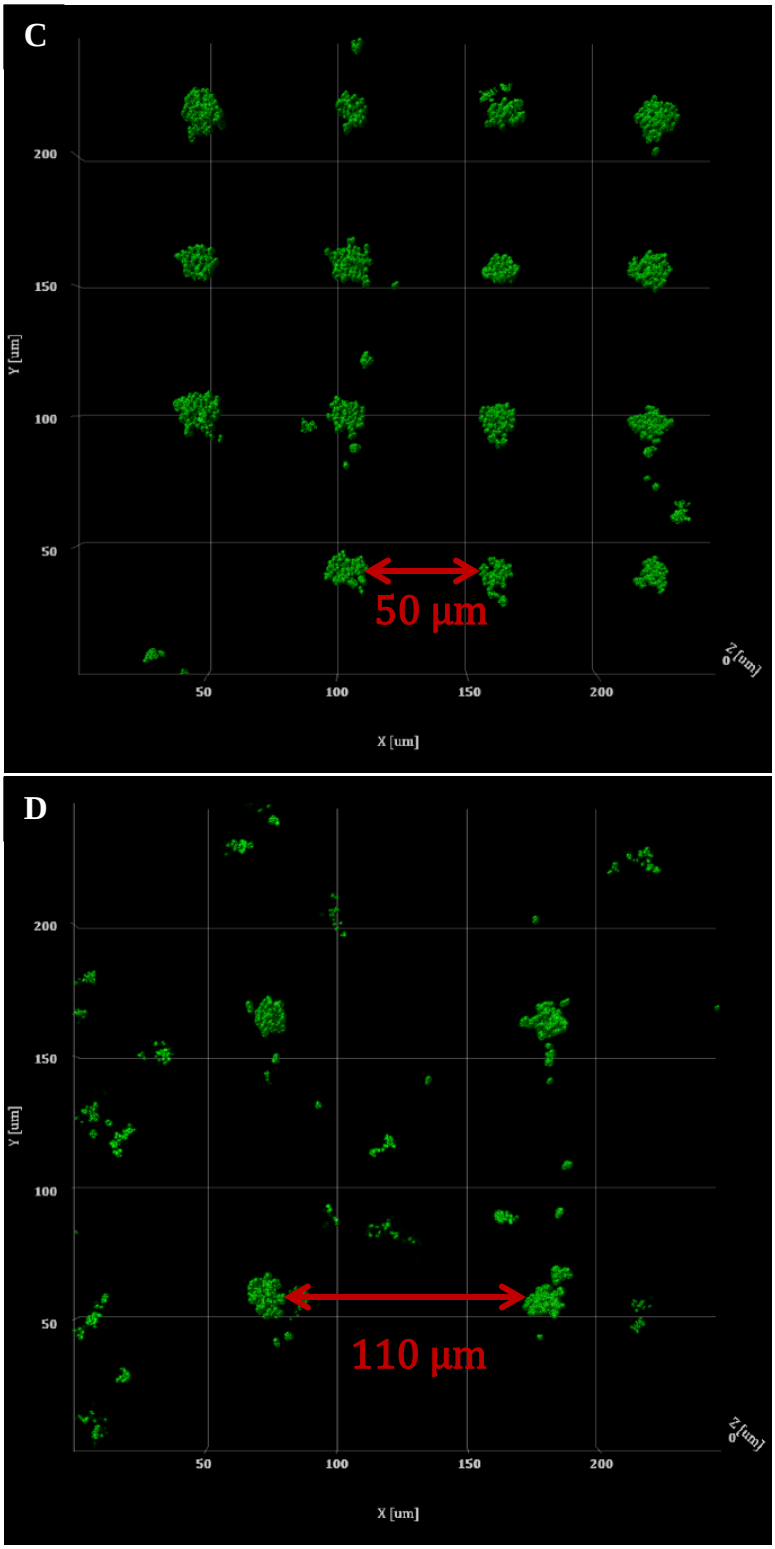

Figure 4.1: Top-down views of *S. aureus* biofilm growth at different substratum configurations showing the arrangement of clusters according to micropatterned substratum

via CLSM and rendered in Imaris. Cells were allowed to adhere via sedimentation on FN coated glass and cultured for 8 hours at 37°C with continuous media flow at 300 s^{-1}. The protein coating was performed at **(A)** Full coverage, or an array of 10 µm dots that are spaced **(B)** 20 µm, **(C)** 50 µm, and **(D)** 110 µm apart. In each image, the direction of flow is along the Y-axis. Each square grid has a length of 50 µm.

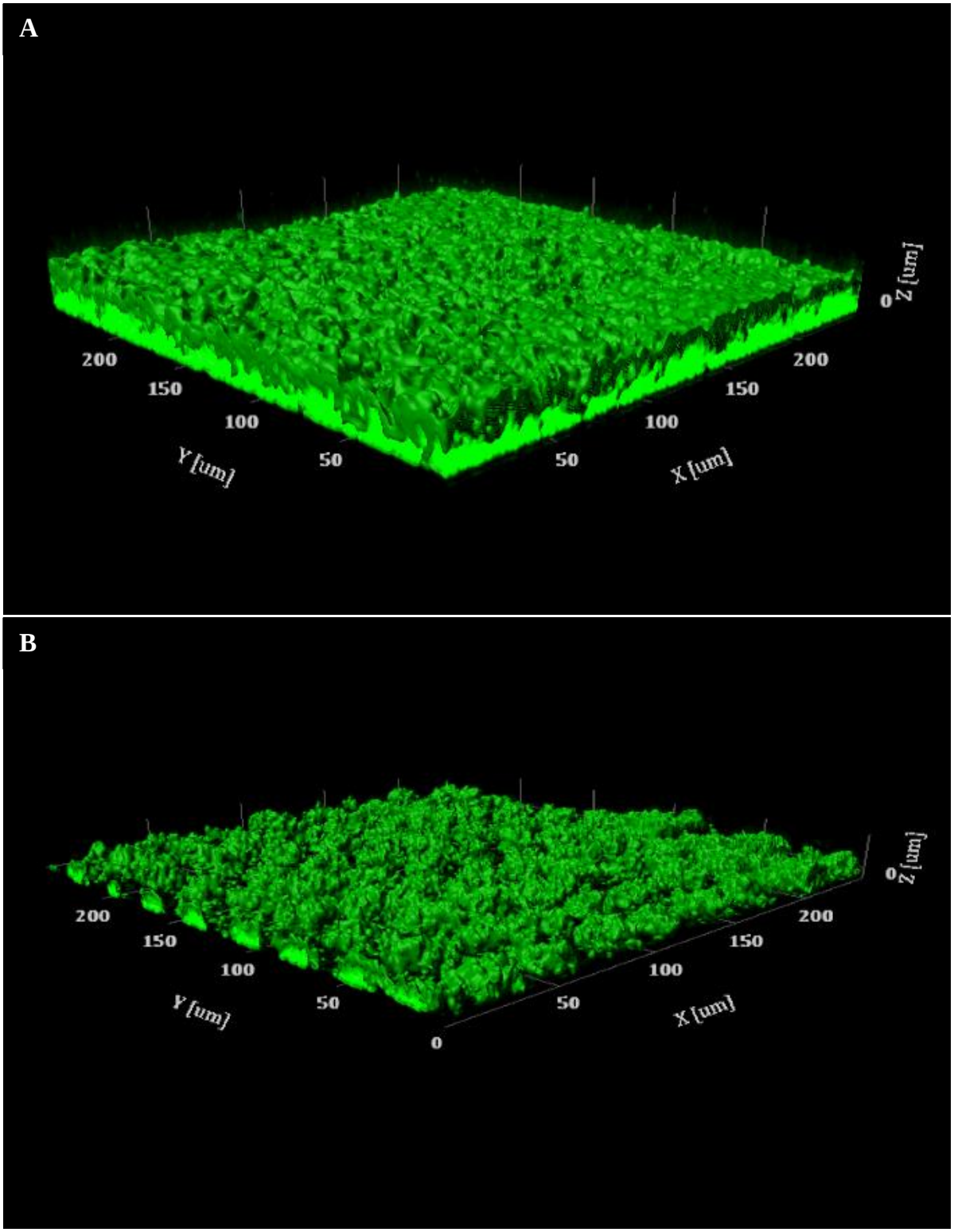
A
200
150
100
Y [um]
50
50
100
150
200
X [um]
0
Z [um]
B
200
150
100
Y [um]
50
0
50
100
150
200
X [um]
0
Z [um]

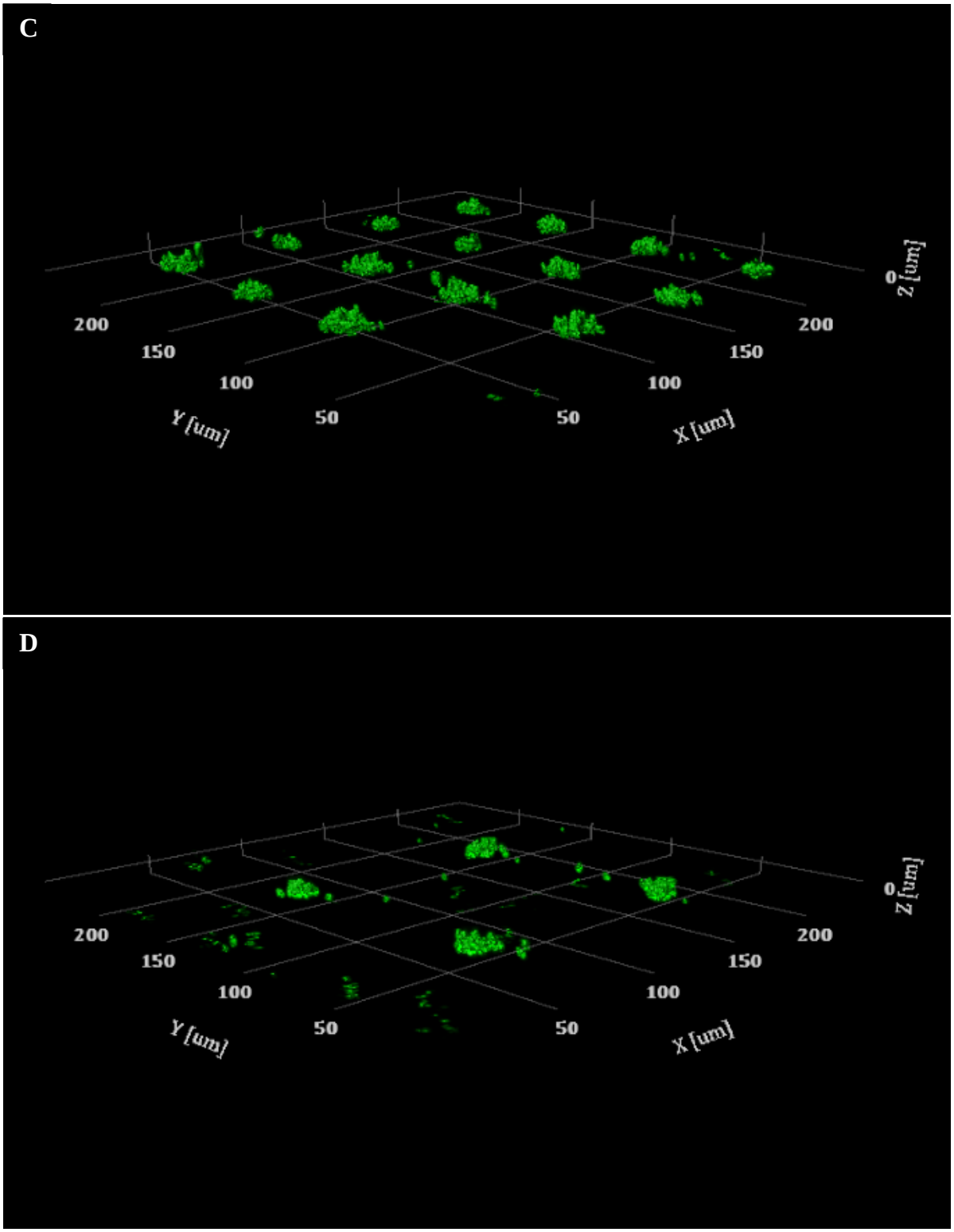

Figure 4.2: *S. aureus* biofilm growth at different substratum configurations showing structural differences in volume and thickness as observed via CLSM and rendered in Imaris.

Cells were allowed to adhere via sedimentation on FN coated glass and cultured for 8 hours at 37°C with continuous media flow at 300 s^{-1}. The protein coating was performed at **(A)** Full coverage, or an array of 10 µm dots that are spaced **(B)** 20 µm, **(C)** 50 µm, and **(D)** 110 µm apart. In each image, the direction of flow is along the Y-axis. Each square grid has a length of 50 µm.

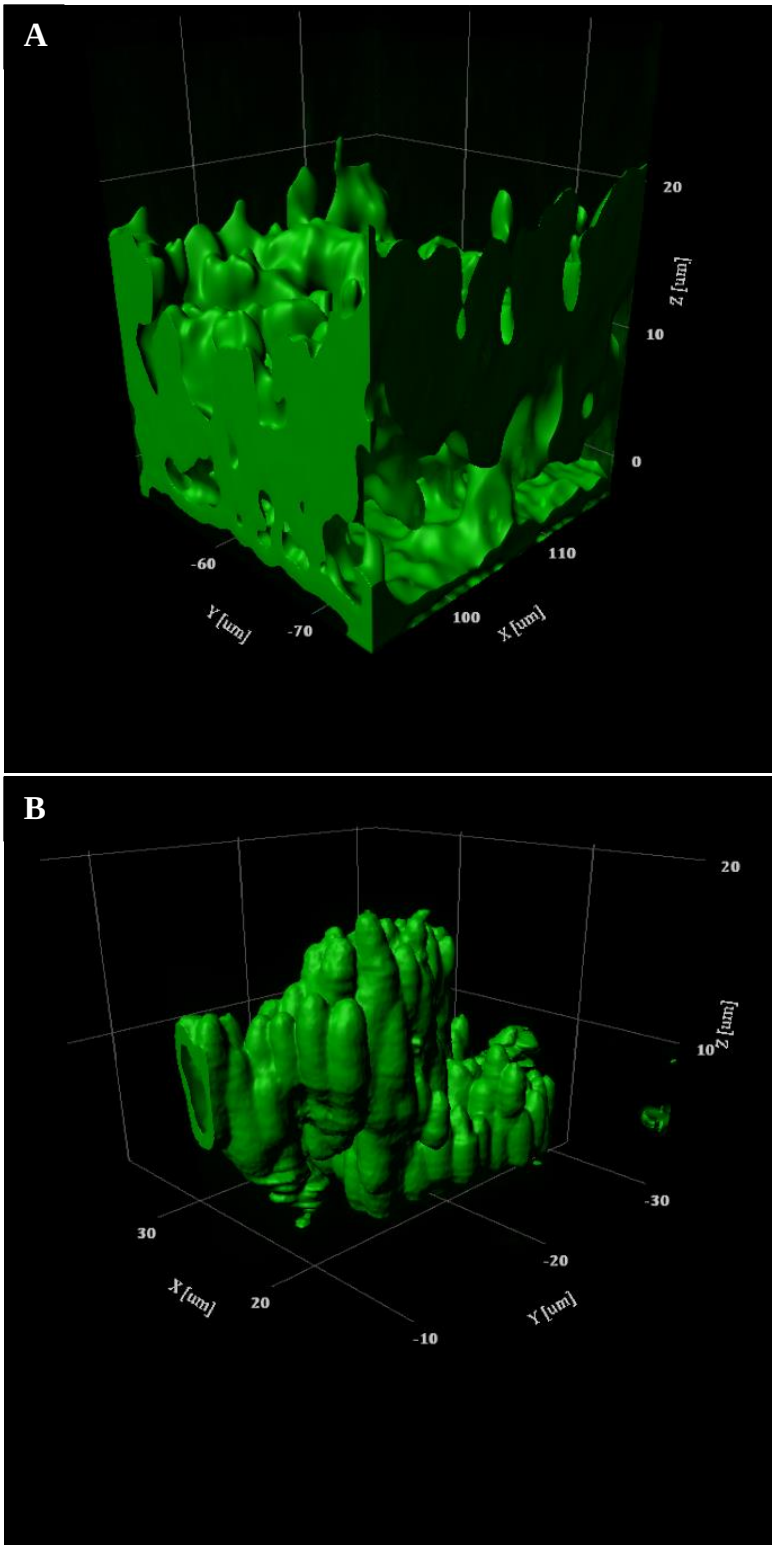
A
20
Z [um]
10
0
-60
Y [um]
-70
100
X [um]
110
B
20
Z [um]
10
-30
30
X [um]
20
-10
-20
Y [um]

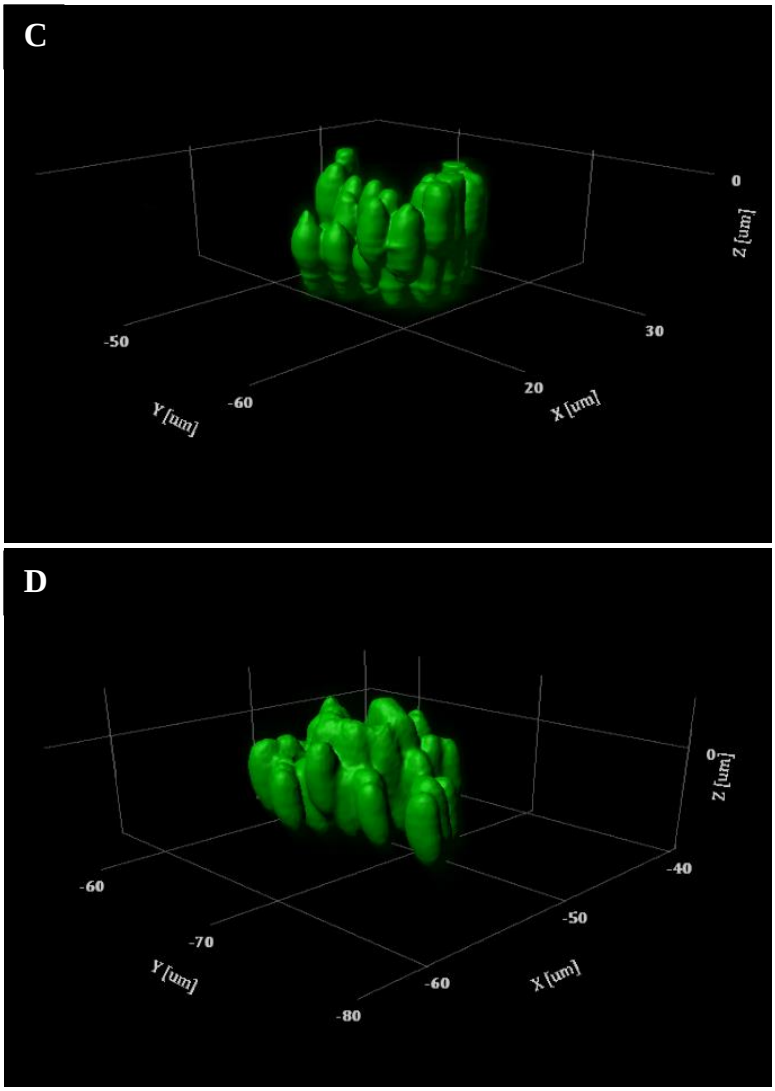

Figure 4.3: Detailed view of biofilm developed from a 10 µm cell cluster. Images were captured via CLSM and rendered in Imaris. In each image the direction of flow is along the Y-axis. The images show biofilm developed from clusters with adjacent spacing: **(A)** Full coverage used as control, **(B)** 20 µm, **(C)** 50 µm, and **(D)** 110 µm. Each square grid has a length of 10 µm.

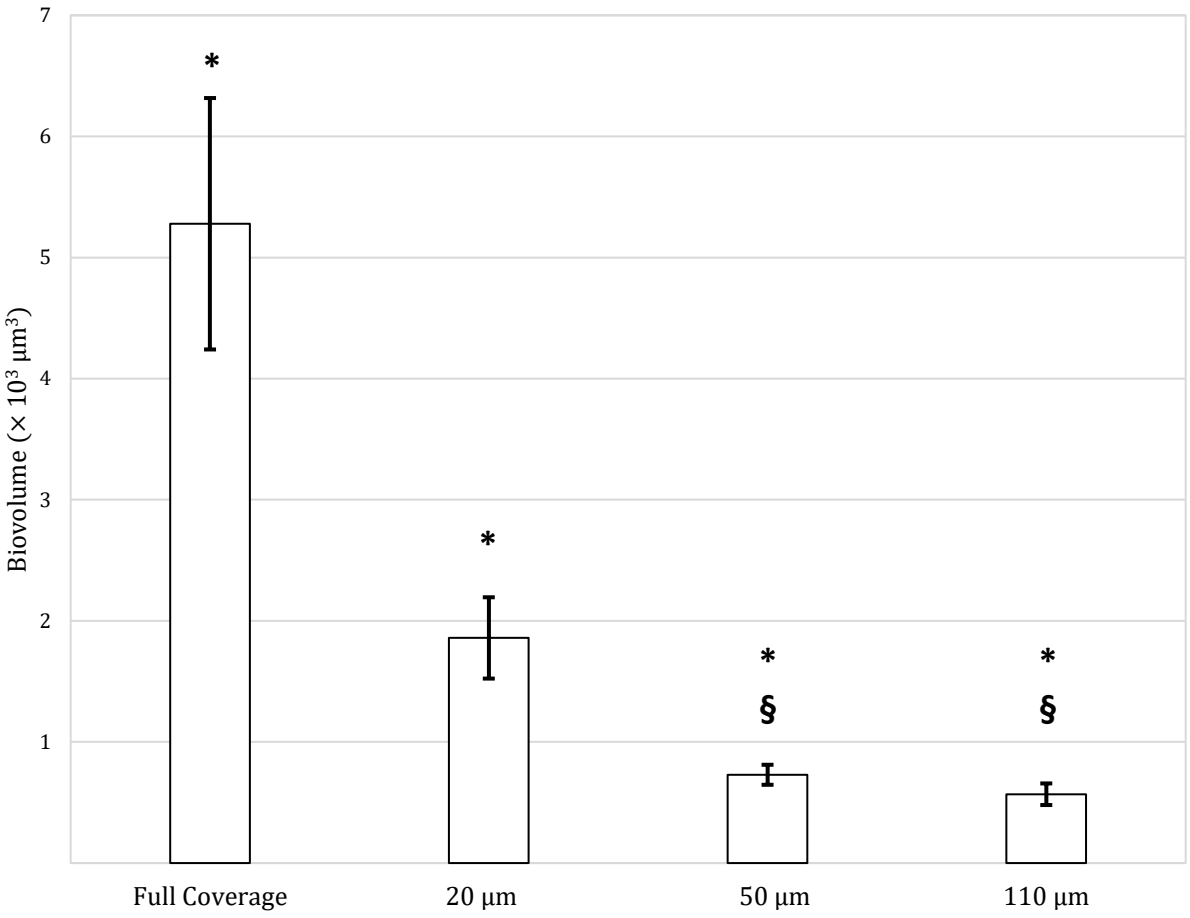

Figure 4.4: Biovolume analysis of *S. aureus* biofilm developed from micropatterned substratum quantified with ISA3D reconstruction of CLSM image stacks. This chart reports the mean biovolume (± 95% confidence interval, n = 16) of the biomass produced by individual single cell clusters spaced by varying distances among adjacent clusters. The images were captured at ~ 300 µm distance from the posterior end of a 4 mm × 4 mm square total array area and biofilm was developed under flow at 300 s^{-1}. Full coverage indicates non-patterned surface and was used as control. * indicates statistically significant difference ($p < 0.001$) compared to full coverage. § indicates statistically significant difference ($p < 0.001$) compared to 20 µm pattern spacing.

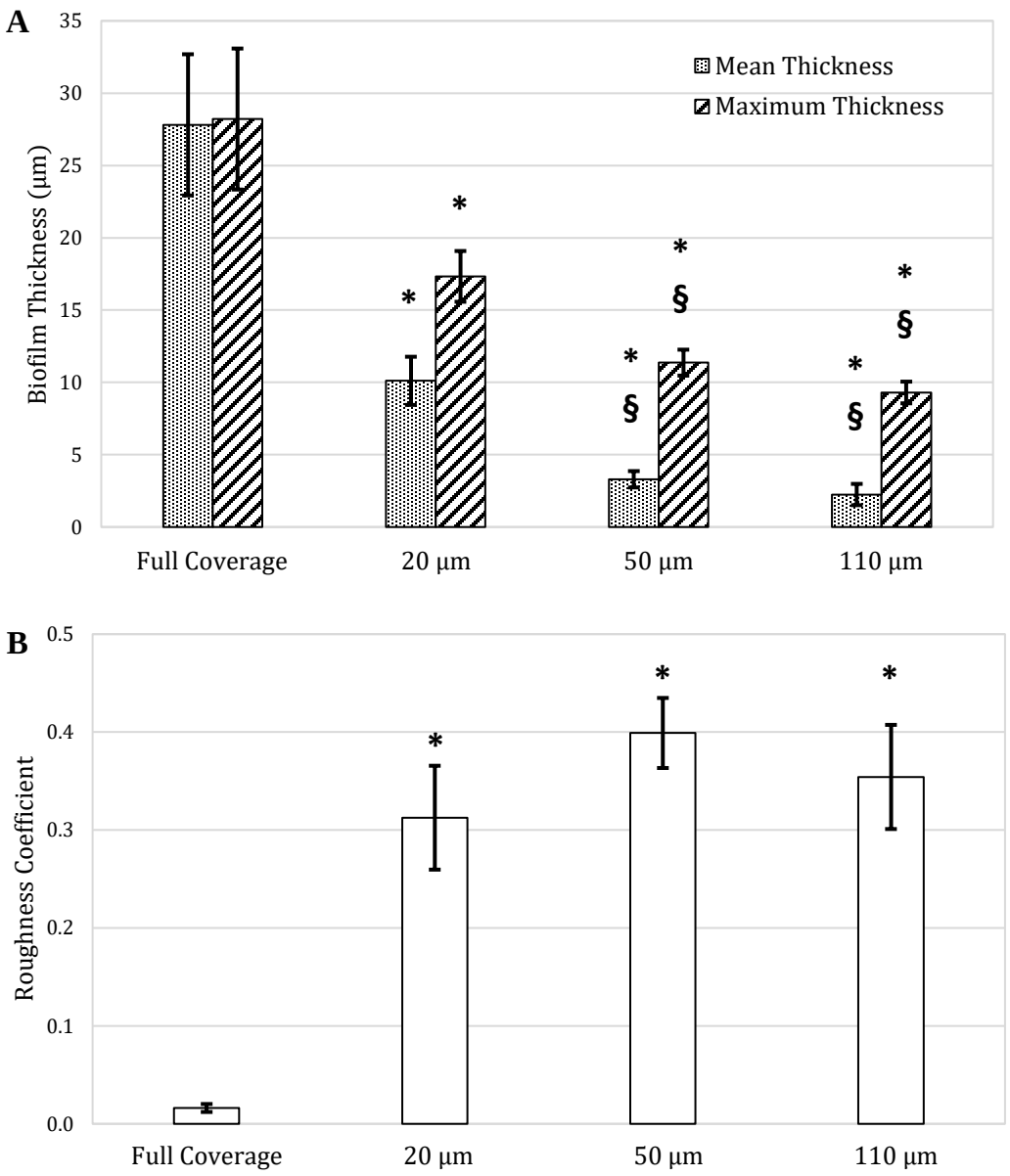

Figure 4.5: *S. aureus* biofilm development with respect to micropatterned substratum showing **(A)** biofilm thickness, and **(B)** roughness coefficient (mean ± 95% CI, n = 16). * indicates statistically significant difference ($p < 0.001$) compared to full coverage. § indicates statistically significant difference ($p < 0.001$) compared to 20 µm pattern spacing.

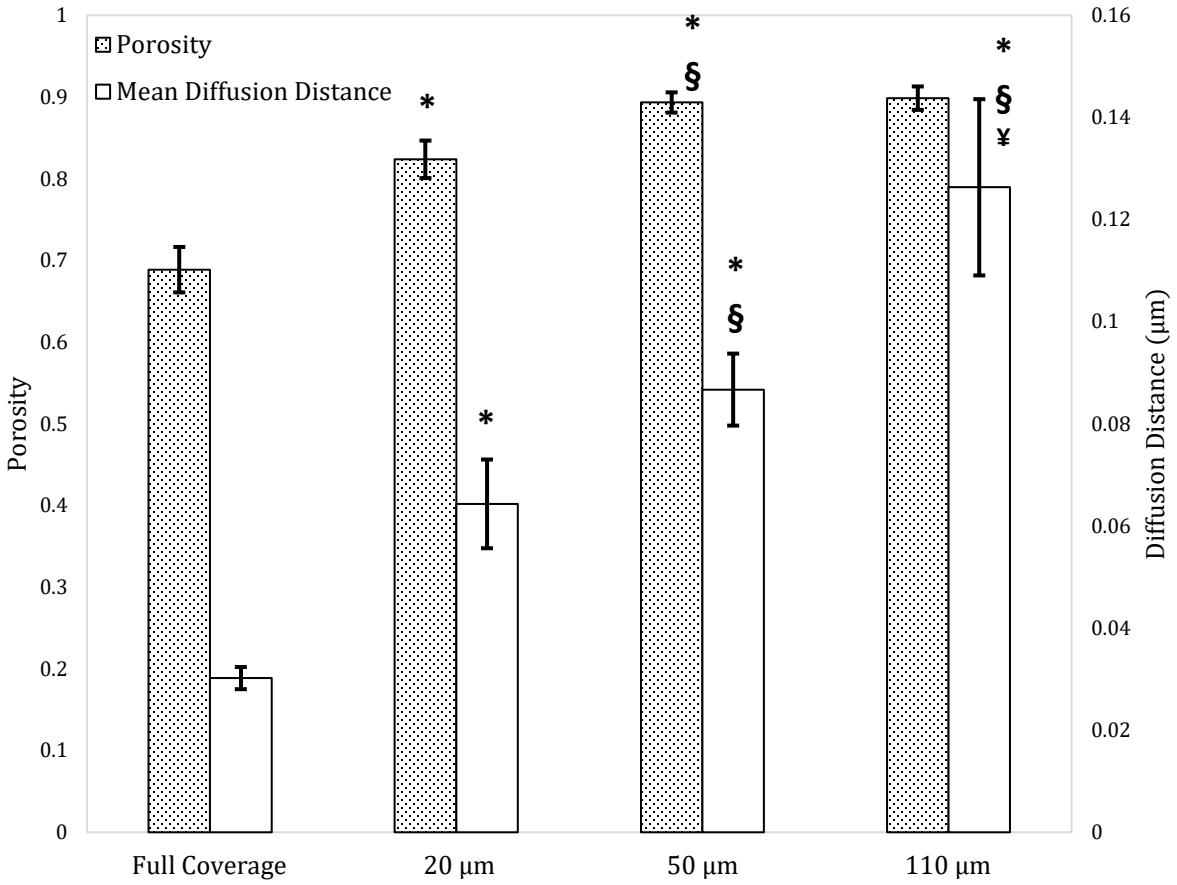

Figure 4.6: Effect of substratum micropattern configuration on the internal development of interstitial space within *S. aureus* biofilm developed under flow. The internal development is described here by the porosity and diffusion distance (mean ± 95% CI, n = 16). * indicates statistically significant difference ($p < 0.001$) compared to full coverage. § indicates statistically significant difference ($p < 0.001$) compared to 20 µm pattern spacing. ¥ indicates statistically significant difference ($p < 0.001$) compared to 50 µm pattern spacing.

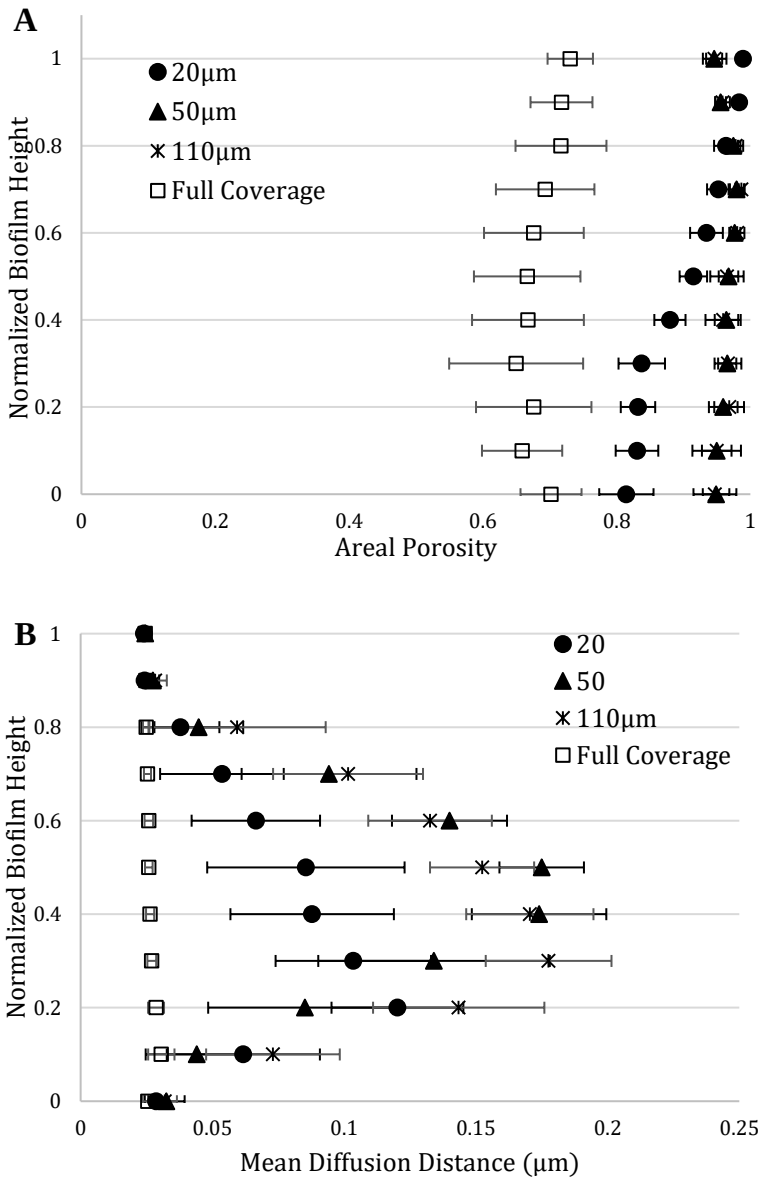

Figure 4.7: Internal height profile of S. aureus biofilm developed on micropatterned substratum. The distribution of interstitial voids along biofilm height **(A)**, and the mean diffusion distance **(B)** shows the variation in internal development with respect to substratum pattern configuration for biofilm developed under flow. Each data point represents the mean ± 95% CI, $n \geq 8$.

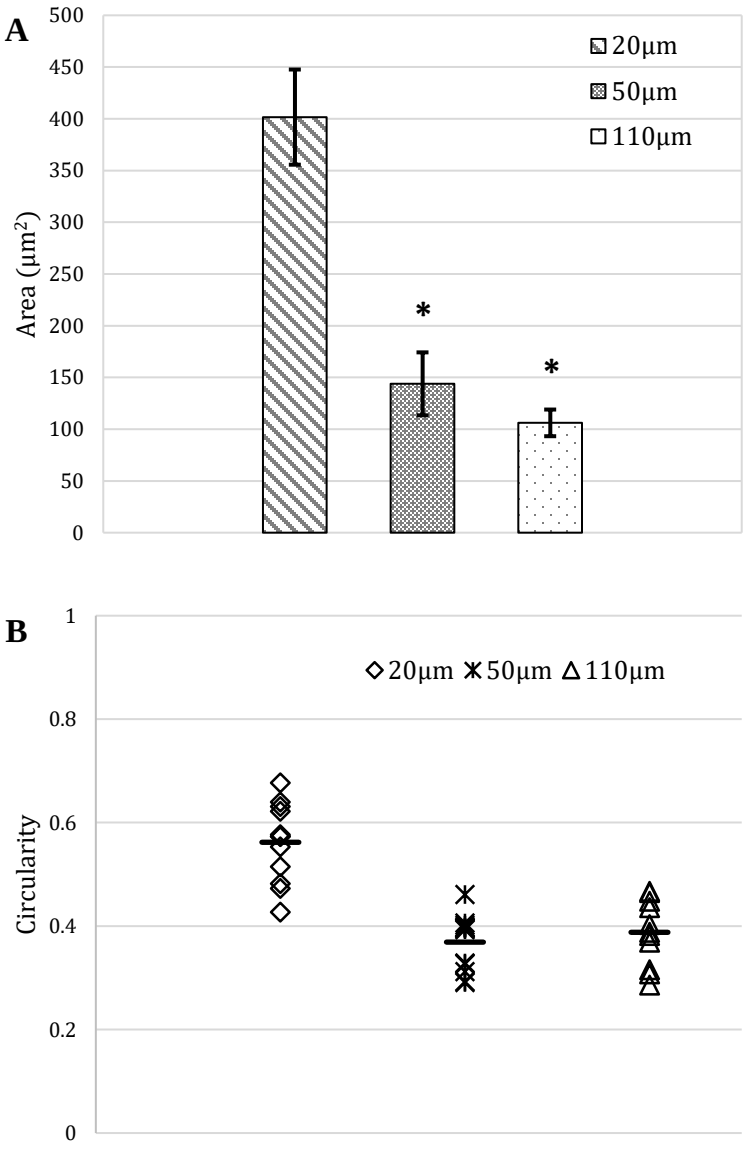

Figure 4.8: Evaluation of the expansion of cell clusters during biofilm development under flow. **(A)** The area (mean ± 95% CI, n ≥ 12) indicates the 2D area of spread outside of the 10 μm initial colony diameter. * indicates statistically significant difference ($p < 0.001$) compared to full coverage. **(B)** The shape factor analysis describes how the general shape of the cluster varies based on the pattern dimensions. Black bar indicates mean shape factor location.

Chapter 5: Influence of physiologically relevant shear on the morphology of *Staphylococcus aureus* biofilms developed from a patterned substratum

5.1 Rationale for study

In the preceding chapter, it was shown that *S. aureus* biofilm development from micropatterned cluster substratum diminished when the spacing between adjacent clusters increased. The total array of clusters in those experiments covered a 4 mm × 4 mm square region. The full-coverage-control configuration can be described as the upper limit of total cluster number as the spacing decreases from 110 µm to 50 µm to 20 µm. Chapter three suggested, via *in silico* simulation, that there was convective influence on AIP mass transfer within the flow chamber on micropatterned cluster geometry. Additionally, the simulated mass transfer of AIP resulted in higher concentration profile magnitudes as the spacing between geometric clusters decreased for the 4 mm × 4 mm configurations. This resulted in the observation that simulations for the full coverage control achieved threshold local AIP concentration for induction faster than the patterned geometries. Additionally, the cluster geometry with 20 µm spacing achieved the threshold faster than the geometry with 110 µm spacing.

Therefore, I postulated, in the previous chapter, that mass transfer of AIP was the underlying reason for the observed differences in biofilm development on the micropatterned substrata. However, in the previous experiments, as long as the total array of clusters covered the same 4 mm × 4 mm square, a decrease in the spacing between adjacent clusters resulted a higher number of clusters within the overall region. The alteration of cluster spacing resulted in a higher total number of cell clusters as spacing decreased from 110 µm to 20 µm while maintaining 4 mm × 4 mm total coverage. This implied that it may be possible that the increased total cell density also impacts biofilm development at the 20 µm spacing

configuration. To study this experimentally in this chapter, the total cluster number was systemically changed by reducing the total array coverage area to 2 mm × 2 mm for all pattern configurations. This rationale ensures the evaluation of similar patterned cluster configurations for any possible effects of total cluster number. The simulations result in chapter three suggest that altering the wall shear rate between experiments, from 100 s^{-1} to 300 s^{-1}, should impact the structural characteristics of developed biofilm. They also suggest that changes in the total cluster number from 2 mm × 2 mm to 4 mm × 4 mm should impact biofilm structural development. However, it was unclear if any interactive effects exist when these parameters are systematically altered. These analyses aim to further elucidate the underlying mass transfer of AIP within all these varying experimental configurations of cluster pattern spacing and total cluster number; and the influence of physiological shear on the developed biofilm.

5.2 Results

5.2.1 Influence of shear rates on structural characteristics of *S. aureus* biofilm development on micropatterned substrata

In the preceding chapter, *S. aureus* biofilm development, under fluid flow, on micropatterned substratum was impacted significantly, having less biomass and thickness compared to full coverage biofilm. This was attributed to the changing mass transfer properties of the system as the micropatterned spacing was increased. Subsequently, this study assesses the influence, of varying the shear rate on the developmental impact already observed previously. Evaluation of the effect of wall shear rate on *S. aureus* biofilm development on micropatterned substratum was performed at shear rate values of 100 s^{-1} and 300 s^{-1}. Additionally, the total area of the square array comprising the substratum coverage was varied between 2 mm × 2 mm and 4 mm × 4 mm. This was performed to achieve an overall four-fold change in total adherent cell cluster number between experiments. For comparative analyses in this study, images were captured at approximately 300 µm from the posterior end of 4 mm × 4 mm coverage area. This represented an approximate 7.5% normalized distance from the posterior end and was arbitrarily selected. The developed biofilms for various micropattern configurations showed qualitative differences via CLSM when the shear rate varied between 100 s^{-1} to 300 s^{-1} (Figures 5.1 & 5.2). For the full coverage and the 20 µm micropattern spacing, biofilms developed at 300 s^{-1} possessed visibly dense structures compared to biofilms developed at 100 s^{-1} shear. Additionally, at 100 s^{-1} shear, the volume and thickness of developed biofilm decreased as spacing between

adjacent clusters increased (Figure 5.3). This aligns with the impact of the micropatterned substratum at equivalent wall shear rate observed in the previous chapter.

The biovolume of developed biofilm at 100 s^{-1} were significantly lower than those developed at 300 s^{-1} (Figure 5.3). This was the case for comparison of shear only on the full coverage and the micropatterned cell clusters. Additionally, the magnitude of the change in biovolume diminished as the micropatterned spacing increased. For example, in response to the increase in shear rate, the 20 µm spacing increased in biovolume by ~500 $µm^3$. In contrast, both the 50 µm and 100 µm spacing responded by minimal magnitudes of ~100 $µm^3$ and the full coverage control changed by more than 1000 $µm^3$. In the analyses of the mean and maximum thickness, the full coverage biofilm increased in both parameters as the shear rate increased from 100 s^{-1} to 300 s^{-1} (Figure 5.4). The 20 µm and 50 µm spacing configurations showed no significant changes to both the mean and maximum thickness in response to the wall shear rate change. However, the 110 µm spacing showed a decrease in thickness as the wall shear rate increased from 100 s^{-1} to 300 s^{-1}.

The porosity and mean diffusion distance were also evaluated for structural changes with wall shear rate change (Figure 5.5). The full coverage and the 110 µm spacing developed biofilm showed no change in porosity with increase in wall shear rate (Figure 5.5 A). However, both the 20 µm and 50 µm spacing responded to increased wall shear rate with decreasing porosity (Figure 5.5 A). In contrast to the observation made in the previous chapter, at 100 s^{-1} only, there was no significant difference in the porosity as the spacing between adjacent patterns increased from 20 µm to 50 µm (Figure 5.5 A). The mean diffusion distance decreased as the wall shear rate increased for the full coverage, 20 µm, and

50 µm spacing (Figure 5.5 B). However, the 110 µm spacing showed a minimal, non-significant increase in diffusion distance in response to increased wall shear (Figure 5.5 B). Overall these analyses suggest that the added reduction of shear diminished biofilm development from the micropatterned cell clusters.

5.2.2 Influence of total cell cluster number of micropatterned substrata on *S. aureus* biofilm development under flow

All data reported thus far were performed with a total area of cluster coverage equivalent to 4 mm × 4 mm. To investigate the effect of the total cell cluster number on the developed biofilm, the total cluster coverage area was reduced by a quarter to 2 mm × 2 mm. This resulted in an equivalent quarter factor reduction of the initial total cell density available for biofilm development while maintaining equivalent micropattern cluster spacing. Biofilm capture on the 4 mm × 4 mm coverage area was performed as previously described. For the 2 mm × 2 mm coverage area, biofilm capture was performed at approximately 150 µm distance, representing 7.5% normalized distance, from the posterior end. Qualitative analysis revealed that the structural compactness of the developed biofilm for the full coverage biofilm and the 20 µm micropatterned spacing configuration exhibited fundamental changes due to the total coverage area changes (Figure 5.6). The biovolume revealed no change in response to total cluster number for the 50 µm and 110 µm spacing at both 100 s^{-1} and 300 s^{-1} wall shear rates (Figure 5.7). However, for the full coverage and 20 µm spacing under the influence of 100 s^{-1} wall shear rate, significant increases were observed in biovolume corresponding to increase in the total coverage area from 2 mm × 2 mm square to 4 mm × 4

mm square arrays. At 300 s^{-1} shear rate, there was no significant change in the full coverage biofilm in response to the total coverage area change, but there was a significant increase in biovolume by the 20 µm spacing (Figure 5.7). Interestingly, the biovolume of the 2 mm × 2 mm coverage-20 µm spacing configuration was significantly higher than the 4 mm × 4 mm coverage-50 µm spacing configurations. This further promotes the influence of spacing since these two configurations are equivalent in the total number of clusters and only differ in the spacing distance.

The change in total cluster number also revealed effects on the porosity of developed biofilm (Figure 5.8). There were no significant changes in porosity among all of the full coverage biofilm structures regardless of coverage area size, although each was significantly lower than their corresponding micropatterned configurations. However, the porosity significantly decreased as total coverage area increased from 2 mm × 2 mm to 4 mm × 4 mm for the 20 µm spacing. For both the 50 µm and 110 µm spacing, the porosity was significantly impacted at 100 s^{-1} shear rate only. Overall, these data suggested that the development of biofilm under flow was subject to mass transfer limitations of the signal peptide, AIP.

5.2.3 Factorial analysis of the impact of shear, cluster spacing and total cluster number on biofilm development

The study of biofilm developmental changes in response to shear rates suggests that the mass transfer of AIP within the flow environment is impacted by the following variables: shear rate and clusters spacing. Convective mass transfer of AIP subsequently determines the

duration before clusters experience local AIP threshold concentration. To assess the relative importance of the variables on biovolume, mean thickness, porosity and mean diffusion distance, full factorial analysis was performed on the data. For this analysis, the cluster spacing variation was defined as two distinct variables: 1) “spacing” referred to the adjacent spacing between clusters which varied between full coverage, 20 µm, 50µm, and 110 µm, and 2) “size” referred to the total cluster number (varied between 2 mm × 2 mm and 4 mm × 4 mm). The Pareto chart, which orders the effect of variables by their magnitude, is provided in Figure 5.9. This analysis showed that spacing between adjacent clusters was the most important variable influencing the biovolume, mean thickness and porosity of developed biofilm (Figure 5.9 A, B & C). However, the mean diffusion distance was suggested to be most influenced by variation in wall shear rate. Overall, these data reveal that shear rate changes affect biofilm structure development on micropatterned substratum and the effect on the patterned substratum are intensified by increase in the micropattern spacing.

5.2.4 Hydrodynamic flow reveals dependency of *S. aureus* biofilm development along the axis of flow

In the simulation analysis provided in chapter three, it was observed that a concentration gradient existed along the axis of flow. This suggested the possibility of location dependent biofilm growth along the direction of flow. Additionally, the analysis of total cluster number from the previous sections of this chapter also suggests this potential. To assess this dependence, comparative analysis was performed on biofilm developed at the anterior and posterior ends of the coverage areas; referred to as upstream and downstream,

respectively (Figures 5.10 & 5.11). For a 2 mm × 2 mm coverage area, the upstream and downstream biofilms were defined by a distance of approximately 150 µm from the anterior and posterior ends, respectively. For the 4 mm × 4 mm coverage area, the same definition was achieved by a distance of approximately 300 µm from respective ends. In both cases, this represented a 7.5% inward distance from each end of biofilm development. This value was arbitrarily selected to allow enough distance for adequate development of biomass, while maintaining a reliable distance between the upstream and downstream ends.

Assessment of the biovolume data revealed significant differences between the developed biofilm at both ends (Figure 5.10). The biovolume significantly increased at the downstream location compared to the upstream location in all cases. However, the magnitude of the biovolume change decreased as the micropattern spacing configuration increased. This was applicable regardless of the shear rate at which biofilm was developed or the total coverage area. Similarly, the porosity at all downstream location was significantly lower than upstream locations for all substrata (Figure 5.11). This further suggests location specific development of biofilm within the dynamic environment.

Therefore, the progression of biofilm development was assessed along the axis of flow by evaluation of developed biofilm at intervals along the direction of flow. To do this, sampling was performed at intervals of approximately 500 µm from the anterior to the posterior end of a 4 mm × 4 mm total coverage area for biofilms developed at 100 s^{-1} shear rate and 37°C for 8 hours. Quantitative analysis of these biofilms reveals a steady increase in biovolume and a decrease in porosity along the axial biofilm length and in the direction of flow (Figure 5.12). For the 20 µm and 50 µm micropattern spacing, the rise in biovolume

along the flow axis suggests that the spatial location of cell clusters in a dynamic environment influences the structural development of biofilm at that location. This is evident from the observation that the biovolume is equivalent along the first 500 µm distance at the 20 µm and 50 µm spacing. However, further downstream the 20 µm spacing increases at a faster pace compared to the 50 µm spacing. Overall, these analyses indicate that the dynamic environment favors cells growing downstream of flow and that developing cells take advantage of the dynamic properties of the environment during biofilm development. The progressive growth of *S. aureus* biofilm along the direction of flow illustrates this point. Downstream cell clusters were able to take advantage of their location benefits towards developing more advanced biofilm within the same duration. In other words, biofilm development along a line parallel to the direction of flow steadily increases in both structural fidelity and internal complexity.

5.3 Discussion

This body of work has established in previous chapters that the substratum micropattern configuration impact biofilm development under hydrodynamic shear. This was attributed to the influence of AIP mass transfer under fluid flow. Additionally, simulation studies suggested an influence of shear on the mass transfer of AIP within the flow chamber system. This resulted in different durations at which varying cluster configurations achieved threshold local AIP concentration for biofilm-dependent growth. This chapter expands this analysis to include assessment of wall shear rate and total cluster number variation. Biofilms were cultured on micropatterned substratum under systematically varied flow at 100 s^{-1} and 300 s^{-1}, and total cluster arrays covering either a 2 mm × 2 mm or 4 mm × 4 mm square region. The developed biofilms revealed structural differences in their overall biomass amount (represented by biovolume and thickness measurements) and on the development of structural characteristics that did not increase biomass (represented by porosity and diffusion distance measurements).

In general, progression of biofilm development is accompanied by an overall increase in biovolume and thickness [111, 115, 138]. This applies to both experimentally-developed biofilm and naturally-formed biofilm. This can therefore be interpreted that biofilms with higher volume or thickness have been in development for a longer duration. The simulation data predicted that the full coverage configuration initiates biofilm-dependent biomass growth. The experimental data agreed with this prediction. The lower cell density exhibited by the 2 mm × 2 mm coverage area exhibited biofilms with larger biovolume and thickness compared with all micropatterned configurations regardless of coverage area, or wall shear

rate. Additionally, regardless of coverage area and wall shear rate, the 20 μm spacing configuration exhibited larger biovolume and thickness than both the 50 μm and 110 μm spacing configurations. These suggest that cluster spacing impacts biomass development. This may due to increased total cluster number at the beginning of the experiment at smaller cluster spacing, or to the achievement of biofilm-dependent growth at an earlier time as suggested by simulation data.

To evaluate the effect of total cluster number, additional experiments were performed with the total array of cells systematically varied between experiments from 2 mm × 2 mm to 4 mm × 4 mm. This meant that at the start of experiments, the number of clusters that were arranged along the axis of flow was reduced by half for the same cluster spacing configurations. Comparative analysis showed that only the 20 μm spacing configuration yielded increased biovolume due to increased total cluster number at both 100 s^{-1} and 300 s^{-1} shear rates. This further agrees with the suggestion proffered in chapter four of a critical combination of cluster size and cluster spacing after which no further changes in biofilm development are observed. Furthermore, comparative analysis of micropattern configurations that were equivalent in total cluster number that differ only in cluster spacing (as was the case of comparing 2 mm × 2 mm coverage-20 μm spacing versus 4 mm × 4 mm coverage-50 μm spacing) was performed. The results indicated that the 20 μm spacing yielded significantly more biovolume; further asserting that the observed influence of cluster spacing was not due to the change in total cluster number.

Theoretical considerations for factors affecting biofilm growth in nature include the hydrodynamic shear, nutrient mass transfer and biofilm associations [172, 173]. There are

many other influences, but those are typically dependent on the three factors mentioned previously. For example, biofilm associations include factors such as single or multi-species biofilm, environmental loss of biofilm, and cell signaling mechanisms [172]. Therefore, in this study, the theoretical considerations are the wall shear rate, nutrient limitation and cell signaling mechanism. However, previous studies performed in our laboratory reported that biofilm development at the shear rates of 100 s^{-1} and 300 s^{-1} utilized in this work was not limited by nutrient mass transfer. Further analysis was performed to investigate the influence of mass transfer gradients of biofilm-dependent metabolites on biofilm development. The results showed that biofilms developed at the same shear rate and on equivalent micropattern spacing varied based on their position along the flow axis. In fact, the biofilm development improved down the axis of flow. This further agreed with the claim that in the absence of nutrient limitations, the mechanism of biofilm development under shear was due to the mass transfer of biofilm-dependent metabolites; speculatively, AIP.

This study reports that biofilm development within a flow environment increases in the direction along the flow axis. This was evident by a steady increase in biovolume, coupled with a steady decrease in porosity, at both the 20 μm and 50 μm spacing. In fact, this was also observed in the full coverage configuration that contained considerably higher biomass amount, overall. Biofilm development in nutrient-dependent conditions usually generate rough biofilm structures while development in growth-dependent conditions yield generally smoother biofilms [138]. Growth-dependence refers to conditions at which the only hindrances to biofilm development are the mechanisms that control biofilm development. In other words, if there was nutrient limitation, the results should indicate a decrease of biofilm

development along the axis of flow. This is because cells would still achieve AIP threshold due to convective mass transfer, however, the downstream clusters (having switched to biofilm-dependent growth due to achieving threshold AIP concentration before upstream clusters), would develop less biovolume in the presence of such nutrient limitation. Overall, these results provide insight into the underlying mechanism of biofilm regulating metabolites, such as AIP, and their convective mass transfer properties under flow. Targeting the cell-signaling phenomena is a viable research subject matter within the scientific community, especially toward therapies aimed at *S. aureus* infections [75, 83, 164]. Due to the high interest level of research on cellular communication mechanism, this study provides further basis for biofilm prevention by targeting the cell-signaling pathway. Additionally, this body of work provides a mechanistic basic route to antibiotic-free biofilm inhibition strategies utilizing micropatterned geometry.

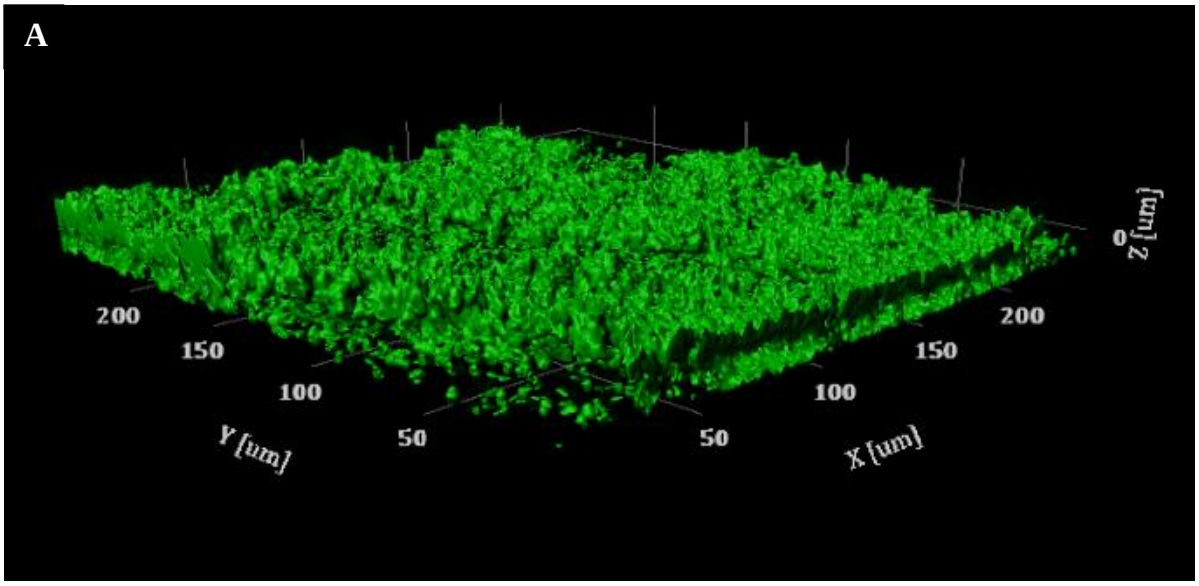
A
200
150
100
Y [um]
50
50
100
150
200
X [um]
0
Z [um]

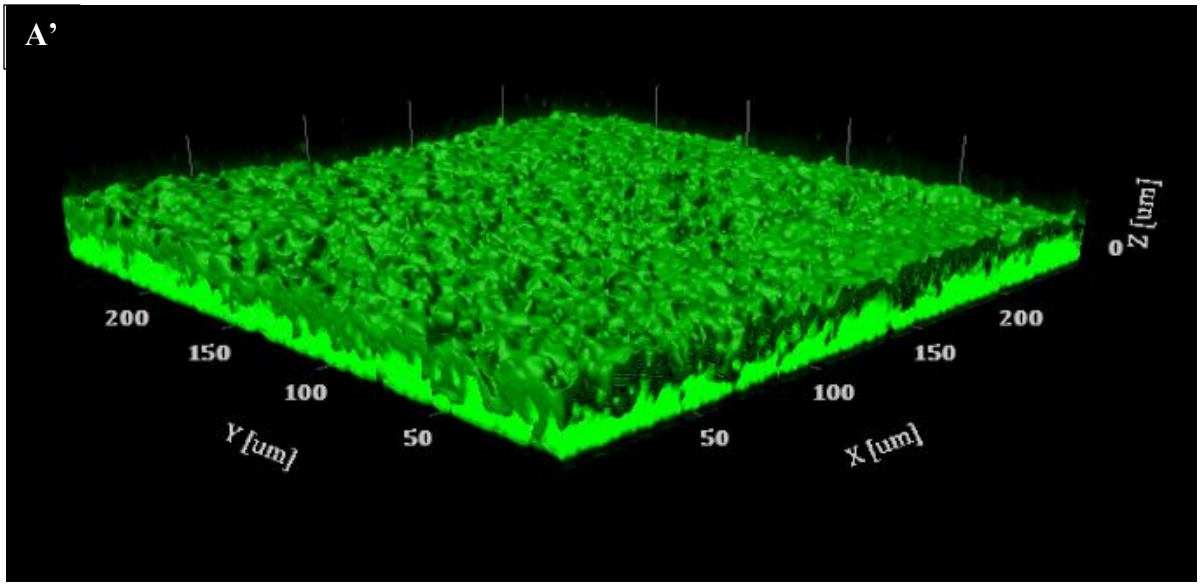
A'
200
150
100
Y [um]
50
50
100
150
200
X [um]
0
Z [um]

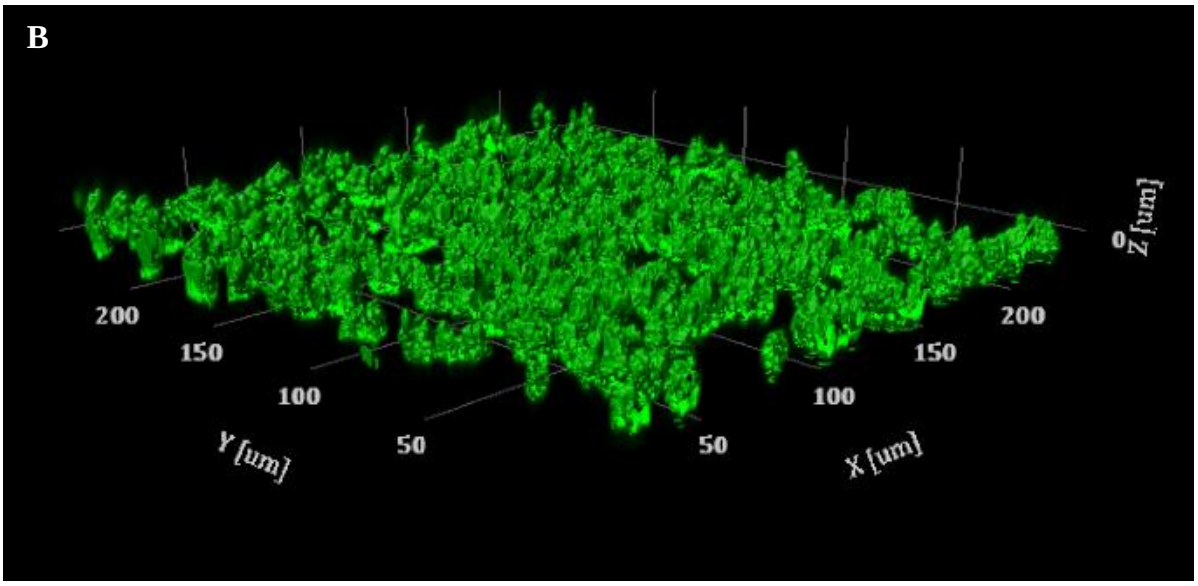
B
200
150
100
Y [um]
50
50
100
150
200
X [um]
0
Z [um]

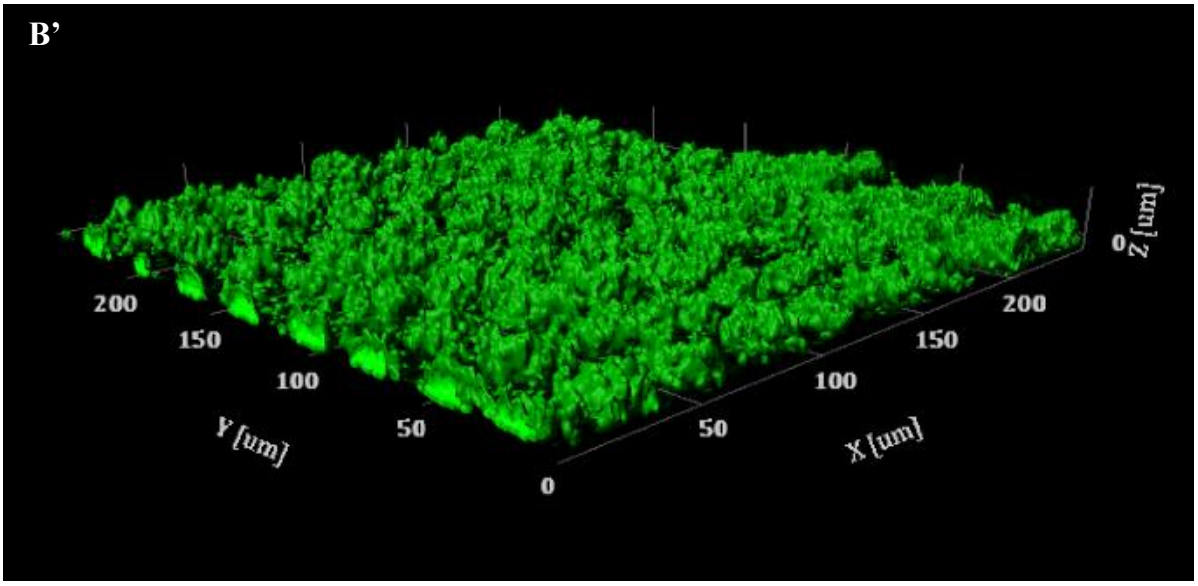
B'
200
150
100
Y [um]
50
0
50
100
150
200
X [um]
0
Z [um]

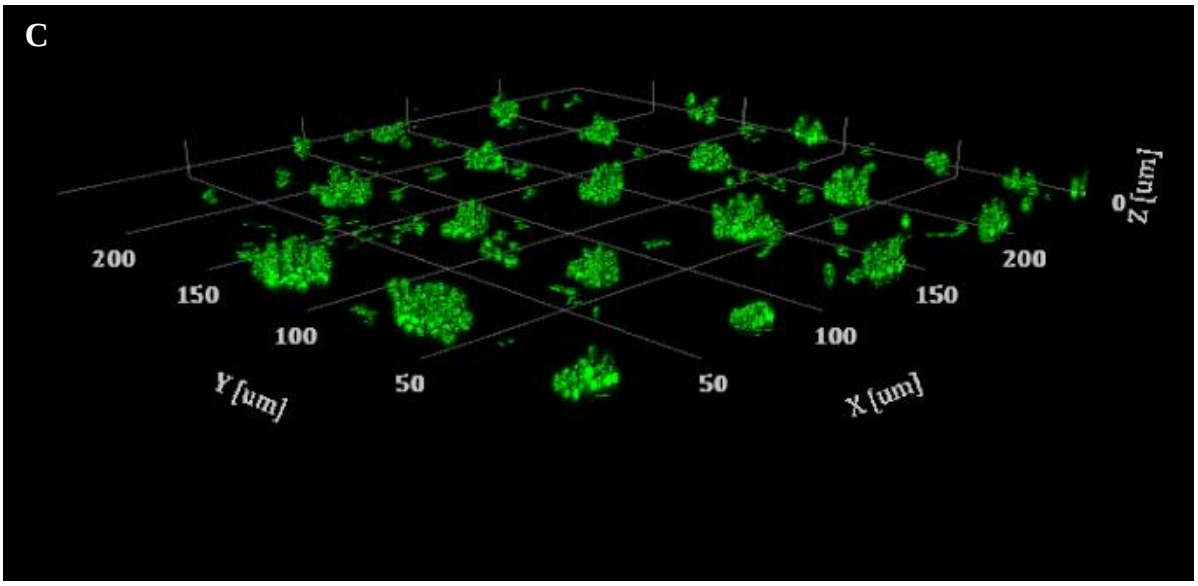
C
200
150
100
50
Y [um]
50
100
150
200
X [um]
0
Z [um]

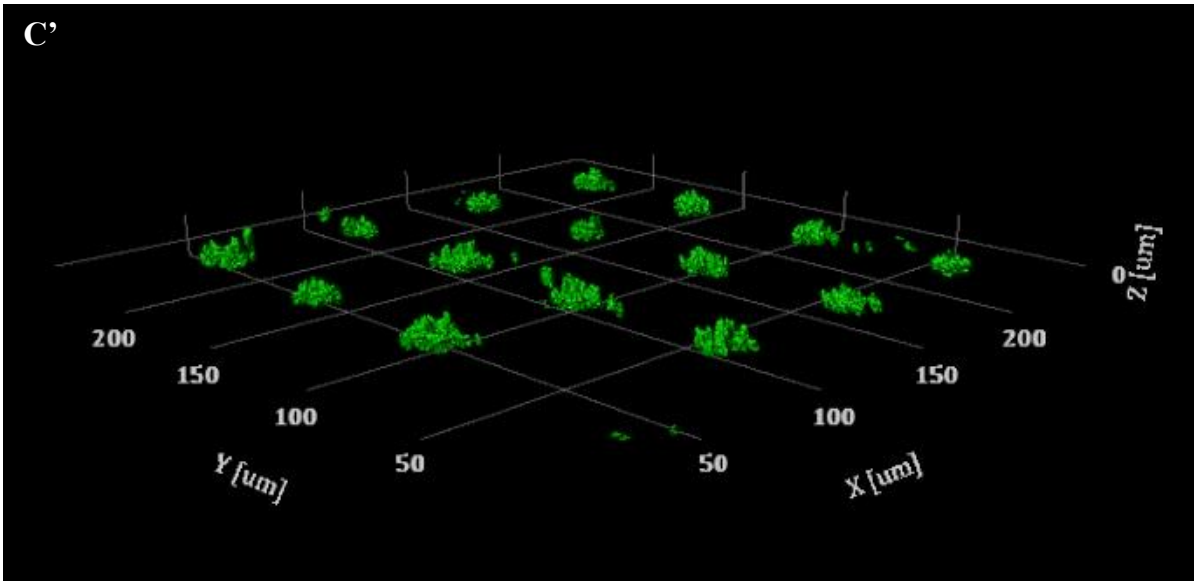
C'
200
150
100
50
Y [um]
50
100
150
200
X [um]
0
Z [um]

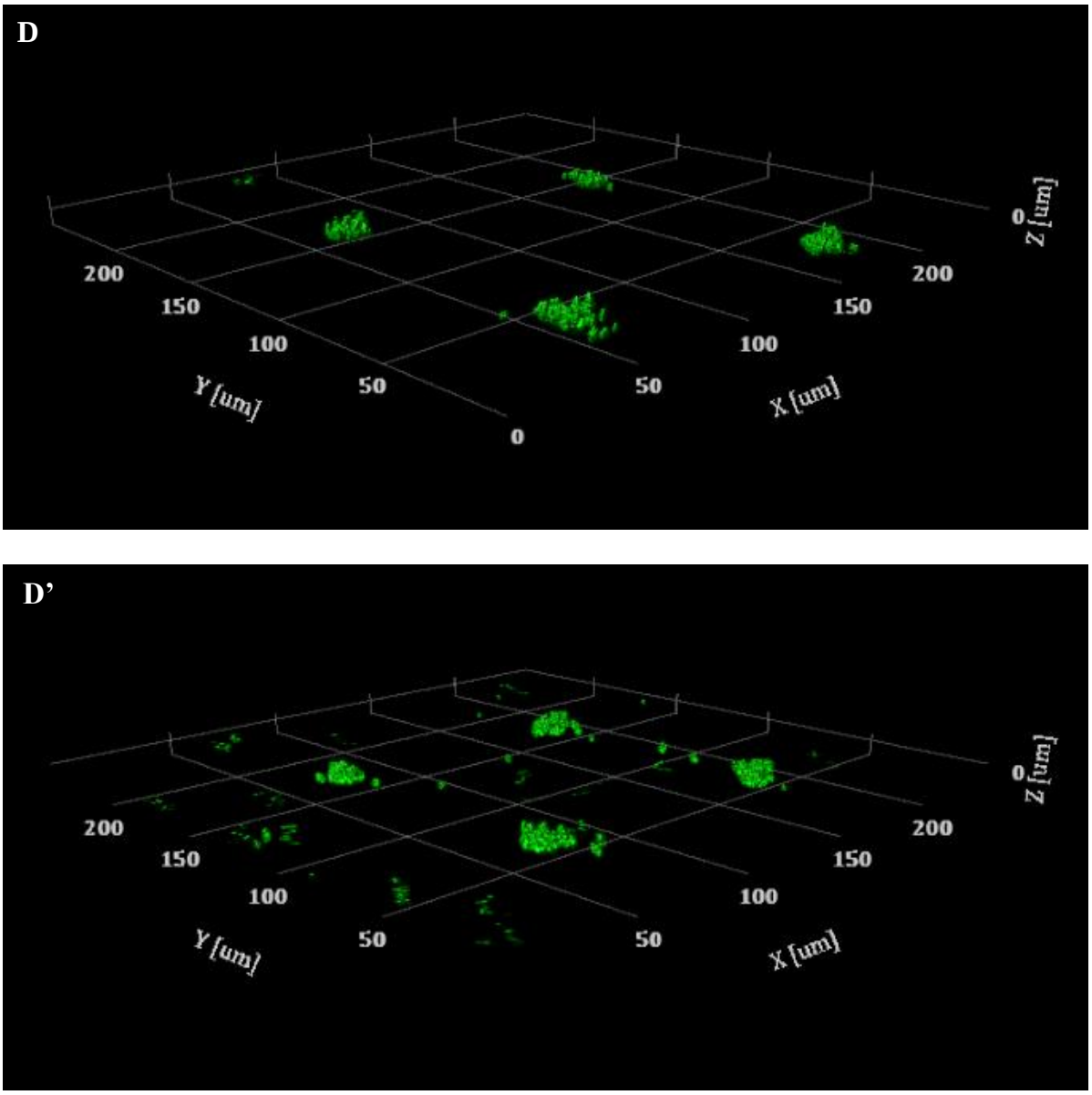

Figure 5.1: Perspective view images of *S. aureus* biofilm developed on micropatterned substratum as a function of physiological shear rates. Images above show biofilms developed at **(#)** 100 s^{-1} and **(#')** 300 s^{-1} shear rates on micropattern substratum configurations. In each image, the direction of flow is along the Y-axis. The configurations at the start of each experiment include **(A)** Full coverage, 10 μm array of clusters with spacing **(B)** 20 μm, **(C)** 50 μm, and **(D)** 110 μm between adjacent clusters. The full coverage biofilm was used as

control. Cells were adhered by sedimentation on glass coverslips that has been pre-coated with either a full or micropatterned coating of FN. Biofilm culture was developed *in situ* for 8 hours at 37°C with continuous media flow. Each square grid represents 50 µm.

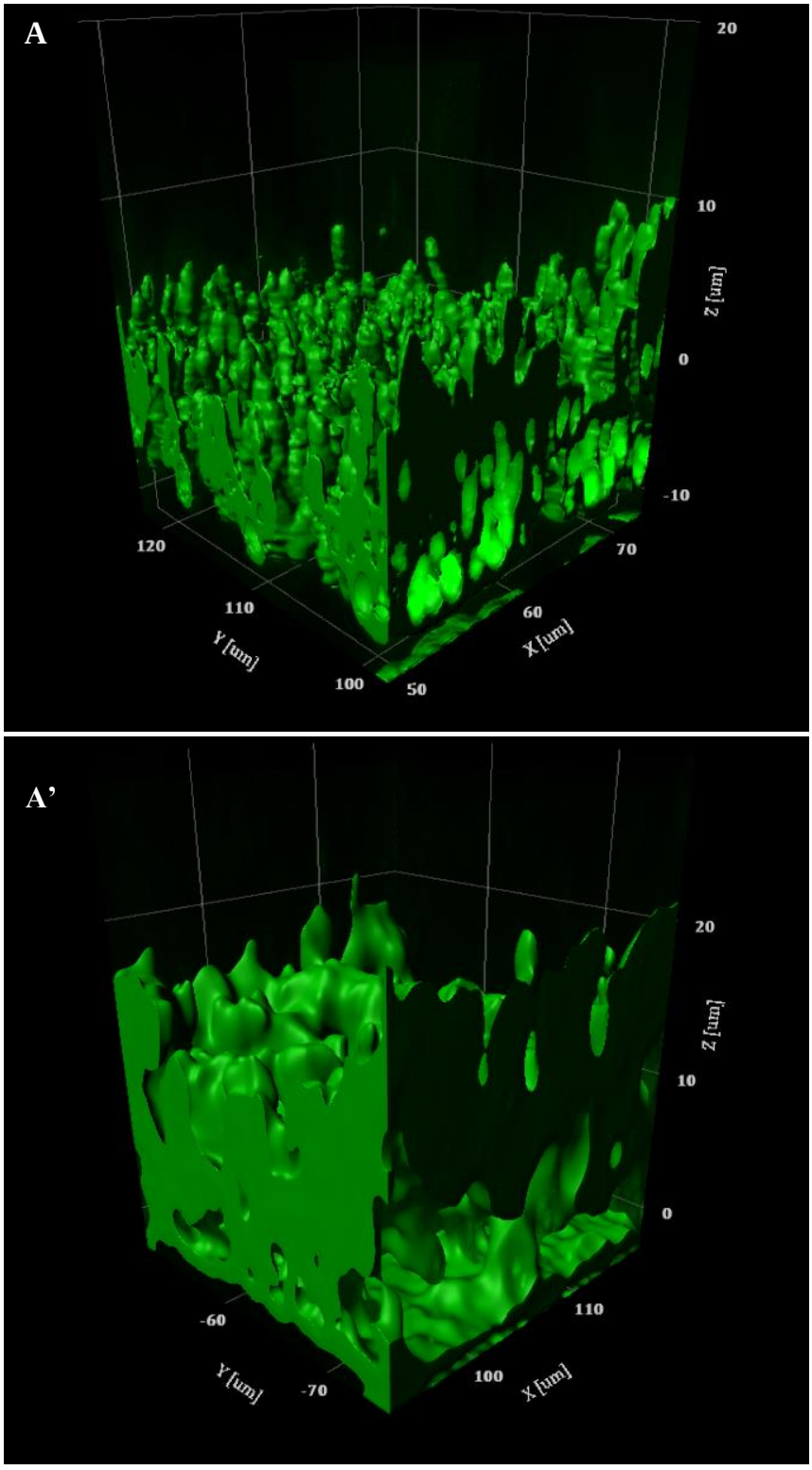
A
20
10
0
-10
Z [um]
120
110
Y [um]
100
50
60
70
X [um]
A'
20
10
0
Z [um]
-60
Y [um]
-70
100
110
X [um]

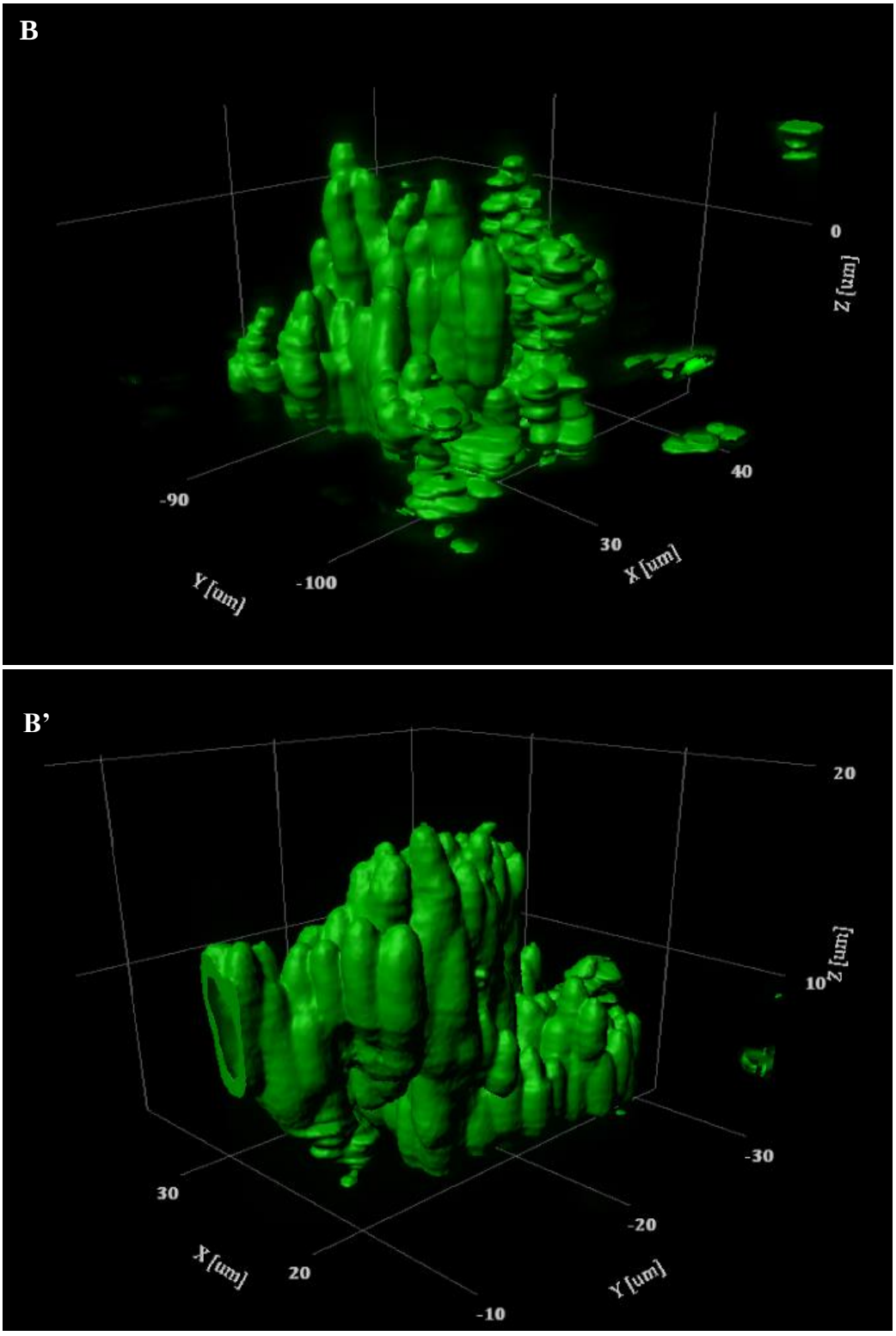
B
0
Z [um]
40
-90
30
Y [um]
-100
X [um]
B'
20
Z [um]
10
-30
30
-20
X [um]
20
Y [um]
-10

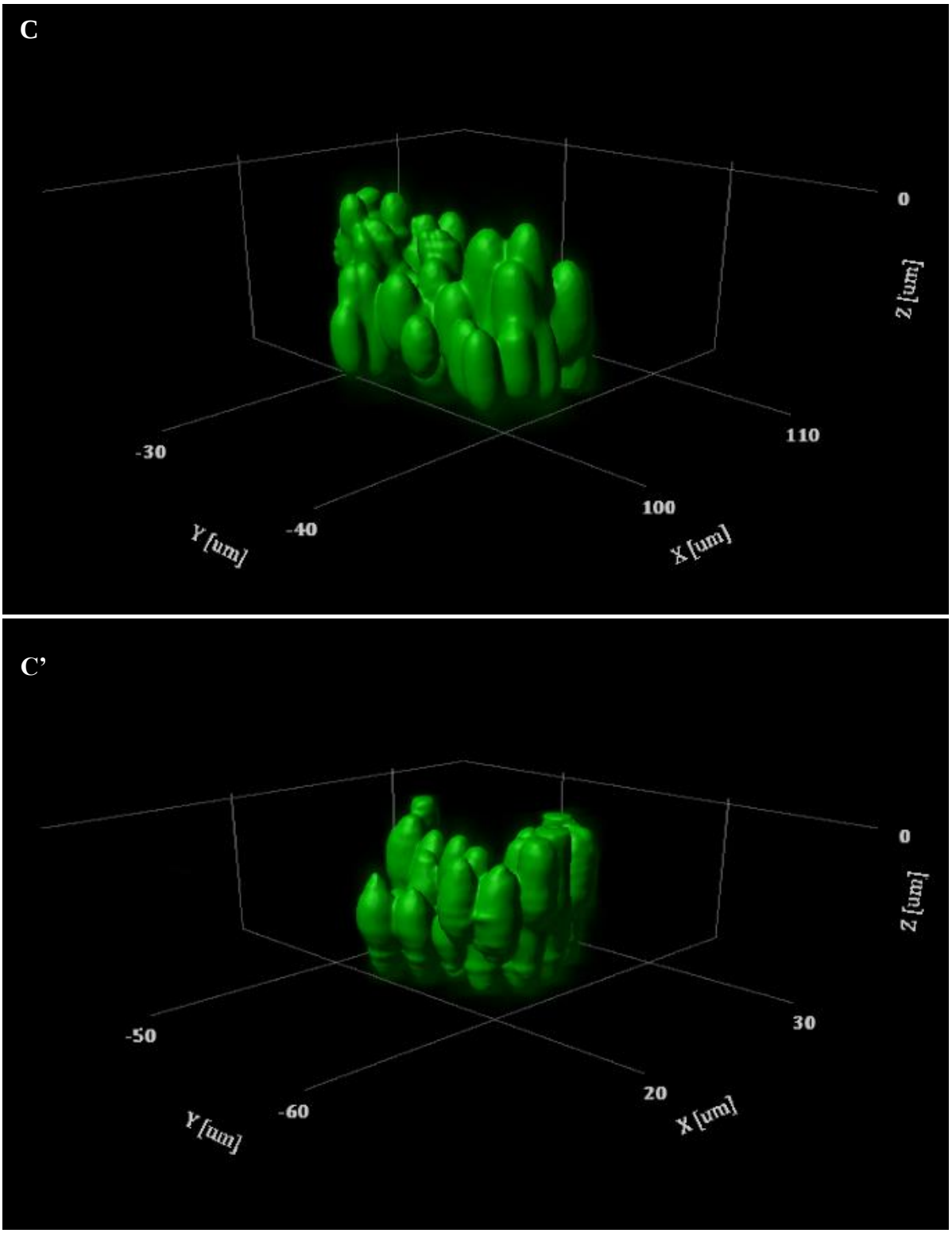
C
0
Z [um]
110
-30
100
-40
Y [um]
X [um]
C'
0
Z [um]
30
-50
20
-60
Y [um]
X [um]

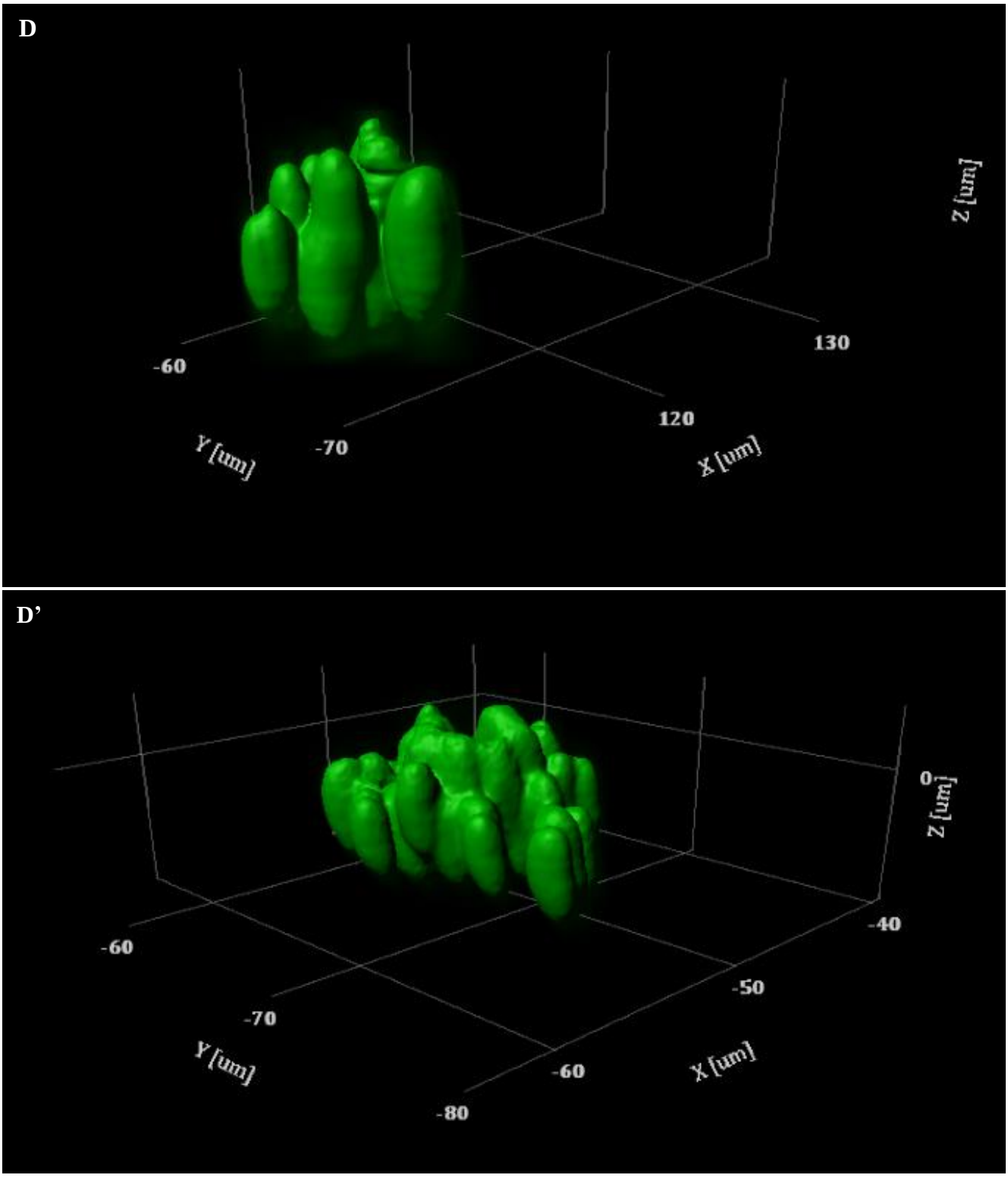

Figure 5.2: Closer perspective views of individual cell clusters of developing biofilm showing the microscale observable differences exhibited by the variation of micropattern

spacing and physiological shear rates. Experiments were performed at **(#)** 100 s^{-1} and **(#')** 300 s^{-1} shear rates on the following substratum configurations: **(A)** Full coverage used as control, **(B)** 20 µm, **(C)** 50 µm, and **(D)** 110 µm. In each image the direction of flow is along the Y-axis. Each square grid represents 10 µm.

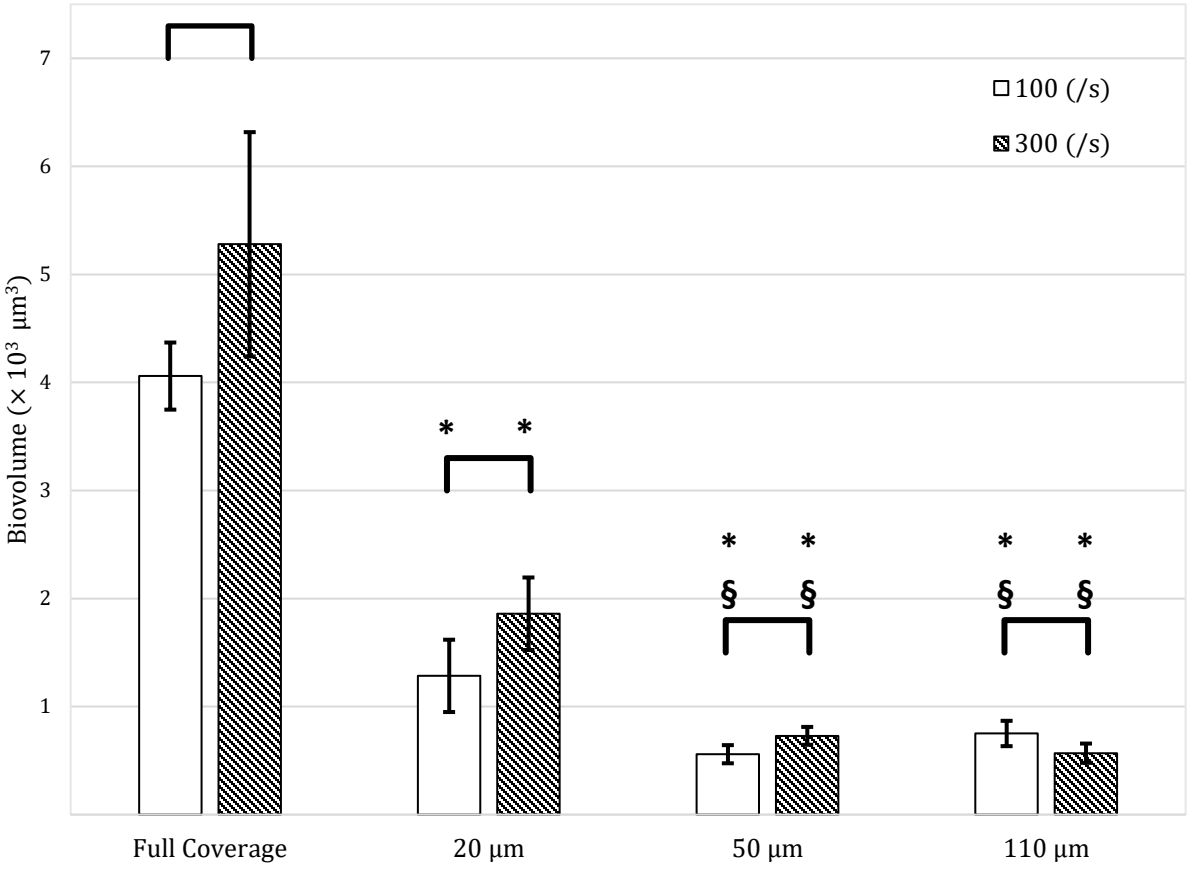

Figure 5.3: Biovolume of *S. aureus* biofilm developed as a function of physiological shear rates on different micropatterned substratum. The above chart reports the mean biovolume (± 95% confidence interval, n = 16) of the biomass produced by individual single cell clusters spaced by varying distances among adjacent clusters. The images were captured at ~ 300 µm distance from the posterior end of a 4 mm × 4 mm square total array area and biofilm was developed under flow. Full coverage indicates non-patterned surface and was used as control. Black bars indicate statistically significant difference ($p < 0.05$) between grouped pairs. * indicates statistically significant difference ($p < 0.001$) compared to full coverage. § indicates statistically significant difference ($p < 0.001$) compared to 20 µm pattern spacing.

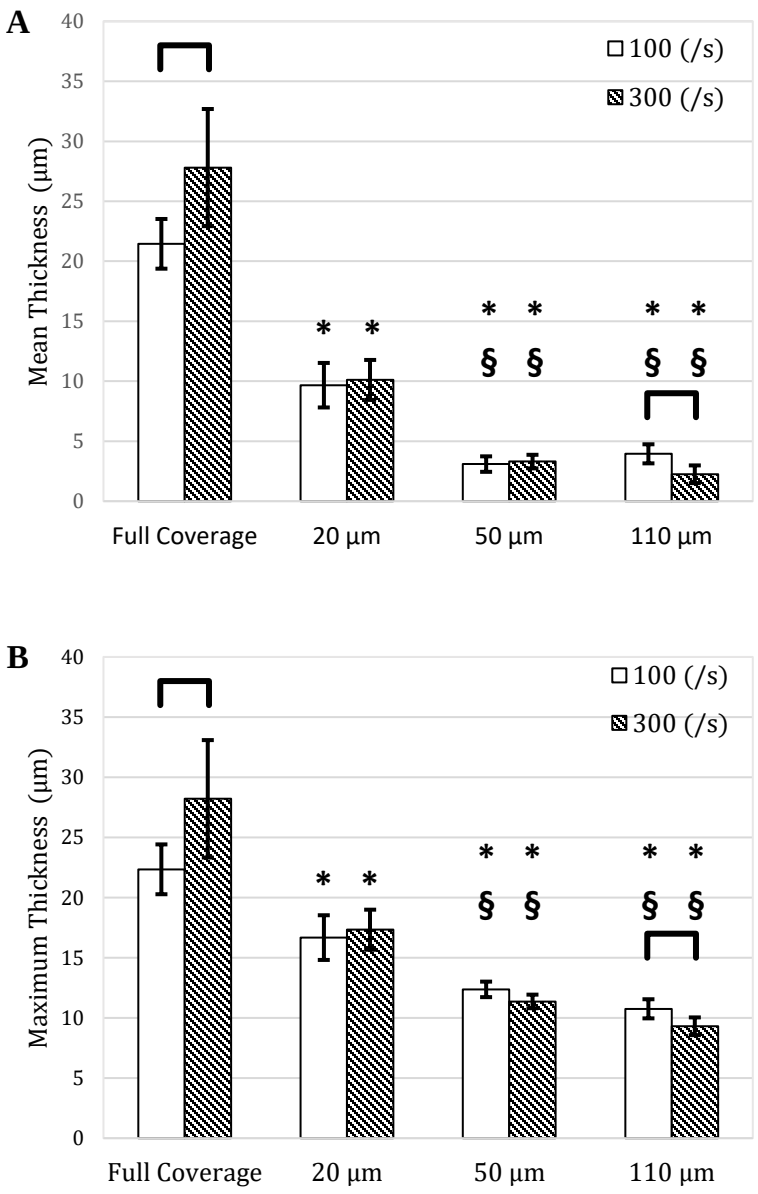

Figure 5.4: The **(A)** mean, and **(B)** maximum thickness (± 95% CI, n = 16) of *S. aureus* biofilm developed as a function of physiological shear rates on different micropatterned substratum. Black bars indicate statistically significant difference ($p < 0.05$) between grouped pairs. * indicates statistically significant difference ($p < 0.001$) compared to full coverage. § indicates statistically significant difference ($p < 0.001$) compared to 20 µm pattern spacing.

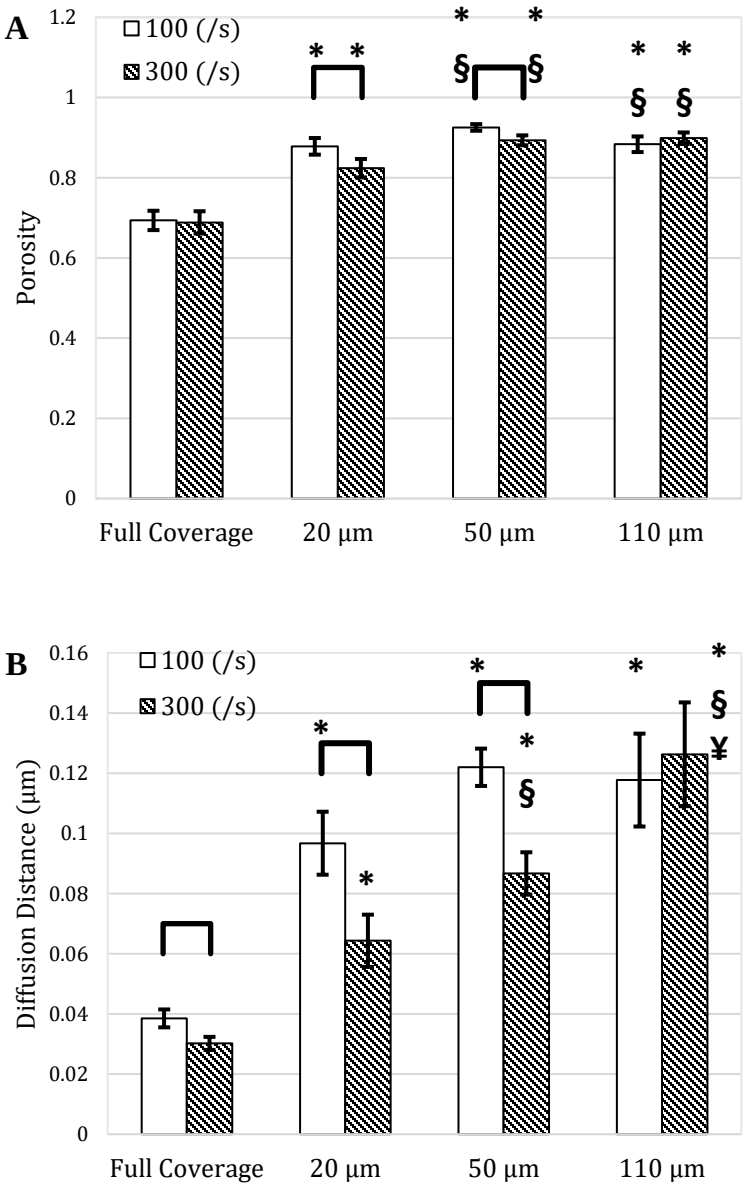

Figure 5.5: (A) Porosity, and **(B)** diffusion distance (± 95% CI, n = 16) of *S. aureus* biofilm developed as a function of physiological shear rates on different micropatterned substratum. Black bars indicate statistically significant difference ($p < 0.05$) between grouped pairs. * indicates statistically significant difference ($p < 0.001$) compared to full coverage. § indicates statistically significant difference ($p < 0.001$) compared to 20 µm spacing. ¥ indicates statistically significant difference ($p < 0.001$) compared to 50 µm spacing.

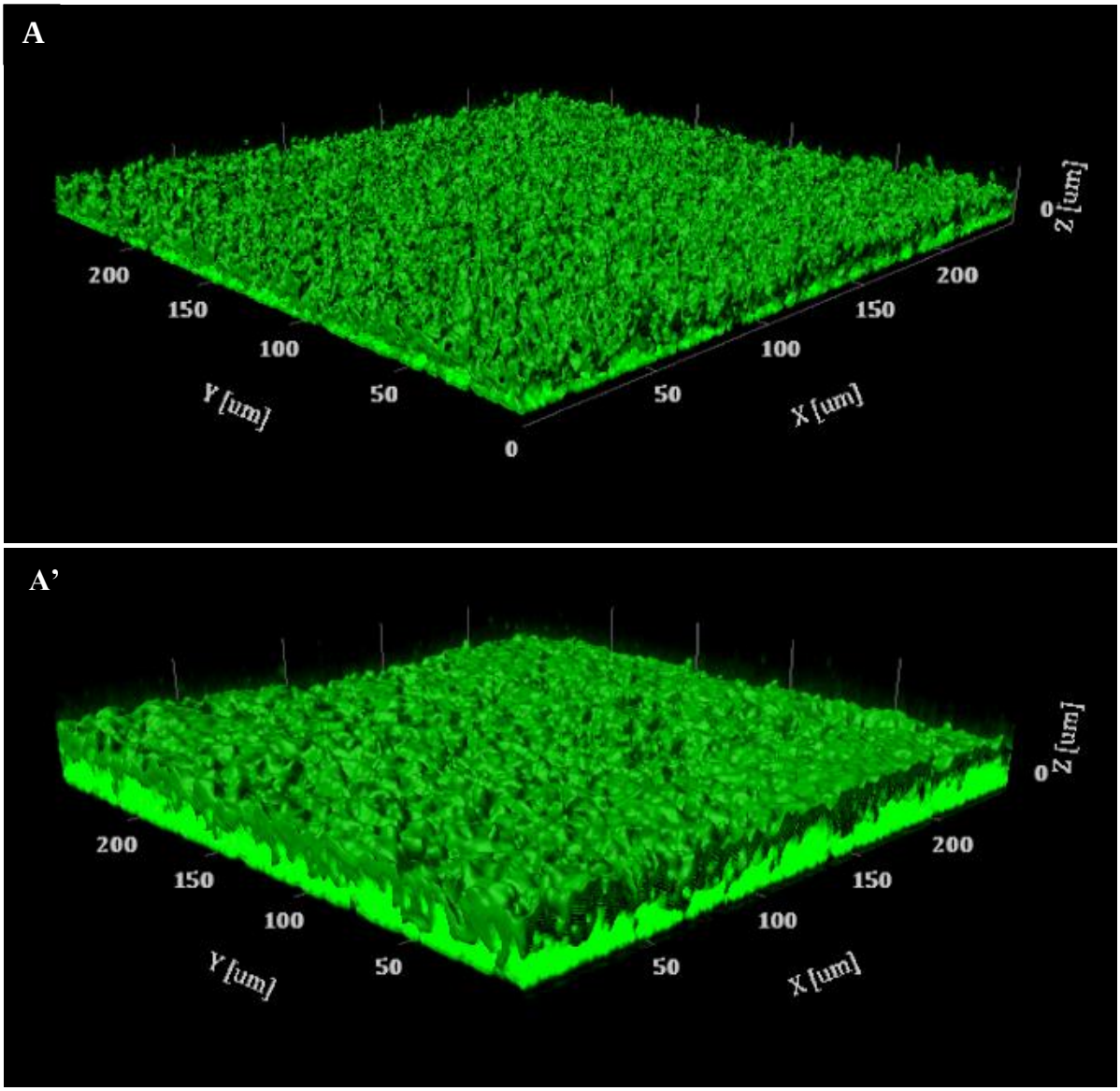
A
200
150
100
Y [um]
50
0
50
100
150
200
X [um]
0
Z [um]
A'
200
150
100
Y [um]
50
50
100
150
200
X [um]
0
Z [um]

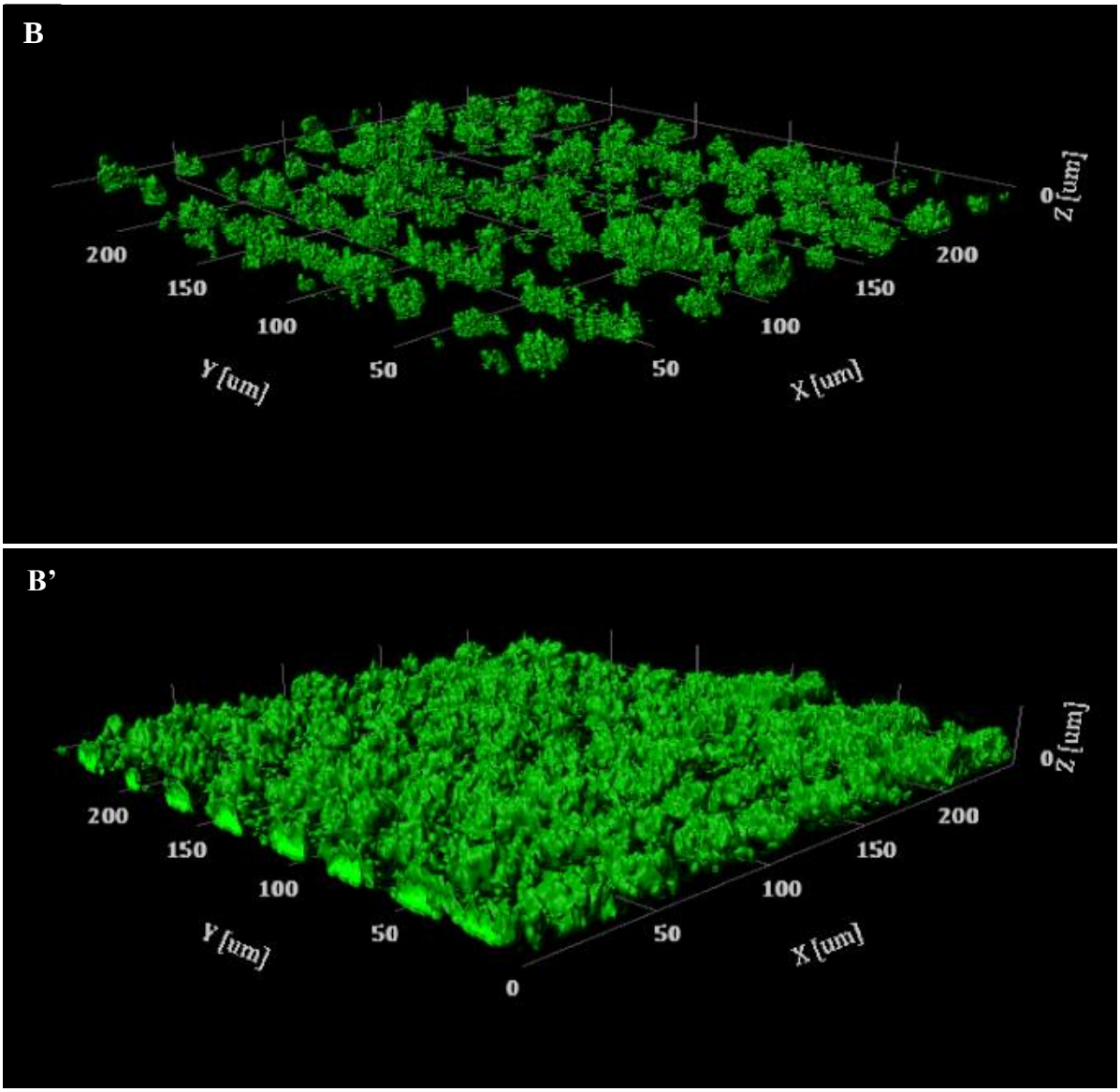
B
200
150
100
50
Y [um]
50
100
150
200
X [um]
0
Z [um]
B'
200
150
100
50
Y [um]
0
50
100
150
200
X [um]
0
Z [um]

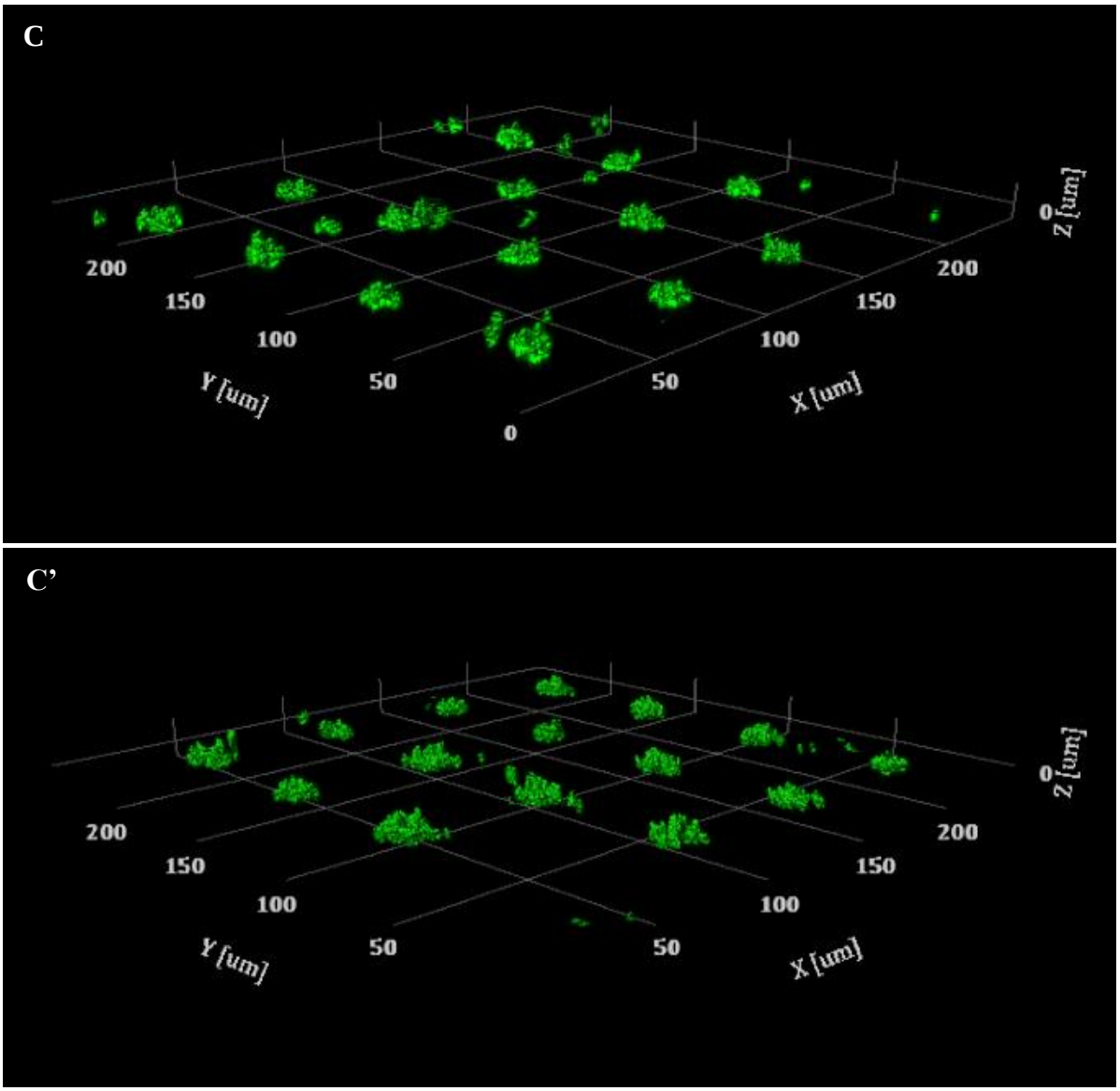
C
200
150
100
Y [um]
50
0
50
100
150
200
X [um]
0
Z [um]
C'
200
150
100
Y [um]
50
50
100
150
200
X [um]
0
Z [um]

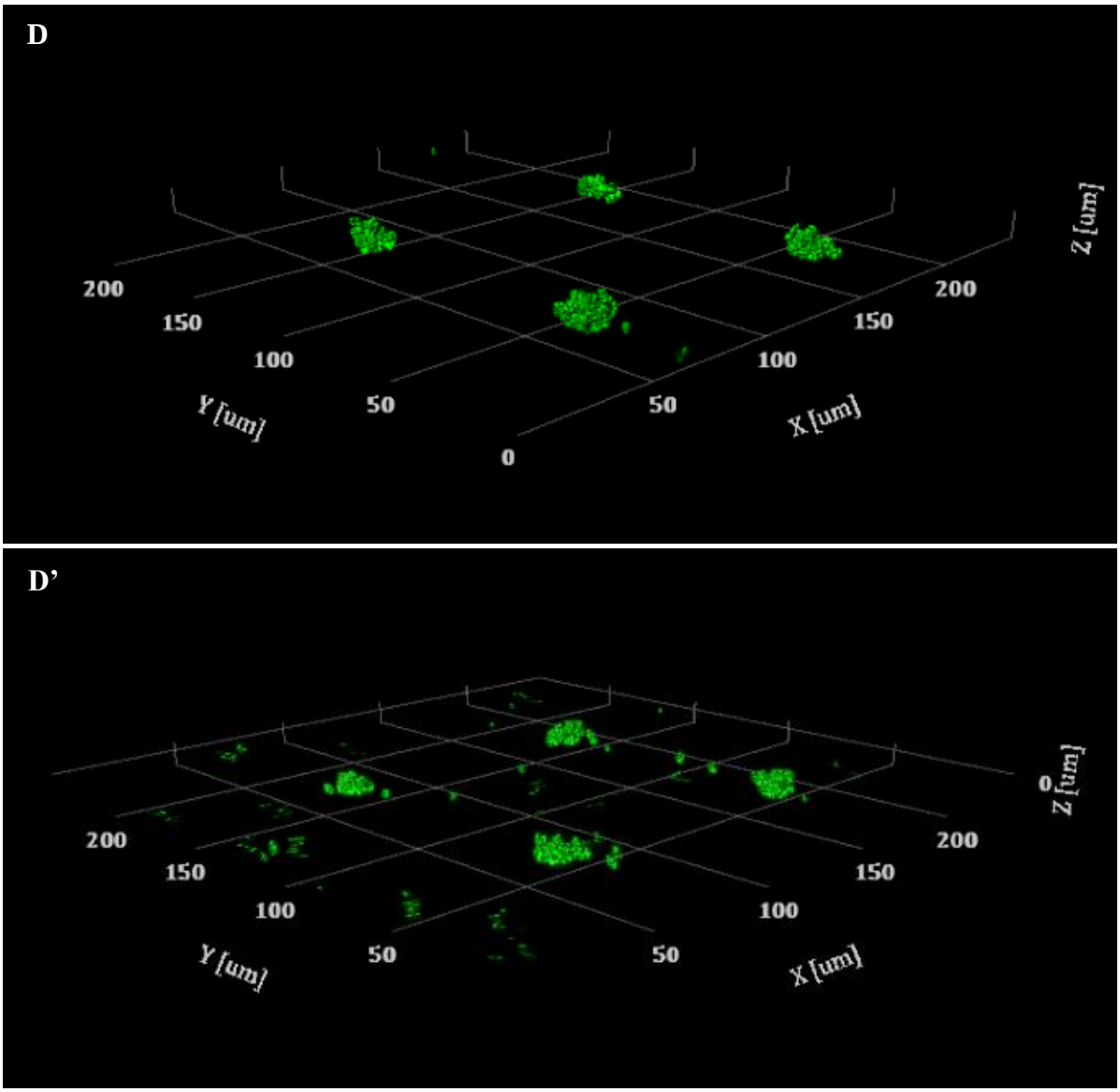

Figure 5.6: The effect of total cluster number on *S. aureus* biofilm development on micropatterned substratum under the influence of physiological shear rates. Images above show perspective views of biofilms developed at 300 s^{-1} shear rate on micropatterned substratum configurations: **(A)** Full coverage, 10 µm clusters with **(B)** 20 µm, **(C)** 50 µm, and **(D)** 110 µm spacing between adjacent clusters. Cells were seeded in systematically different total cluster number by altering the total array size between experiments from **(#)** 2

mm × 2 mm to **(#')** 4 mm × 4 mm. In each image the direction of flow is along the Y-axis. Each square grid represents 50 µm.

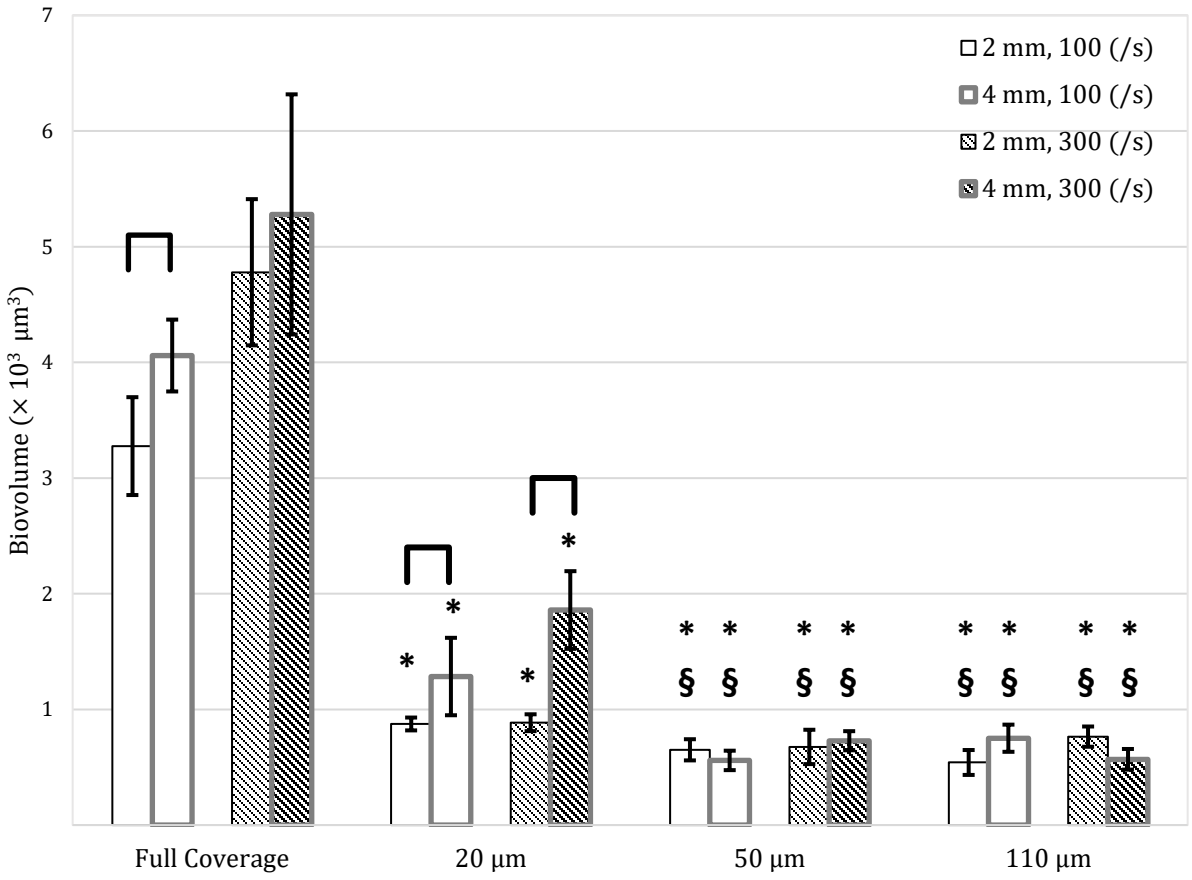

Figure 5.7: Biovolume (mean ± 95% confidence interval, n = 16) of *S. aureus* biofilm developed with varying physiological shear rates on different micropatterned substratum, at total substratum coverage of 2 mm × 2 mm or 4 mm × 4 mm. The images were captured at ~ 150 µm distance from the posterior end of the 2 mm × 2 mm array and ~ 300 µm distance from the posterior end of the 4 mm × 4 mm array. Full coverage indicates non-patterned surface and was used as control. Black bars indicate statistically significant difference ($p < 0.05$) between grouped pairs. * indicates statistically significant difference ($p < 0.001$) compared to full coverage. § indicates statistically significant difference ($p < 0.001$) compared to 20 µm pattern spacing.

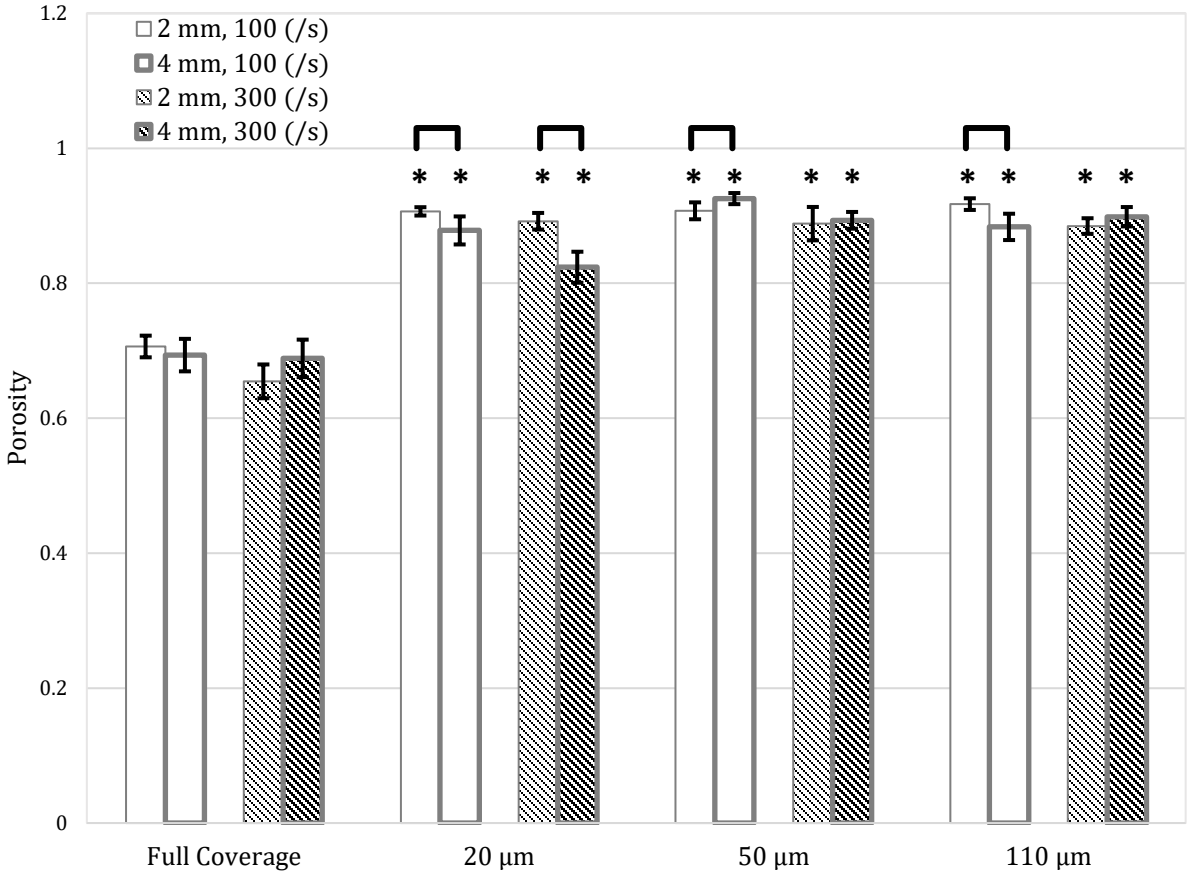

Figure 5.8: Porosity (mean ± 95% CI, n = 16) of *S. aureus* biofilm developed with varying physiological shear rates on different micropatterned substratum, and at total substratum coverage of 2 mm × 2 mm or 4 mm × 4 mm. Black bars indicate statistically significant difference ($p < 0.05$) between grouped pairs. * indicates statistically significant difference ($p < 0.001$) compared to full coverage.

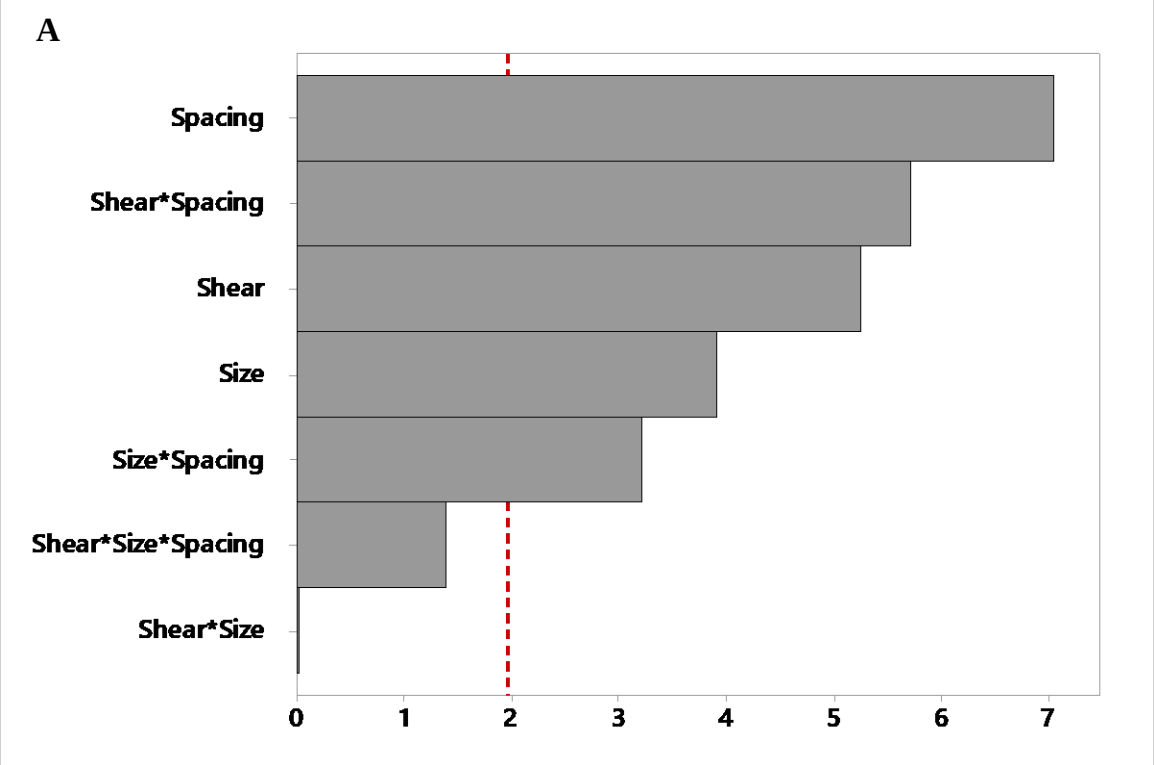
A
Spacing
Shear*Spacing
Shear
Size
Size*Spacing
Shear*Size*Spacing
Shear*Size
0
1
2
3
4
5
6
7

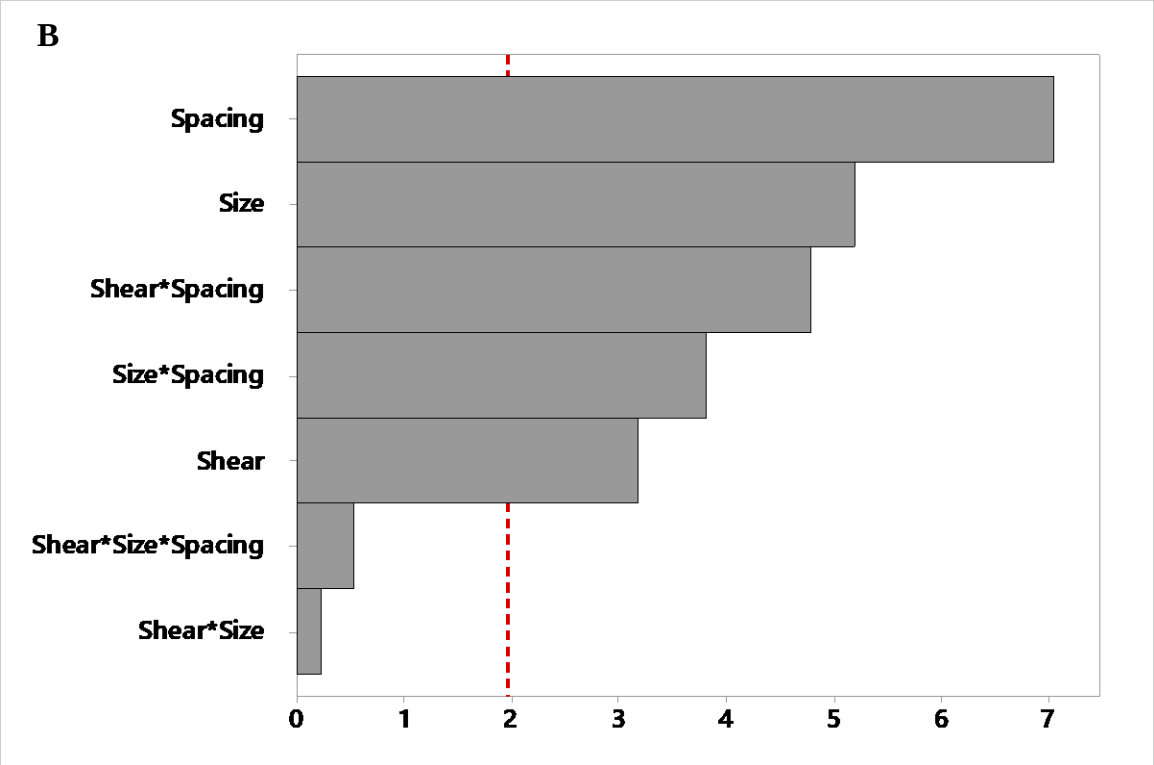
B
Spacing
Size
Shear*Spacing
Size*Spacing
Shear
Shear*Size*Spacing
Shear*Size
0
1
2
3
4
5
6
7

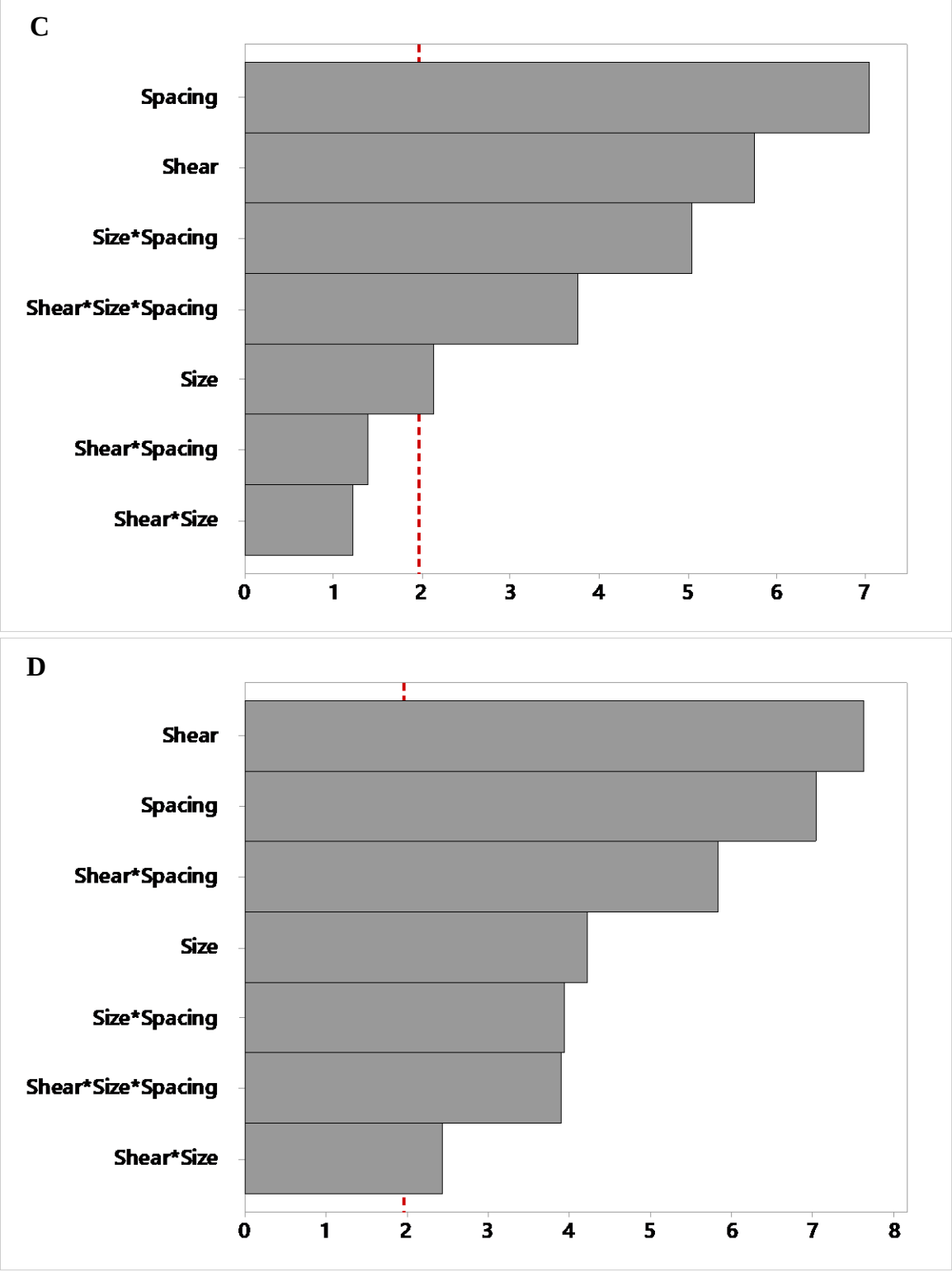

Figure 5.9: Full-factorial Pareto charts of standardized effects of the following responses: **(A)** biovolume, **(B)** mean biofilm thickness, **(C)** porosity, and **(D)** mean diffusion distance.

Plots show the rankings of effect sizes on *S. aureus* biofilm developed with varying physiological shear rates on different micropatterned spacing at varied total size. All readings were acquired from the posterior end of the developed biofilm for comparative analysis. For each response, the effects are ranked from the highest effect to the lowest. Main effect bar values that are lower than the average effects reference line (shown as red dash) is considered not statistically significant to the response ($\alpha = 0.05$).

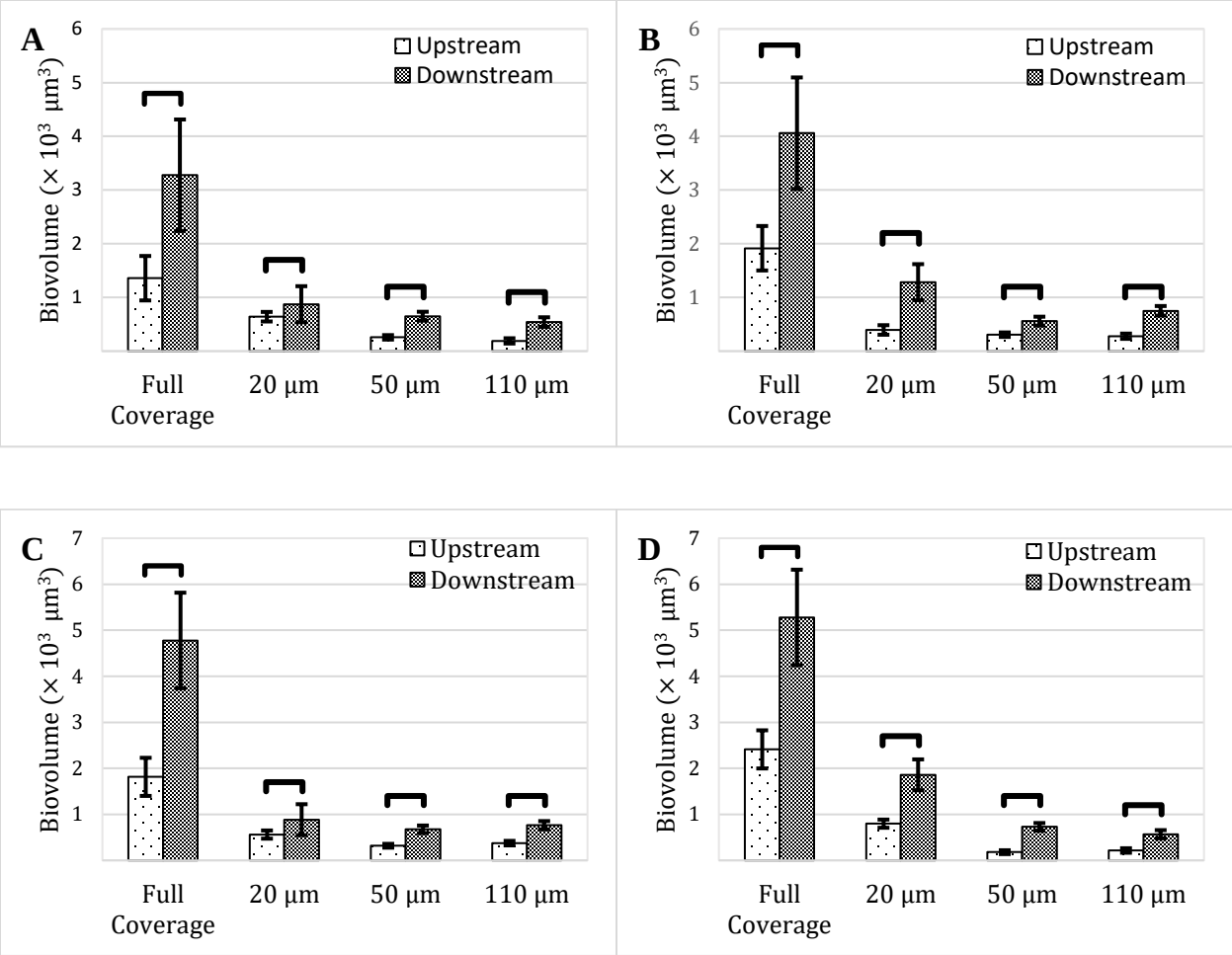

Figure 5.10: Comparison of the upstream and downstream biovolume (mean ± 95% CI, n = 16) of *S. aureus* biofilm developed under flow as a function of micropatterned substratum and the total coverage area. Graphs are shown for biofilms developed at **(A)** 2 mm × 2 mm; 100 s^{-1}, **(B)** 4 mm × 4 mm; 100 s^{-1}, **(C)** 2 mm × 2 mm; 300 s^{-1}, and **(D)** 4 mm × 4 mm 300 s^{-1}. For the 2 mm × 2 mm and 4 mm × 4 mm coverage areas, upstream and downstream represents biofilms at ~150 µm and ~300 µm, respectively from the anterior and posterior ends of the total coverage area. Black bars indicate statistically significant difference ($p < 0.05$) between grouped pairs.

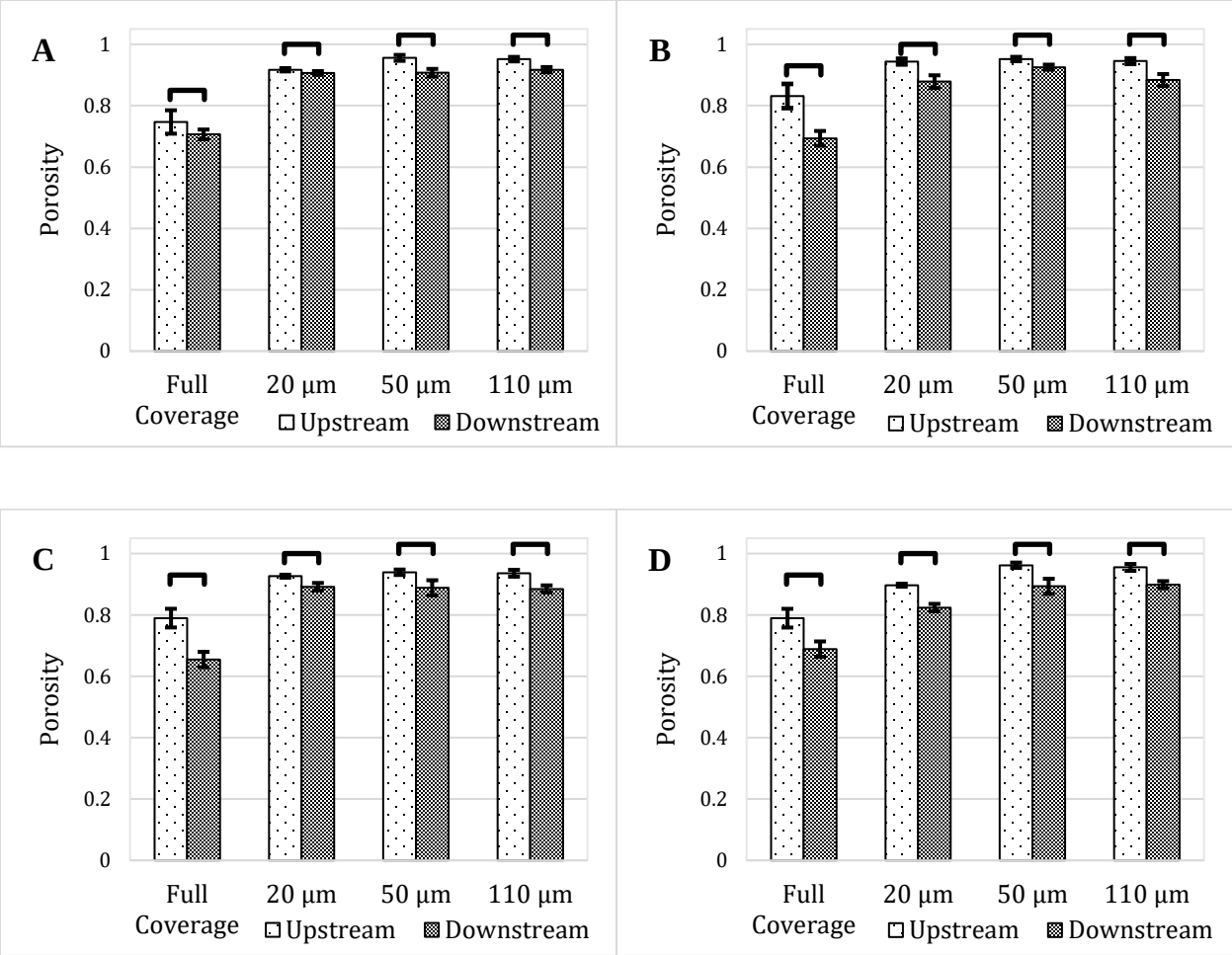

Figure 5.11: Comparison of the upstream and downstream porosity (mean ± 95% CI, n = 16) of *S. aureus* biofilm developed under flow as a function of micropatterned substratum and total coverage area. Graphs are shown for biofilms developed at **(A)** 2 mm × 2 mm; 100 s^{-1}, **(B)** 4 mm × 4 mm; 100 s^{-1}, **(C)** 2 mm × 2 mm; 300 s^{-1}, and **(D)** 4 mm × 4 mm; 300 s^{-1}. For the 2 mm × 2 mm and 4 mm × 4 mm coverage areas, upstream and downstream represents biofilm at ~150 µm and ~300 µm, respectively from both the anterior and posterior ends of the total coverage area. Black bars indicate statistically significant difference ($p < 0.05$) between grouped pairs.

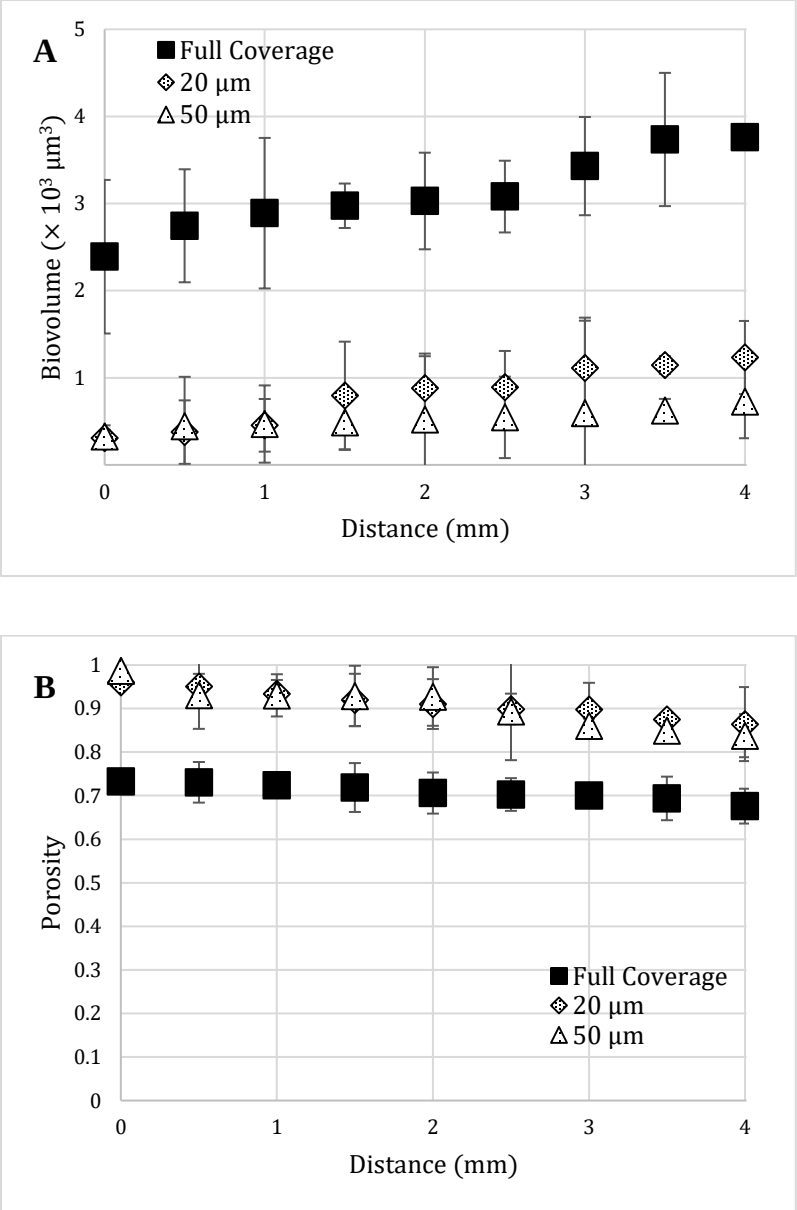

Figure 5.12: Developmental progression of *S. aureus* biofilm along the axis of flow. The **(A)** biovolume and **(B)** porosity (mean ± 95% CI, n = 4) of developed biofilm captured at the locations indicated by the distance axis along a 4 mm length of total coverage area. Biofilm was developed under flow at 100 s^{-1} at 37°C for 8 hours. The direction of flow is along the "distance" axis from left to right.

Chapter 6: Conclusion & perspectives for future studies

6.1 Contributions of the current dissertation

Bacterial cells, in nature, prefer to exist as a surface-attached coalescent community of slime encased cells known as biofilms [42-44, 46, 174]. This biofilm-forming existence offers several advantages to the cells involved including evasiveness to host immune response, resistance to antimicrobial and antibiotic therapies, communal expression of metabolites, and overall increased survivability in unfavorable environmental conditions [9, 29, 151, 152, 174]. Biofilm formation has been observed for several species of bacteria across multiple scientific disciplines and affecting a wide variety of industries including the food industry, waste treatment, manufacturing pipelines, and healthcare [4, 6, 7, 42-44, 175, 176]. In healthcare settings, *S. aureus* is a major etiological agent of biofilm-based nosocomial and community-acquired infections of indwelling medical devices in humans [9, 177]. For example, the persistence of *S. aureus* in cardiovascular related infections in humans has been linked to its development of biofilm as an intrinsic step in infection pathogenesis [2, 9, 13, 15-17, 53, 177]. Furthermore, the hydrodynamic environment of the cardiovascular system complicates the eradication of biofilm-based infection due to the metastasizing of eroded cells to multiple infection sites [42, 51, 54, 178-180]. Therefore, remediation efforts of staphylococcal infections have been aimed at the prevention of the initial formative steps as well as biochemical disruption of biofilm development [15, 23, 54, 154, 181]. There is also scientific focus on the subject matter of non-biochemical related biofilm eradication. One such subject matter involves the use of physical mechanisms for the purpose of obstructing the development of biofilm or weakening the structure of developed biofilm [106].

Biofilm-based *S. aureus* infections initiates by adhering to host extracellular matrix or indwelling implant devices, followed by accumulation into clonal or non-clonal microcolonies on the path toward biofilm development. Cell-to-cell communication via the release and detection of AIP is a regulator of biofilm-dependent accumulation. Cells that are growing as biofilm produce components that make up the EPS such as polysaccharides, extracellular DNA and exo-proteins [9, 81, 182, 183]. The primary goal of this body of work was to investigate the effects of controlled adhesion of cell clusters on the development of *S. aureus* biofilm under fluid flow. In the course of the studies presented in this dissertation, it was demonstrated that: 1) *in silico* modeling of AIP mass transfer within the experimental environment was a viable tool in experimental design which may enhance biofilm research; 2) increasing the adjacent spacing between microcolonies of equal sizes inhibited the structural development of *S. aureus* biofilm up to a limit after which further inhibition was negligible; 3) the influence of the micropatterned colonies on biofilm development was due to the difference in convective mass transfer of AIP; and 4) the inhibitory effect of micropatterned clusters on biofilm development was improved by increase in the shear rate.

There is growing scientific interest in the specific disruption of the cell-signaling pathway that constitutes an intrinsic step in biofilm-based infection pathogenesis. The research performed in this body of work extend the understanding AIP mass transfer pathways within a dynamic environment. Through bypassing of initial adhesion and accumulation stages of biofilm development, this body of work applied focus on the cell-sensing mechanism. Three cell-signaling theories that are currently used to describe bacterial intercellular communication include QS, DS and ES [35, 36]. The QS theory describes

cellular communication in sole response to cell population density while DS describes response to local environmental conditions experienced by individual cells. The ES theory describes cell sensing in response to local environmental cues for the purpose to efficiently take advantage of these environmental conditions. Thus, the cell-sensing mechanism within the dynamic flow environment utilized in this work, appear to favor ES as opposed to a simple quorum detection or diffusion detection. To elucidate this point, the following considerations are made from the data presented in this body of work: 1) quorum sensing only should result in similar biofilm progression for equivalent total cluster number and cluster spacing at different shear rates since nutrient limitation did not occur; and 2) diffusion sensing only should result in increased shear having the most influence on biofilm progression based on the improved convective mass transfer.

Studies have reported that the diminishing effect of micropatterned geometric barriers on biofilm development under static experimental conditions, has a critical set of micropattern dimensions, after which, further biofilm inhibition is negligible [39, 40]. In those experiments, the reported critical cluster size was a square 20 μm × 20 μm and the critical spacing between that cluster size was 20 μm. In addition to being performed under static conditions, those studies were performed using *E. coli* as the bacterial pathogen of interest. The studies presented in this body of work represent the first reports of the impact of non-barrier-based micropatterned substrata on *S. aureus* biofilm development under hydrodynamic flow conditions. At the cluster size of 10 μm dots, under the flow conditions utilized in this study, the critical spacing between adjacent clusters exists in the 20 μm-to-50 μm range. This implies that the critical dimensionality of biofilm inhibition due to cluster

arrangement includes the parameters of cluster size and spacing together. These dimensions interact with each other, within a dynamic experimental setup, such that an increase in the critical cluster size accompanies an increase in the critical cluster spacing.

The implications of the results presented in this body of work may be of interest to the bioengineering of implant devices. Once an implant device comes in contact with the host plasma, the device is instantly coated with host matrix proteins such as fibronectin and collagen [182]. This is one of the required characteristics for the biocompatibility of implant devices as outlined by the food and drug administration [184]. The protein-coated implant device surface is subsequently available for bacterial adhesion, should an infection occur. The results presented in this body of work implies that such bioengineering of implants can be implemented to allow only a specifically coated area of the implant device by matrix proteins. This would result in the coating of host matrix protein in a specific pattern ensuring that any invasion of bacteria on these host proteins would occur within the specified pattern. Thus, any bacterial infection on these micropatterned implant devices, having inhibited biofilm progression, are susceptible to host immune response and a reduced burden of antibiotic use.

Natural scientific progression implies that improvements to the research presented here will further elucidate the assertion made within this body of work. These improvements may include further refinement of the micropattern design space based technological availability. Additionally, the focus on the events following adhesion implied that true modeling of infection pathogenesis *in vivo* was not exact. Thus, the subject matter of future studies may include the study of adhesion properties of cells on patterned protein arrays

under flow. Furthermore, to expand on mass transfer properties of AIP (or other biofilm-dependent metabolites) within the flow system, probing of local AIP concentration within the flow chamber may be a viable improvement for consideration. These considerations for further improvements to this study are described in the subsequent sections.

6.2 Simulation development toward improved mimicry of experimental conditions

The simulation model provided in this body of work lays the ground work for in silico modeling of biological systems within COMSOL. Due to the complex nature of microbial growth and proliferation, mathematical models of microbial systems have generally been a challenge in the scientific community. For this body of work in particular, the difficulty was intrinsic to the geometry development of the simulation model. The present model focuses on two-dimensional model analysis of the concentration profile of AIP along the axis of flow. Within the experimental system, each cell cluster was arranged as circular 10-µm-diameter dots of attached cells. However, the simulation clusters were simplified to single 10-µm long rectangular planes; representing a cross-section of the cluster along the diameter. This model was, in part, restricted by the available computing resources that made developing complex models difficult. Additionally, the current simulation model focused on dependencies on mass transfer of autoinducer molecules imposed by the distance between adjacent patterns in one dimension. This means that these dependencies were based on mass transfer along the axis of flow. The experimental system comprised a two-dimensional array of clusters. The simulation model assumed the mass transfer in the direction perpendicular to the direction flow to be negligible. A three-dimensional simulation may be insightful in corroborating or contradicting this assumption. While the simulation model is adequate in terms of chemical engineering principles of laminar flow between parallel plate geometry, the three-dimensional environment of our experimental system makes it a necessity to improve upon the current model. This three-dimensional simulation would be a closer model of

experimental conditions which may be useful in elaborating the validity, or otherwise, of assumptions that have been made in the current simulation.

6.3 Refinement of micropattern design space to reveal critical size and spacing dimensions of biofilm impedance

One of the main outcomes of this body of work is the implication that further increase in micropattern spacing from 20 µm to 50 µm and 100 µm yielded no further significant impedance to the development of biofilm. This result suggests the existence of set of dimensionally critical parameters of cluster size and adjacent spacing that result in complete impedance of biofilm development while under hydrodynamic shear. This parameter set may include a smaller sized cluster and less spacing between adjacent clusters. The process of determining this set of design parameters exhibits analogs to engineering optimization of process parameters. The movement of a design space toward a desired effect involves changes to the parameters that influence that effect. In this subject matter, the desired effect is inhibition of biofilm development by the physical means of adjusting cluster size and spacing. The current body of work experienced limitations to the size of clusters that was achieved; equivalent to 10 µm. However, individual *S. aureus* cells are spherically shaped ~1 µm diameter entities. To avoid major differences in cluster size, cells were adhered by sedimentation to ensure that total coverage of each individual dot was achieved. In an ideal situation of cells packed completely adjacent to each other on single patterned dots, this results in clusters of ~100 cells μm^{-2}. It is currently known that in static environments, as little as a single cell can induce cell-signaling response [37, 38]. However, the limitation on cell numbers for response in dynamic environments is unknown. Further refinement of this micropattern design space may offer advances in the elucidation of this inquiry among also expounding on the proclamations of mass transfer limitations outlined in this dissertation.

6.4 Investigating autoinducer peptide concentration *in situ* via in-line sampling

The studies presented in this work agreed with previous findings of the influence of wall shear rates on biofilm development. This influence, at low wall shear rates is impacted further by nutrient mass transfer in the growth broth; however, at high shear rates the role of nutrient mass transfer diminished [64, 141, 145]. This body of work 1) showed via in silico modeling an increasing concentration profile for AIP along the axis of flow; 2) suggested that mechanistic influence of shear was based on this AIP metabolite gradient; 3) the result of the AIP concentration profile directly influenced the development of advanced biofilm at downstream positions. During the course of this study, analytical methods utilizing ultra-high pressure liquid chromatography coupled mass spectrometry (UHPLC-MS) for direct quantitation of AIP in tryptic soy broth (TSB) media was developed based on reported protocols [130]. To confirm the influence of AIP mass transfer on biofilm development under the influence of shear, future experimental designs involving the use of probe-fitted flow cells would be necessary. It is necessary to probe for the presence and concentration of this metabolite *in situ* due to the low concentrations of expression. These studies may also employ the use of reporter *S. aureus* strains that have been tagged specifically for signal transduction upon independent activation of the P2 and P3 transcription units of the accessory gene regulator. The protocol for such studies would involve live imaging during growth focused on varying positions along the length of biofilm development in the direction parallel to the flow axis. The results of such studies may further elucidate the expression patterns of S. aureus during biofilm development under flow and how micropatterned substrata influence this expression patterns *in situ*.

GLOSSARY

µCP	Micro-contact printing
Abiotic	Non-living organism
agr	Accessory gene regulator
AIP	Autoinducer peptide
Arthritis	Inflammatory disease associated with joints
Biocompatibility	A property of a material to be biocompatible so that it does not elicit a response from a living system
Biofilm	A collective community of exo-polymeric slime encased cells derived from an assembly of surface-associated microbial cells
Biotic	Derived from a living organism
BSA	Bovine serum albumin
CLSM	Confocal laser scanning microscopy
DS	Diffusion sensing
ECM	Extracellular matrix
Endocarditis	Inflammatory disease of heart and its valves
EPS	Exo-polymeric substance
ES	Efficiency sensing
FN	Fibronectin
Genomics	Research focused on structure, function, evolution, and mapping of genomes.

Laminar flow	Fluid flow such that movement of fluid molecules occur in layers and each layer moves parallel to each other without inter mixing
Metastatic	Phenomenon of disease spread by transference from an initial infection site to a secondary site.
MSCRAMMs	Microbial surface recognizing adhesive matrix molecules for the purpose of attaching ECM proteins
Nosocomial	Originating from the hospital setting
Osteomyelitis	Inflammatory disease of the bone
Pathogen	Disease causing microbe
Pathogenesis	The manner of disease development
PBS	Phosphate buffered saline
PDMS	Poly (dimethyl siloxane)
Phenotype	Observable characteristics of genotype expressions of an organism
Pixel	A minute measurement of an image in two-dimensions
Planktonic	Free floating microbial cell
Proteomics	Research focused on function of proteins expressed by cells, tissues, or organisms
QS	Quorum sensing
Reynolds number	A dimensionless number that represents the ratio of inertial forces to viscous forces and describes the regime of fluid flow
sar	Staphylococcal accessory regulator
Sepsis	Tissue damage originated from presence of harmful bacterial toxins

Sessile	Non-moving cell, usually by attachment to a surface
sGFP	Superfolder green fluorescent protein
Shear rate	Rate of shear deformation by the movement of parallel layers of fluid across each other or an interface
TSST	Toxic shock syndrome toxin
Virulence	Capacity for expression of disease-causing toxins by a microbe
Voxel	A minute element that constitutes part of a three-dimensional structure
YFP	Yellow fluorescent protein

APPENDIX

Appendix A – Determining correlations between experimental and biofilm variables by dimensional analysis

Dimensional analysis is a technique that can be utilized in determining the correlations between different physical properties that affect a process of interest. These physical properties make up the measured dependent variables as well as the independent variables that are manipulated during experimentation. The Buckingham-Pi method is a key method of dimensional analysis that is utilized in determining physically meaningful dimensionless groups (known as Pi-groups). These Pi-groups are nondimensionalized forms of the dependent and independent variables which can be used to determine their relationships via experimentation. The advantage to using the dimensional analysis lies in the efficiency of experimentation. Experimentation can be performed such that the independent dimensionless Pi-group variables are manipulated and correlated with the relevant dimensionless dependent variables.

In the preceding body of work, the independent variables include the diameter of dots (d), spacing between dots (s), fluid flow velocity (v), fluid density (ρ), fluid viscosity (μ), and diffusion coefficient of AIP-1 (D_c). The dependent variables are the parameter outputs of ISA3D which include biovolume (BV), volume-to-surface area ratio ($V2SA$), biofilm thickness (Th), etc. For the purpose of this analysis, consider that the biovolume of developed biofilm depends on some unknown function of the independent variables:

$$BV = f(d, s, \rho, \mu, v, D_c,)$$

These variables possess three main dimensional units of mass (M), length (L), and time (T). The following dimensional units for each of the variables is derived as follows:

BV	d	s	ρ	μ	v	D_c
L^3	L	L	$\frac{M}{L^3}$	$\frac{M}{LT}$	$\frac{L}{T}$	$\frac{L^2}{T}$

The repeating variables are deliberately chosen as ρ, v, s in order to have all three dimensions represented. There are therefore four dimensionless groups that can be generated from the combination of the repeating groups with each of the remaining variables.

$$\pi_1 = BV\rho^a v^b s^c \;\Big|\; \pi_2 = d\rho^a v^b s^c \;\Big|\; \pi_3 = \mu\rho^a v^b s^c \;\Big|\; \pi_4 = D_c\rho^a v^b s^c$$

The values of the exponents for each of the Pi-groups are subsequently calculated by substituting the dimensional units into each group as follows:

$$\pi_1 = BV\rho^a v^b s^c \Rightarrow L^3\left(\frac{M}{L^3}\right)^a\left(\frac{L}{T}\right)^b L^c \;\Big|\; \begin{matrix} M: a = 0 \\ L: 3 - 3a + b + c = 0 \Rightarrow c = -3 \\ T: \; -b = 0 \end{matrix} \;\Big|\; \pi_1 = \frac{BV}{s^3}$$

$$\pi_2 = d\rho^a v^b s^c \Rightarrow L\left(\frac{M}{L^3}\right)^a\left(\frac{L}{T}\right)^b L^c \;\Big|\; \begin{matrix} M: a = 0 \\ L: 1 - 3a + b + c = 0 \Rightarrow c = -1 \\ T: \; -b = 0 \end{matrix} \;\Big|\; \pi_2 = \frac{d}{s}$$

$$\pi_3 = \mu\rho^a v^b s^c \Rightarrow \frac{M}{LT}\left(\frac{M}{L^3}\right)^a\left(\frac{L}{T}\right)^b L^c \;\Big|\; \begin{matrix} M: 1 + a = 0 \Rightarrow a = -1 \\ L: -1 - 3a + b + c = 0 \Rightarrow c = -1 \\ T: \; -1 - b = 0 \Rightarrow b = -1 \end{matrix} \;\Big|\; \pi_3 = \frac{\mu}{\rho v s} = \frac{1}{Re_s}$$

$$\pi_4 = D_c \rho^a v^b s^c \Rightarrow \frac{L^2}{T}\left(\frac{M}{L^3}\right)^a \left(\frac{L}{T}\right)^b L^c \quad \left| \begin{array}{c} M: a = 0 \\ L: 2 - 3a + b + c = 0 \Rightarrow c = -1 \\ T: -1 - b = 0 \Rightarrow b = -1 \end{array} \right| \quad \pi_4 = \frac{D_c}{vs}$$

Therefore, this analysis results in the following functional relationship between the four dimensionless groups:

$$\frac{BV}{s^3} = f\left(\frac{s}{d}, \frac{1}{Re_s}, \frac{D_c}{vs}\right)$$

The dimensionless biovolume to spacing ratio $\left(\frac{BV}{s^3}\right)$ is a function of the spacing to distance ratio $\left(\frac{s}{d}\right)$, the inverse of the Reynolds number $\left(\frac{1}{Re_s}\right)$, and the ratio of the diffusion coefficient versus the product of the velocity and spacing $\left(\frac{D_c}{vs}\right)$. The dimensionless biovolume is normalized by the cube of the spacing between the adjacent distance between clusters of adhered cells. The Reynolds number is a ratio of the inertial forces versus the viscous forces. This analysis implies that dimensionless biovolume depends on the ration of the viscous versus inertial forces which is a property of the fluid flow during experimentation. The overall function of the dimensionless biovolume to the derived dimensionless independent variables is yet unknown. By utilizing the experimental data, the relationships between the biovolume and the flow regime (determined by the Reynolds number) can be developed (Figure A.1). The resulting data agrees with the previous conclusion regarding the influence of pattern spacing on biofilm development. When analyzed as a function of the inverse Reynolds number, the 50 µm and 110 µm spacing results in a straight line indicating that there was no change in the biovolume between these two spacing configurations regardless of the shear rate. For the 20 µm spacing, a decrease in the Reynolds number results in an

increase in the dimensionless biovolume suggesting that a lower Reynolds number (based on a greater velocity, wall shear rate or a reduced spacing between dots) correlates to greater biovolume of developed biofilm. Additionally, the relationship between the biovolume and the ratio of spacing to distance can also be derived (Figure A.2). The analysis shows that the 20 μm spacing dots resulted in an increased biovolume regardless of the wall shear rates compared to the 50 μm and 110 μm spacing dots.

Overall, these analyses show the usefulness of dimensional analysis for determining the relationship between several independent variables and the dependent variables that describe biofilm development. It is noted that the dimensionless Pi-groups that were derived for biovolume differ from those that will be obtained from other ISA3D parameters. Therefore, it is important to determine which parameters will be utilized for biofilm analysis in order to develop their dimensionless Pi-groups. The respective parameters may subsequently be analyzed for their relationships to the respective dimensionless independent variables.

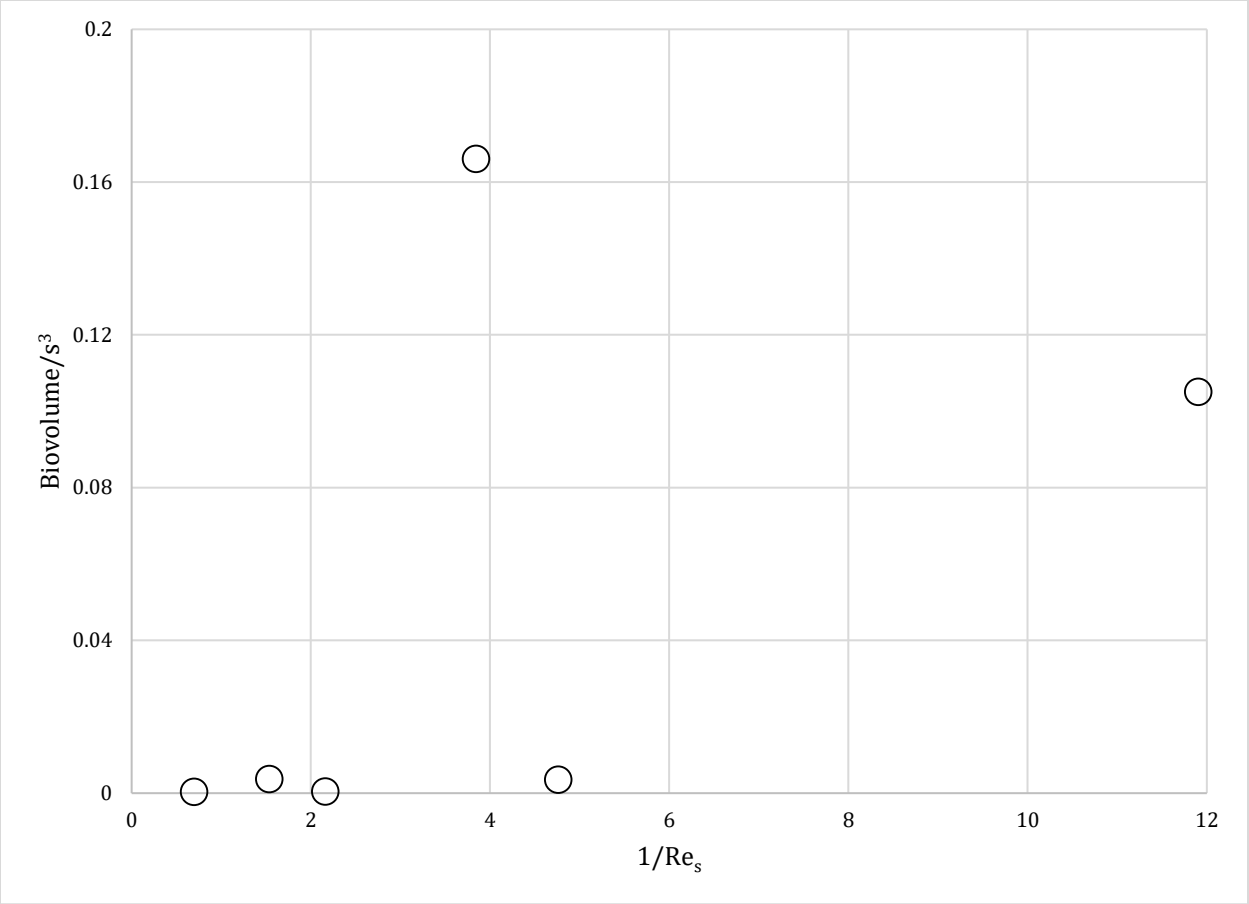

Figure A.1: Relationship between the dimensionless biovolume (biovolume/s^3) versus the Reynolds number with respect to the spacing between adjacent clusters.

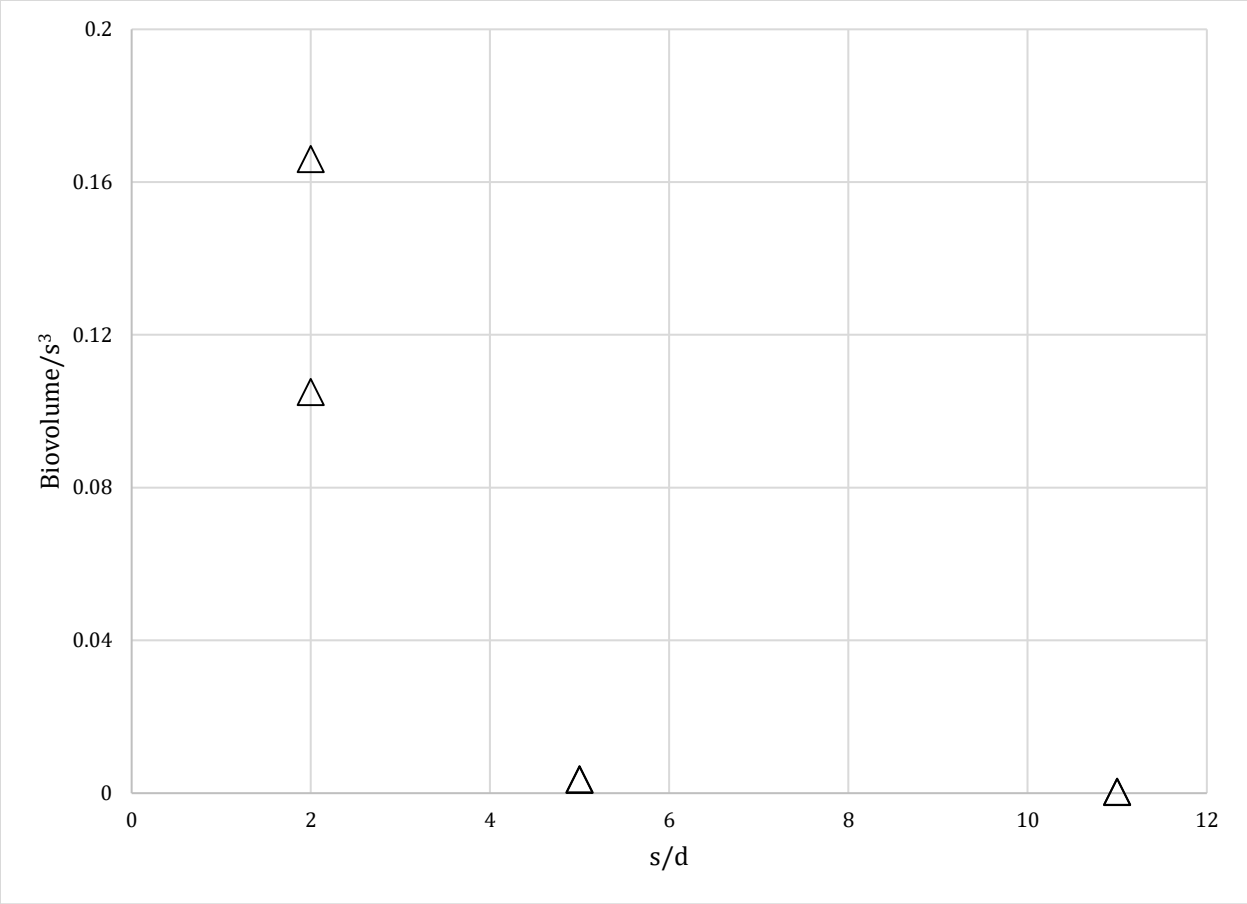

Figure A.2: Relationship between the dimensionless biovolume (biovolume/s^3) versus the dimensionless ratio of the spacing and dot diameter.

Appendix B - Quantifying autoinducer peptide concentrations by UHPLC-MS

Ultra-high-performance liquid chromatography coupled mass spectrometry (UHPLC-MS) was performed at the Molecular Characterization and Analysis Complex (MCAC) located at UMBC. Acknowledgement is given to the MCAC staff for their assistance in performing the UHPLC-MS analyses as well as conducting the method development for mass spectrometry. Samples for chromatography were collected from the effluent stream of the flow chamber experiments at hourly intervals beginning at 1 hour. At each time point, 1 mL of effluent was collected in a vial and transferred to a 3 mL piston syringe. The sample was subsequently filtered through a Millex-GP 0.22 μm sterile syringe filters with a PES membrane (EMD Millipore, Cat. No. SLGP033RS) to evacuate cells. The cell-free filtrate was stored in a glass vial at -80°C until time for analysis.

The UHPLC-MS method was adapted from previously described protocol [130]. Liquid chromatography was performed on an Altus A30 UPLC system (Perkin Elmer Inc. Shelton, CT) with an Acquity UHPLC BEH C18 column (2.1 × 50 mm, 1.7 mm packing, P/N: 186002350, S/N: 03143806625147; Waters, Milford, MA). Samples were analyzed utilizing a QSight Triple Quad LC/MS/MS (Perkin Elmer Inc.). The liquid chromatography flow rate was 0.25 mL min-1, and injection volume was 10 μL. Samples were eluted at 0.25 mL/min using the following interval: start flow with 1 % B and hold until 2 minutes at 1 % B, ramp for a duration of 5 minutes to 100 % B at 7.00 minutes and hold until 8.5 minutes at 100 % B, ramp for a duration of 0.1 minutes to 1 % B at 8.6 minutes and hold until 12 minutes at 1 % B. The mobile phase comprised solvents A: water containing 0.1 % v/v formic acid and solvent B: methanol. Mass spectrometry was conducted in multiple reaction

monitoring (MRM) scan mode. The selected ion peak of interest has a fragment mass of 961.50 and entrance voltages was 30 V. The complete parameters for the LC/MS/MS method are provided in Table A.1.

Autoinducer peptide (AIP) concentration was calculated based on a calibration curve generated as area under the curve of the relevant selected ion peak versus concentration. Serial dilutions of AIP-I (≥ 95 % purity by HPLC, MW 961.2 g mol-1; Anaspec Inc., Eurogentec Group, 69740-AIP-1, Lot 1856351) were prepared in (a) TSB media, and (b) water containing 0.1 % v/v formic acid serial dilution. The two different mobile phases were tested to determine any impact the media components had on the detection of AIP-I by UHPLC-MS. The AIP-I concentrations were calculated using the slope of the best-fit line of this calibration curve, as determined with linear regression analysis (Figure A.1 A). Additionally, the degradation of the AIP-I signal in the presence of the complex TSB media was analyzed in a time-dependent manner for samples stored cryogenically and those stored at room temperature (Figure A.1 B). The degradation study revealed that AIP degrades as a function of time in TSB media at room temperature, while samples stored cryogenically maintained AIP concentrations for longer periods.

Liquid Chromatography	
Parameter	**Value**
Injection Volume	10 µL
Mobile Phase	(A) Water + 0.1 % v/v formic acid (B) Methanol
Flow Rate	0.25 mL min^{-1}
Column	Waters Acquity UHPLC BEH, C18, 1.7 µm, 2.1 × 50 mm Part No. 186002350, Serial No. 03143806625147
Gradient	5 % B, hold until 2 minutes; ramp to 100 % B at 7 minutes, hold until 8.5 minutes; ramp to 1 % B at 8.6 minutes, hold until 12 minutes
Mass Spectrometry	
Parameter	**Value**
Scan Mode	MRM
Scan time (min)	6.4 – 8.4
HSID Temperature (°C)	250
Electrospray V1 Position	4500
Source Temperature (°C)	200
Entrance Voltage (V)	30
AIP-I Fragment mass	961.50
Dwell time (milliseconds)	295

Table B.1: UHPLC-MS method details following method development for the detection and quantitation of AIP-I in TSB media.

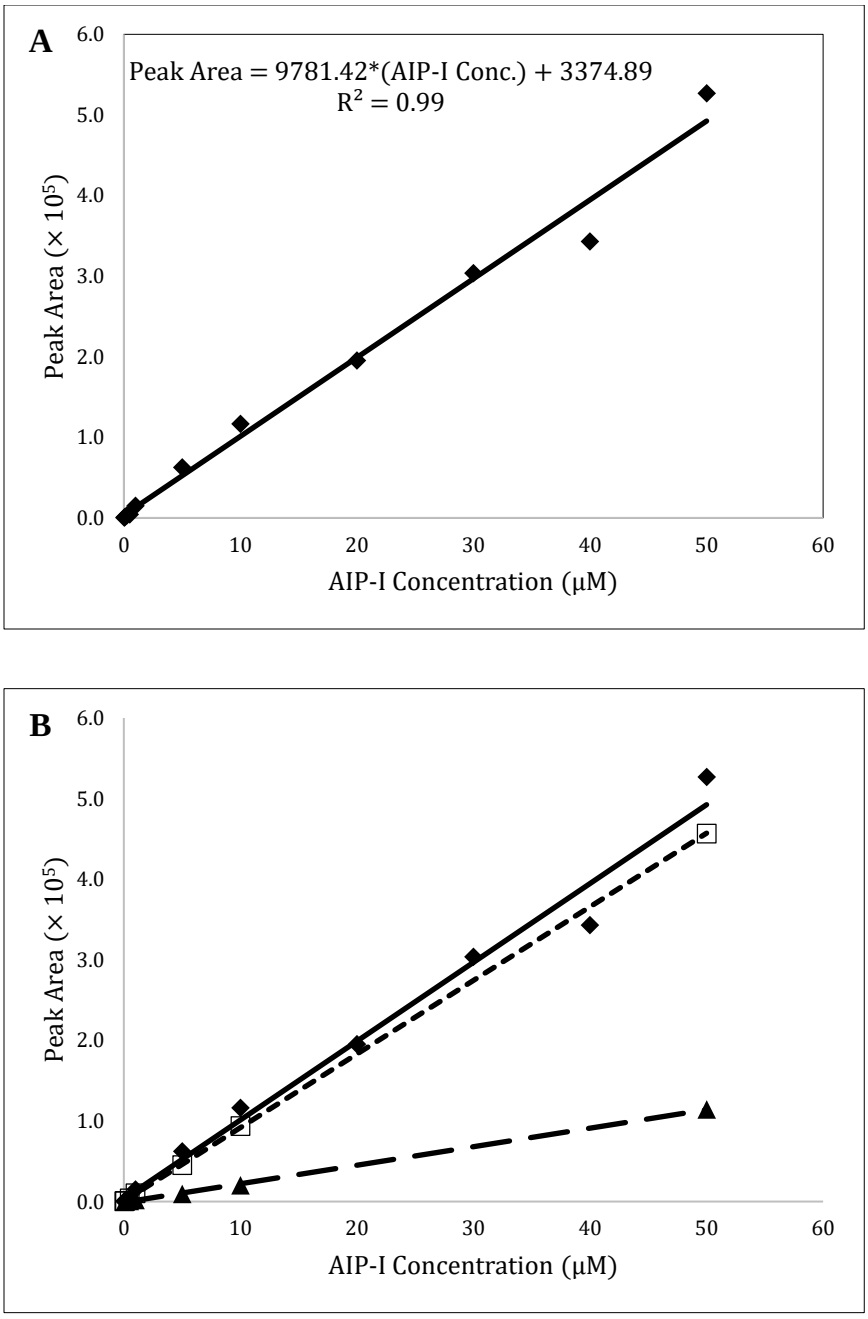

Figure B.1 (A): Standard calibration curve for autoinducer peptide I (AIP-I) in TSB media. The slope equation of the regression line was used to derive AIP-I concentration from unknown solutions. **(B):** Standard curves for AIP-I calibration (Solid), AIP-I samples in TSB media stored at room temperature for 24 hours (Short-dashed), and AIP-I samples frozen at -80°C for 10 days (Long-dashed).

Appendix C – Inhibitory effect of acetylsalicylic acid on *S. aureus* biofilm development

It was reported that complication rates due to *S. aureus* infection, as a result of heart valve surgery, was reduced in patients receiving aspirin as part of their daily regimen [11]. Studies into this phenomenon revealed that the active ingredient contained within aspirin, acetylsalicylic acid (ASA), was the primary actor in this observed effect. This chemical species has been shown to affect the development of *S. aureus* biofilm at various steps in the pathogenesis including initial adhesion [185-187], proliferation and accumulation [188-192], and dispersion [181]. To investigate the effects of aspirin in the laboratory, TSB media preparations were supplemented with concentration of ASA equivalent to low dose and regular dose aspirin regimen of 16.2 mg L^{-1} and 65 mg L^{-1} respectively. This subject matter of this preliminary study was aspirin's effect on already developed biofilm. To do this, biofilm was developed for 8 hours with regular TSB media, under flow at 100 s^{-1} from a full coverage of cells on a 4 mm × 4 mm coating of fibronectin on glass. Following the initial biofilm development for 8 hours, the feed media was switched to ASA supplemented media and the culture was resumed for an additional 4 hours. As a control, an additional 4 hours of TSB media perfusion was performed. Results show that ASA reduces the biovolume and thickness of developing biofilms (Figure B.1). This effect appears to be in form of increasing dispersion in addition to reducing growth as evident by the reduction in biomass. Additionally, the ASA effect was not affected by the dose. The preliminary exploration reveals a possibility for antibiotic-free therapeutic treatments for *S. aureus* biofilm-based in infections.

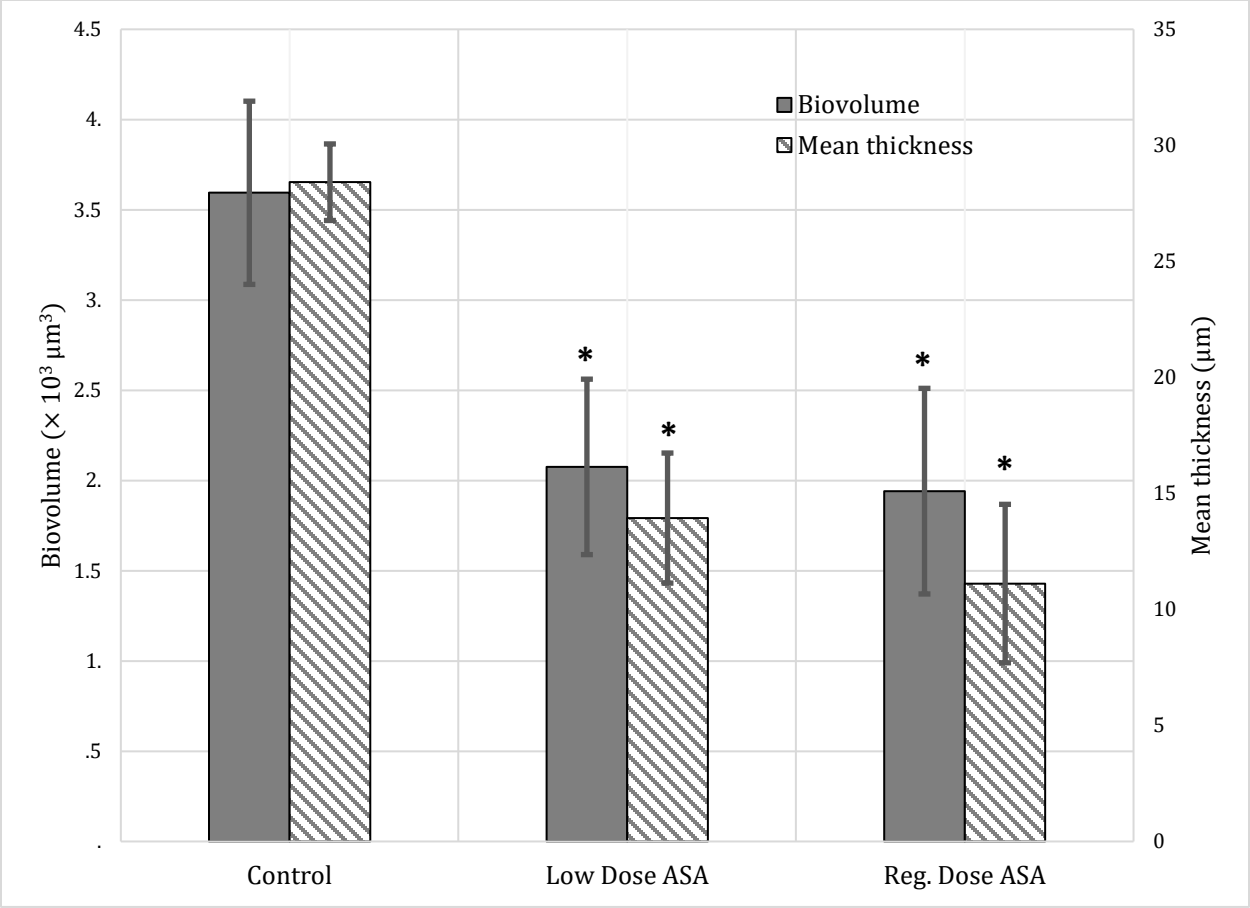

Figure C.1: Effect of acetylsalicylic acid (ASA) on biovolume and mean thickness of *S. aureus* biofilm development. Biofilm was developed for an initial time of 8 hours under flow in regular TSB media plus an additional 4 hours in media supplemented with ASA. Control represents biofilm development for an additional 4 hours in TSB media. * represents statistically significant difference ($p < 0.001$) compared to control.

BIBLIOGRAPHY

1. Acton DS, Tempelmans Plat-Sinnige MJ, Wamel W, Groot N, Belkum A: Intestinal carriage of Staphylococcus aureus: how does its frequency compare with that of nasal carriage and what is its clinical impact? In. Germany: Springer Science + Business Media; 2009: 115.
2. Archer GL: Staphylococcus aureus: A Well-Armed Pathogen. In.: University of Chicago Press; 1998: 1179.
3. Kluytmans J, Van Belkum A, Verbrugh H: Nasal Carriage of Staphylococcus aureus: Epidemiology, Underlying Mechanisms, and Associated Risks. In. United States: AMERICAN SOCIETY FOR MICROBIOLOGY; 1997: 505.
4. Peton V, Le Loir Y: Staphylococcus aureus in veterinary medicine. *Infection, Genetics and Evolution* 2014, 21:602-615.
5. Nagase N, Sasaki A, Yamashita K, Shimizu A, Wakita Y, Kitai S, Kawano J: Isolation and species distribution of staphylococci from animal and human skin. In. Japan: JAPANESE SOCIETY OF VETERINARY SCIENCE; 2002: 245.
6. Roberson JR, Fox LK, Hancock DD, Gay JM, Besser TE: Ecology of Staphylococcus aureus isolated from various sites on dairy farms. *Journal Of Dairy Science* 1994, 77(11):3354-3364.
7. Haran KP, Godden SM, Boxrud D, Jawahir S, Bender JB, Sreevatsan S: Prevalence and Characterization of Staphylococcus aureus, Including Methicillin-Resistant Staphylococcus aureus, Isolated from Bulk Tank Milk from Minnesota Dairy Farms. In. United States: AMERICAN SOCIETY FOR MICROBIOLOGY; 2012: 688.
8. Chu VH, Crosslin DR, Friedman JY, Reed SD, Cabell CH, Griffiths RI, Masselink LE, Kaye KS, Corey GR, Reller LB *et al*: Clinical research study: Staphylococcus aureus bacteremia in patients with prosthetic devices: Costs and outcomes. *The American Journal of Medicine* 2005, 118:1416.e1419-1416.e1424.

9. Archer NK, Mazaitis MJ, Costerton JW, Leid JG, Powers ME, Shirtliff ME: Staphylococcus aureus biofilms: properties, regulation, and roles in human disease. *Virulence* 2011, 2(5):445-459.

10. Bartlett AH, Hulten KG: Staphylococcus aureus pathogenesis: secretion systems, adhesins, and invasins. *The Pediatric Infectious Disease Journal* 2010, 29(9):860-861.

11. Damon PE, Corey GR, Emma SM, Vance GF, Jr., Jose MM, Chris HC, Alan CS, Marcelo Goulart P, Adina I, Ru-San T *et al*: Reduced valve replacement surgery and complication rate in Staphylococcus aureus endocarditis patients receiving acetyl-salicylic acid. *Journal of Infection*, 58:332-338.

12. Wang A: Recent Progress in the Understanding of Infective Endocarditis. *Current Treatment Options in Cardiovascular Medicine* 2011, 13(6):586.

13. Fong IW: New Perspectives of Infections in Cardiovascular Disease. *Current Cardiology Reviews* 2009, 5(2):87-104.

14. Tobis JM, Abudayyeh I: Review: New devices and technology in interventional cardiology. *Journal of Cardiology* 2015, 65:5-16.

15. Wilson W, Taubert KA, Gewitz M, Lockhart PB, Baddour LM, Levison M, Bolger A, Cabell CH, Takahashi M, Baltimore RS *et al*: Prevention of infective endocarditis: guidelines from the American Heart Association: a guideline from the American Heart Association Rheumatic Fever, Endocarditis, and Kawasaki Disease Committee, Council on Cardiovascular Disease in the Young, and the Council on Clinical Cardiology, Council on Cardiovascular Surgery and Anesthesia, and the Quality of Care and Outcomes Research Interdisciplinary Working Group. *Circulation* 2007, 116(15):1736-1754.

16. Jung CJ, Yeh CY, Shun CT, Hsu RB, Cheng HW, Lin CS, Chia JS: Platelets enhance biofilm formation and resistance of endocarditis-inducing streptococci on the injured heart valve. *Journal of Infectious Diseases* 2012, 205(7):1066-1075.

17. Hoerr V, Franz M, Pletz MW, Diab M, Niemann S, Faber C, Doenst T, Schulze PC, Deinhardt-Emmer S, Löffler B: S. aureus endocarditis: Clinical aspects and experimental approaches. *International Journal of Medical Microbiology* 2018.

18. Chambers HF, DeLeo FR: Waves of resistance: Staphylococcus aureus in the antibiotic era. *Nature Reviews Microbiology* 2009, 7(9):629-641.

19. Kyaw MH, Kern DM, Zhou S, Tunceli O, Jafri HS, Falloon J: Healthcare utilization and costs associated with S. aureus and P. aeruginosa pneumonia in the intensive care unit: a retrospective observational cohort study in a US claims database. *BMC Health Services Research* 2015, 15:241-241.

20. Speziale P, Pietrocola G, Rindi S, Provenzano M, Provenza G, Di Poto A, Visai L, Arciola CR: Structural and functional role of Staphylococcus aureus surface components recognizing adhesive matrix molecules of the host. *Future Microbiol* 2009, 4(10):1337-1352.

21. Bhattacharyya D, Banerjee J, Bandyopadhyay S, Mondal B, Nanda PK, Samanta I, Mahanti A, Das AK, Das G, Dandapat P *et al*: First Report on Vancomycin-Resistant Staphylococcus aureus in Bovine and Caprine Milk. *Microbial Drug Resistance (Larchmont, NY)* 2016, 22(8):675-681.

22. Hiramatsu K: Vancomycin-resistant Staphylococcus aureus: a new model of antibiotic resistance. *The Lancet Infectious Diseases* 2001, 1(3):147-155.

23. Römling U, Balsalobre C: Biofilm infections, their resilience to therapy and innovative treatment strategies. *Journal Of Internal Medicine* 2012, 272(6):541-561.

24. Styers D, Sheehan DJ, Hogan P, Sahm DF: Laboratory-based surveillance of current antimicrobial resistance patterns and trends among Staphylococcus aureus: 2005 status in the United States. *Annals Of Clinical Microbiology And Antimicrobials* 2006, 5:2-2.

25. Mascari L, Ross JM: Hydrodynamic shear and collagen receptor density determine the adhesion capacity of S. aureus to collagen. *Annals Of Biomedical Engineering* 2001, 29(11):956-962.

26. Patti JM, Bremell T, Krajewska-Pietrasik D, Abdelnour A, Tarkowski A, Rydén C, Höök M: The Staphylococcus aureus collagen adhesin is a virulence determinant in experimental septic arthritis. *Infection And Immunity* 1994, 62(1):152-161.

27. McGavin MH, Krajewska-Pietrasik D, Rydén C, Höök M: Identification of a Staphylococcus aureus extracellular matrix-binding protein with broad specificity. *Infection And Immunity* 1993, 61(6):2479-2485.

28. Palma M, Haggar A, Flock JI: Adherence of Staphylococcus aureus Is Enhanced by an Endogenous Secreted Protein with Broad Binding Activity. In. United States: AMERICAN SOCIETY FOR MICROBIOLOGY; 1999: 2840.

29. Arciola CR, Campoccia D, Speziale P, Montanaro L, Costerton JW: Biofilm formation in Staphylococcus implant infections. A review of molecular mechanisms and implications for biofilm-resistant materials. *Biomaterials* 2012, 33(26):5967-5982.

30. Williams DL, Sinclair KD, Jeyapalina S, Bloebaum RD: Characterization of a novel active release coating to prevent biofilm implant-related infections. *Journal Of Biomedical Materials Research Part B, Applied Biomaterials* 2013.

31. Deep A, Chaudhary U, Gupta V: Quorum sensing and Bacterial Pathogenicity: From Molecules to Disease. *Journal of Laboratory Physicians* 2011, 3(1):4-11.

32. Atkinson S, Williams P: Quorum sensing and social networking in the microbial world. *Journal Of The Royal Society, Interface / The Royal Society* 2009, 6(40):959-978.

33. Platt TG, Fuqua C: Opinion: What's in a name? The semantics of quorum sensing. *Trends in Microbiology* 2010, 18:383-387.

34. Yarwood JM, Bartels DJ, Volper EM, Greenberg EP: Quorum sensing in Staphylococcus aureus biofilms. *Journal Of Bacteriology* 2004, 186(6):1838-1850.

35. Hense BA, Kuttler C, Müller J, Rothballer M, Hartmann A, Kreft J-U: Does efficiency sensing unify diffusion and quorum sensing? *Nature Reviews Microbiology* 2007, 5(3):230-239.

36. West SA, Winzer K, Gardner A, Diggle SP: Review: Quorum sensing and the confusion about diffusion. *Trends in Microbiology* 2012, 20:586-594.

37. Carnes EC, Lopez DM, Donegan NP, Cheung A, Gresham H, Timmins GS, Brinker CJ: Confinement-induced quorum sensing of individual Staphylococcus aureus bacteria. *Nature Chemical Biology* 2010, 6(1):41-45.

38. Boedicker JQ, Vincent ME, Ismagilov RF: Microfluidic Confinement of Single Cells of Bacteria in Small Volumes Initiates High-Density Behavior of Quorum Sensing and Growth and Reveals Its Variability. *Angewandte Chemie* 2009.

39. Gu H, Hou S, Yongyat C, De Tore S, Ren D: Patterned biofilm formation reveals a mechanism for structural heterogeneity in bacterial biofilms. *Langmuir: The ACS Journal Of Surfaces And Colloids* 2013, 29(35):11145-11153.

40. Hou S, Gu H, Smith C, Ren D: Microtopographic Patterns Affect Escherichia coli Biofilm Formation on Poly(dimethylsiloxane) Surfaces. *LANGMUIR* 2011, 27(6):2686-2691.

41. Chung KK, Schumacher JF, Sampson EM, Burne RA, Antonelli PJ, Brennan AB: Impact of engineered surface microtopography on biofilm formation of Staphylococcus aureus. *Biointerphases* 2007, 2(2):89-94.

42. Donlan RM: Biofilms: microbial life on surfaces. *Emerging Infectious Diseases* 2002, 8(9):881-890.

43. Jefferson KK: What drives bacteria to produce a biofilm? In. Netherlands: Elsevier Science B.V., Amsterdam.; 2004: 163.

44. Schuster JJ, Markx GH: Biofilm architecture. *Adv Biochem Eng Biotechnol* 2014, 146:77-96.

45. López D, Vlamakis H, Kolter R: Biofilms. *Cold Spring Harb Perspect Biol* 2010, 2(7):a000398.

46. Parsek MR, Fuqua C: Biofilms 2003: emerging themes and challenges in studies of surface-associated microbial life. *J Bacteriol* 2004, 186(14):4427-4440.

47. Boudarel H, Mathias JD, Blaysat B, Grédiac M: Towards standardized mechanical characterization of microbial biofilms: analysis and critical review. *NPJ Biofilms Microbiomes* 2018, 4:17.

48. Beyenal H, Lewandowski Z, Harkin G: Quantifying biofilm structure: facts and fiction. *Biofouling* 2004, 20(1):1-23.

49. Houry A, Gohar M, Deschamps J, Tischenko E, Aymerich S, Gruss A, Briandet R: Bacterial swimmers that infiltrate and take over the biofilm matrix. *Proceedings of the National Academy of Sciences of the United States of America* 2012, 109(32):13088-13093.

50. Hall-Stoodley L, Stoodley P: Developmental regulation of microbial biofilms. *Current Opinion In Biotechnology* 2002, 13(3):228-233.

51. Ymele-Leki P, Ross JM: Erosion from Staphylococcus aureus Biofilms Grown under Physiologically Relevant Fluid Shear Forces Yields Bacterial Cells with Reduced Avidity to Collagen. *Applied & Environmental Microbiology* 2007, 73(6):1834-1841.

52. Fey PD, Olson ME: Current concepts in biofilm formation of Staphylococcus epidermidis. *Future Microbiology* 2010, 5(6):917-933.

53. Götz F: Staphylococcus and biofilms. *Mol Microbiol* 2002, 43(6):1367-1378.

54. Bhattacharya M, Wozniak DJ, Stoodley P, Hall-Stoodley L: Prevention and treatment of Staphylococcus aureus biofilms. *Expert Rev Anti Infect Ther* 2015, 13(12):1499-1516.

55. Lindsay D, von Holy A: Bacterial biofilms within the clinical setting: what healthcare professionals should know. *J Hosp Infect* 2006, 64(4):313-325.

56. van Loosdrecht MC, Lyklema J, Norde W, Zehnder AJ: Influence of interfaces on microbial activity. *Microbiol Rev* 1990, 54(1):75-87.

57. George NPE, Ymele-Leki P, Konstantopoulos K, Ross JM: Differential binding of biofilm-derived and suspension-grown Staphylococcus aureus to immobilized platelets in shear flow. *The Journal Of Infectious Diseases* 2009, 199(5):633-640.

58. George NPE, Konstantopoulos K, Ross JM: Differential kinetics and molecular recognition mechanisms involved in early versus late growth phase Staphylococcus aureus cell binding to platelet layers under physiological shear conditions. *The Journal Of Infectious Diseases* 2007, 196(4):639-646.

59. Mohamed N, Teeters MA, Patti JM, Höök M, Ross JM: Inhibition of Staphylococcus aureus adherence to collagen under dynamic conditions. *Infection And Immunity* 1999, 67(2):589-594.

60. Mohamed N, Rainier Tr, Ross JM: Novel experimental study of receptor-mediated bacterial adhesion under the influence of fluid shear. *Biotechnology and Bioengineering* 2001(6):628.

61. Mascari LM, Ross JM: Quantification of Staphylococcal-Collagen Binding Interactions in Whole Blood by Use of a Confocal Microscopy Shear-Adhesion Assay. *Journal of Infectious Diseases* 2003, 188(1):98.

62. Li ZJ, Mohamed N, Ross JM: Shear stress affects the kinetics of Staphylococcus aureus adhesion to collagen. *Biotechnology Progress* 2000, 16(6):1086-1090.

63. George NPE, Wei Q, Shin PK, Konstantopoulos K, Ross JM: Staphylococcus aureus adhesion via Spa, ClfA, and SdrCDE to immobilized platelets demonstrates shear-dependent behavior. *Arteriosclerosis, Thrombosis, And Vascular Biology* 2006, 26(10):2394-2400.

64. Ymele-Leki P: Quantitative analysis of the accumulation, architectural organization, detachment and reseeding of Staphylococcus aureus biofilms under physiological fluid shear conditions. *Thesis (Ph D).* University of Maryland, Baltimore County, 2009.; 2009.

65. Singh RP, Desouky SE, Nakayama J: Quorum Quenching Strategy Targeting Gram-Positive Pathogenic Bacteria. *Advances In Experimental Medicine And Biology* 2016, 901:109-130.

66. QAZI SNA, COUNIL E, MORRISSEY J, REES CED, COCKAYNE A, WINZER K, CHAN WC, WILLIAMS P, HILL PJ: agr-expression precedes escape of internalized Staphylococcus aureus fom the host endosome. In.: 2001.; 2009.

67. Boles BR, Horswill AR: agr-Mediated Dispersal of Staphylococcus aureus Biofilms. *PLoS Pathogens* 2008, 4(4):1-13.

68. Thoendel M, Horswill AR: Identification of Staphylococcus aureus AgrD residues required for autoinducing peptide biosynthesis. *The Journal Of Biological Chemistry* 2009, 284(33):21828-21838.

69. Lauderdale KJ, Boles BR, Cheung AL, Horswill AR: Interconnections between Sigma B, agr, and proteolytic activity in Staphylococcus aureus biofilm maturation. *Infection And Immunity* 2009, 77(4):1623-1635.

70. agr-expression precedes escape of internalized Staphylococcus aureus fom the host endosome. In.: 2001.; 2009.

71. Yarwood JM, Schlievert PM: Quorum sensing in Staphylococcus infections. *J Clin Invest* 2003, 112(11):1620-1625.

72. Kong KF, Vuong C, Otto M: Staphylococcus quorum sensing in biofilm formation and infection. *Int J Med Microbiol* 2006, 296(2-3):133-139.

73. MDowell P, Affas Z, Reynolds C, Holden MT, Wood SJ, Saint S, Cockayne A, Hill PJ, Dodd CE, Bycroft BW *et al*: Structure, activity and evolution of the group I thiolactone peptide quorum-sensing system of Staphylococcus aureus. *Mol Microbiol* 2001, 41(2):503-512.

74. Malone CL, Boles BR, Horswill AR: Biosynthesis of Staphylococcus aureus autoinducing peptides by using the synechocystis DnaB mini-intein. *Applied And Environmental Microbiology* 2007, 73(19):6036-6044.

75. Tan L, Li SR, Jiang B, Hu XM, Li S: Therapeutic Targeting of the *Staphylococcus aureus* Accessory Gene Regulator (agr) System. *Frontiers in Microbiology* 2018, 9:55.

76. Kavanaugh JS, Thoendel M, Horswill AR: A role for type I signal peptidase in Staphylococcus aureus quorum sensing. In. Great Britain: Blackwell Publishing Ltd; 2007: 780.

77. Wang B, Zhao A, Novick RP, Muir TW: Key driving forces in the biosynthesis of autoinducing peptides required for staphylococcal virulence. *Proc Natl Acad Sci U S A* 2015, 112(34):10679-10684.

78. Goerke C, Campana S, Bayer MG, Döring G, Botzenhart K, Wolz C: Direct quantitative transcript analysis of the agr regulon of Staphylococcus aureus during human infection in comparison to the expression profile in vitro. *Infect Immun* 2000, 68(3):1304-1311.

79. Goerke C, Fluckiger U, Steinhuber A, Zimmerli W, Wolz C: Impact of the regulatory loci agr, sarA and sae of Staphylococcus aureus on the induction of alpha-toxin during device-related infection resolved by direct quantitative transcript analysis. *Mol Microbiol* 2001, 40(6):1439-1447.

80. Yarwood JM, McCormick JK, Paustian ML, Kapur V, Schlievert PM: Repression of the Staphylococcus aureus accessory gene regulator in serum and in vivo. *J Bacteriol* 2002, 184(4):1095-1101.

81. Lister JL, Horswill AR: Staphylococcus aureus biofilms: recent developments in biofilm dispersal. *Frontiers In Cellular And Infection Microbiology* 2014, 4:178-178.

82. Gov Y, Bitler A, Dell'Acqua G, Torres JV, Balaban N: RNAIII inhibiting peptide (RIP), a global inhibitor of Staphylococcus aureus pathogenesis: structure and function analysis. *Peptides* 2001, 22(10):1609-1620.

83. Salam AM, Quave CL: Targeting Virulence in Staphylococcus aureus by Chemical Inhibition of the AGR system In vivo. *mSphere* 2018, 3(1).

84. Redfield RJ: Is quorum sensing a side effect of diffusion sensing? *Trends in Microbiology* 2002, 10(8):365.

85. Davies DG, Parsek MR, Pearson JP, Iglewski BH, Costerton JW, Greenberg EP: The involvement of cell-to-cell signals in the development of a bacterial biofilm. *Science* 1998, 280(5361):295-298.

86. Brackman G, Breyne K, De Rycke R, Vermote A, Van Nieuwerburgh F, Meyer E, Van Calenbergh S, Coenye T: The Quorum Sensing Inhibitor Hamamelitannin Increases Antibiotic

Susceptibility of Staphylococcus aureus Biofilms by Affecting Peptidoglycan Biosynthesis and eDNA Release. *Sci Rep* 2016, 6:20321.

87. Kiran MD, Adikesavan NV, Cirioni O, Giacometti A, Silvestri C, Scalise G, Ghiselli R, Saba V, Orlando F, Shoham M *et al*: Discovery of a quorum-sensing inhibitor of drug-resistant staphylococcal infections by structure-based virtual screening. *Mol Pharmacol* 2008, 73(5):1578-1586.

88. Vermote A, Brackman G, Risseeuw MD, Vanhoutte B, Cos P, Van Hecke K, Breyne K, Meyer E, Coenye T, Van Calenbergh S: Hamamelitannin Analogues that Modulate Quorum Sensing as Potentiators of Antibiotics against Staphylococcus aureus. *Angew Chem Int Ed Engl* 2016, 55(22):6551-6555.

89. Weibel DB, DiLuzio WR, Whitesides GM: Microfabrication meets microbiology. *Nature Reviews Microbiology* 2007, 5(3):209-218.

90. Whitesides GM, Ostuni E, Takayama S, Jiang X, Ingber DE: SOFT LITHOGRAPHY IN BIOLOGY AND BIOCHEMISTRY. *Annual Review of Biomedical Engineering* 2001, 3(1):335.

91. Gates BD, Qiaobing X, Love JC, Wolfe DB, Whitesides GM: UNCONVENTIONAL NANOFABRICATION. *Annual Review of Materials Research* 2004, 34(1):339-372.

92. Chee M, Yang R, Hubbell E, Berno A, Huang XC, Stern D, Winkler J, Lockhart DJ, Morris MS, Fodor SP: Accessing genetic information with high-density DNA arrays. *Science* 1996, 274(5287):610-614.

93. Lockhart DJ, Dong H, Byrne MC, Follettie MT, Gallo MV, Chee MS, Mittmann M, Wang C, Kobayashi M, Horton H *et al*: Expression monitoring by hybridization to high-density oligonucleotide arrays. *Nat Biotechnol* 1996, 14(13):1675-1680.

94. Fodor SP, Rava RP, Huang XC, Pease AC, Holmes CP, Adams CL: Multiplexed biochemical assays with biological chips. *Nature* 1993, 364(6437):555-556.

95. Schena M, Shalon D, Davis RW, Brown PO: Quantitative monitoring of gene expression patterns with a complementary DNA microarray. *Science* 1995, 270(5235):467-470.

96. Song F, Ren D: Stiffness of Cross-Linked Poly(Dimethylsiloxane) Affects Bacterial Adhesion and Antibiotic Susceptibility of Attached Cells. In. United States: ACS AMERICAN CHEMICAL SOCIETY; 2014: 10354.

97. Hou S, Burton E, Wu R, Luk YY, Ren D: Prolonged control of patterned biofilm formation by bio-inert surface chemistry. In. Great Britain: Royal Society of Chemistry; 2009: 1207.

98. Hongwei M, Jinho H, Zhanping Z, Beebe TP, Jr., Chilkoti A: Fabrication of biofunctionalized quasi-three-dimensional microstructures of a nonfouling comb polymer using soft lithography. *Advanced Functional Materials* 2005, 15(4):529-540.

99. Singh AV, Vyas V, Patil R, Sharma V, Scopelliti PE, Bongiorno G, Podestà A, Lenardi C, Gade WN, Milani P: Quantitative Characterization of the Influence of the Nanoscale Morphology of Nanostructured Surfaces on Bacterial Adhesion and Biofilm Formation. *PLoS ONE* 2011, 6(9):1-12.

100. Desai RA, Rodriguez NM, Chen CS: "Stamp-off" to micropattern sparse, multicomponent features. *Methods In Cell Biology* 2014, 119:3-16.

101. Kim HJ, Boedicker JQ, Choi JW, Ismagilov RF: Defined Spatial Structure Stabilizes a Synthetic Multispecies Bacterial Community. In.: National Academy of Sciences; 2008: 18188.

102. Schumacher JF, Aldred N, Callow ME, Finlay JA, Callow JA, Clare AS, Brennan AB: Species-specific engineered antifouling topographies: correlations between the settlement of algal zoospores and barnacle cyprids. *Biofouling* 2007, 23(5-6):307-317.

103. Carman ML, Estes TG, Feinberg AW, Schumacher JF, Wilkerson W, Wilson LH, Callow ME, Callow JA, Brennan AB: Engineered antifouling microtopographies--correlating wettability with cell attachment. *Biofouling* 2006, 22(1-2):11-21.

104. Mann EE, Manna D, Mettetal MR, May RM, Dannemiller EM, Chung KK, Brennan AB, Reddy ST: Surface micropattern limits bacterial contamination. *Antimicrob Resist Infect Control* 2014, 3:28.

105. Reddy S, Chung K, McDaniel C, Darouiche R, Landman J, Brennan A: Micropatterned Surfaces for Reducing the Risk of Catheter-Associated Urinary Tract Infection: An In Vitro Study on the Effect of Sharklet Micropatterned Surfaces to Inhibit Bacterial Colonization and Migration of Uropathogenic Escherichia coli. In. United States: Mary Ann Liebert, Inc.; 2011: 1547.

106. Xu B, Wei Q, Mettetal MR, Han J, Rau L, Tie J, May RM, Pathe ET, Reddy ST, Sullivan L *et al*: Surface micropattern reduces colonization and medical device-associated infections. *J Med Microbiol* 2017, 66(11):1692-1698.

107. Song F, Ren D: Stiffness of cross-linked poly(dimethylsiloxane) affects bacterial adhesion and antibiotic susceptibility of attached cells. *Langmuir: The ACS Journal Of Surfaces And Colloids* 2014, 30(34):10354-10362.

108. Qin D, Xia Y, Whitesides GM: Soft lithography for micro- and nanoscale patterning. *Nature Protocols* 2010, 5(3):491-502.

109. Desai RA, Khan MK, Gopal SB, Chen CS: Subcellular spatial segregation of integrin subtypes by patterned multicomponent surfaces. *Integrative Biology* 2011, 3(5):560-567.

110. Yang X, Beyenal H, Harkin G, Lewandowski Z: Quantifying biofilm structure using image analysis. *Journal Of Microbiological Methods* 2000, 39(2):109-119.

111. Beyenal H, Donovan C, Lewandowski Z, Harkin G: Three-dimensional biofilm structure quantification. *Journal of Microbiological Methods* 2004, 59:395-413.

112. Lewandowski Z: Notes on biofilm porosity. *Water Research* 2000, 34(9):2620-2624.

113. Yang X, Beyenal H, Harkin G, Lewandowski Z: Evaluation of biofilm image thresholding methods. *Water Res* 2001, 35(5):1149-1158.

114. Kuehn M, Hausner M, Bungartz HJ, Wagner M, Wilderer PA, Wuertz S: Automated confocal laser scanning microscopy and semiautomated image processing for analysis of biofilms. *Appl Environ Microbiol* 1998, 64(11):4115-4127.

115. Heydorn A, Nielsen AT: Quantification of biofilm structures by the novel computer program COMSTAT. *Microbiology (13500872)* 2000, 146(10):2395.

116. Xavier JB, White DC, Almeida JS: Automated biofilm morphology quantification from confocal laser scanning microscopy imaging. *Water Sci Technol* 2003, 47(5):31-37.

117. Zielinski J, Zielinska A, Bouaynaya N: Three-Dimensional Morphology Quantification of Biofilm Structures from Confocal Laser Scanning Microscopy Images; 2018.

118. Lewandowski Z, Beyenal H: Biofilm monitoring: a perfect solution in search of a problem. *Water Sci Technol* 2003, 47(5):9-18.

119. Malone CL, Boles BR, Lauderdale KJ, Thoendel M, Kavanaugh JS, Horswill AR: Fluorescent reporters for Staphylococcus aureus. *Journal of Microbiological Methods* 2009, 77:251-260.

120. Horsburgh MJ, Aish JL, White IJ, Shaw L, Lithgow JK, Foster SJ: sigmaB modulates virulence determinant expression and stress resistance: characterization of a functional rsbU strain derived from Staphylococcus aureus 8325-4. *Journal Of Bacteriology* 2002, 184(19):5457-5467.

121. Arciola CR, Campoccia D, Borrelli AM, Donati ME, Montanaro L: Congo red agar plate method: improved accuracy and new extended application to Staphylococcus aureus. In. Italy: LUIGI PONZIO E FIGLIO EDITORI; 2001: 355.

122. Kaiser TDL, Pereira EM, dos Santos KRN, Maciel ELN, Schuenck RP, Nunes APF: Bacteriology: Modification of the Congo red agar method to detect biofilm production by Staphylococcus epidermidis. *Diagnostic Microbiology & Infectious Disease* 2013, 75:235-239.

123. del Campo A, Greiner C: SU-8: a photoresist for high-aspect-ratio and 3D submicron lithography. *JOURNAL OF MICROMECHANICS AND MICROENGINEERING* 2007, 17(6):R81-R95.

124. Jenkins G: Rapid prototyping of PDMS devices using SU-8 lithography. *Methods Mol Biol* 2013, 949:153-168.

125. Papaioannou TG, Stefanadis C: Vascular wall shear stress: basic principles and methods. *Hellenic J Cardiol* 2005, 46(1):9-15.

126. Lichstein HC, Soule MH: Studies of the Effect of Sodium Azide on Microbic Growth and Respiration: I. The Action of Sodium Azide on Microbic Growth. *J Bacteriol* 1944, 47(3):221-230.

127. Houda S, Belarbi R, Zemmouri N: A CFD Comsol model for simulating complex urban flow. *Energy Procedia* 2017, 139:373-378.

128. Pontes PC, Chen K, Naveira-Cotta CP, Costa Junior JM, Tostado CP, Quaresma JNN: Mass transfer simulation of biodiesel synthesis in microreactors. *Computers & Chemical Engineering* 2016, 93:36-51.

129. Dickinson EJF, Ekström H, Fontes E: Mini review: COMSOL Multiphysics®: Finite element software for electrochemical analysis. A mini-review. *Electrochemistry Communications* 2014, 40:71-74.

130. Junio HA, Todd DA, Ettefagh KA, Ehrmann BM, Kavanaugh JS, Horswill AR, Cech NB: Quantitative analysis of autoinducing peptide I (AIP-I) from Staphylococcus aureus cultures using ultrahigh performance liquid chromatography-high resolving power mass spectrometry. *J Chromatogr B Analyt Technol Biomed Life Sci* 2013, 930:7-12.

131. Hense BA, Müller J, Kuttler C, Hartmann A: Spatial heterogeneity of autoinducer regulation systems. *Sensors (Basel)* 2012, 12(4):4156-4171.

132. Goldsmith HL, Turitto VT: Rheological aspects of thrombosis and haemostasis: basic principles and applications. ICTH-Report--Subcommittee on Rheology of the International Committee on Thrombosis and Haemostasis. *Thromb Haemost* 1986, 55(3):415-435.

133. Anderson EJ, Knothe Tate ML: Open access to novel dual flow chamber technology for in vitro cell mechanotransduction, toxicity and pharamacokinetic studies. *Biomed Eng Online* 2007, 6:46.

134. Verotta D, Haagensen J, Spormann AM, Yang K: Mathematical Modeling of Biofilm Structures Using COMSTAT Data. *Comput Math Methods Med* 2017, 2017:7246286.

135. Fisher HP: Mathematical Modeling of Complex Biological Systems. *Alcohol Research & Health* 2008, 31(1):49-59.

136. Mogilner A, Wollman R, Marshall WF: Quantitative modeling in cell biology: what is it good for? *Dev Cell* 2006, 11(3):279-287.

137. Matsumoto T, Tanaka T, Kondo A: Engineering metabolic pathways in Escherichia coli for constructing a "microbial chassis" for biochemical production. *Bioresource Technology* 2017, 245(Pt B):1362-1368.

138. Picioreanu C, Xavier JB, van Loosdrecht MCM: Advances in mathematical modeling of biofilm structure. In. Great Britain: CAMBRIDGE UNIVERSITY PRESS; 2004: 337.

139. Kissel JC, McCarty PL, Street RL: Numerical Simulation of Mixed-Culture Biofilm. *Journal of Environmental Engineering* 1984, 110(2):393.

140. Benefield L, Molz F: Mathematical simulation of a biofilm process. *Biotechnology & Bioengineering* 1985, 27(7):921.

141. Horn H, Lackner S: Modeling of biofilm systems: a review. *Adv Biochem Eng Biotechnol* 2014, 146:53-76.

142. Rittman BE: The effect of shear stress on biofilm loss rate. *Biotechnology And Bioengineering* 1982, 24(2):501-506.

143. Peyton BM, Characklis WG: A statistical analysis of the effect of substrate utilization and shear stress on the kinetics of biofilm detachment. *Biotechnology And Bioengineering* 1993, 41(7):728-735.

144. Peyton BM, Characklis WG: Kinetics of biofilm detachment. In*: 1992 1992; Great Britain*. PERGAMON PRESS: 1995.

145. Chang I, Gilbert ES, Eliashberg N, Keasling JD: A three-dimensional, stochastic simulation of biofilm growth and transport-related factors that affect structure. In. Great Britain: SOCIETY FOR GENERAL MICROBIOLOGY; 2003: 2859.

146. Wang Q, Zhang T: Review of mathematical models for biofilms. *Solid State Communications* 2010, 150:1009-1022.

147. Jabbari S, King JR, Koerber AJ, Williams P: Mathematical modelling of the agr operon in Staphylococcus aureus. In. Austria: Springer Science + Business Media; 2010: 17.

148. Koerber AJ, King JR, Williams P: Deterministic and stochastic modelling of endosome escape by Staphylococcus aureus: "quorum" sensing by a single bacterium. *Journal Of Mathematical Biology* 2005, 50(4):440-488.

149. Gustafsson E, Nilsson P, Karlsson S, Arvidson S: Characterizing the Dynamics of the Quorum-Sensing System in Staphylococcus aureus. In. Great Britain: HORIZON SCIENTIFIC PRESS; 2004: 232.

150. Bird RB, Stewart WE, Lightfoot EN: Transport phenomena: New York : J. Wiley, c2007.

Rev. 2nd ed.; 2007.

151. Costerton JW, Lewandowski Z, Caldwell DE, Korber DR, Lappin-Scott HM: Microbial biofilms. *Annu Rev Microbiol* 1995, 49:711-745.

152. Costerton JW: Overview of microbial biofilms. *J Ind Microbiol* 1995, 15(3):137-140.

153. Keller L, Surette MG: Communication in bacteria: an ecological and evolutionary perspective. *Nat Rev Microbiol* 2006, 4(4):249-258.

154. Chung PY, Toh YS: Anti-biofilm agents: recent breakthrough against multi-drug resistant Staphylococcus aureus. *Pathog Dis* 2014, 70(3):231-239.

155. Zhou Y, Zhao R, Ma B, Gao H, Xue X, Qu D, Li M, Meng J, Luo X, Hou Z: Oligomerization of RNAIII-Inhibiting Peptide Inhibits Adherence and Biofilm Formation of Methicillin-Resistant Staphylococcus aureus In Vitro and In Vivo. *Microb Drug Resist* 2016, 22(3):193-201.

156. Otto M, Echner H, Voelter W, Götz F: Pheromone cross-inhibition between Staphylococcus aureus and Staphylococcus epidermidis. *Infect Immun* 2001, 69(3):1957-1960.

157. Tal-Gan Y, Ivancic M, Cornilescu G, Blackwell HE: Characterization of structural elements in native autoinducing peptides and non-native analogues that permit the differential modulation of AgrC-type quorum sensing receptors in Staphylococcus aureus. *Org Biomol Chem* 2016, 14(1):113-121.

158. Wang B, Muir TW: Regulation of Virulence in Staphylococcus aureus: Molecular Mechanisms and Remaining Puzzles. *Cell Chem Biol* 2016, 23(2):214-224.

159. Zhang Y, Wang JF, Dong J, Wei JY, Wang YN, Dai XH, Wang X, Luo MJ, Tan W, Deng XM *et al*: Inhibition of α-toxin production by subinhibitory concentrations of naringenin controls Staphylococcus aureus pneumonia. *Fitoterapia* 2013, 86:92-99.

160. Leonard PG, Bezar IF, Sidote DJ, Stock AM: Identification of a hydrophobic cleft in the LytTR domain of AgrA as a locus for small molecule interactions that inhibit DNA binding. *Biochemistry* 2012, 51(50):10035-10043.

161. Sully EK, Malachowa N, Elmore BO, Alexander SM, Femling JK, Gray BM, DeLeo FR, Otto M, Cheung AL, Edwards BS *et al*: Selective chemical inhibition of agr quorum sensing in Staphylococcus aureus promotes host defense with minimal impact on resistance. *PLoS Pathog* 2014, 10(6):e1004174.

162. Daly SM, Elmore BO, Kavanaugh JS, Triplett KD, Figueroa M, Raja HA, El-Elimat T, Crosby HA, Femling JK, Cech NB *et al*: ω-Hydroxyemodin limits staphylococcus aureus quorum sensing-mediated pathogenesis and inflammation. *Antimicrob Agents Chemother* 2015, 59(4):2223-2235.

163. Canovas J, Baldry M, Bojer MS, Andersen PS, Grzeskowiak PK, Stegger M, Damborg P, Olsen CA, Ingmer H: Cross-Talk between *Staphylococcus aureus* and Other *Staphylococcal* Species via the agr Quorum Sensing System. *Front Microbiol* 2016, 7:1733.

164. Murray EJ, Crowley RC, Truman A, Clarke SR, Cottam JA, Jadhav GP, Steele VR, O'Shea P, Lindholm C, Cockayne A *et al*: Targeting Staphylococcus aureus quorum sensing with nonpeptidic small molecule inhibitors. *J Med Chem* 2014, 57(6):2813-2819.

165. Huan G, Dacheng R: Materials and surface engineering to control bacterial adhesion and biofilm formation: A review of recent advances. *Frontiers of Chemical Science and Engineering* 2014, 8(1):20-33.

166. Hsu LC, Fang J, Borca-Tasciuc DA, Worobo RW, Moraru CI: Effect of micro- and nanoscale topography on the adhesion of bacterial cells to solid surfaces. *Appl Environ Microbiol* 2013, 79(8):2703-2712.

167. Whitehead KA, Colligon J, Verran J: Retention of microbial cells in substratum surface features of micrometer and sub-micrometer dimensions. *Colloids Surf B Biointerfaces* 2005, 41(2-3):129-138.

168. Kastrup CJ, Boedicker JQ, Pomerantsev AP, Moayeri M, Bian Y, Pompano RR, Kline TR, Sylvestre P, Shen F, Leppla SH *et al*: Spatial localization of bacteria controls coagulation of human blood by 'quorum acting'. *Nat Chem Biol* 2008, 4(12):742-750.

169. Feng G, Cheng Y, Wang SY, Borca-Tasciuc DA, Worobo RW, Moraru CI: Bacterial attachment and biofilm formation on surfaces are reduced by small-diameter nanoscale pores: how small is small enough? *NPJ Biofilms Microbiomes* 2015, 1:15022.

170. Lagree K, Mon HH, Mitchell AP, Ducker WA: Impact of surface topography on biofilm formation by Candida albicans. *PLoS ONE* 2018, 13(6):1-13.

171. Micropatterned Surfaces for Reducing the Risk of Catheter-Associated Urinary Tract Infection: An In Vitro Study on the Effect of Sharklet Micropatterned Surfaces to Inhibit Bacterial Colonization and Migration of Uropathogenic Escherichia coli. In. United States: Mary Ann Liebert, Inc.; 2011: 1547.

172. Stoodley P, Boyle JD, Dodds I, Lappin-Scot HM: Consensus Model of Biofilm Structure. In.: Cardiff; BioLine: 1.

173. Stoodley P, Dodds I, Boyle JD, Lappin-Scott HM: Influence of hydrodynamics and nutrients on biofilm structure. *Journal Of Applied Microbiology* 1998, 85 Suppl 1:19S-28S.

174. Costerton JW, Geesey GG, Cheng KJ: How Bacteria Stick. *Scientific American* 1978(1):86.

175. Kümmel J, Stessl B, Gonano M, Walcher G, Bereuter O, Fricker M, Grunert T, Wagner M, Ehling-Schulz M: Staphylococcus aureus Entrance into the Dairy Chain: Tracking S. aureus from Dairy Cow to Cheese. *Frontiers In Microbiology* 2016, 7:1603-1603.

176. Avila-Novoa M-G, Iñíguez-Moreno M, Solís-Velázquez O-A, González-Gómez J-P, Guerrero-Medina P-J, Gutiérrez-Lomelí M: Biofilm Formation by Staphylococcus aureus Isolated from Food Contact Surfaces in the Dairy Industry of Jalisco, Mexico. *Journal of Food Quality* 2018:1-8.

177. Tong SYC, Davis JS, Eichenberger E, Holland TL, Fowler VG, Jr.: Staphylococcus aureus infections: epidemiology, pathophysiology, clinical manifestations, and management. *Clinical Microbiology Reviews* 2015, 28(3):603-661.

178. Fux CA, Wilson S, Stoodley P: Detachment Characteristics and Oxacillin Resistance of Staphylococcus aureus Biofilm Emboli in an In Vitro Catheter Infection Model. In. United States: AMERICAN SOCIETY FOR MICROBIOLOGY; 2004: 4486.

179. Brading MG, Jass J, Lappin-Scott HM: Dynamics of Bacterial Biofilm Formation. In*: 1995 1995; Great Britain*. CAMBRIDGE UNIVERSITY PRESS: 46.

180. Fleming D, Rumbaugh K: The Consequences of Biofilm Dispersal on the Host. *Sci Rep* 2018, 8(1):10738.

181. Ferreira Alves FR, Silva MG, Rôças IN, Siqueira Jr JF: Biofilm biomass disruption by natural substances with potential for endodontic use. *Brazilian Oral Research* 2013, 27(1):20.

182. Kiedrowski MR, Horswill AR: New approaches for treating staphylococcal biofilm infections. *Annals of the New York Academy of Sciences* 2011, 1241(1):104-121.

183. Parsek MR, Singh PK: BACTERIAL BIOFILMS: An Emerging Link to Disease Pathogenesis. *Annual Review of Microbiology* 2003, 57(1):677-701.

184. Use of International Standard ISO 10993-1, "Biological evaluation of medical devices - Part 1: Evaluation and testing within a risk management process" [https://www.fda.gov/downloads/medicaldevices/deviceregulationandguidance/guidancedocuments/ucm348890.pdf]

185. Alvarez LP, Barbagelata MS, Cheung AL, Sordelli DO, Buzzola FR: Salicylic acid enhances Staphylococcus aureus extracellular adhesin protein expression. *Microbes And Infection / Institut Pasteur* 2011, 13(12-13):1073-1080.

186. Herrmann M: Salicylic acid: an old dog, new tricks, and staphylococcal disease. *The Journal Of Clinical Investigation* 2003, 112(2):149-151.

187. Nowatzki PJ, Koepsel RR, Stoodley P, Min K, Harper A, Murata H, Donfack J, Hortelano ER, Ehrlich GD, Russell AJ: Salicylic acid-releasing polyurethane acrylate polymers as anti-biofilm urological catheter coatings. *Salicylsäure freisetzende Polymere aus Polyurethanacrylat als Biofilm vermeidende Beschichtungen in urologischen Kathetern* 2012(5):1869.

188. Alvarez LP, Barbagelata MS, Gordiola M, Cheung AL, Sordelli DO, Buzzola FR: Salicylic acid diminishes Staphylococcus aureus capsular polysaccharide type 5 expression. *Infection And Immunity* 2010, 78(3):1339-1344.

189. Dowd SE, Sun Y, Smith E, Kennedy JP, Jones CE, Wolcott R: Effects of biofilm treatments on the multi-species Lubbock Chronic Wound Biofilm model. *Journal of Wound Care* 2009, 18(12):508.

190. Kupferwasser LI, Yeaman MR, Shapiro SM, Nast CC, Sullam PM, Filler SG, Bayer AS: Acetylsalicylic acid reduces vegetation bacterial density, hematogenous bacterial dissemination, and frequency of embolic events in experimental Staphylococcus aureus endocarditis through antiplatelet and antibacterial effects. *Circulation* 1999, 99(21):2791-2797.

191. Kupferwasser LI, Yeaman MR, Nast CC, Kupferwasser D, Xiong Y-Q, Palma M, Cheung AL, Bayer AS: Salicylic acid attenuates virulence in endovascular infections by targeting global regulatory pathways in Staphylococcus aureus. *The Journal Of Clinical Investigation* 2003, 112(2):222-233.

192. Teichberg S, Farber BF, Wolff AG, Roberts B: Salicylic Acid Decreases Extracellular Biofilm Production by Staphylococcus epidermidis: Electron Microscopic Analysis. *The Journal of Infectious Diseases* 1993(6):1501.